



HAL
open science

Design, fabrication and characterization of a multimodal optical sensor with nanostructures

Melissa Najem

► **To cite this version:**

Melissa Najem. Design, fabrication and characterization of a multimodal optical sensor with nanostructures. Micro and nanotechnologies/Microelectronics. Université de Montpellier, 2022. English. NNT : 2022UMONS082 . tel-04117747

HAL Id: tel-04117747

<https://theses.hal.science/tel-04117747>

Submitted on 5 Jun 2023

HAL is a multi-disciplinary open access archive for the deposit and dissemination of scientific research documents, whether they are published or not. The documents may come from teaching and research institutions in France or abroad, or from public or private research centers.

L'archive ouverte pluridisciplinaire **HAL**, est destinée au dépôt et à la diffusion de documents scientifiques de niveau recherche, publiés ou non, émanant des établissements d'enseignement et de recherche français ou étrangers, des laboratoires publics ou privés.

THÈSE POUR OBTENIR LE GRADE DE DOCTEUR DE L'UNIVERSITÉ DE MONTPELLIER

En Électronique, Photonique et Systèmes

École doctorale Information, Structures, Systèmes

Unité de recherche Institut d'Electronique et des Systèmes, UMR5214

Conception, fabrication et caractérisation d'un capteur optique multimodal à nanostructures.

Présentée par **Melissa NAJEM**

Le 12 décembre 2022

Sous la direction de **Thierry TALIERCIO**

Devant le jury composé de

Nordin FELIDJ, Professeur des universités, Université Paris Diderot

Caroline BONAFOS, Directrice de recherche, CEMES-CNRS

Paolo BIAGIONI, Associate professor, Politecnico di Milano

Nathalie DESTOUCHES, Professeur des universités, Université Jean Monnet Saint-Etienne

Fernando GONZALEZ-POSADA FLORES, Maître de conférences, IES, Université de Montpellier

Thierry TALIERCIO, Professeur des universités, IES, Université de Montpellier

Président du jury

Rapporteur

Rapporteur

Examinatrice

Co-encadrant

Directeur de thèse



**UNIVERSITÉ
DE MONTPELLIER**

Acknowledgment

This thesis would not have been possibly achieved without the contribution of many people to whom I dedicate these few words.

First of all, I would like to thank all the members of my thesis committee. I thank Prof. Nordin Felidj for chairing the jury and for constantly showing interest in my work, Dr. Caroline Bonafos and Dr. Paolo Biagioni for taking the necessary time and effort to review the manuscript, I appreciate all your valuable comments and suggestions which helped me in improving the quality of the manuscript. Thank you Prof. Nathalie Destouches for appreciating my work and for your thoughtful notes and questions during the oral defense. I also want to thank you all for letting my defense be an enjoyable moment.

I would like to express my gratitude to my supervisor, Thierry Taliercio, who guided me throughout this project. Thank you for taking the time to discuss the simulation and the optical characterization results. I would like to thank Fernando Gonzalez-Posada for also supervising this thesis. Thank you for your great availability and also for your help and advice with the cleanroom and detection parts of this work. Thank you both for your assistance and for taking the time to discuss our research results, for always believing in my skills and supporting me during these three years in all the bittersweet situations.

I wish to extend my special thanks to Franck Carcenac for the outstanding technical and scientific exchange and for hosting me in the LAAS in Toulouse for the fabrication of the antennas using the EBL of the cleanroom and the metallization equipment. Thank you for enjoying taking the risk to engineer these sophisticated structures. I wish also to acknowledge the help provided by the technical staff in the CTM of the University of Montpellier, in particular, Frederic Pichot, Jean-Marie Peiris and Renaud Felix who helped me using the deposition machines, and for training me to manipulate acid solution. I would also like to show my deep appreciation to Michel Ramonda for all the AFM measurements, and to Philippe Camps and Boris Rigault, thanks to their IT assistance I was able to remotely launch all the FDTD simulations and to be easily connected to my work frame. Thanks to all the administration staff, specially to Karine Fleurot, Jean-Francois Gayraud, Daylet Ross and Ludivine Maisonneuve-Dordan.

I wish to thank Paolo Biagioni, Michele Celebrano and Attilio Zilli for hosting me in Politecnico di Milano for a week of non-stop optical measurements and discussions, and for the kind help of Francesco, Agostino, and Yigong.

I would like to thank my M2-internship supervisor Mikhael Bechelany for his support and for the SEM images acquired at the IEM. I would like to thank Prof. Claire Mangeney, Prof. Annemarie Pucci and Dr. Christian Huck for the fruitful discussions. Thank you Dr. Frank Neubrech for sharing the Eiler's smoothing program for the evaluation of SEIRA signals. Thank you Mrs. Aude Mezy and Mrs. Celine Schmitt from Sikémia for collaborating in the interpretation of the IR spectral lines. Thank you Dominique Coquillat and Jeremie Torres from Laboratory Charles Coulomb with whom I did some THz measurements for a parallel project.

A special thanks goes to the teaching team at the Faculty of Pharmacy, especially to Jerome Bourien, Patrick Azema, Joumana Florensa for supporting me and giving me the confidence as a teacher and for appreciating my PhD work. Best wishes for all my students. I also address a thought to all my school teachers and professors at the University of Montpellier and at the Lebanese University, thanks to whom I have formed my whole knowledge especially in physics, math, chemistry, coding, biology and nanomaterial science.

My thesis was carried out at the IES laboratory within the nanoMIR team. I wish to address my genuine thanks to the head of the laboratory Philippe Combette, and all the team members: to Eric Tournié, Aurore Vicet, Laurent Cerutti, Jean-Baptiste Rodriguez, Jean-Philippe Perez, Michaël Bahriz, Richard Arinéro, Yves Rouillard, Philippe Christol, Roland Tessier, Alexei Baranov, Ariane Meguekam, Jean-Marc Aniel and Guilhem Boissier, and to Zayneb and Hadrien from MIRsense. This is also an opportunity to wish a good luck for all the post-docs and the PhD students: Dilek, Daniel, Patricia, Anis, Tarek, Clara, Maxime, Julien, Pierre, Diba, Julien, Davide, Michele, Salah, Elena, Maeva, Andres, Audrey. I would like to thank my interns, Luka et Mohamed with whom I have worked for 3 months, thank you for your contributions to this research.

To my parents, I am here today thanks to your continued love and support. I am forever grateful for my caring and encouraging brothers, family and friends. At the end, thank you God for giving me the strength to keep going, and for being here at every single step of the way.

Contents

Lexicon.....	i
General introduction.....	1
Chapter 1: Plasmonics Overview and State-of-art	5
1.1. Overview of Plasmonics	7
1.1.1. Brief history: recall the past to build the future	7
1.1.2. The physics behind this emerging field	9
1.1.3. Scattering, absorption and extinction cross-sections.....	17
1.2. Generalities of plasmonic biosensors and gas sensors	19
1.2.1. Introduction to biosensors.....	19
1.2.2. SPR- Refractometric sensing	21
1.2.3. SERS and SEIRA sensing	25
1.3. Materials and designs for surface-enhanced sensing.....	30
1.3.1. Plasmonic materials	30
1.3.2. Plasmonic nanoantenna	33
1.4. Conclusion	47
1.5. Objectives of our study	48
Chapter 2: Conception of a barcode-like optical transducer	51
2.1. Total-field Scattered-field (TFSF) Source.....	54
2.1.1. Al prism free-standing, on SiO ₂ layer and in a MIM structure.....	55
2.1.2. Al Bowtie within a MIM	60
2.2. Plane-wave source	66
2.2.1. Coupling effects under light polarization for BT within a MIM in a 1D array.....	66

2.2.2.	Periodic BT arrays with different geometric parameters	68
2.2.3.	Compact configuration of Al triangles: Honeycomb-like resonators	75
2.3.	Conclusion	83

Chapter 3: Fabrication of a barcode-like optical transducer 85

3.1.	Main substrate fabrication	88
3.2.	Fabrication process of BT based on Metallization and Lift-off	92
3.2.1.	Dose test sample for all L and g values.....	94
3.2.2.	Final BT sample for visible and NIR coverage	96
3.2.3.	Final BT sample for a wide IR coverage	99
3.3.	Fabrication Process of HC with Dry Etching and Plasma Cleaning.....	101
3.3.1.	Argon etching optimization	101
3.3.2.	Final HC sample for a wide IR coverage.....	106
3.4.	Conclusion	112

Chapter 4: Optical characterization of a barcode-like optical transducer... 113

4.1.	The experimental setups.....	115
4.2.	BT Optical Transducer properties	117
4.2.1.	BT covering the visible and the NIR ranges	117
4.2.2.	BT covering the IR	119
4.3.	HC Optical Transducer properties	125
4.3.1.	Side length (L) effect	125
4.3.2.	Gap (g) effect	127
4.3.3.	Polarization effect.....	128
4.3.4.	Comparison of both EBL exposure modes.....	129
4.4.	Conclusion	131

Chapter 5: SEIRA sensing investigation using Aluminum metasurfaces	133
5.1. Oxide stability.....	134
5.2. SEIRA Sensing proof	135
5.2.1. Al-Bowties for SEIRA demonstration	136
5.2.2. Al-Honeycombs for SEIRA demonstration	150
5.2.3. Gas-SEIRA sensing.....	157
5.3. Conclusion	162
General Conclusions and Perspectives	165
Bibliography.....	171
Annexes.....	187
1.1. Annexe.1.1. Wave vector matching mechanisms.....	187
1.1.1. Evanescent coupling	187
1.1.2. Grating coupling.....	188
1.2. Annexe.3.1. Trial sample: BT and HC fabrication by metallization and lift-off.....	189
Morphology SEM and AFM images.....	191
1.3. Annexe.3.2. Morphology analysis in relation to the dose factor.....	193
1.4. Annexe.3.3. Table 1 and 2 for the small BT, L, and g	196
1.5. Annexe.3.4. Argon etching optimization	198
1.6. Annexe.5.1. SEIRA vibrational signal calculation	201
1.7. Annexe.5.2. EF error propagation formula	203
Communication	205
Abstract	207
Résumé.....	209

Lexicon

AFM	atomic force microscopy
Al	Aluminum
anisole	methoxybenzene
BC	Background correction
BL	baseline
BT	Bowties
CaF ₂	calcium fluoride
CBP	4,4'-bis(N-carbazolyl)-1,1'-biphenyl layer
CMOS	Complementary Metal Oxide Semiconductor
CO ₂	carbon dioxide
Co-pol	E-field component along the tip-to-tip faced triangles
Cross-pol	E-field component across the tip-to-tip faced triangles
DMSO	dimethyl sulfoxide
EBL	electron beam lithography
EDX	energy-dispersive X-ray spectroscopy
EF	enhancement factor
FDTD	finite-difference time-domain
FEG	field emission gun
FPA	focal plane array
FTIR	Fourier-transform infrared
FWHM	full width at half maximum
<i>g</i>	gap
HC	Honeycomb
HF	hydrofluoric acid
ICP	inductively coupled plasma
IPA	isopropanol
KBr	potassium bromide
<i>L</i>	length of the triangle's side
LSPR	localized surface plasmon resonance
MCT	mercury-cadmium-telluride

MIBK	methyl isobutyl ketone
MIM	metal-insulator-metal
N. A.	numerical aperature
NA	nanoantenna
ODT	octadecanethiol
PECVD	plasma enhanced chemical vapor deposition
PML	perfectly matched layer
PMMA	polymethylmethacrylate
RF	radio-frequency
RI	refractive index
RIU	refractive index unit
RMS	roughness mean square
SA	stearic acid
SAM	self-assembled monolayer
SEIRA	surface-enhanced infrared absorption
SEM	scanning electron microscope
SERS	surface-enhanced Raman scattering
SiC	silicon carbide
SNR	signal-to-noise ratio
SPR	surface plasmon resonance
TFSF	total-field scattered-field
4-NTP	4-nitrothiophenol
A_0	area/volume as reference unit cell
A_{SEIRA}	active areas/volume covered/filled with molecules
A_{eff}	smallest effective area/volume
S_0	unenhanced signal strength
S_{SEIRA}	enhanced signal strength
ω_{res}	plasmonic resonance frequency
ω_{vib}	molecular vibration frequency
$\omega_{vib}/\omega_{res}$	tuning ratio

General introduction

Biosensors have received great interest and investments in the last decade in a wide scope of applications ranging from medical analysis, healthcare, control and development of pharmaceuticals, food safety up to environmental monitoring, agriculture, defense, and security. They can be integrated into various point-of-care systems, such as for water quality, forensics, and drug delivery. Given their interactions with high-affinity biomolecules, they find application in the sensitive detection of analytes, even in small sample volumes.

Recently, during the COVID-19 crisis, biosensors are incorporated into the rapid detection kits. Plasmonic-based biosensors have the potential to reach high sensitivity and specificity for the detection of molecules using optical read-out techniques. Indeed, surface plasmon-polaritons (SPPs) are collective oscillations of an electron cloud at the metal/dielectric interface coupled to an incident electromagnetic wave, generating strong field confinement and enhancement. Moreover, the SP frequency depends on the refractive index of the dielectric material. Hence, SP can be useful for measuring the variation of the refractive index induced by the presence of an analyte and/or for enhancing its absorption features.

The main requirement of such a biosensor is boosting the performance of the optical transducer such as its sensitivity, fast-response time, reproducibility, and low detection limits even down to individual molecule detection. In line with this, to enhance the interaction between the plasmonic evanescent field and the deposited molecule, the surface is tailored to simply couple the incoming light with any wave vector k . As consequence, the near-field is locally confined at the extremities of the metallic nanostructures, owing to the lightning-rod effect. Thus, compared to other conventional biochemical assays, localized surface plasmon resonance (LSPR) biosensing might be an extremely sensitive, label-free, and real-time method. It is suitable for measuring the slight variation of the surrounding medium refractive index induced by the adsorbed molecules at the vicinity of the nanostructures compared to the commercial SPPs sensors.

In addition to the LSPR sensing, this manuscript contributes to an innovative technique to enhance the interaction cross-section of molecules in the promising IR range, where the molecular fingerprint and the functional groups of any living tissue are found. Furthermore, surface

nanostructures exhibit great potential to overcome the weak interaction cross-sections from which classic Raman and IR spectroscopies suffer, typically between the micrometric dimension of the incident radiation and the nanometric molecules. For surface-enhanced spectroscopy techniques, surface engineering plays a major role in further enhancing the near EM-field, especially once the nanostructures are closely placed, producing the so-called gap effect.

Furthermore, the substrate can be cleverly built to sustain advanced near EM-field confinements. In particular, a metal-insulator-metal (MIM) configuration with a thin spacer can promote gap-plasmon effects, thus reinforcing the local confinement. The near-field enhancement of the plasmonic nanoantennas combines the lightning-rod and the gap effects at the antenna hotspots. The surface-enhanced infrared absorption (SEIRA) spectroscopy benefits from the coupling between the molecules placed at the hotspots and the enhanced near EM-fields. This resonant SEIRA is expressed as asymmetric features, *i.e.* Fano-like profiles, by tuning the plasmonic resonances (via a change in the antenna length) with the spectral signal of the molecules. Moreover, our designed platform is multiresonant in a wide IR range. Thus, it is suitable for a flexible detection of many characteristic features of any molecule in a single test.

The limitation of biosensors is their cost-effective miniaturization. The intrinsic volume of the most studied transducers is not compatible with the miniaturization in a lab-on-a-chip platform. However, the advancement of silicon photonics technology proposes a miniaturization of measurement devices with a conceivable integration of a source, a detector, mirrors, lenses, and spectrometers into the same platform. Hence, in this manuscript, we present a Si-based MIM structure, in which aluminum is used as an alternative material to gold and silver as it presents good optical quality in the IR, more affordable, abundant, and CMOS compatible. Thus, such a platform is promising for the mass-production of competitive and reasonably-priced portable devices.

This doctoral thesis is concerned with the conception, fabrication, and optical characterization of a MIM-integrated multiresonant surface of bowties and honeycomb structures to locally enhance the near EM-fields at their sharp apexes. An extra enhancement is provided thanks to the thin spacer layer of the MIM configuration sustaining a gap-plasmon effect. To tune the spectral

overlap between the plasmonic resonance of the antennas and the addressed molecular vibration frequencies, the geometric parameters of both antennas types, namely the triangle side length, L , and their tip-to-tip and corner-to-corner gaps, g , are subsequently varied. The effect of the light polarization on the far-field and the near-field behaviors of both nanostructures will be considered as well.

The thesis manuscript is organized in five chapters. It retraces the four main skills assimilated in the framework of this thesis: numerical simulation, cleanroom fabrication, optical characterization, and data analysis and realization of SEIRA detection in a wide spectral range using advanced plasmonic nanostructures to address the IR absorption features of liquid and gas analytes.

Chapter 1 introduces a global theoretical background by giving an overview of the plasmons theory and notably localized surface plasmons-polaritons. The characteristics of the material of choice for plasmonic applications will be discussed, and an alternative material to noble metals will be proposed. The design of the plasmonic resonators will be reported especially for those tailored using electron beam lithography (EBL). Some generalities of plasmonic biosensors and gas sensors will be presented. The materials and designs for surface-enhanced sensing are offered. IR spectroscopy techniques, namely surface-enhanced IR spectroscopies are detailed. Special attention will be devoted to the design and the composition of the SEIRA-serving substrates. Given the extensiveness of plasmonic-based applications, the last section of **Chapter 1** will be dedicated to offering a glance at the most advanced findings in SEIRA sensing. In the end, the objectives of the thesis developed in the manuscript are presented.

Chapter 2 will focus on the conception of the structures using numerical finite-difference time-domain (FDTD) simulations, starting with a single equilateral triangle up to periodic arrays of bowties toward a compact honeycomb-like arrangement of triangles. The fabrication approaches of both plasmonic nanoantenna arrays will be the subject of **Chapter 3**. Both methods succeeded by combining electron beam lithography, EBL, with either metallization and lift-off processes for bowties, or physical etching and resist cleaning for honeycombs. The fabricated antennas will be

then optically characterized via a Fourier transform infrared (FTIR) spectrometer, the results are highlighted in **Chapter 4**. Numerical simulations are recalled to support the experimental results.

Chapter 5 deals with the proof-of-concept of a broadband SEIRA demonstration to detect analytes such as organic molecules in solution and inorganic gas compounds. Based on the acquired understanding from numerical approaches and the optical characterizations, the surface-enhanced sensing with Al-based plasmonic nanostructures is successfully proved and is showing some promising results that match the SEIRA state-of-art.

Financial Acknowledgments:

This research project was done in collaboration with LAAS-CNRS micro and nanotechnologies platform, a member of the Renatech French national network. I acknowledge a doctoral grant from the National French Ministry for University Education, Research, and Innovation. Partial fundings are acknowledged from the following projects: SEA (Occitanie French Region-ESR-PREMAT-238), EXTRA (ANR 11-EQPX-0016), NanoElastir (ASTRID 2020-2023), and ENVIRODISORDERS (MUSE UM 2021-2023).

Chapter 1: Plasmonics Overview and State-of-art

Science is like a brick wall, let's build it up.

This first chapter will give an overview of Plasmonics and its different excitations. The characteristic of the material of choice for Plasmonic applications will be discussed, and an alternative material will be proposed. Plasmonics has a long history, from stained glass in ancient cathedrals, all the way into the actual nanotechnology era, where it blossoms as an extremely active field of research with potential applications in a wide variety of expertise.

The continuous evolution of nanofabrication techniques in the past decades has enabled the controlled fabrication of devices with sub-100 nm features, allowing the investigation and control of physical phenomena at the nanoscale. Certainly, one of the fields that has benefited the most from this miniaturization trend is plasmonic-based sensing, where the integration of various plasmonic resonators on a single chip has steadily increased over the years, as anticipated by Moore.

Given the breadth of the materials, phenomena, and applications related to plasmonics, this chapter will be dedicated to offering a glance at the most advanced findings in plasmonic-enhanced absorption sensing in the IR.

To gain a wider and a deeper view of the physics of light interaction with metal nanostructures and for a complete theoretical background about plasmonics, readers are invited to check the Maier's book,¹ and to attend the edX MOOC "Plasmonics: From Fundamentals to Modern Applications" online class.²

The chapter ends with a presentation of the thesis project and a definition of the desired objectives.

Contents

Chapter 1: Plasmonics Overview and State-of-art.....	5
1.1. Overview of Plasmonics.....	7
1.1.1. Brief history: recall the past to build the future	7
1.1.2. The physics behind this emerging field	9
1.1.3. Scattering, absorption and extinction cross-sections	17
1.2. Generalities of plasmonic biosensors and gas sensors	19
1.2.1. Introduction to biosensors	19
1.2.2. SPR- Refractometric sensing	21
1.2.3. SERS and SEIRA sensing.....	25
1.3. Materials and designs for surface-enhanced sensing	30
1.3.1. Plasmonic materials	30
1.3.2. Plasmonic nanoantenna	33
1.4. Conclusion.....	47
1.5. Objectives of our study.....	48

1.1. Overview of Plasmonics

1.1.1. Brief history: recall the past to build the future

“Let there be light” and it was light (Genesis 1:3). Since the commencement, light glory is underlined. Light is vital: as humans, we need light to see, then based on what is seen, one can perceive. Dating back to the very beginning of civilization, optical glamour has been highlighted: people admire the shiny attractiveness of gold, silver, and all precious stones as charming accessories. From auroras and rainbows to the human eye, light has fascinated scientists for centuries. Plus, scientists wanted to understand the motion of the moon and the stars by observing the night sky. Thus, the fabrication of glass lenses was the only solution to overcome the limitation of our naked eyes: telescopes for seeing distant objects and microscopes for seeing the otherwise invisible tiny objects. Both perspectives were exanimated around the same decade in which Snell’s law was proposed in 1626. The base of this optical performance remains in the light-matter interaction response.

Then, since the prediction of Prof. Ritchie in 1957, about the existence of self-sustained collective oscillations at the metal surface taking into account energy losses characteristic, a great interest has been dedicated to implement these collective electron density waves. Known as surface plasmons (SP), they could couple to light in specific conditions. The effects of SP on optical properties can be amazing. Some of the most stunning plasmonic effects are not even found in modern research labs but in a visit to a museum or medieval cathedrals. Medieval glass blowers used unconsciously metallic nanostructures with strong plasmonic effects. The Lycurgus cup in the British Museum in London (**Figure 1.1a**) whose glass looks green in reflected light but ruby red in transmitted light,³ and some stained-glass windows in cathedrals such as the “Christ of Wissembourg” (**Figure 1.1b**) and the rose window in the gothic Notre Dame de Paris (**Figure 1.1c**) are the most prominent examples of this art.^{4,5} The presence of noble metal nanoparticles with different sizes and geometries embedded in the glass yields magnificent colors that can be observed from inside the cathedral (transmitted light), while from the outside (reflected light), these windows appears colorless.⁶

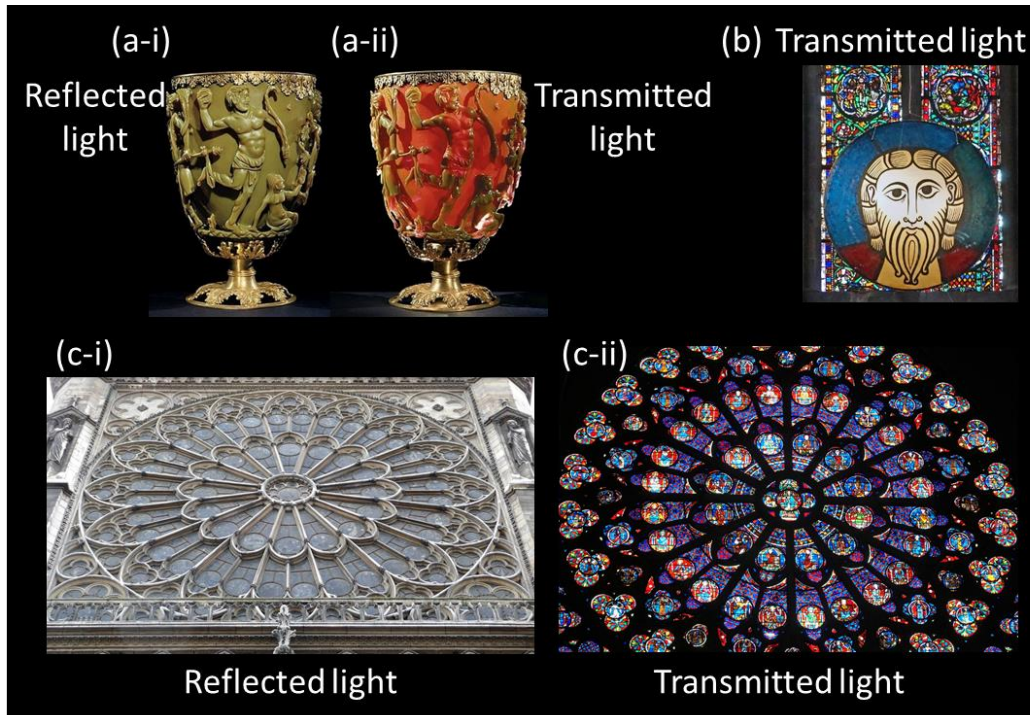


Figure 1. Plasmonics in medieval art. (a) The Lycurgus cup in the British Museum in London (4th century) looks (a-i) “opaque - green” with reflected light, and (a-ii) “deep wine-red” with transmitted light. <https://www.amusingplanet.com/2016/12/lycurgus-cup-piece-of-ancient-roman.html>. Those colors are complementary, evidence that there is little optical loss inside the glass. Some stained-glass windows in cathedrals such as (b) the “Christ of Wissembourg” (a medieval artistic window 11th century) from https://commons.wikimedia.org/wiki/File:Le_Christ_de_Wissembourg_%28%C3%89glise_St_Pierre_et_St_Paul,_Wissembourg%29_%2835412275323%29.jpg) and (c) the rose window in Notre Dame de Paris (12th century), photographed from (c-i) outside and (c-ii) inside, check <https://www.scientifiquesnotre-dame.org/les-roses-les-vitraux>.

The ability of the SP to interact with light at wavelengths much longer than the size of those nanostructures, and the capability to modify and manipulate the local light fields makes Plasmonics such an attractive field of research. “Plasmonics has given to Photonics the ability to go to the nanoscale and properly takes its place among the nanosciences,” as Harry Atwater, a physicist from the California Institute of Technology, describes it. Furthermore, “Plasmonics” as research-specialty name was firstly given by Harry Atwater’s group at the beginning of 2000s, following the discovery of the extraordinary optical transmission (EOT) by Thomas Ebbesen in 1998. As he illuminates a thin film of metal containing millions of nanometre-sized holes, Ebbesen found that the metallic film was more transparent than he expected.⁷ The holes were much smaller than the wavelength of visible light, which should have made it almost impossible for the light to get through them all. However, when the incoming photons struck the metal film, they

excited SP around its natural oscillation frequency, which select photons and carried them through the holes, re-radiating them to the other side of the film, thus, giving its transparency. Thus, plasmons can focus light into the tiniest of spots, direct it along complex circuits or manipulate it in many other ways. Far below the resolution limits of conventional optics, plasmons can couple light at the nanoscale, *i.e.* several orders of magnitude smaller than the light's wavelength.¹ Hence, Plasmonics has become one of the hottest fields in Photonics. Besides, inspired by the vision of Richard Feynman in 1959, "*There's Plenty of Room at the Bottom*", Plasmonics is nowadays involving all the studies that are concerned with the originality, the fabrication, and the application of plasmon-based nanostructures. Owing to the recent flowering of nanotechnology,⁸ which brought with it a multiplication of techniques for fabricating structures at the nanoscale, Plasmonics is progressing from laboratory curiosity to practical applications. Plasmonics is exploring potential applications in solar cells,^{9,10} biosensing,¹¹ gas sensing,^{4,12} optical computing,¹³ and even cancer early detection and treatments.^{14,15} A new awareness of the social impact of this research has arisen as a consequence of the COVID-19 pandemic.¹⁶

1.1.2. The physics behind this emerging field

Plasmonics is the research field that investigates the interaction of electromagnetic waves with the free-electrons in metals.¹ Such a behavior was predicted by German physicist Paul Karl Ludwig Drude more than 100 years ago.^{17,18} Advanced comprehension of light as an electromagnetic wave is considered a great starting point to describe and understand Plasmonics. The coupling of incident photons with the density wave oscillation of free carriers (electron cloud), mainly existing at metal/dielectric interface, generates the so-called plasmonic resonance. The interaction of metals with electromagnetic fields can be firmly understood in a classical framework based on Maxwell's equations.

The optical properties of metals can be explained by a plasma model, where a gas of free-electrons moves against a fixed background of positive ion cores, *i.e.* is delocalized, under the influence of a driving electric field, illustrated in **Figure 1.2**.

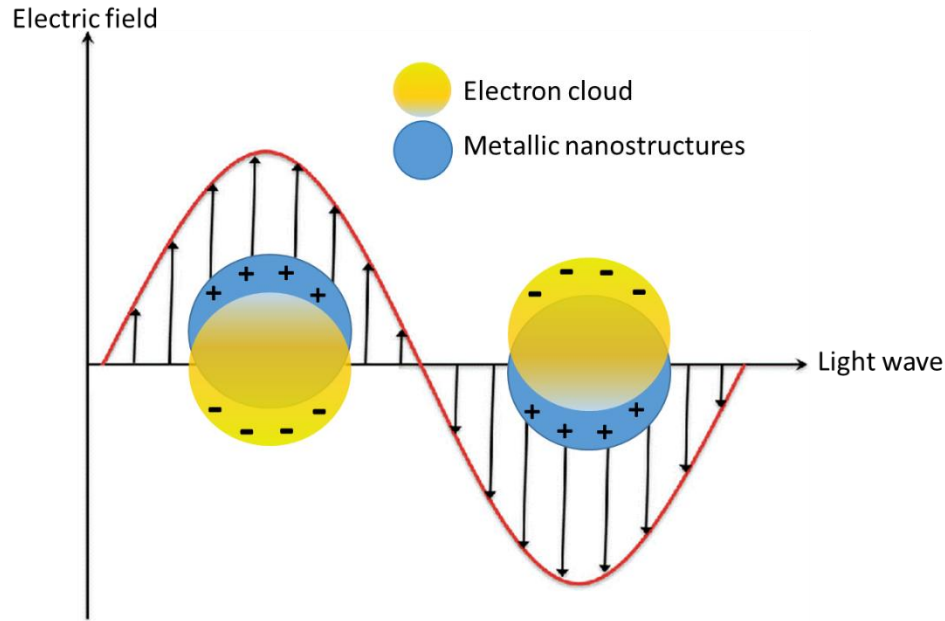


Figure 1. 2. Schematic of a collectively oscillating electron cloud as free charges in a metallic particle. The driving force is the applied electromagnetic field of a light wave.

The quantum of these charge oscillations in metal is called plasmons. Plasmon, phonon and photon are quantum quasi-particles because they decay in space or over time. While the quantum of the electromagnetic (EM) wave propagating in vacuum is a photon, it is called polariton when the EM wave propagates into the matter. Polariton is also a quasi-particle and can couple to the elementary excitation of the medium consisting of free-electrons, *i.e.* plasmons, creating thus a form of mixed excitations like the plasmon-polariton.

To describe the reaction of a material to an EM field, the dielectric function $\epsilon(\omega)$ is provided thanks to a simple model included in the extension of the Lorentz model, named the Drude model. In other words, the electron gas directly defines the response of metals to an external EM field, so it gives the main contribution to the metal permittivity.

Note that the Drude dielectric function $\epsilon(\omega)$ links the electric field \mathbf{E} with the electric displacement vector \mathbf{D} in the matter, and it defines a dipole polarizability (Lorentzian description).

Drude model permittivity of free-electron gas is described in **Equation 1.1**, as:

$$\epsilon(\omega) = 1 - \frac{\omega_p^2}{\omega^2} \quad (1.1)$$

where $\omega_p^2 = \frac{n|e|^2}{\epsilon_0 m_e}$ and ω_p is the plasma frequency, which depends on the charge of the carriers, their mass, and concentration. The permittivity is a function of the frequency. Here $\epsilon_\infty = 1$ for a perfect Drude metal, a free-electron gas model where the contribution of bound electrons which are localized in the vicinity of ions is neglected.

It is important to analyze the frequency dependence of the metal permittivity predicted by Drude, and as illustrated in **Figure 1.3**:

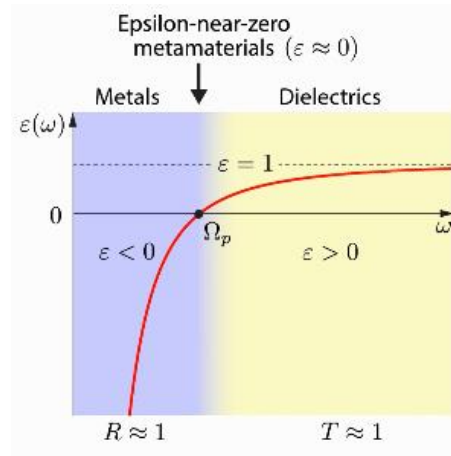


Figure 1.3. The frequency dependence of the Drude dielectric function $\epsilon(\omega)$ for both metallic and dielectric zones.²

- $\omega < \omega_p$: $\epsilon < 0$; $\epsilon \rightarrow -\infty \rightarrow R \approx 1$ (negative permittivity results in a high reflectivity of metals)
- $\omega > \omega_p$: $\epsilon > 0$; $\epsilon \approx 1 \rightarrow T \approx 1$ (where electron gas is almost transparent for EM waves)
- $\omega \approx \omega_p$: $\epsilon \approx 0 \rightarrow$ epsilon-near-zero phenomena, under active study in metamaterial community, this behavior can be achieved at fixed frequency in metal (plasma frequency) or dielectric (phonon frequencies) or at tunable frequency with heavily doped semiconductors.¹⁹

Given the accidental collisions of electrons, absorption of energy from the incident EM wave arises. Hence, the Drude model permittivity of metal could be written as in **Equation 1.2**:

$$\epsilon(\omega) = \epsilon_\infty \left(1 - \frac{\omega_p^2}{\omega(\omega + i\gamma)} \right) \quad (1.2)$$

where $\gamma = \frac{1}{\tau}$ is the momentum relaxation time (damping parameter) and τ is the mean free path time. ϵ_∞ is the material permittivity at high frequencies, and is often defined as 1 for the response of a free electron gas or an ideal material without any background polarizability.

1.1.2.1. Surface plasmons

Due to the longitudinal nature of the excitation, “pure” plasmons do not couple to transverse electromagnetic waves as free space incident light. Plasmons relevant to plasmonics applications are the surface plasmon-polaritons (SPP). In general, there are two different types of SP: those propagating along a planar metal/dielectric interface, which are usually called surface plasmon polaritons (SPPs), and those localized at metallic nanoparticles, which are usually called localized surface plasmons (LSPs). SPPs and LSPs are of the same physical origin, but their appearances are quite different. Despite this, both of them exhibit electromagnetic fields which are localized at metallic surfaces and significantly enhanced compared to the excitation fields.

Let’s consider an EM wave propagating along the metal/dielectric interface. The coordinate system is shown in **Figure 1.4**. The interface relies in the xy - plane ($z = 0$). The bottom half space ($z < 0$) is occupied by the metal and the upper half space ($z > 0$) consists of the dielectric. The wave propagates along the x - axis. It has necessarily two components of the electric field, E , following the interface (along x -axis) and normal to the interface (along z -axis), and a component of the magnetic field, H , along the y -axis. The SPP are electromagnetic excitations propagating at the metal/dielectric interface, and are essentially two-dimensional electromagnetic waves. By solving Maxwell’s equations, and considering Helmholtz’s equations, the following conclusions are found:

- SPP is a wave as E & H are found proportional to $e^{-i\omega t + ik_z z}$, \mathbf{k}_z is the wave vector component along the z -axis (in the normal plane to the metal/dielectric interface).
- SPP is defined as a hybrid TM electromagnetic mode with a transverse and a longitudinal E-Field component, $E (E_x, 0, E_z)$ and $H (0, H_y, 0)$, where no solution is found in TE-polarization form, as illustrated in **Figure 1.4a**.
- SPP is a surface EM wave propagating along the interface metal/dielectric following the golden rule $\epsilon_1 \epsilon_2 < 0$ to obtain a nontrivial solution for the dispersion equation.

- SPP is pinned at the surface: $E \& H \sim e^{-ik|x|}$, where k is the inverse of penetration depth of the incident field and it is responsible of the exponential decay component of the field in both media (metal and dielectric), as described in **Figure 1.4b**.
- The dispersion equation found by solving the Helmholtz equation for TM-polarization is given by **Equation 1.3**. k_{spp} is the SPP wave vector, defined as well along x -axis (the metal/dielectric interface) by k_x . Note, the metal media is at the negative- z part (bottom part), while the dielectric media is at the positive- z part (top part), having ϵ_m and ϵ_d as respective permittivities.

$$k_x = k_{SPP} = \frac{\omega}{c} \sqrt{\frac{\epsilon_m \epsilon_d}{\epsilon_m + \epsilon_d}} \quad (1.3)$$

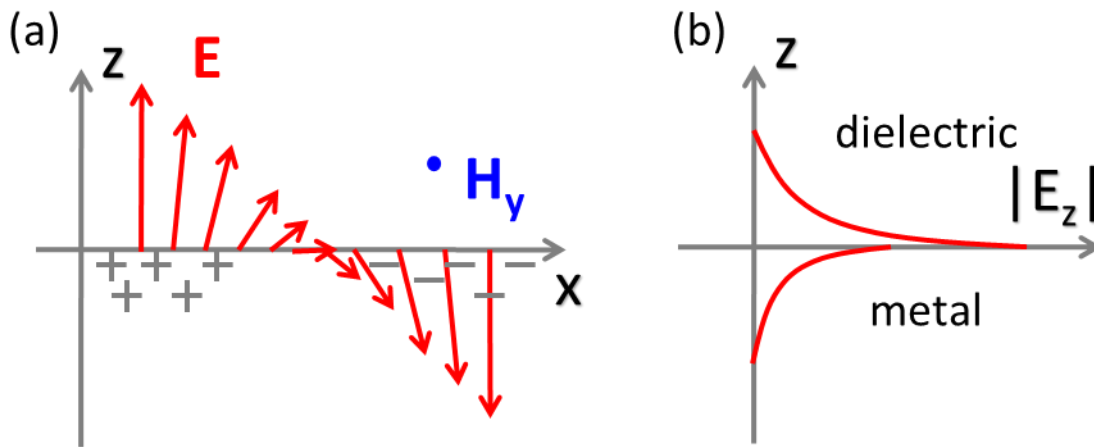


Figure 1. 4. SPP at the metal (bottom part)/dielectric (top part) interface. (a) SPP is a hybrid electromagnetic mode with a transverse and a longitudinal E-Field component. (b) SPP is pinned at the metal/dielectric interface and E-Field decays in both media.

Noteworthy, the field confinement is achieved since the SPP wave vector, k_{spp} , is greater than the wave vector k in the dielectric, leading to evanescent decay on both sides of the interface. Indeed, at the resonance SPP becomes strongly localized in the vicinity of the interface, which induces a strong enhancement of the local EM-field. This enhancement is crucial for many plasmonic-based applications such as for surface-enhanced sensing, as it will be further detailed in this manuscript.

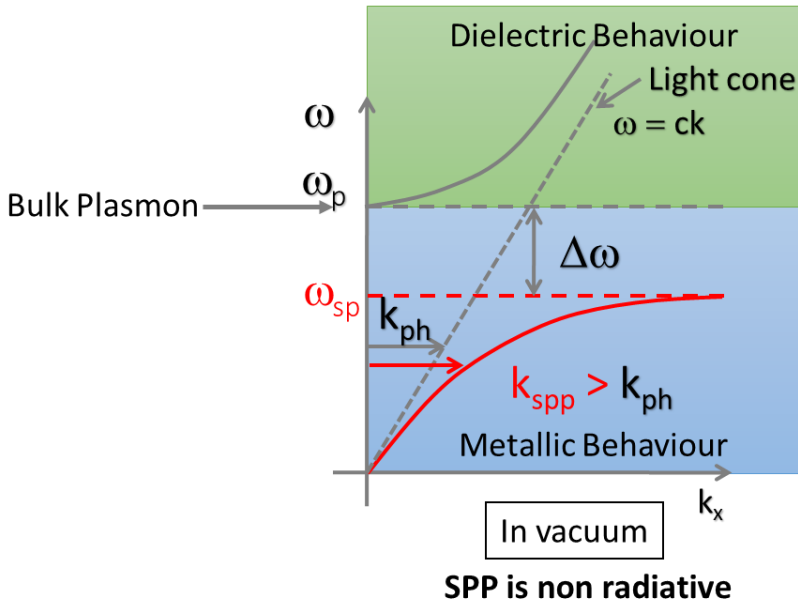


Figure 1.5. The dispersion curve of SPP lies outside the light cone since the SPP wave vector, k_{spp} , is larger than the in-plane component of the incident photon's wave vector, k_{ph} . The coupling between SPP and light cannot occur. SPP is thus nonradiative.

However, the SPP dispersion curve lies outside the light line as illustrated in **Figure 1.5**. For a given energy, the in-plane component of the incident photon's wave vector, k_{ph} , is smaller than the one of a SPP. So the coupling cannot occur unless special techniques for phase-matching are employed. Coupling mechanisms via prisms or gratings allow to match the wave vectors of the photon and the SPP. For more details about the wave vector matching mechanisms, please refer to **Annexe 1.1**. These coupling tools are complicated to implement, yet, individual metallic objects can sustain localized SPP which are excited by any wave vector, and can couple to the outgoing light. Localized SPP (or simply LSP) are radiative modes, easily accessible in comparison with the excitation of SPP modes in layered systems which require sophisticated coupling mechanisms.

1.1.2.2. Localized surface plasmons

Individual metallic objects of subwavelength size like nanoparticles sustain localized surface plasmon modes. Due to the rupture of the symmetry in the 3 directions of space, the SPPs are localized and can be excited by any wave vector \mathbf{k} . For an analytical evaluation of the LSP, the Mie theory and the quasi-static approximation are usually addressed, treating the case of a subwavelength spherical particle. The deep description of both methods goes beyond the purpose of this general introduction to Plasmonics. For more theoretical details, please refer to

Barho's thesis.²⁰ Nevertheless, based on the quasi-static approximation (where $\lambda \gg 2R$, R is the sphere radius) a sphere made of an ϵ_m of permittivity material is placed in a surrounding media of an ϵ_d as permittivity, this system is placed into an external homogenous electric field, E_0 its amplitude. In consequence, some positive and negative electric charges will appear on the opposite sides of the sphere as illustrated in **Figure 1.6**:

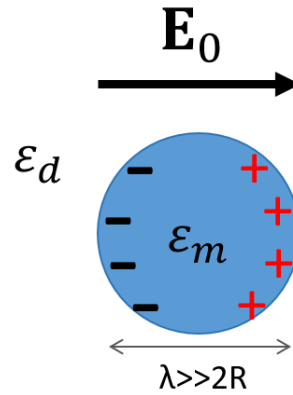


Figure 1. 6. A metallic sphere made of an ϵ_m of permittivity material is placed in a surrounding media of an ϵ_d permittivity. The system is placed into an external homogenous electric field, E_0 its amplitude, inducing a positive and negative electric charge distributions on the opposite sides of the sphere.

\mathbf{p} is the electric dipole vector and it describes the field outside of the nanoparticle, so this dipole moment governs the field in the dielectric medium. The electrical dipole is proportional to the external electric field, as in **Equation 1.4**,

$$\mathbf{p} = \alpha \mathbf{E}_0 \quad (1.4)$$

where α is the coefficient that ties together these two quantities namely, the electric polarizability, or electric dipole polarizability coefficient, as in **Equation 1.5**:

$$\alpha = 4\pi\epsilon_0\epsilon_m R^3 \frac{\epsilon_m - \epsilon_d}{\epsilon_m + 2\epsilon_d} \quad (1.5)$$

The polarizability strongly depends on the volume of nanoparticle, R^3 , and then on the permittivities ratio.

- For normal dielectric materials, where $\epsilon_m, \epsilon_d > 0$, $\epsilon_m + 2\epsilon_d > 0$

- For metals, $\varepsilon_1(\omega) < 0$, $\varepsilon_m = -2\varepsilon_d$, $\varepsilon_m + 2\varepsilon_d \rightarrow 0$, this condition is what is called localized surface plasmon resonance, for which $\alpha \rightarrow \infty$, so, a strong enhancement of polarizability is obtained (**Equation 1.5**). In this case, the Drude model will give **Equation 1.6**:

$$\omega \rightarrow \omega_{LSPR} = \frac{\omega_p}{\sqrt{2\varepsilon_d + \varepsilon_\infty}}, \text{ as } \varepsilon_m = \varepsilon_\infty - \frac{\omega_p^2}{\omega^2} \quad (1.6)$$

Note, in reference to **Equation 1.2**, the damping parameter γ is not considered in **Equation 1.6**. However, the background polarizability ε_∞ is taken into account as it represents a residual polarization due to the positive background of the ion core (**Figure 1.2**).

In sum, the resonance conditions are indicated in **Table 1.1**, in the simplified cases of quasi-static treatments for bulk plasmon, for the planar surface, resulting in the SP frequency, and for the sphere, resulting in the dipolar plasmon frequency. They are found by inserting the dielectric function of the metal described by a Drude model at the resonance condition.¹ Noteworthy, the surface resonances depend on the surrounding medium refractive index as $\varepsilon_d = n^2$. Therefore, are extremely promising for the surface-enhanced sensing.

Structure	Resonance condition	Resonance frequency Drude metal ($\varepsilon_\infty = 1$)	Resonance frequency of a Drude metal in vacuum $\varepsilon_d = 1$
Bulk metal	$\varepsilon_m(\omega_p) = 0$	$\omega_p = \sqrt{\frac{Ne^2}{m_0\varepsilon_0}}$	ω_p
Metal surface	$\varepsilon_m(\omega_{sp}) = -\varepsilon_d$	$\omega_{SPP} = \frac{\omega_p}{\sqrt{\varepsilon_d + \varepsilon_\infty}}$	$\omega_{sp} = \frac{\omega_p}{\sqrt{2}}$
Metal sphere	$\varepsilon_m(\omega_{lsp}) = -2\varepsilon_d$	$\omega_{LSPR} = \frac{\omega_p}{\sqrt{2\varepsilon_d + \varepsilon_\infty}}$	$\omega_{lsp} = \frac{\omega_p}{\sqrt{3}}$

Table 1. 1. Summary of the different structures and their corresponding resonance conditions and frequencies based on the description of the Drude dielectric function.

1.1.3. Scattering, absorption and extinction cross-sections

For an electromagnetic wave, the scattering (or absorption) cross section is introduced by the ratio between the power of the scattered light at the object surface (or the absorbed power inside the object), and the power of incident light flux which is passing through a particular unit area, as detailed in **Equation 1.7**.

$$\sigma_{scat/abs} [m^2] = \frac{W_{scat/abs} [Watts]}{I_{inc} [watts/m^2]} \quad (1.7)$$

By summing up these two quantities (**Equation 1.8**), the extinction cross-section could be obtained, representing what exactly happens with photons, some of them are scattered, others are absorbed.

$$\sigma_{ext} = \sigma_{scat} + \sigma_{abs} \quad (1.8)$$

The total scattering cross-section, σ_{ext} , represents the amount of energy detected on the far-away collector, after scattering (diffusion) and absorption.

Let's define a geometric size parameter $x = kR$ for a metallic nanosphere (ϵ_m) with radius R , having a dielectric material (ϵ_d). Considering a Rayleigh particle ($\lambda \gg 2R$), the quasi-static limit is introduced to study the scattering/absorption cross section for small nanoparticles,² for example, **Equation 1.9-1.12** are retrieved as:

$$\sigma_{abs} = \frac{k}{\epsilon_0 \epsilon_d} \text{Im}(\alpha) = 4\pi x R^2 \text{Im}\left(\frac{\epsilon_m - \epsilon_d}{\epsilon_m + 2\epsilon_d}\right) \quad (1.9)$$

$$\sigma_{sca} = \frac{k^4}{6\pi \epsilon_0^2 \epsilon_d} |\alpha|^2 = \frac{8}{3} \pi x^4 R^2 \left| \frac{\epsilon_m - \epsilon_d}{\epsilon_m + 2\epsilon_d} \right|^2 \quad (1.10)$$

Noteworthy, σ_{abs} is proportional to the imaginary part of the quasi-static polarizability defined in (1.5) and presents thus the optical losses. It is proportional to R^3 . The scattering cross section is proportional to the modulus squared of the polarizability. It is proportional to R^6 .

Total extinction (absorption and scattering) cross-sections can be also defined according to Mie theory as:

$$\sigma_{ext} = 12 k\pi \epsilon_d^{3/2} R^3 \frac{\text{Im}(\epsilon_m)}{|\text{Re}(\epsilon_m) + 2\epsilon_d|^2 + |\text{Im}(\epsilon_m)|^2} \quad (1.11)$$

For other types of NPs with consistent shapes (rods, discs, spheroids, etc.), the **Equation 1.11** is modified with a geometrical form factor (in analogy to x), while for complicated shapes, no analytical solution exists, and numerical solutions are needed, such as using COMSOL multiphysics, the discrete dipole approximation or FDTD. Yet, to achieve maximum extinction, the term in the denominator should be minimum, leading to the resonance condition, so-called Fröhlich condition $|Re(\epsilon_m) + 2\epsilon_d| = 0$, to achieve the LSPR.

It is also important to introduce the efficiencies of scattering and absorption cross-sections, Q , which is simply a ratio of the scattering/ absorption cross section to the geometrical cross-section (πR^2 for a sphere):

$$Q_{abs} = \frac{\sigma_{abs}}{\pi R^2} = 4 kR \operatorname{Im} \left(\frac{\epsilon_m - \epsilon_d}{\epsilon_m + 2\epsilon_d} \right) = 4 x \operatorname{Im} \left(\frac{\epsilon_m - \epsilon_d}{\epsilon_m + 2\epsilon_d} \right) \quad (1.12)$$

$$Q_{sca} = \frac{\sigma_{sca}}{\pi R^2} = \frac{8}{3} (kR)^4 \left| \frac{\epsilon_m - \epsilon_d}{\epsilon_m + 2\epsilon_d} \right|^2 = \frac{8}{3} x^4 \left| \frac{\epsilon_m - \epsilon_d}{\epsilon_m + 2\epsilon_d} \right|^2 \quad (1.13)$$

These parameters are extremely important while trying to understand the origin and nature of the plasmonic modes. However, in **Chapter 2**, these quantities will be calculated numerically using a FDTD solver.

1.2. Generalities of plasmonic biosensors and gas sensors

In this part, the field of biosensors will be introduced. Biosensors rely on different approaches to transform a biological signal into physical signals, *e.g.* optic or electric. Herein, we will focus our discussion on the optical sensing methods, especially those that are based on Plasmonics. Surface plasmon resonance (SPR, or localized-SPR, LSPR) sensing and surface-enhanced spectroscopies are investigated. The state-of-the-art in the fields of SPR sensing and surface-enhanced infrared spectroscopy (SEIRA) are presented in the following sections.

1.2.1. Introduction to biosensors

Biosensors have been always attractive devices for academia, industries, and research laboratories owing to their remarkable ability to recognize a biological event on a transducer device through a signal-based quantification of the binding reaction response.²¹ Biosensors were first reported by Leland Charles Clark Jr. in 1962, who perceived the idea of demonstrating the components of a biosensor and the strategy to integrate a bioreceptor with a transducer device.²²

At this stage, it is important to recall that all biosensors consist of a biorecognition layer that is covering a transducer that will amplify the outcome signal. The signal transducing element is the core of the biosensor. Many types of transducers are studied such as electrochemical, electrical, optical, gravimetric, or acoustic transducers, among all, we will focus on the optical one. Herein, the light-matter interaction takes place through many methodologies, namely, SPR, LSPR, SEIRA, SERS owing to pinning of the evanescent wave at the metal/ dielectric interface.

Biosensors monitor diseases and disease-causing bacteria, in biological solutions such as blood, urine, saliva, tears, and sweat. In recent years, biosensors have opened up new horizons in a wide scope of applications from medical analysis, healthcare, control and development of pharmaceuticals, and food safety up to environmental monitoring, agriculture, defense, and security. Recently, biosensors are incorporated into the Internet of Things (IoT), *e.g.* built-in sensors to alert the driver when the tire pressure is low, and certainly in the current COVID-19 rapid detection kits.¹⁶ Furthermore, they can integrate various point-of-care applications, such as water quality, forensics, and drug delivery. Given their interactions with high-affinity biomolecules, they find application in the sensitive detection of analytes, even in small sample

volumes. This ability could be improved by adding microfluidics channels to the miniaturized devices to finely control, coordinate, and modify micro-volumes of fluid for better heat and mass transport. This is extremely required for creating crucial platforms in biomedical diagnosis.²¹

Device miniaturization has now become a mutual interest, particularly in biosensing analysis. Indeed, devices can be packed and integrated into a single interface, enabling sensitive and non-invasive detection of several biomarkers corresponding to a biological sample such as saliva, urine, and blood in a repetitive, continuous, rapid, low-cost, and reliable manner. Multiple strategies have been employed to develop and fabricate miniaturized biosensors, including design optimization, characterization, and testing.

The main limiting factors of the biosensor development are:

- (a) The efficiency of monitoring the biorecognition signals such as electrochemical, electrical, optical, gravimetric, or acoustic signals.
- (b) The improvement of the transducer performances such as its sensitivity, fast-response time, reproducibility, and low detection limits even down to individual molecules detection.
- (c) The size miniaturizing and integration of the biosensing device using micro/nanotechnologies for mass production.

The main solution for all these challenges is found in the nanostructuring of materials acting as transducer elements. The design and composition of the structures will be discussed later on in the following sections. Plus, the nature of the signal enhancement depends on the electric field near the plasmonic structure, thus, the signal intensity is very sensitive to the distance between samples and the transducer elements. In line with this, surface chemistry is a crucial point in the detection of analytes of interest. In consequence, substrates can be functionalized by adding a biorecognition element to promote a molecular interaction for specific detection (such as antibodies, or other small molecules designed to specifically attach to the targeted analyte). The binding of the analyte to the biorecognition element will cause a change in the detected signal.¹¹

Noteworthy, as stated by Minopoli *et al.*, LSPR and surface lattice resonance (SLR) are categorized as inherent resonance-based biosensors, and surface-enhanced Raman spectroscopy (SERS),

SEIRA and plasmon-enhanced fluorescence (PEF) are classified as external signal amplification-based biosensors. The former category includes plasmonic biosensors whose sensing parameters rely on changes in the structure optical response, whereas the latter contains nanostructured platforms employed as signal enhancers in Raman-, infrared (IR)-, and fluorescence-based biosensing. Such a classification is flexible as many nanostructured substrates might boost mutual applications, since they can be useful for both inherent resonance-based biosensing and external signal amplification. A concrete illustration of both categories is given in **Figure 1.7**. For more details about each category please refer to Minopoli *et al.* review.²³

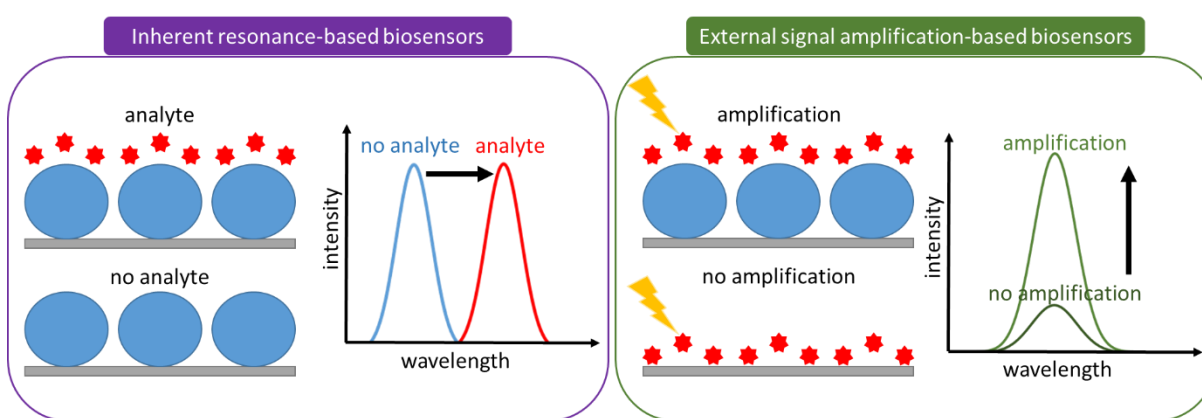


Figure 1.7. Classification of the metal nanoparticle-based biosensors. Plasmon resonance shift induced by analyte detection (violet panel) and surface-enhanced amplification (green panel) are representative examples of inherent resonance- and external signal amplification- based biosensors, respectively. Both categories could occur simultaneously.

In this context, we will briefly introduce the SPR sensing mechanism in presence of an analyte. Then, SERS and SEIRA techniques will be introduced as well. The SLR- and PEF- based biosensing goes beyond the scope of this manuscript and further information can be found in Minopoli *et al.* review.²³

1.2.2. SPR- Refractometric sensing

Upon the excitation of SPR, a surface EM field is created along the metal/dielectric interface that exponentially decays in both media. Being highly sensitive to the refractive index (RI) change of the dielectric medium, it is useful to realize SPR-based sensors. SPR excitation requires a coupling medium to provide the required photon momentum match along the interface. This is conventionally achieved via prism coupling (Kretschmann configuration in **Annexe 1.1**), assisting

total internal reflection at the prism–metal interface. Liedberg and co-workers reported in 1983 the first experimental demonstration of using this phenomenon for sensing.²⁴ Here, one should mention the pioneering Biacore SPR-based sensor, which was provided by Pharmacia Biacore and commercially released in 1990.²⁵ Such devices that use prism couplers offer low detection limit of bulk sensing in the range of 10^{-7} to 10^{-6} RIU and that of surface sensing at $1 \text{ pg}\cdot\text{mm}^{-2}$. Nevertheless, its intrinsic volume is not compatible with miniaturization in a lab-on-a-chip platform and portable devices.²⁶ SPR biosensing have been used for multiple clinical application in virology, including serological assays related to Salmonella in 2002,²⁷ for example, and the first severe acute respiratory syndrome in 2009 (SARS-COV)²⁸. Indeed, in the COVID-19 pandemic era, health care became an area of particular interest. The standard diagnosis of SARS-COV-2 viral genetics relies on respiratory samples, mainly RT-PCR (reverse transcription polymerase chain reaction), which is extremely sensitive and selective, but requires centralized and specialized laboratory stations, and between 3 to 48 hours to deliver the result. In march 2021, this restriction was disabled by the research of Lechuga *et al.* where a rapid ($< 15 \text{ min}$) identification and quantification of sever SARS-COV-2 antibodies were achieved in clinical samples thanks to a plasmonic portable and label-free device.²⁹ This SPR-sensing method is overcoming the limitation of the traditional immunotests platforms as ELISA (enzyme-linked immunosorbent assay) and CLIA (chemiluminescence immunoassay). Both need specific equipment in dedicated laboratories and can be time-consuming because of the sample manipulation and long incubation time.

LSPR is another potential candidate to realize plasmonic biosensing with high sensitivity. It is a category of SPR phenomena, where the resonant EM field is confined at the closest vicinity of the nanostructures that are smaller than the light wavelength. The LSPR is translated into the far-field as a peak in the extinction spectra of the nanostructure ($\text{extinction} = 1 - T - R$), and in the near-field it is accompanied by an intensification of the EM-field at the extremities of the metallic nanostructure due to the lightning-rod effect. The physical meaning of the lightning-rod effect is understood as the concentration of charges in a small volume, occurring at a sharp tip.³⁰ LSPR biosensing is an extremely sensitive, label-free, and real-time method compared to other conventional biochemical assays. In addition, it is simple, cost-effective, and suitable for measuring the slight variation of the surrounding medium RI induced by the presence of adsorbed

molecules in the vicinity of the nanostructures, compared to the commercial propagating SP resonance (PSPR) sensors.^{31,32}

As illustrated in **Figure 1.5**, thanks to the coupling between the free-space incident light and the free-electron gas at the metal/dielectric interface (similarly occurring at the sub-wavelength-sized metal nanostructures), an extremely enhanced field is generated while decaying evanescent waves penetrate both neighboring media (**Figure 1.4b**). The evanescent field that penetrates the surrounding dielectric medium is extremely sensitive to the changes of RI, caused by the adsorption and/or recognition of the biomolecules, close to the metal surface which will lead to a shift in the LSPR peaks. In particular, based on the Drude model (**Table 1.1**), the LSPR frequency is inversely proportional to $\sqrt{\epsilon_d} = n$, where n is the RI of the surrounding dielectric medium. Plasmon resonance shift prompted by an analyte detection is well illustrated in the violet panel of **Figure 1.7**.

Commonly, the RI sensing performances are evaluated via several quantifiers allowing to judge the quality of the plasmonic platform.³³ RI sensitivity (S), often measured in nm/RIU (nm per refractive index unit), is probably the most important one. It represents the ratio between resonance wavelength shift ($\Delta\lambda$ typically measured in nm) and the RI variation (Δn) of the surrounding medium, and can be defined as in **Equation 1.14**:

$$S = \frac{\Delta\lambda}{\Delta n} \quad (1.14)$$

The figure of merit (FOM) can be also considered, being defined as the ratio of the RI sensitivity to the resonance width, where $FWHM$ represents the full width at half maximum of the resonance band in nm. It is given in **Equation 1.15** as:

$$FOM = \frac{S}{FWHM} \quad (1.15)$$

To quantify the grade of the LSPR sensor, the Q-factor is calculated as in **Equation 1.16**. It strongly depends on the absorption caused by the imaginary part of the dielectric function of the material. Hence, the broader the resonance, the smaller the Q-factor. The Q-factor is expressed as:

$$Q = \frac{\lambda_{central}}{FWHM} \quad (1.16)$$

where $\lambda_{central}$ is the central wavelength of the LSPR.

Based on the nanoparticle-light interaction, in 2019 Masson and his team tested a portable “plasmonic tongue” for the classification of taste profiles in maple syrup. The test tube consists of Au nanoparticles and maple syrup solution. The flavor-distorting amino acids, and amines bind to the Au nanoparticles and cause them to aggregate, altering the incident light interaction with the solution. This effect shifts the solution from red to blue in a minute as it is seen with the naked eye and through data analysis.³⁴ This device is simple but opens the route for developing the early detection of cancer and neurodegenerative diseases for example. Altug and her colleagues are rising sensors for neurodegenerative diseases. For instance, they focus on pinpointing the biochemical changes in the brain that happen years before Parkinson’s disease onset, by detecting proteins in the IR such as α -synuclein that misfold and clump together into toxic aggregates using an array of gold nanoantennas.³⁵ This tool for detecting protein misfolding and protein aggregation will help to identify new therapeutics that could prevent and stop the pathological progress. Several groups are aiming to develop screening tools for cancer early detection, or for monitoring the treatment efficiency by pinpointing specific biomarkers, DNA, proteins, and cytokines through nano-biosensors. Successful research is reported by Altug and her team in May 2021, wherein one of their biosensors detects a subcategory of extracellular vesicles called exosomes, nanometre-sized sacs which are ejected from cells that contain components such as DNA and proteins.³⁶ In particular, Altug’s team tracked exosomes that had been released by breast cancer cells in real-time, with a limit of detection of 267 ng/ml, and this concentration is clinically relevant for the detection of cancer-related extracellular vesicles.³⁷ Nevertheless, many obstacles are suspending the mass production of such health point-of-care devices, the chief among them all is manufacturing economics as the realization remains high-priced, making it difficult to convince companies to produce these devices in large enough quantities to make them affordable and cost-effective.

In 2022, interesting refractometric sensing was achieved using Si pedestal gratings which present a high-Q factor, *i.e.* narrow resonances. Bulk sensitivity of 536 nm/RIU is found in glycerol in deionized water solution. The surface sensitivity was also evaluated by depositing 2 to 5 nm thick layers of aluminum, hafnium, and titanium oxides with different refractive indices. An increase in

the thickness of the deposited film leads to a red-shift of the dip in the reflection spectrum. Additionally, this shift is higher for oxides with a higher refractive index. To evaluate the operation capability in solution, once functionalized with biotin, the sensor could achieve avidin sensing.³⁸

An overview of some recently reported LSPR-based devices using metallic nanostructures (mainly silver, gold, and aluminum) is provided in a recently published review of Minopoli *et al.* giving a typical $S \propto 10^2$.²³ Among all the reported studies, we would like to highlight the theoretical findings of Wang *et al.*³⁹ who reported the RI-sensing and SERS capability of Al Bowties integrated into MIM structures to detect low concentrations of glycerol in deionized water with a sensitivity of ~ 500 nm/RIU. The same platform serves for SERS with an enhancement factor as high as 10^9 .³⁹ Indeed, this recent theoretical study is extremely promising. However, the presented Al BT structures that cover a wide IR range are not fabricated yet. In this manuscript, the conception of our BT NA integrated into a MIM structure will be inspired by Wang *et al.*³⁹, but instead of performing SERS, our Al BT will be used this time for a real and extended SEIRA sensing demonstration.

1.2.3. SERS and SEIRA sensing

To detect and identify molecules, it is crucial to study the corresponding vibrational energy levels. Vibrational spectroscopy measures the characteristic Raman or IR absorption lines of the molecules existing in a sample. Raman scattering and direct absorption of IR radiation are complementary techniques and both provide information based on different selection rules. However, the limiting factor for both techniques is the low interaction cross-section with the incident radiation. Raman scattering has a low probability compared to elastic (Rayleigh) scattering. For IR absorption, the reason for the weak interaction cross-section is the large mismatch between the typical micrometric dimension of the incident radiation and the nanometric size of molecules. To overcome this drawback, *i.e.* to enhance the interaction between the molecular vibrations and the incident IR radiation, an additional component is introduced, namely, the plasmonic structures. Thus, the surface-enhanced vibrational spectroscopy techniques are introduced. Surface-enhanced spectroscopies capitalize on the surface structuration which plays a major role in enhancing the near EM-field at the close

proximities of the nanostructure. In addition, a further enhancement could be achieved once these nanostructures are closely placed, creating the so-called gap. The most advanced nanoantennas for surface-enhanced sensing will be stated in the following sections.

The inspiring discovery of surface-enhanced Raman scattering (SERS) in the early 1970s opened the field of surface-enhanced spectroscopy. The phenomenon has subsequently also been witnessed at longer wavelengths since the 1990s and, eventually, led to the recognition of surface-enhanced infrared absorption spectroscopy (SEIRA).⁴⁰ SERS and SEIRA have received great attention in the bio-nanotechnology field where bio-molecules, *e.g.* DNA or proteins, are combined with surface antennas. In both techniques, electromagnetic enhancement plays a major role in the detection mechanism. When a molecule is spatially confined within the zone of greatly enhanced electromagnetic fields, its vibrational lines are enhanced. This enhancement could be boosted by creating a gap where the electromagnetic fields will be enhanced by many orders of magnitude.⁴⁰ Although the enhancement factor of SEIRA could be smaller than that of SERS (order of 10^6 – 10^{14}),⁴¹ the cross-section for IR absorption is several orders of magnitude higher than the corresponding Raman cross-section. Consequently, the modest enhancement of SEIRA is sufficient for many applications.⁴² Note that SEIRA enhancements are proportional to $|E/E_0|^2$ while the SERS enhancement factor is proportional to $|E/E_0|^4$ (as given by the product of the electric field ($|E/E_0|^2$) enhancement at the excitation wavelength and the electric field ($|E/E_0|^2$) enhancement at the scattering wavelength).

1.2.3.1. Resonant SEIRA principles

Molecular vibrations can be excited when molecules absorb IR radiation. The IR spectral range is remarkable as it contains many valuable molecular information because the vibrational properties are directly associated with the molecular constituents, their chemical bonds, as well as their configuration.⁴³ The IR range is divided into the functional group (4 000 - 1 500 cm^{-1}) and the fingerprint spectral range (1 500 - 500 cm^{-1}) as presented in **Figure 1.8**.

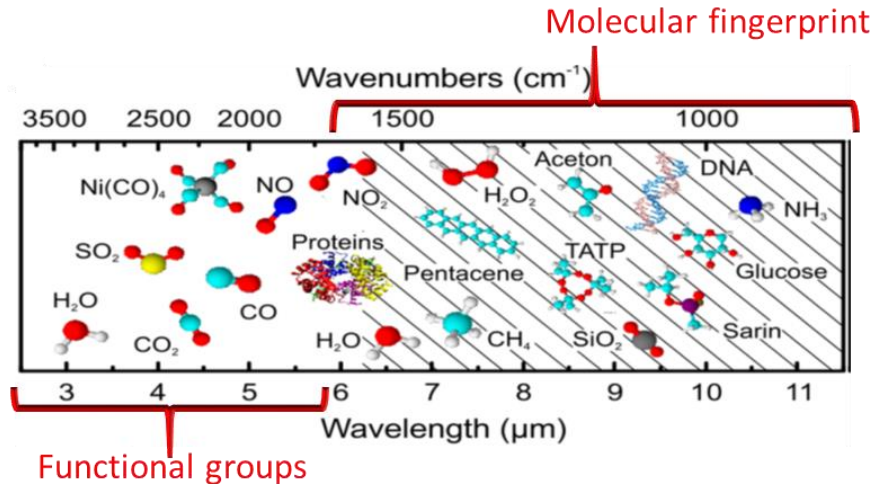


Figure 1. 8. Characteristic infrared vibrations of selected molecular species. The fingerprint and the functional group regions are labeled.⁴³

As previously mentioned, mediated by near-field enhancement of the plasmonic antenna, SEIRA spectroscopy arises from the coupling between the molecules placed at “hotspots” and the near-enhanced EM-fields, as illustrated in **Figure 1.9a**. In fact, upon the excitation of the antenna resonance, the incident far-field radiation is transferred into highly enhanced localized electromagnetic near-fields. Molecules that are situated within these so-called “hotspots” will couple to the resonance, leading to an increase of their absorption cross-section by many orders of magnitude.⁴³ This coupling can be understood based on the simple interaction between two damped harmonic oscillators, presented in **Figure 1.9b**. The damped harmonic oscillator in violet will denote the plasmonic resonance mode, while the one in pink illustrates the molecular vibrational mode. The plasmonic mode is strongly driven by the incident IR light by the force term and is therefore called “bright” mode. However, the far-field radiation interacts weakly with the molecular vibration mode due to its low molecular cross-section and is referred to as approximately “dark” mode. Nevertheless, this “dark” mode can be excited thanks to the occurring coupling (enabled by the μ parameter) between the molecular vibrational mode and the “bright” antenna mode.^{43,44} In consequence, the vibration is not directly observed as an absorption feature in the spectrum, but it appears as a modulation on top of the plasmonic resonance, as plotted in **Figure 1.9c**.⁴⁵ Spectral response of both uncoupled (black) and coupled (red) systems are revealed in **Figure 1.9c**. The coupled system (red) shows an increased

transmittance peak at the position of the molecular vibration ω_{vib} (orange) on top of the unperturbed resonance (black). This coupling (red curve) is achieved thanks to the spectral overlap of ω_{vib} (orange) and ω_{res} (black) and is evaluated through a tuning ratio $\omega_{vib}/\omega_{res}$. Also, in this model, line-shapes ranging from anti-absorption (induced transmission) to asymmetric Fano-profiles appear with dependence of a resonance tuning.⁴⁶

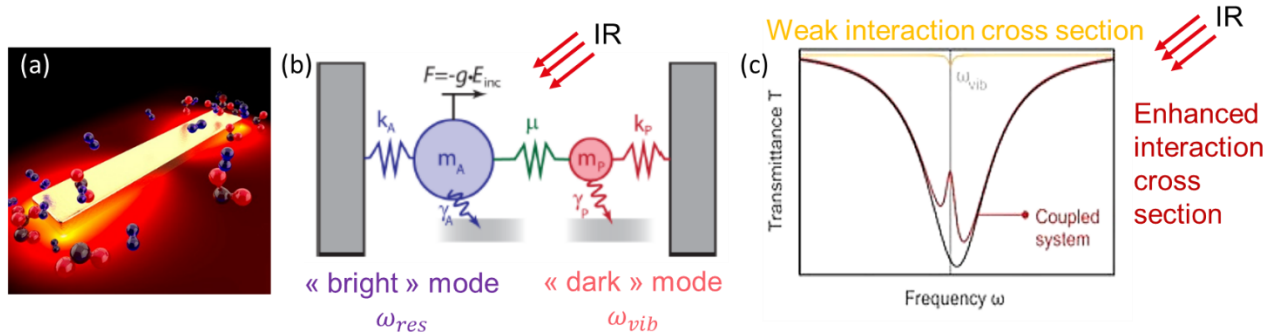


Figure 1. 9. SEIRA sensing principle and methodology (a) Molecules located in the enhanced electromagnetic near-field of an IR plasmonic nanoantenna.⁴⁷ (b) Coupling conception assimilated to the one between two damped harmonic oscillators: the coupled modes, i.e. bright (violet, A) denotes ω_{res} and dark (pink, P) denotes ω_{vib} mode. Mode A is driven by external radiation, via $g \cdot E_{inc}$, and it feels damping at a rate γ_A . Mode P is dark, as it does not interact directly with external radiation or the driving field. Its damping rate, γ_P is typically much smaller than γ_A . The two modes are coupled by some rate, μ .⁴⁴ (c) The enhancement of the interaction cross-section is due to the coupling that occurs for a spectral match between ω_{vib} and ω_{res} and is seen as a modulation on top of the plasmonic resonance feature.⁴⁵

This kind of hybrid coupling between ω_{vib} and ω_{res} is revealed through asymmetric line-shapes and can be interpreted in analogy to Fano-type interaction (interaction between a continuum and a discrete state).⁴³ In line with this, plasmonic excitations denote the continuum (broad) resonances, and the discrete excitations or narrow resonances resemble molecular vibrations. Consequently, the asymmetric line shape of the vibrational signal marks constructive and destructive interferences of the electromagnetic field of the plasmonic antenna and a narrower field associated to the vibrational dipoles of the molecules. Depending on the phase of this electromagnetic interaction, which is described by the parameter q in the Fano-formalism (**Equation 1.17** below shows the intensity of the Fano-line), different kinds of line shapes for several vibrational bands can be observed as reported by Vogt *et al.*⁴⁶

$$I \propto \frac{(q\gamma + \omega - \omega_0)^2}{(\omega - \omega_0)^2 + \gamma^2} \quad (1.17)$$

Modulated by a tuning ratio $\omega_{vib}/\omega_{res}$, the size of the Fano-lines differs and their shape flips depending on their relative position to the perfect match value $\omega_{vib}/\omega_{res} \approx 1$. For a detuning above 1, the shape of the Fano-line remains asymmetric but with inverted minimum and maximum compared to the one found below 1. As soon as the antenna resonance is detuned compared to the molecular vibrations, the signal strength of the enhanced vibrational signals decreases. Typically, a maximum value for the Fano-line is retrieved for a tuning ratio slightly below 1, where the near EM-field is maximized.⁴⁶ Indeed, considering plasmons as driven damped harmonic oscillators, the near EM-field intensity is slightly shifted towards lower energy in comparison with the far-field extinction peak as theoretically stated.⁴⁸ This spectral shift has been experimentally confirmed using near-field optical microscopy and its influence on SEIRA enhancement has been numerically studied for IR nanoantennas as reported by Alonso-Gonzalez *et al.*⁴⁹

To quantify the sensitivity of SEIRA, a conventional parameter is required. In some studies, it is the number of molecules from which the enhanced vibrational signal arises, or the concentration (molar) of the detected molecules adsorbed in the hotspots multiplied by their weight, or even the enhancement factor (EF), which links the enhanced signal strengths to standard IR techniques (transmission, reflection).⁴³ Even though multiple arrays of nanoantennas are measured, all these values of “sensitivity” are commonly given per nanoantenna. Given this, EF is defined in **Equation 1.18** as:

$$EF = \frac{S_{SEIRA}}{S_0} \times \frac{A_0}{A_{SEIRA}} \quad (1.18)$$

where S_{SEIRA} and S_0 are the respective enhanced and unenhanced signal strengths. A_{SEIRA} and A_0 denote the areas covered with molecules in SEIRA and reference measurements, respectively. More precisely, as the molecular vibrations ω_{vib} are enhanced by the electromagnetic near-field that is localized at the sharp apex of nanoantennas, such enhancement estimation will only embrace those molecules found near to the plasmonic hotspots, defining A_{SEIRA} . Furthermore, to improve SEIRA sensibility it is extremely important to establish an appropriate delivery of the molecules to the active hotspots using diazonium salt for example.⁵⁰

1.3. Materials and designs for surface-enhanced sensing

1.3.1. Plasmonic materials

A perfect plasmonic material could theoretically be a metal, a semiconductor or any composite comprising a large density of free carriers with a large negative real part and small positive imaginary part of dielectric permittivity.^{1,51}

1.3.1.1. Noble metals

The majority of LSPR sensing experiments have been carried out on noble metals, gold or silver.⁵¹ Gold is the material of choice for biological application, because of its chemically inert nature, resistance to oxidation, biocompatibility, and thiol-gold association that has been well developed for the immobilization of biomolecules.⁵¹⁻⁵⁶ Unfortunately, it is subject to misleading. Silver is another popular material for LSPR at visible frequencies. However, silver is easily oxidized under ordinary laboratory conditions, this degrades its plasmonic performance.⁵⁷

1.3.1.2. Alternatives to noble metals

Copper (Cu) is a non-noble metal able to support plasmon resonances in the visible-near infrared region as the noble metals, Au and Ag. However, the main limitation of Cu-bases biosensing is that the LSPR of the Cu nanostructures is unstable and significantly affected by the presence of oxides, such as Cu₂O and CuO.⁵¹

Graphene is a low-loss plasmonic material, exhibiting a tunable LSPR in the IR and terahertz region, which crosses the spectrum range of the molecular vibration frequencies of biomolecules. However, up to now the application of graphene faces the challenge of difficult technological processes, high price, and difficulty for mass production.⁵¹

Semiconductors are another potential material for plasmonic biosensing, due to the simplicity of fabrication and the flexibility of tuning their properties such as carrier concentration. For example, heavily-doped semiconductors can exhibit a negative dielectric constant under the incident light in IR frequencies. Owing to their large bandgap and high carrier mobility, heavily-doped semiconductors serve as a low-loss plasmonic material.¹⁹

Composite materials are also low-losses materials, due to the reduction of the carrier concentration once non-metallic elements are introduced into the metal lattice. These metallic compounds possess many advantages such as optical tunability, ease of fabrication, and integration. For example, metal silicides and germanides, ceramics such as carbides, borides, and nitrides, were all found to exhibit negative real permittivities in different parts of the optical spectrum. Yet, these materials are not sufficiently explored for biosensing.⁵¹ Based on a recent publication, these materials might possess a desirable properties for electrochemical sensing.⁵⁸ This exceeded our main scope of performing IR optical biosensing.

Transparent conducting oxides (TCOs) are large bandgap dielectrics with a density of free carriers in between doped semiconductors and noble metals. Despite investigations of the plasmonic response of metal oxides, their performance in plasmon-enhanced spectroscopy is yet unknown.⁵⁹

As emerging applications might require the extension of plasmonics in a wider spectral range, alternative metals, such as aluminum, often described as poor metals can achieve that goal. Aluminum (Al) appears to be one of the most appealing for extending plasmonics towards ultraviolet energies,⁶⁰ or even deeply to the IR⁶¹, as it exhibits good plasmonic properties from the infrared to the deep UV. Furthermore, Al presents non-linear optical properties as reported by Gérard *et al.*⁶⁰

Aluminum is considered as a very good metal exhibiting a high density of free electrons, with 3 electrons per atom in its conduction band (versus 1 electron/atom for gold and silver). Based on the simplest Drude model, *i.e.* bulk plasmon Drude frequency in **Table 1.1**, for Al $\omega_p \approx 15$ eV ($\omega_p \approx 8-9$ eV for gold and silver). In **Table 1.1**, the SPP (or LSP) arises in the frequency range $0 \leq \omega \leq \omega_{sp}$ and $\omega_{sp} = \frac{\omega_p}{\sqrt{2}}$. Therefore, the relatively high value of ω_p shows wide-ranging frequencies where surface plasmons are allowed in aluminum (wider than for Au and Ag). Moreover, the optical properties of aluminum can be understood by considering **Figure 1.10**, showing the real and imaginary parts of the dielectric function of Al in the IR range, provided by CRC Handbook of Chemistry & Physics by E. Shiles.⁶² . Note, the $\lambda = 0.8 \mu\text{m}$ feature associated with the interband transition is not considered here. **Figure 1.10** provides a comparison between both

parts of the dielectric function of Al and those of Au and Ag in the IR range. Looking at the dielectric function (ϵ), Al keeps a negative value of its real part ($Re(\epsilon)$), exhibiting thus a "Drude-like" (free-electron gas) behavior, *i.e.* metallic character over a broader range than Au and silver Ag.⁶⁰ This is a direct consequence of the above-mentioned value of ω_p . The imaginary part of dielectric function ($Im(\epsilon)$) is directly related to losses inside the metal and the situation is theoretically less favorable to Al (high values) with respect to Au and Ag in the visible.⁶⁰ Even in the IR, Al is considered as a lossy-material, this will directly affect the bandwidth of the plasmonic resonance.

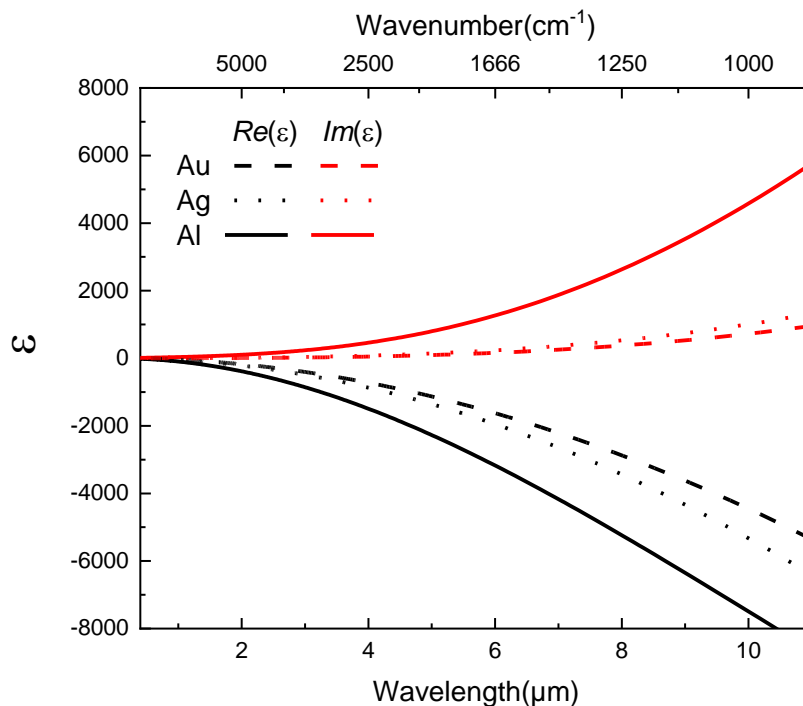


Figure 1. 10. Real (Re) and imaginary (Im) parts of the dielectric function (ϵ) for Au, Ag and Al along the IR range, provided by CRC Handbook of Chemistry & Physics by E. Shiles.⁶²

Besides its optical properties, Al has drawn lately great attention for holding attractive features including low cost, high natural abundance, good adhesion to many substrates without the need of any additional layer, as well as the flexibility of refinement by various methods including complementary metal-oxide-semiconductor (CMOS) technology.^{63–65} Based on this unique characteristic, it can overcome the limitations of Au and Ag. Therefore, Al has a special potential

to customize on-demand highly-performant refractive index bio sensors,^{32,66,67} SERS^{68,69}, and SEIRA platforms.^{70,71} Al provides some unique prospects as SEIRA candidate compared to Au antennas, despite the presence of a native oxide layer contributing to greater losses and a more moderate SEIRA enhancement. Precisely, the omnipresent 2–4 nm thick oxide layer, spontaneously formed upon its exposure to the atmosphere, passivates the antenna structure against further oxidation and enables a broader range of covalent binding schemes for molecules to the antenna than Au or Ag.⁶⁵ This layer can be easily functionalized using phosphonic acid for SEIRA demonstrations using Al,⁷² like indium-tin oxide (ITO) which has also been used for SEIRA.⁵⁹

1.3.2. Plasmonic nanoantennas

In analogy to the radio-frequency (RF) antennas, plasmonic antennas are acting as resonant structures responding at a specific frequency depending on the antenna's geometry, composition, and arrangement,^{19,73} as well as on their surrounding environments.⁵⁶ Indeed, technological progress allows researchers to produce new plasmonic systems by controlling all the previously described parameters. Besides the intrinsic property of the materials, the plasmonic resonance can be tailored thanks to the micro- and nano-engineering of the structures. Therefore, the choices of both the materials and the designs of micro- and nanostructures are the core topics to address a specific sensing range. For example, Au Bowties (BT) with a 3 nm gap were fabricated by using EBL and assisted SERS sensing as proven by Dodson *et al.*⁶⁸ The effect of the rounded-corner BT was experimentally observed and it has a significant impact on the LSPR that is red-shifted for increasing sharpness of the BT corners, and on the electric field enhancement (Raman enhancement factor) that is increased with decreasing gap size for both round and sharp bowties, but the increase was more dramatic for the sharp bowties.

In the following sections, great interest will be devoted to Al nanoantennas serving as plasmonic resonators. Many Al nanostructures are reported for plasmonic biosensing in the UV and visible applications, RI-sensing, surface-enhanced fluorescence (SEF), and SERS as summarized in Li *et al* review.³²

1.3.2.1. Al nanoantennas

The ability to fabricate well-defined Al nanostructures in a quite large extend to finely tune their plasmonic response is of paramount importance in the development of future Al plasmonic applications. Al nanostructures could be fabricated using electron beam lithography, photolithography, focused ion beam lithography, colloidal lithography, interference lithography, nanoimprint lithography, self-assembled thin film, laser ablation, and chemical synthesis.^{64,74} Each technique is well adapted to produce the required geometric criteria and thus is only suitable for a specific range of applications. To review the details of the fabrication techniques of aluminum nanostructures within the context of plasmonics, please refer to the work of Martin and Plain.⁶⁴

In our case, the electron beam lithography (EBL) will be the center of interest as our Al nanostructures will be strictly fabricated by this mean (see **Chapter 3**).

In the literature, EBL offers an extensive panel where different applications appeal to different material and plasmonic nanostructures. Here are some selected examples of interest for EBL-fabricated Al nanostructures on different substrates. The research of Knight *et al.* was based on simple structures of Al nanodisks (**Figure 1.11a**), using which further experimental studies was carried out on the native oxide thickness.⁶¹ These individual nanodisks with corresponding diameters going from 180 nm down to 70 nm are covering the UV and the visible ranges. Lecarme *et al.* have worked on Al nanorods (**Figure 1.11b**) with variable side lengths to cover a spectral range from the IR to the visible region of the EM spectrum.⁶⁶ To perform SERS in the UV, Al Bowties (BT) were fabricated by Li *et al.* (**Figure 1.11c**) to detect liquid benzene with an enhancement of 5 orders in the signal intensity.⁶⁹ The EBL-designed Al Cayley trees (**Figure 1.11d**) show a promising potential for a wide range of applications, such as non-linear optics to light harvesting, photodetection and SEIRA spectroscopy as recently reported in 2022 by Simon *et al.*⁷⁵ An amazing application exploiting the plasmonic properties of EBL-made Al nanostructures is the color generation printing applications as reproducing for Claude Monet's painting, *Soleil Levant*, as reported by Tan *et al.*⁷⁶ EBL has been used to fabricate Al-capped nano-pillars with varying diameters on a silicon substrate serving as a $300 \times 300 \mu\text{m}^2$ "plasmonic painting" as illustrated in **Figure 1.11e**.

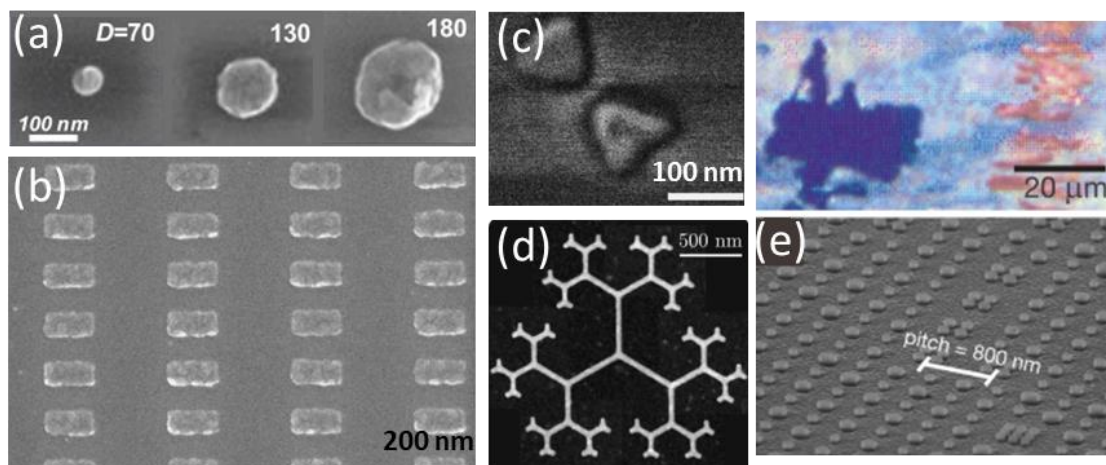


Figure 1. 11. State-of-art Al nanostructures fabricated by EBL. (a) Nanodisks on SiO₂ for UV-Vis coverage.⁶¹ (b) Nanorods on KTaO₃ for transmittance measurements from UV to IR.⁶⁶ (c) Bowtie on silica formed by two equilateral triangles of 100nm side length with 20nm apex to apex gap distance, for benzene detection using UV-SERS.⁶⁹ (d) Caylee tree on Si₃N₄ promoting a wide range of applications.⁷⁵ (e) Nanopillars on Al for plasmonic painting application in the UV as for Monet's impression, Soleil levant.⁷⁶

1.3.2.2. Plasmonic antennas for SEIRA sensing

This section will be directly concerned with presenting the most advanced nanostructures used for SEIRA sensing investigations. These nanoantennas are mainly fabricated using gold. Besides, Wang *et al.* review gives an extensive view of the advanced design from nano/microstructures to macro-optical design implemented for SEIRA.⁴⁰

Herein, some of the nanostructures will be addressed. By detuning the resonance via a change in the antenna length, a Fano-type behavior of the spectral signal is observed, which is supported by the so-called SEIRA enhancement factor (EF). To access biomolecular vibrational information on the single molecule level, fine-tuning and engineering are needed to boost the SEIRA enhancement. There are several tactics to push the detection limit either with higher electric near field intensities or substrate engineering. A cleverly designed substrate could be an added value to enhance the localized EM-field, such as a metal-insulator-metal configuration with either a thick spacer for perfect absorption^{77,78} or serving as an optical cavity;⁵⁵ or with a thin spacer, sustaining thus a gap plasmon effect.⁵⁰ Besides, one of the best ways to locally intensify the electric field is to confine it into a gap region, *i.e.* between two closely placed nanostructures.⁴⁷

To our best knowledge, SEIRA experiments have been frequently performed with Au antennas that sustain, only by varying their length, a spectral match between their corresponding plasmonic resonance and the molecular vibrations frequencies. Mainly, it is done using either a single rod geometry, where the EM-enhancement is mainly at the extremities of the antenna, as originated by the lightning rod effect⁷⁹⁻⁸¹, or a double-rod geometry with an extra enhancement provided at the nanogapped sites^{43,82}. The combination of these three effects, *i.e.* tunable localized plasmon resonances, hotspots created by the lightning rod effect, and extremely activated gap, allows to reach an extremely pronounced field enhancement, which is a fundamental parameter for SEIRA spectroscopy.

A glance at the reported results will be provided in **Figures 1.12-1.15** and **Table 1.2** for various antennas geometries from a single nanoantenna to complex nanoantenna.

- Single nanoantenna

Neubrech *et al.* reported in 2008 the earliest demonstration of the resonant SEIRA using a single gold nanoantenna which was functionalized with a monolayer of octadecanethiol (ODT) molecules as a model system. The CH₂ vibrations in ODT at 2 850 cm⁻¹ and 2 920 cm⁻¹ were successfully enhanced by exciting the LSPR along the long antenna axis (black curve in **Figure 1.12a**). Obviously, the enhanced absorption signatures appear as transmittance peaks on top of the pure plasmonic resonance (**Figure 1.12a**), enabling the detection of attomoles (10⁵ molecules) of analyte located at the hotspot of the single nanoantenna. By switching the incident polarization by 90°, the plasmon is absent from the spectrum, hence turning off the SEIRA effect as well (red curve in **Figure 1.12a**).

Aside from this first demonstration, many other SEIRA researches were grounded on single metallic nanostructures, such as Au cross antennas by Brown *et al.* in 2013,⁸² or single Au nanoantenna for detecting folding dynamics of proteins by Semenyshyn *et al.* in 2019,⁸³ to name just a few. Nevertheless, even though single metallic nanostructures have a large geometrical extinction cross-section, advanced light sources, such as synchrotron radiation or IR lasers, are often required to reach sufficient signal-to-noise-levels.⁴³

- Nanoantenna array

To overcome the need for advanced light sources, it is crucial to arrange the plasmonic nanoresonators to be easily implemented for simplest SEIRA demonstrations using conventional FTIR spectroscopy with a standard broadband light source.

In 2014, Vogt *et al.* studied the influence of the impact of the plasmonic near-and far-field resonance-energy shift on the enhancement of infrared vibrational signals using an array of gold nanorods with different lengths, thus different far-field resonance energies. Gold nanoantenna arrays were prepared on a $\text{CaF}_2(100)$ substrate with a thickness of 1 μm . The distance between the nanoantenna along their long axis was set to 50 nm, as illustrated in **Figure 1.12b-i**. The SEIRA test molecule is a layer of 4,40-bis(N-carbazolyl)-1,10-biphenyl (CBP). Vibrational signals are enhanced with respect to the tuning ratio of the plasmonic resonance and the molecular vibrational frequencies and maximized for a tuning ratio slightly below 1, giving a maximum SEIRA enhancement of 10^4 (**Figure 1.12b-ii**).

The arrangement of the nanoantennas does not only affect the modulation of the plasmonic resonance but can also increase its Q factor. In line with this, careful attention should be paid to the filling ratio of the antennas (**Figure 1.12c-i**), as reported by Bagheri *et al.* in 2015.⁸⁴ In this study, the highest SEIRA signals are not corresponding to the highest antenna densities within an array. As seen in **Figure 1.12c-ii**, the signal enhancement strongly depends on the match between vibrational frequency and the plasmonic resonance frequency and is retrieved for an antenna density of $(d_x, d_y) = (1, 2) \mu\text{m}$, where d_x is the spacing along the long antenna axis and d_y is the short antenna axis. Thus, as expected the SEIRA enhancement is found maximized for antenna spacing close to a critical coupling distance, *i.e.* for a perfect match between resonance and vibrational frequencies of the 5 nm thick CBP.

In 2015, Brown *et al.* have introduced a special type of IR nanostructure, namely the fan-shaped (and rod) antenna in a 3 x 3 array, which incorporates very sharp metallic tips in the center, illustrated in **Figure 1.12.d**.⁸⁵ Such an arrangement improves the intensity of the near-field in two ways. In the first place, thanks to the lightning rod effect, the sharp ends increase the near-field intensity.⁸⁶ In the second place, the narrow gaps between the antenna arms can further

concentrate the near-fields.^{47,87} As consequent result, the incident radiation is enhanced by up to 5 orders of magnitude within these hot spots (**Figure 1.12.d-i**).

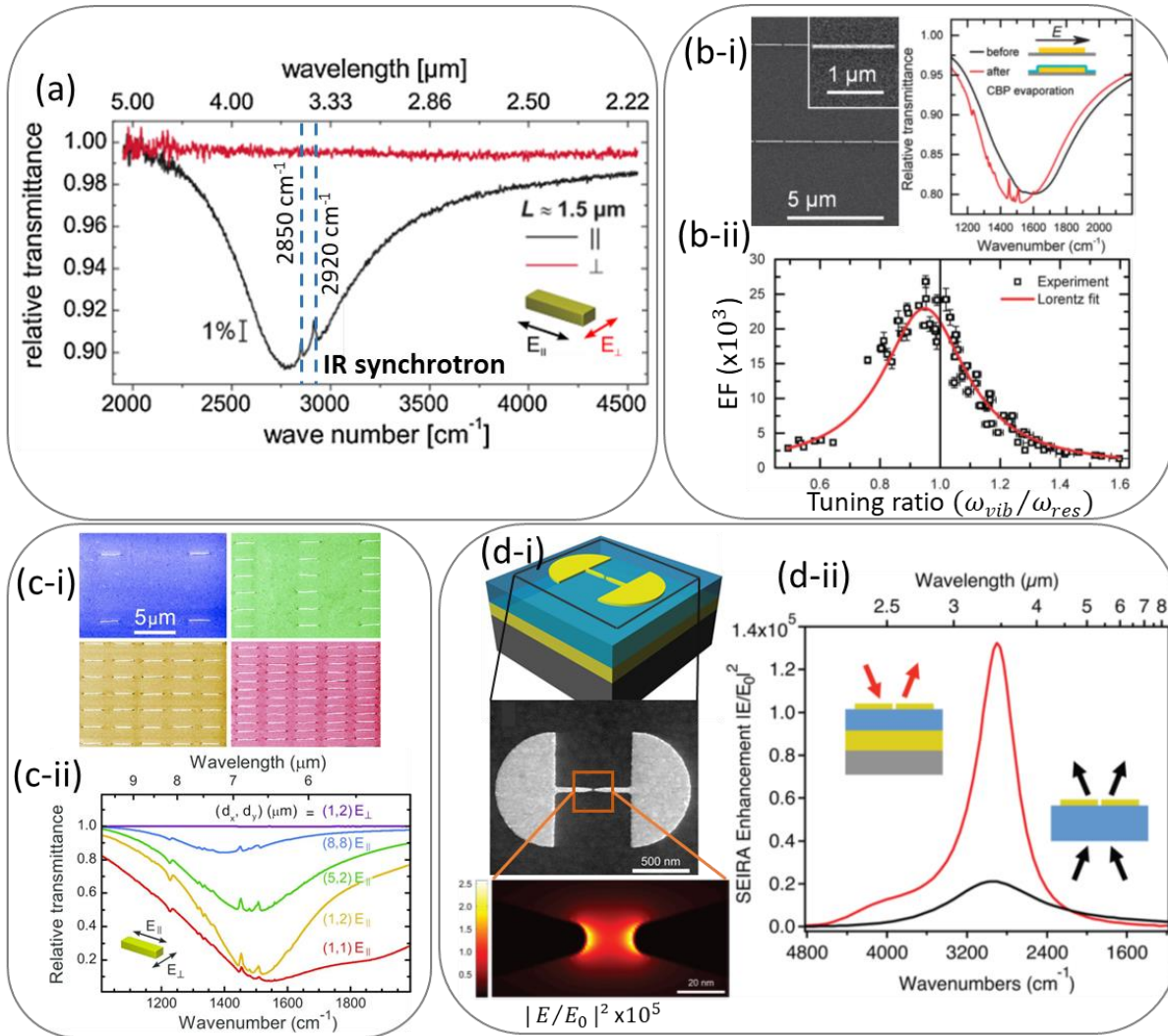


Figure 1. 12. SEIRA state-of-art using Au nanoantennas. (a) The first SEIRA demonstration provided by Neubrech *et al.*⁷⁹ using a single nanorod radiated along and across its long axis with an IR synchrotron to achieve a good signal-to-noise ratio. CH_2 vibrations in ODT were enhanced appearing as modulations on top of the plasmonic resonance (black line) and are absent without the plasmonic excitation (red line). 10^5 molecules were detected at the hotspots. (b) SEIRA demonstration by Vogt *et al.*⁴⁶ using an array of nanorods distant by 5 nm along their long axis. Asymmetric features evidenced the SEIRA enhancement of the vibrational modes of CBP. A maximized enhancement factor (EF) of 10^4 is found at a tuning ratio slightly below 1. (c) Impact of the packing density of plasmonic antenna arrays (c-i) on the SEIRA signal (c-ii) proved by Bagheri *et al.*⁸⁴ Notably, the highest SEIRA signals (yellow curve) do not coincide with the highest packing densities (red curve). (d) Substrate engineering and the introduction of small gaps between plasmonic resonators offer two opportunities to further increase the SEIRA enhancement (d-i), as stated by Brown *et al.*⁸⁵ and Dong *et al.*⁸⁷. For a fan-type resonator, the electric field intensity can be enhanced up to 5 orders of magnitude while a gold layer underneath with appropriate spacer layer thickness further increases the enhancement (d-ii).

Above all, the authors introduced a gold mirror underneath the structures separated by a dielectric SiO₂ spacer layer, to create a MIM structure.⁸⁵ The MIM system is tuned into the perfect absorbing regime by carefully tailoring the spacer layer,^{78,88,89} leading to much higher SEIRA enhancement (**Figure 1.12.d-ii**). This helped to enhance the detection of self-assembled monolayer (SAM) of octadecanethiol (ODT) owing to the reached enhancement factor of 10⁵, and to detect as few as 10 000 molecules of ODT using conventional FTIR spectroscopy.

With the same spirit, in 2017, Dong *et al.* reported the best value so far of 10⁷ for the SEIRA enhancement, which is 2 orders of magnitude higher than Brown *et al.* SEIRA designs. It is achieved using a 3 nm gap BT antenna integrated within a MIM configuration (with 325 nm of SiO₂ as spacer) which enables to detect as few as 500 molecules of 4-nitrothiophenol (4-NTP).⁸⁷

- Innovative fractal-like geometries

Recently, a variety of advanced nanostructures has been proposed and realized depending on the target application. The majority of these plasmonic metasurfaces sustains multiple resonances besides the near-field engineering.⁹⁰⁻⁹² For example, Rodrigo *et al.*⁹² have introduced in 2018 a multiresonant structure consisting of plasmonic rod antennas with different lengths (**Figure 1.13a**) and with multiple periodicities. By modifying the lengths of the antennas in each sub-arrays, plasmonic resonances in the mid-IR could be achieved, besides additional resonance in the near-IR to enable refractometric detection (**Figure 1.13b**). Thus, by exciting a high number of resonances, the self-similarity of the multiperiodic array obtained by a fractal-like generation enables a wide spectral coverage and thus a unique sensing method from the near-IR to the mid-IR. Indeed, IR resonances are targeted at different molecular vibrations, allowing Rodrigo *et al.* to sensitively detect the presence of different molecules with spectrally separated vibrational bands, especially those of poly(methyl methacrylate) (PMMA) and poly(styrene-*b*-1,4-butadiene-*b*-styrene) (PS-PBd-PS) in **Figure 1.13c** which are diluted in methoxybenzene (*i.e.* anisole) and chloroform, respectively.

Similarly, a multi-resonant system with different antenna orientations is introduced as being more selective,⁹³ where plasmonic resonances with different spectral locations are excited depending

on the incident light polarization. Likewise, advanced nanostructures with more complex geometries have been developed to produce a variety of spectrally distinct plasmonic resonances advantageous for SEIRA experiments, such as dendrites^{90,91,94} or Cayley trees^{95,96}. Among all, Wallace *et al.* have provided resonances from the near- to the mid-IR (**Figure 1.13d**) owing to the activated geometry of dendritic resonators featuring different shapes and branch numbers.⁹⁰ By this, the authors proved the suitability of their metasurfaces for SEIRA by performing spectroscopic measurements with 4-nitrothiophenol (4-NTP) functionalized dendritic fractals.

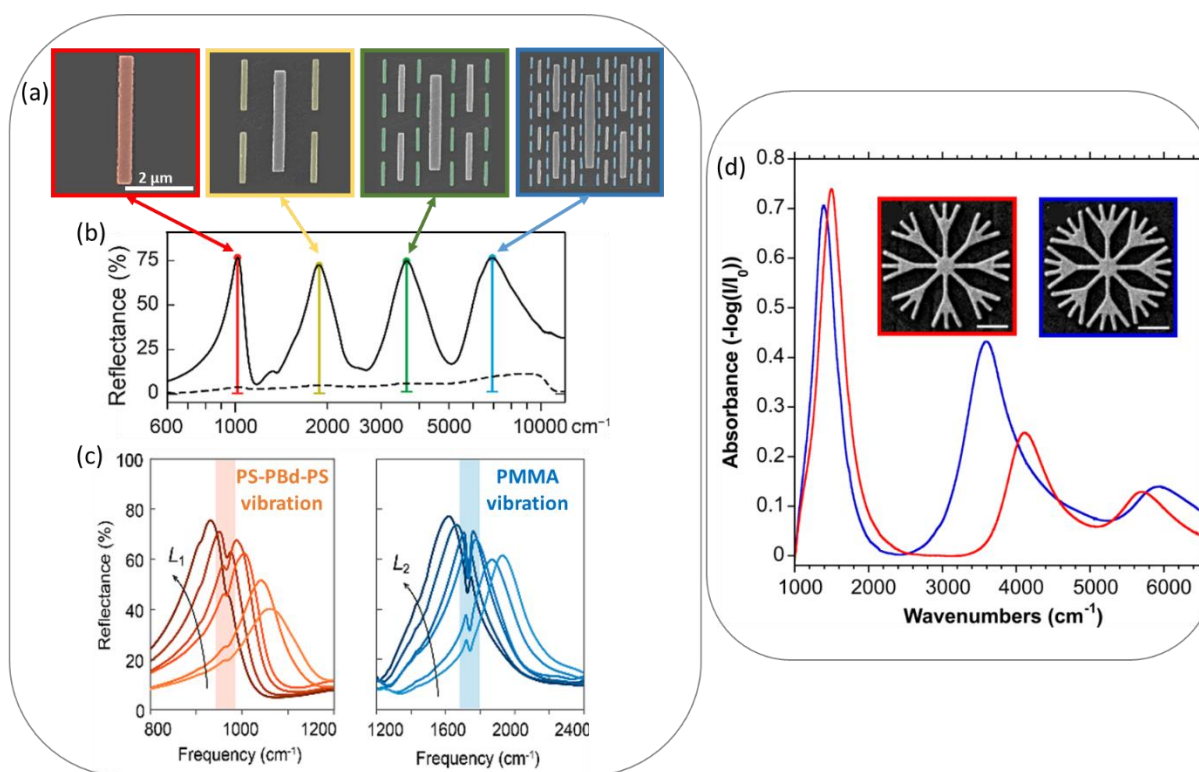


Figure 1. 13. The state-of-art of the advanced fractal-like nanostructures for SEIRA demonstration. As reported by Rodrigo *et al.* (a) SEM images of a self-similar plasmonic metasurface sustaining plasmonic resonances throughout a wide IR spectral region (b). (c) By careful tailoring of the rod length, the fundamental plasmonic resonances can be tuned to match several vibrational bands of the target analyte molecules leading to noticeable SEIRA signals.⁹² Wallace *et al.* stated dendritic fractals resonators (d) inset are the corresponding SEM images (scale bar: 400 nm) and the resultant color-coded absorption spectra.⁹⁰

Reference /year	Structure	Operating range (cm ⁻¹)	Analyte	Tuning ratio	EF
Neubrech <i>et al.</i> /2008	Single nanorod	2000 - 4000	ODT	1.02	Not reported
Vogt <i>et al.</i> /2014	Nanorods array	1000 - 2000	CBP	0.95	10 ³
Bagheri <i>et al.</i> /2015	Dense nanorods array	1000 - 2000	CBP	0.96	10 ⁴
Brown <i>et al.</i> /2015	Fan with a 20 nm gap in MIM	2500 – 3000	ODT	0.99	10 ⁵
Wallace <i>et al.</i> /2017	Dentric	1200 - 1800	4-NTP	0.96	10 ^{3.5}
Dong <i>et al.</i> /2017 *	3nm gapped-BT in a MIM	1200 - 1800	4-NTP	0.99	10 ⁷ *
Rodrigo <i>et al.</i> /2018	Multiperiodic nanorods	800 - 1200	PS- PBD-PS	0.98	Not reported
		1200 - 2400	PMMA	0.99	Not reported
Barho <i>et al.</i> /2018	HC-SC, rectangles array	800 - 1000	Vanillin	0.97	10 ³

Table 1. 2. State-of-art of SEIRA-triggering nanostructures. The research timeline will be mainly provided for Au nanoantennas. The results of highly-doped semiconductors(HD-SC) is cited. *This is the best-reported value for the highest achieved SEIRA EF.

- CMOS-compatibility for SEIRA

Metals such as Ag and Au have been widely used for SEIRA owing to their outstanding ability to support plasmonic resonances with strong electric near-field enhancements to improve the light-matter interaction and enable low detection limit sensing. In particular, Au is a material of choice for biosensing due to its chemical inertness to biological materials and straightforward

functionalization using thiol molecules.⁹⁷ Despite their advantages, such traditional plasmonic metals are limited because of the lack of dynamical tunability and the major issue of incompatibility with CMOS fabrication processes. This lack of CMOS integration significantly delays the prospect of mass fabrication and integration of low-cost SEIRA sensors.

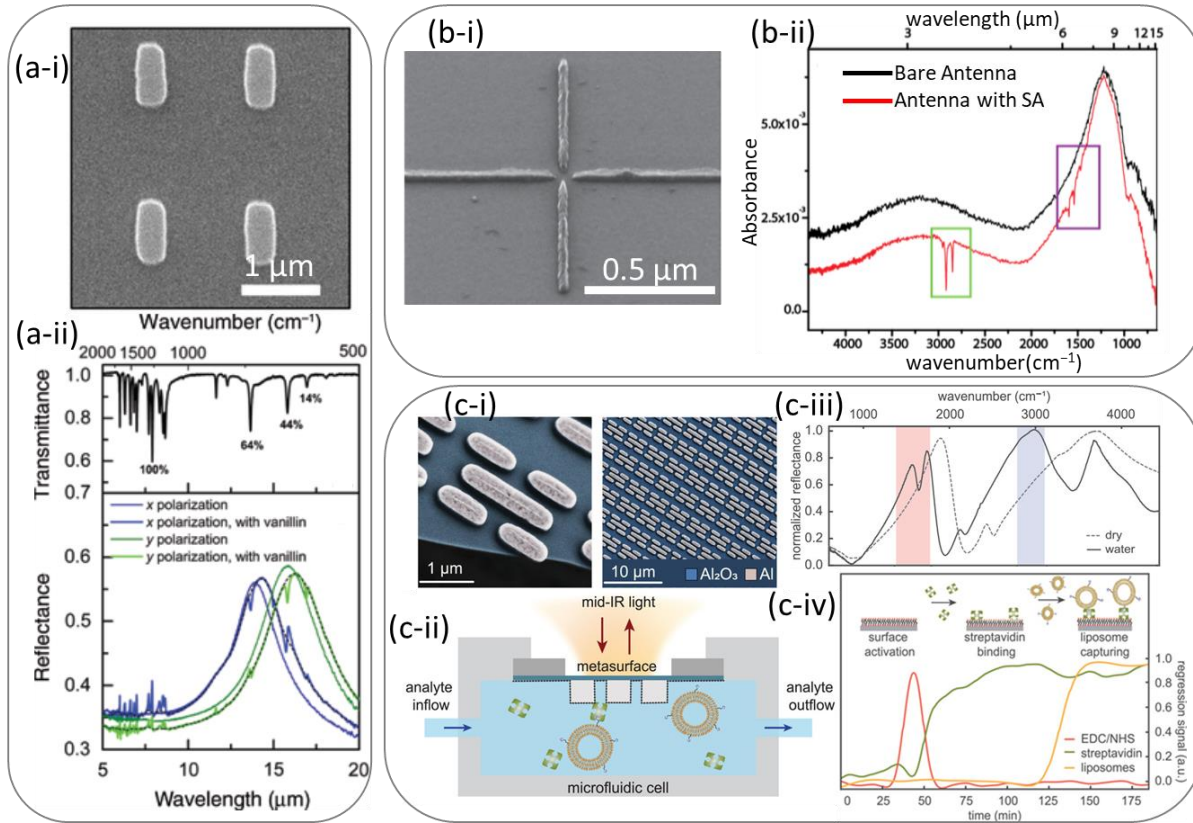


Figure 1. 14. CMOS-compatible plasmonic resonators for SEIRA investigation. (a) Highly-doped semiconductors tailored in rectangular arrays. (a-i) SEM image of the fabricated antennas. As reported by Barho *et al.*,⁷⁸ the polarization is giving a new chance to tune their plasmonic resonance as illustrated in (a-ii) where SEIRA demonstration with both light polarization is achieved using vanillin as a test molecule. Cerjan *et al.*⁶⁵ demonstrated a SEIRA feasibility using asymmetric-crossing Al antenna as shown in (b-i) and (b-ii) where the absorption features of stearic acid (SA) SAM are plasmonic-enhanced. In a recent Altug's work,⁹⁸ Al antennas on Al_2O_3 (c-i), integrated into a microfluidic circuit (c-ii) have shown a promising ability to (c-iii) target lipid and protein absorption bands as respectively shaded in red and blue, metasurface reflectance spectra are acquired in dry (dashed curve) and aqueous solution (solid curve). And to monitor the protein and liposome capturing events on a metasurface functionalized with phosphonic acids whose carboxyl groups were activated with an initial EDC/NHS solution as a real-time regression signal in (c-iv).

To overcome this limitation, intentionally doped semiconductors are an appealing substitute for traditional plasmonic metals because they can offer CMOS compatibility while still supporting plasmonic resonances. Their plasma frequency ω_p is flexible and easily tunable by the doping

level. It is lower than for metals, and therefore doped semiconductors are not viable alternative materials in the visible and near-IR spectral ranges.⁹⁹ Nevertheless, in the mid-IR, doped semiconductors are appealing for SEIRA applications.¹⁹ In line with this, the work of Barho *et al.* is showing a promising proof-of-concept for a SEIRA demonstration of vanillin using rectangular arrays of Si-doped InAsSb on the GaSb substrate resonating in the mid-IR, as shown in **Figure 1.14a**.⁷⁸ Herein, the light polarization was an additional degree of freedom to tune the plasmonic resonance of the antenna to easily access the target vibrational modes (**Figure 1.14b**).

Besides the highly doped semiconductors, Al is widely presented as a CMOS-compatible, low-cost, and abundant material suitable for plasmonic SEIRA chips.^{65,72} In this context, Cerjan *et al.* have already proved SEIRA feasibility using asymmetric antennas (**Figure 1.14b-i**) for enhancing the absorption lines of a SAM of stearic acid (SA) as detailed in **Figure 1.14b-ii**.⁶⁵ In a recent work of Altug's group, multi-resonant Al antenna arrays were fabricated at a wafer scale with deep ultraviolet (DUV) lithography on transparent Al₂O₃ nanomembranes (**Figure 1.14c-i**). After integration with microfluidics, the sensor chips assisted in situ SEIRA via the backside reflection configuration (**Figure 1.14c-ii and 14c-iii**). The authors demonstrate that such a biosensing platform can detect protein-lipid interactions in real-time (**Figure 1.14c-iv**).⁹⁸

- Dielectric resonators

Besides the pre-mentioned “metallic” antennas, the non-metallic metasurfaces are proved as useful for advanced surface-enhanced spectroscopies, especially in the mid-IR. Indeed, all-dielectric resonators are a crucial building block for developing nanophotonic platforms with low losses (compared to plasmonics), broad spectral coverage, and strongly enhanced electromagnetic near-fields as they can sustain a multitude of electric and magnetic Mie-type resonant modes, which are ideal for shaping light-matter interactions.^{1,100} The key aspect is to implement high refractive index dielectrics as resonator materials, such as silicon and germanium, or compounds like titanium dioxide and gallium phosphide.¹⁰¹ Even though the use of low-loss dielectrics avoids the intrinsic material losses traditionally associated with plasmonics, many

common all-dielectric geometries such as spheres, disks, or rod-type structures are still affected by the radiative loss.

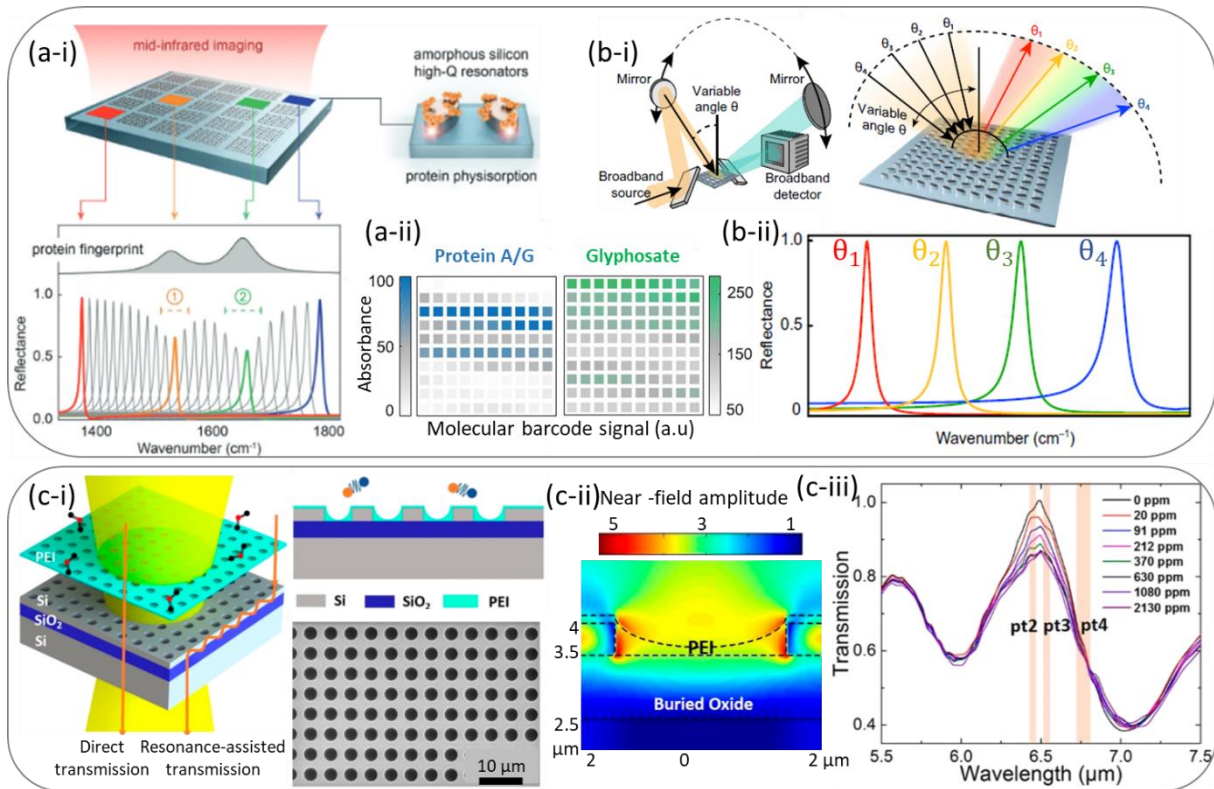


Figure 1. 15. All-dielectric-based platforms for spectroscopy. Tittl *et al.* proposed (a-i) Two tilted amorphous Si ellipses, designed as pixelated metasurfaces, having high-Q resonances, used for spatially encoding the spectral absorption fingerprint information of molecules. (a-ii) Imaging-based read out of this information produces a molecular barcode signal suitable for chemical identification in a target analyte, as for protein A/G and glyphosate.¹⁰² An extra tunability degree is proposed by Leitis *et al.* (b-i) Angle variation achieved by a simple moving mirror system, combined with the spectral selectivity of high-Q resonances of germanium ellipsoids, permits a broadband activation and an angle-to-plasmonic resonance correlation, for better control of the detection selectivity.¹⁰³ A promising sensing capability is stated by Chang *et al.* for gas sensing using (c-i) a Si-based photonic crystal slab covered with polyethylenimine (PEI) sustaining guided resonances for carbon dioxide sensing. (c-ii) Strong surface sensitivity is numerically confirmed by the calculated electromagnetic near-fields. (c-iii) Experimental investigation of CO₂ detection in the ppm range.¹⁰⁴

Herein, pixelated metasurface platforms with extra-sharp resonances have been implemented by Tittl *et al.* as a new style for detecting the characteristic molecular fingerprints of several molecules. In particular, two tilted amorphous silicon ellipses are designed to provide many high-Q resonances at different wavenumbers within the spectral range of interest (**Figure 1.15a**).¹⁰² Each pixelated metasurface will target a specific molecule as it sustains

ultrasharp resonances, each tuned to a discrete frequency (**Figure 1.15a-i, bottom**), enabling the read-out of several molecular absorption signatures at multiple spectral points. For example, after covering the sample with a thin biomolecules layer of protein A/G, a clear amplitude decrease and broadening of the pixelated metasurface resonances related to the vibrational bands of the molecules in question. Therefore, the whole multi-pixelated surface of the sample will act as a barcode-like spatial absorption map for imaging the detection of compounds from varied research domains such as biology, environmental monitoring, and materials science, as illustrated in **Figure 1.15a-ii** for protein A/G and glyphosate. Because of the high-Q resonances and spectrally clean line shapes, specific absorption signals could be read out even when using broadband illumination and detection (*i.e.*, without the need for spectrometry), producing an image-based illustration of the molecular fingerprint that is suitable for further analysis using pattern recognition and machine learning methodologies.¹⁰⁵ In addition, Leitis *et al.* have employed the incidence angle of light impinging on germanium tilted ellipsoids (**Figure 1.15b-i**) to control the associated optical response, finding a one-to-one correlation between angle and resonance position (**Figure 1.15b-ii**).¹⁰³ The authors show a promising technological integration similar to established SPR-based sensing systems, only by implementing a simple moving mirror arrangement to nicely analyze a bioassay for the detection of human odontogenic ameloblast-associated protein (ODAM) via specific binding to single-stranded DNA aptamers.¹⁰³

Beyond solid and liquid analytes detection, Chang *et al.* have extended the scope of all-dielectric vibrational sensing when they proved the vibrational gas sensing of carbon dioxide (CO₂).¹⁰⁴ Their sensor consists of a resonant hole array structure fabricated from a silicon-on-insulator wafer and subsequently covered with the gas-selective polymer polyethyleneimine (PEI) as illustrated in **Figure 1.15c-i** to enhance to an interaction between the absorbed CO₂ molecules and the enhanced near-electromagnetic fields of the photonic crystal slab (**Figure 1.15c-ii**). Following various optimization of the resonators geometry, *i.e.* radius to period ratio, the authors proved the detection of the vibrational signature of CO₂ for concentrations down to the low ppm range (**Figure 1.15c-iii**) thanks to a pronounced resonance at a wavelength of around 6.5 μm.

Subsequently, they have stated that a thicker coating improved the response time, providing valuable design guidelines for future SEIRA-based gas sensing techniques.

Besides this optical way of gas sensing, recently the community is focusing on electric-noses (e-noses) using carbon nanotubes¹⁰⁶ or functionalized graphene¹⁰⁷ to detect diseases related to the respiratory system and lung with enhanced selectivity which is promising for successful discrimination of biomarkers in animal or human breath.

1.4. Conclusion

In this chapter, an overview of plasmonics and its different excitations was detailed. The plasmonic characteristics of metals were addressed and alternative materials were proposed. Considerable attention was focused on the design of plasmonic antennas (individual and arrays of nanoantennas, fractal-like geometries, nanogapped structures, bowties, etc...). These nanostructures provide tunable resonances over a wide spectral range by simply varying their size. The achieved optimum near EM-field enhancements are suitable for sensitive sensing applications at the hotspots sites, owing to the combination of the lightning-rod and the gap effects. A great section was devoted to the biosensors and especially the surface-enhanced IR absorption spectroscopy (SEIRA). A glance at the state-of-art of SEIRA was provided using gold, CMOS-compatible materials as highly-doped semiconductors and Al, dielectric materials as Si and Ge.

Above all, a final choice of plasmonic materials requires a balance between quality factors, production cost, and feasibility. Compared to conventional noble materials, Al possesses the properties of low cost, tunable plasmon resonances in UV and IR regions, and CMOS compatibility, which are important requirements of new plasmonic sensing material. Al is extremely appealing and worth a complete scientific demonstration to prove the capability to conceive, fabricate and optically characterize Al nanoresonators. Subsequently, thanks to the local enhancement of the near electromagnetic fields, such nanoantennas will demonstrate a sensing ability through surface-enhancing the absorption features of interesting molecules in the IR range.

1.5. Objectives of our study

Inspired by the insightful structures of Brown *et al.*⁸⁵ and Dong *et al.*⁸⁷, and based on the theoretical study of Wang *et al.*³⁹, we will combine the effects of both the MIM and the closely placed sharp apexes to create bowtie nanoantenna integrated within a MIM configuration with thin spacer, holding the gap-plasmon effect. The CMOS-metallic material will be Al owing to its good optical properties in the IR where we will investigate the SEIRA sensing using a trial molecule. Inspired by the multiplexing approach demonstrated by Rodrigo *et al.*⁹², a similar design will be incorporated on the same sample surface. Multiple zones are structured with adequate geometries to easily tune their corresponding plasmonic resonances to many vibrational modes of interest. In analogy to scanning a barcode, a unique spectral coupling will be established between a selected vibrational mode and a suitable wide plasmonic resonance. The efficiency of the befalling coupling is interpreted through the amplitude of the resulting Fano-like features.

The PhD project main objective is to achieve a barcode-like nanostructured surface as optical transducer from the near to the far IR with enhanced E-field intensity in subsequent selected spectral regions. This main objective can be split in the following specific objectives:

1. To conceive periodic arrays of aluminum sharp nanoantennas, namely, bowties (BT) and honeycomb (HC) nanostructures. To study their geometry, distance arrangement and gap to cover specific regions of the EM with enhanced intensity of coupled light. To analyze their integration within a MIM platform, compatible with Si-technology. This objective is mainly covered in **Chapter 2**, where single and dimer antennas are also presented. Simulations are done using Lumerical with customized codes. The simulation of the electrical field confinement will provide a reference of the order of magnitude of the near E-field intensity expected in relation to the nanometric tip-to-tip gap values. The results of this objective will be the input for the fabrication process in **Chapter 3** and will be compared to the optical characterization in **Chapter 4**. Note, the simulation of the near-field localization will be of great interest for the SEIRA evaluation in **Chapter 5**.
2. To establish a reliable fabrication process in a clean room environment based in electron-beam lithography, metal deposition, dielectric evaporation, lift-off techniques and surface

treatments. This objective will be implemented in **Chapter 3** where a close collaboration between the “Centrale Technologique de Montpellier” and the LAAS Clean Room facilities has been established in the framework of RENATECH program. The optical transducers were designed and conceived following two different strategies based on metallization with lift-off and Ar-etching for the BT and HC design respectively. The optimization of the process and the structures characterization will be presented in **Chapter 3**.

3. To realize the optical characterization of the BT and HC in relation to the geometry with a single FTIR and Focal-plane-array (FPA) detectors under polarized light. In **Chapter 4**, a systematic comparison with the previous numerical simulations will be established. For the study in the visible and NIR range, a short internship of one week gave access to the experimental set-up in collaboration with the Nano-optics lab at Politecnico di Milano.
4. To demonstrate the sensing features of the optical transducers based in the MIM structured with engineered HC and BT. FPA and single detector FTIR measurements will be used to demonstrate a SEIRA effect in different plasmonic active zones of the transducer with a trial molecule (Vanillin). To evaluate the enhancement factor of the structures and give the spectral information on both far-field behavior and near-field enhancement of several vibrational lines. To notice and comment the behavior of the asymmetric vibrational signals (so-called Fano-like lines) in function of the tuning factor. In **Chapter 5**, a comparison with the SEIRA state-of-art will be presented given the number of detected molecules per antenna and the pre-achieved enhancement factors. Preliminary results of a prospective plasmonic-enhanced gas detection with a pronounced absorption line of CO₂ situated at 2 353 cm⁻¹ will be also proved using the same multi-tunable platform.

The achievement of these objectives is encouraging for the introduction of compact, low-cost and selective, and sensitive bio- and gas- sensors to Si-technology. Consequently, a mass production of such a sensor could be easily imagined and realized.

Chapter 2: Conception of a barcode-like optical transducer

From a single triangle to a bowtie toward a compact honeycomb structure.

Metallic nanoantennas (NAs) are excellent candidates for plasmonic applications. The particle shape, size, and material will affect its optical and electromagnetic properties (*e.g.* resonance energy) and the accompanying E-field localization and intensity. In bowtie (BT) NAs, *i.e.* triangular prisms dimers, the local electric field is strongly enhanced at their sharp apexes (facing tip-to-tip) compared to spherical, cylindrical, and rectangular dimers. In this chapter, we investigate the electromagnetic modes supported by a single triangular prism being placed on several substrates using Finite-Difference Time-Domain, FDTD, as well as its optical behavior under different light polarization. Then, the cases of a single BT NA and a pair of BT NAs are studied, to conclude with BT as honeycomb (HC) arrays.

The electromagnetic responses of the NAs have been simulated by three-dimensional FDTD calculations using Ansys Lumerical 2021 R2.3 Finite difference solver. FDTD is a powerful method for solving Maxwell's equations based on the Yee algorithm in both space and time domains for complex geometries. Moreover, FDTD gives complete access to a wide range of meaningful physical quantities like the Poynting vector, the light reflectance/transmittance, and the 3D-mapping of the electric and magnetic fields thanks to the frequency solution offered by Fourier transforms. These magnitudes are extremely helpful to predict the comportment of single NA and NA arrays illuminated under different polarizations. For the Al, we referred to the dielectric constants reported in the CRC Handbook of Chemistry & Physics by E. Shiles.⁶² The SiO₂ material data are based on the Handbook of Optical Constants of Solids I - III by E. Palik¹⁰⁸, but are slightly modified to match the real quality of the deposited material.

The main simulation input is a metal-insulator-metal (MIM) structure. It has been modeled as a 50 nm-thick aluminum (Al) structured into NAs, with variable side length L and spacing g , on a 20 nm thick dielectric SiO₂ layer stacked on top of a 100 nm thick Al layer.³⁹ This configuration allows to access also to the "gap plasmon" which corresponds to a specific plasmonic effect whose E-field is compressed between both Al layers. For the honeycomb (HC) structures, a pre-defined etch material is introduced as described in section 2.2.3. An axiomatic refractive index equals

to 1 (representing air) is maintained in the structure surroundings to create an asymmetric environment.

The FDTD simulations are firstly carried out using Total-Field Scattered-Field (TFSF) source. TFSF source is perfectly adapted to calculate the scattering and the absorption from a single NA up to a dimer of NAs. Then, BT arrays were accurately generated with a home-made script along x -axis, as well along y -axis but with a larger separation. Plane-wave source is the ultimate solution for considering the periodicity and to obtain the far- and near-field behaviors of the NA arrays within the MIM structures. For both TFSF and plane-wave sources, incident light is co-polarized or cross-polarized (parallel or perpendicular to the NA main axis) and launched backward along the z -axis. Furthermore, taking advantage of both the periodicity and the symmetry of the model, symmetric and anti-symmetric boundary conditions are selected to reduce the simulation time and the memory requirement. In all cases, the boundary conditions along the z -axis (the direction of the injected plane wave propagation) support Perfectly Matched Layers (PML), where all incident energy is conventionally absorbed so that no energy could be scattered back into the calculation zone. Thereafter, the optical responses are collected using a monitor placed above the excitation source, the so-called reflectance monitor. A field monitor is mainly introduced in the xy -plane to represent the electric field cartography. Throughout both monitors, the influence of geometrical parameters on the plasmonic behavior is studied. Please note that all the FDTD scripts involved to simulate the corresponding BT or the HC NAs will be provided via GitHub <https://github.com/MelissaNajem/FDTD>.

In sum, the aim of both numerical simulation methodologies is to finely define and correlate the modes of a single NA, a dimer of NAs, a BT, a dimer of BT and arrays of BT. Therefore, describe the arising EM-modes upon the anticipated couplings of periodic BTs, leading to the intentional construction of a honeycomb-like compact structure.

Contents

Chapter 2: Conception of a barcode-like optical transducer.....	51
2.1. Total-field Scattered-field (TFSF) Source	54
2.1.1. Al prism free-standing, on SiO ₂ layer and in a MIM structure	55
2.1.2. Al Bowtie within a MIM.....	60
2.2. Plane-wave source.....	66
2.2.1. Coupling effects under light polarization for BT within a MIM in a 1D array	66
2.2.2. Periodic BT arrays with different geometric parameters	68
2.2.3. Compact configuration of Al triangles: Honeycomb-like resonators.....	75
2.3. Conclusion.....	83

2.1. Total-field Scattered-field (TFSF) Source

Thinking inside and outside the box

The Total-Field and Scattered-Field (TFSF) source is an advanced type of the plane-wave source, designed mainly for particle scattering simulations. In absence of a particle, *i.e.* in empty space, the injected plane wave propagates along the box within the source. It remains an ideal plane wave inside the box as there are no structures to cause any perturbations. However, in presence of a particle inside the source box, the plane wave propagation will be disturbed. Any light scattered from the object will propagate through the source boundary into the scattered field region. Moreover, the particle contribution due to the material absorption will be detected by the box inside the source. Hence, the TFSF simulation splits the simulation region (orange box) into two distinct parts: Absorption and Scattered regions. By this, the absorption and scattered cross-sections are calculated using dedicated analysis groups (yellow boxes) placed respectively inside and outside the source box (gray box) as illustrated in **Figure 2.1**.

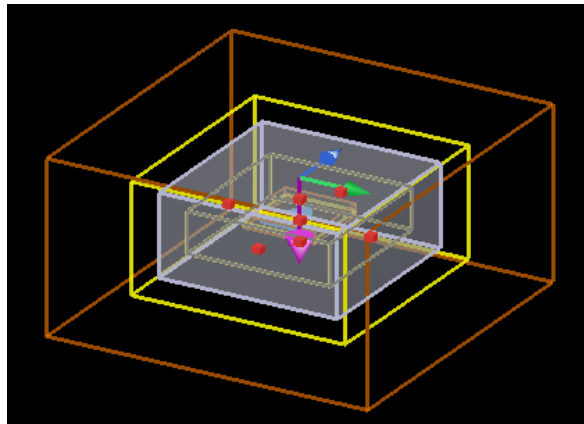


Figure 2. 1. Scheme of the TFSF simulation features. The gray box represents the TFSF source. The yellow box inside the source box collects the absorption cross-sections and the one outside of it collects the scattered cross-section. All these boxes are wrapped with the simulation box (orange box). Field monitors are also involved in these simulations in the 3D-cross-sectional planes (check **Figure 2. 2**).

In the following simulations, the source wavelength is spanning from 0.2 to 2.0 μm . An extra script is developed to retrieve the efficiency, by dividing the cross-sections by the structure's area. To identify the involved modes, electric (E) and magnetic (H) field magnitudes are collected through near-field monitors mainly crossing the structure as detailed in **Figure 2.2**. For homogeneity and

comparison, the side-length, L , of the simulated triangles in this section is set to $0.3 \mu\text{m}$. A mesh-override with a step of 5 nm is wrapping the triangle for good accuracy.

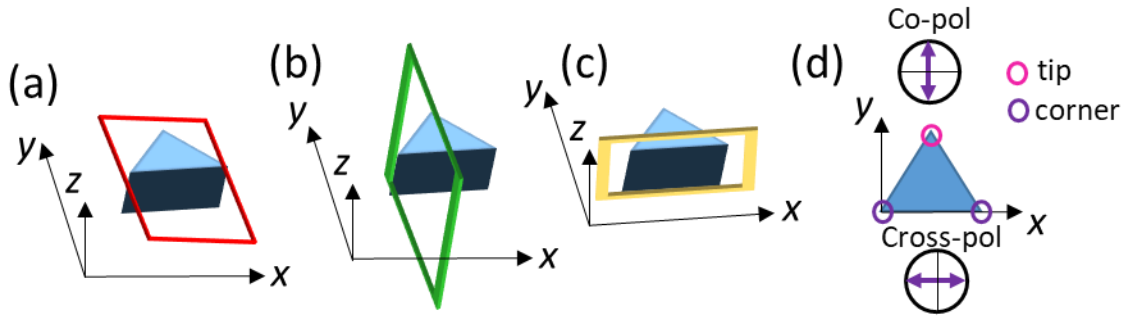


Figure 2.2. Sketch of the planes of the monitors. (a) is in xy -plane, (b) is in yz -plane, (b) is in xz -plane. The y -axis is parallel to the triangle's height; x -axis is perpendicular to it. (d) shows the tip and corner definitions of a triangle and the polarization directions in the xy -plane.

2.1.1. Al prism free-standing, on SiO_2 layer and in a MIM structure

An equilateral triangle (prism) with a height (thickness) of 50 nm and a side length, L , equal to $0.3 \mu\text{m}$ is our first building block thanks to its simplicity. Its geometric shape leads to different electromagnetic behaviors depending on the incident light polarization. For this purpose, far-field and near-field numerical results are examined. In the far-field, the scattering and the absorption cross-section efficiencies are evaluated. For all the simulations, the figures present a similar format: the scattering efficiencies (labelled "Scat") is represented in a black line and the absorption efficiencies ("Abs") in red. Under a co-polarized light (co-pol), when the E-field is parallel to the triangle's height, both efficiencies are plotted in solid lines. Under a cross-polarized light (cross-pol), when the E-field is perpendicular to the triangle's height, both efficiencies are in dotted lines. The near-field mappings are collected through 2D planar monitors as presented in **Figure 2.2**, where also the polarization directions are shown. Note, the red monitor (parallel to the xy -plane) is situated at $z = 25 \text{ nm}$ (at the middle of the prism height). Considering the corner of the prism as origin (0,0), the green monitor (parallel to the yz -plane) is situated at $x = 0.15 \mu\text{m}$ (at the middle of the prism's side), and the yellow monitor (parallel to the xz -plane) is situated at $y = 5 \text{ nm}$ away from the prism's side.

Firstly, a free-standing Al prism is considered inside the source box. Scat and Abs cross-section efficiencies are calculated under both polarizations, as illustrated in the blue section of **Figure 2.3**. In **Figure 2.3a-i**, the Abs is referring to the absorption related to the Al internal losses (interband transitions around $\lambda = 0.8$ to $0.9 \mu\text{m}$). Al losses are due not only to interband transitions but also to Drude scattering. In this case, the scattering of the prism is dominating (in black). On top of the corresponding Scat, a first mode ("M1") appears. Then, a second mode ("M2") takes place at a higher energy (lower wavelength). For each mode, a specific distribution of the near EM-fields occurs. As shown in **Figure 2.3b-i and 2.3c-i**, the M1 is a dipole mode as the E-field is pinned at the prism tip under a co-pol and at the corners under a cross-pol. This statement is confirmed by the corresponding H-field distributions. Indeed, for a dipole mode, the H-field is showing 1 lobe at the prim's sides. However, M2 is a quadrupole mode as the E-field is pinned at the prism tip and sides under a co-pol and at the corners and sides under a cross-pol. This statement is confirmed by the corresponding H-field distributions which show 3 lobes at the prim's sides. Note that the lobe's definition is based on the symmetry reasons due to the electric field orientation of the incident light.

Secondly, the prism is deposited on an SiO₂ semi-infinite medium. Systematic simulations were done as illustrated in the green section of **Figure 2.3**. Likewise, the Abs in **Figure 2.3a-ii** is referring to the absorption related to the Al internal losses. Yet, it is slightly compressed due the introduction of the substrate, so the medium is not considered isotropic as for the free-standing prism case. Note, a perfect coupling to the particle absorption is done in isotropic medium. Interestingly, the scattering mechanism is still dominant. Moreover, the M1 is red-shifted as the surrounding medium refractive index has changed once the SiO₂ was introduced as substrate ($n_{\text{SiO}_2} > n_{\text{air}}$). This confirms that M1 is the actual plasmonic mode. In **Figure 2.3b-ii and 2.3c-ii**, similar near E-field distributions are retrieved for M1 and M2 in the xy -plane. Plus, the near E-field distributions in the xz -plane demonstrate its effective localization at the Al/SiO₂ interface. This is the main effect of the SiO₂ substrate, it "attracts" the E-Field at the interface compared to the free-standing case.

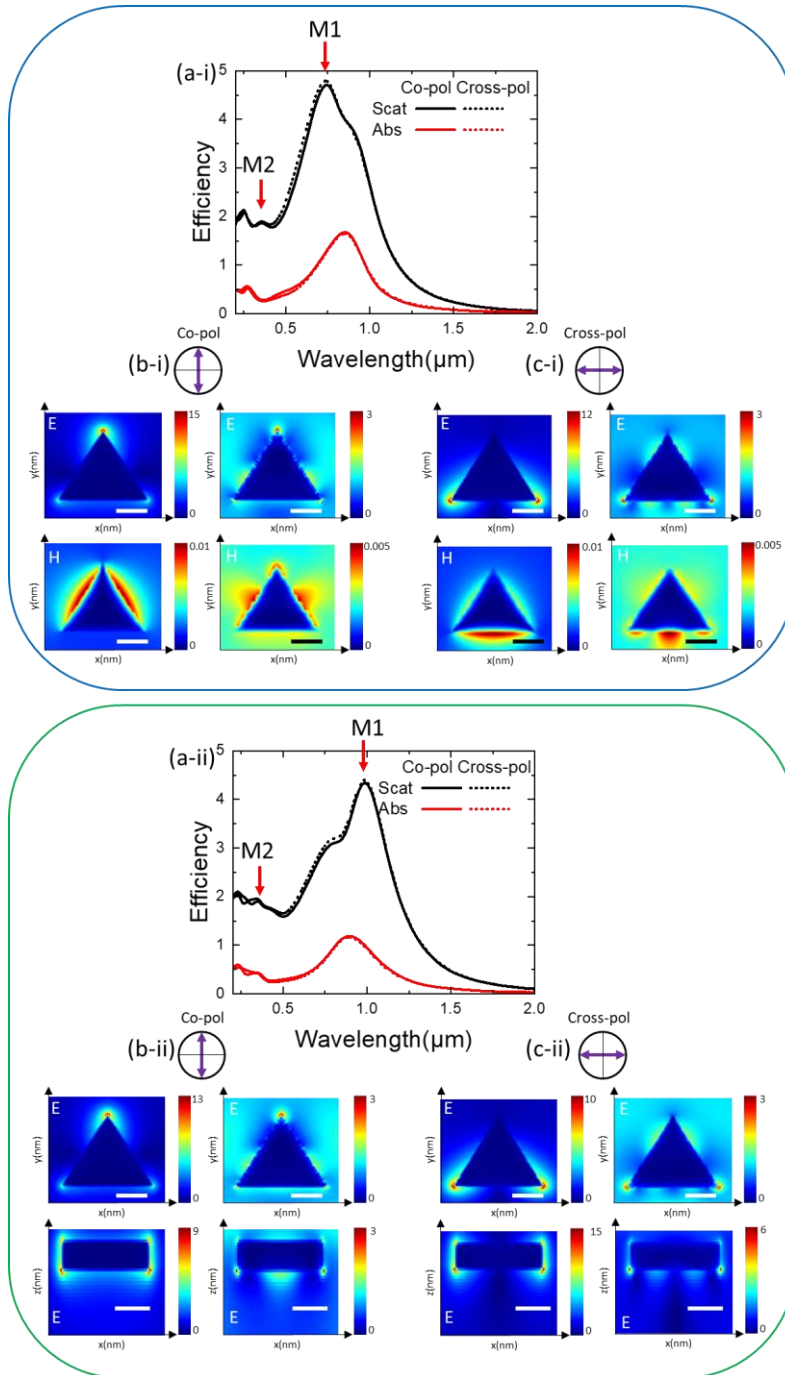


Figure 2. 3. Blue section: the behavior of a free-standing Al prism under a co- and cross-polarized light source. In the far-field (a), the scattering and the absorption cross-sections efficiencies are plotted. The vertical red arrows correspond to the two first localized plasmonic modes of the Al prism. In the near-field, the E- and H-fields magnitudes (E/E_0 and H/H_0) are illustrated in the xy-plane respectively at $\lambda= 0.970$ (left-side panels) and 0.290 μm (right-side panels) under co-pol in (b); and at $\lambda= 0.930$ (left-side panels) and 0.280 μm (right-side panels) under cross-pol in (c). Green section: same analyses are done when introducing the prism on top of the SiO_2 . Note, in (b-ii) and (c-ii) only the profile of the E-field is represented in the xy-plane and the xz-plane. All scale bars are 100 nm long. SiO_2 .

To go further in complexity, an Al mirror is introduced underneath the combination of the Al prism on SiO₂. This creates a metal-insulator-metal (MIM) structure (Al/ SiO₂/ Al). The thickness of SiO₂ layer is set to 20 nm, as done by Wang *et al.*³⁹ This layer is acting as a spacer between a semi-infinite medium of Al as a mirror and the top 50 nm Al layer as prism. This configuration allows to access to the gap plasmon effect where the E-field is compressed between both Al layers. The analysis of far- and near-field features are continued inside the TFSF source. The results for such a MIM configuration are plotted in **Figure 2.4**.

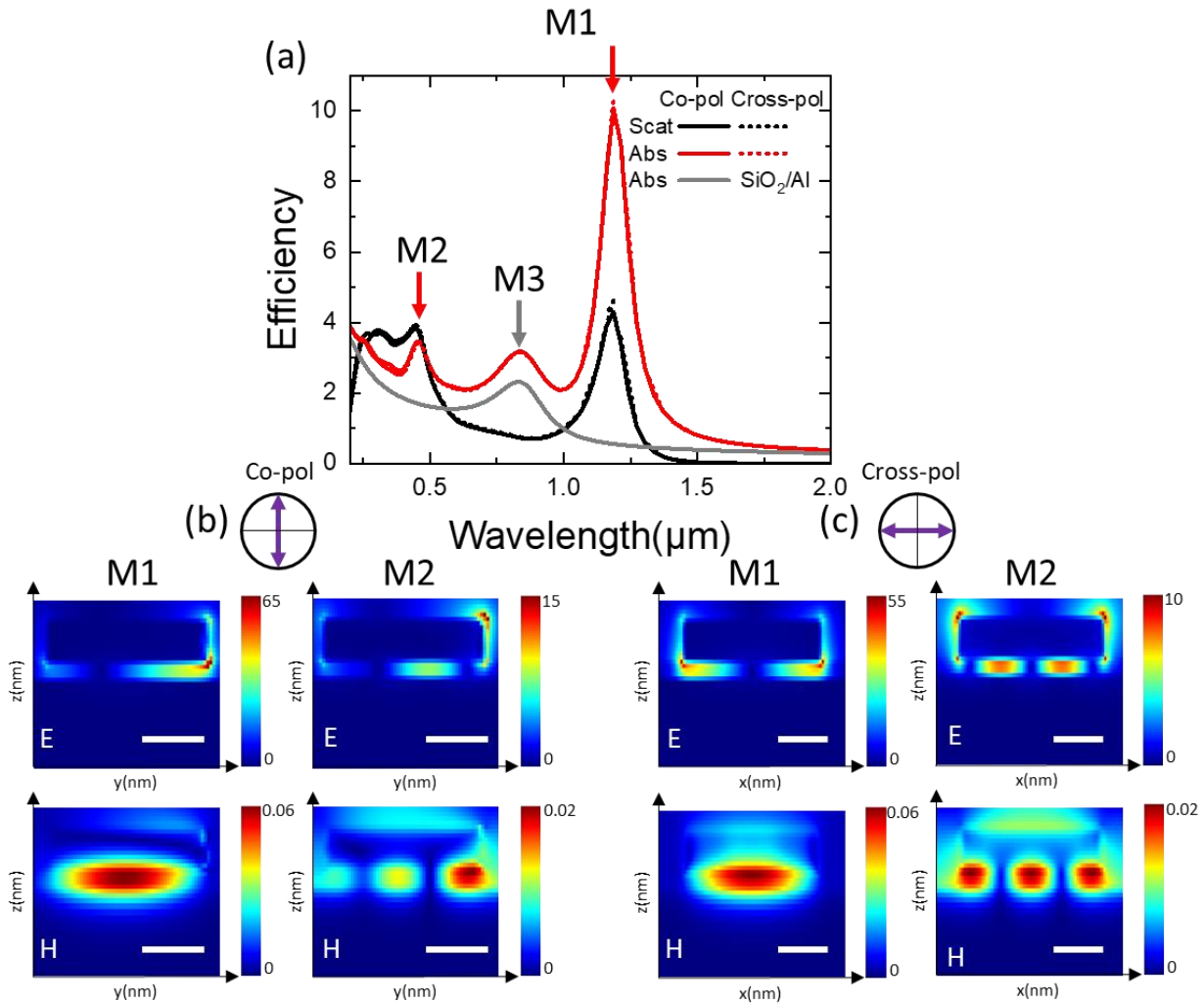


Figure 2. 4. Al prism within a MIM configuration under a co- and cross-polarized light source. In the far-field (a), the scattering and the absorption cross-section efficiencies are plotted. The absorption cross-section efficiency of the bare substrate (SiO₂/Al) is plotted to show a maximum (M3) at 0.82 μm (gray arrow). In the near-field, the E- and H-fields magnitudes are illustrated in the cross-sectional yz- ((b) for co-pol) and xz-planes ((c) for cross-pol) respectively at $\lambda = 1.186$ and 0.476 μm (red arrows). All scale bars are 100 nm long.

In the far-field, the Abs cross-section efficiency show the well-defined modes M1 and M2 aligned with those of the scattering at $\lambda = 1.186$ and $0.476 \mu\text{m}$ (red arrows) in **Figure 2.4a**. This underlines the existence of a trapped gap-plasmon inside the spacer (insulator) of the MIM structure. In consequence, the absorption dominates in this case, and it will indicate the occurring plasmonic modes. Moreover, the cross-section efficiencies in the MIM case are narrower and more amplified than the ones recorded for a simple SiO_2 as substrate. The third resonance mode, M3, is still appearing at $\lambda = 0.82 \mu\text{m}$ (gray arrow), close to the interband transition of Al. To understand its origin, an extra simulation is strictly done by considering the bare substrate (without the Al prism, *i.e.* only considering SiO_2/Al). A similar mode M3 appears in the grey curve in **Figure 2.4a** stating even clearer the SiO_2/Al intrinsic response.

In the near-field, **Figure 2.4b and 2.4c** show a complementary study of the near-field mappings. The H-field images (lower panel) allow the definition of the two resonance modes. The resonance M1 at higher wavelength is assigned to a magnetic dipolar (1 lobe is trapped into the gap underneath the prism) and M2 to a quadrupole mode (3 lobes) at lower wavelength. The existence of two lobes of the magnetic field into the spacer is not possible for symmetry reasons due to the electric field orientation of the incident light (horizontally in the represented cross-sectional planes). Noteworthy, the near-field distributions of both modes are quite different under both polarizations. Under a co-pol, the E-field is enhanced at the tip of the triangle. Under a cross-pol, the E-field is enhanced at the corners of the triangle. Conventionally, the localized E-field that is manifested at M1 (at lower energy) is much more pronounced than the one at M2. This statement might be translated in the far-field. Indeed, the domination of the scattering at M2 in **Figure 2.4a** could occur due to the modest near E-field enhancement at this energy.

2.1.2. Al Bowtie within a MIM

2.1.2.1. Individual bowtie

In this section, a single bowtie (BT) behavior will be analyzed as the top layer of the MIM structure to identify the specificity of this geometry compared to the one of a simple prism. The effects of the polarization as well as the tip-to-tip spacing gap are examined in detail. The normal monitors in cross-sectional xz - and yz -planes were lengthened to slit the whole BT along its main axis, following the tip-to-tip facing triangle axis through the tips (along y -axis), and across it, set along x -axis, *i.e.* the triangle's corner bases. (see **Figure 2.5**).

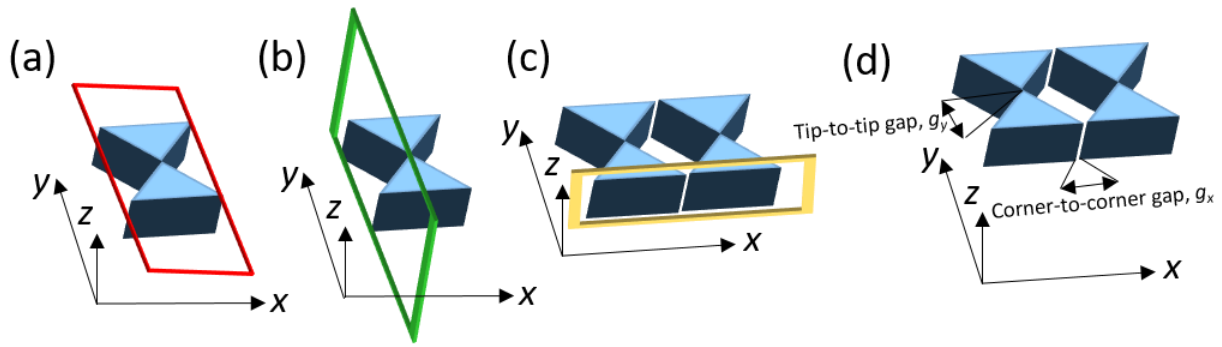


Figure 2. 5. Sketch of the plane of the monitors. (a) is in xy -plane, (b) is in yz -plane, (b) is in xz -plane. The y -axis is parallel to the tip-to-tip facing triangles (BT main axis), x -axis is perpendicular to it, so, parallel to the corner-to-corner closely placed triangles. Note in (a) and (b) an individual BT is represented. A pair of BT is illustrated in (c) and (d) with the corresponding tip-to-tip gap along the y -axis, g_y , and the corner-to-corner gap along the x -axis, g_x .

Firstly, the tip-to-tip gap is fixed at 100 nm and the polarization is flipped from a co-pol to a cross-pol. The far- and near-field characteristics are illustrated in **Figure 2.6**. Based on the far-field cross-section efficiencies, two pronounced modes that are related to the nanostructure appear at the same position, M1 and M2, at $\lambda = 1.186$ and $0.476 \mu\text{m}$ (respective red arrows in **Figure 2.6**), as found for a single prism within a MIM (**Figure 2.4**). Thus, an individual BT with a $g = 100$ nm acts like a single prism. Being a unit cell of the BT, the Al prism and its distinguished behaviors under both polarized E-fields are extremely supportive of the near-field study of BT. In analogy to a single prism, under a co-pol the induced E-field is mainly trapped at the facing triangle tips; and the H-field is showing a single lobe inside the spacer at a lower energy (a higher wavelength), and

3 lobes at higher energy (a lower wavelength) with an E-field localization at the corners of the triangle.

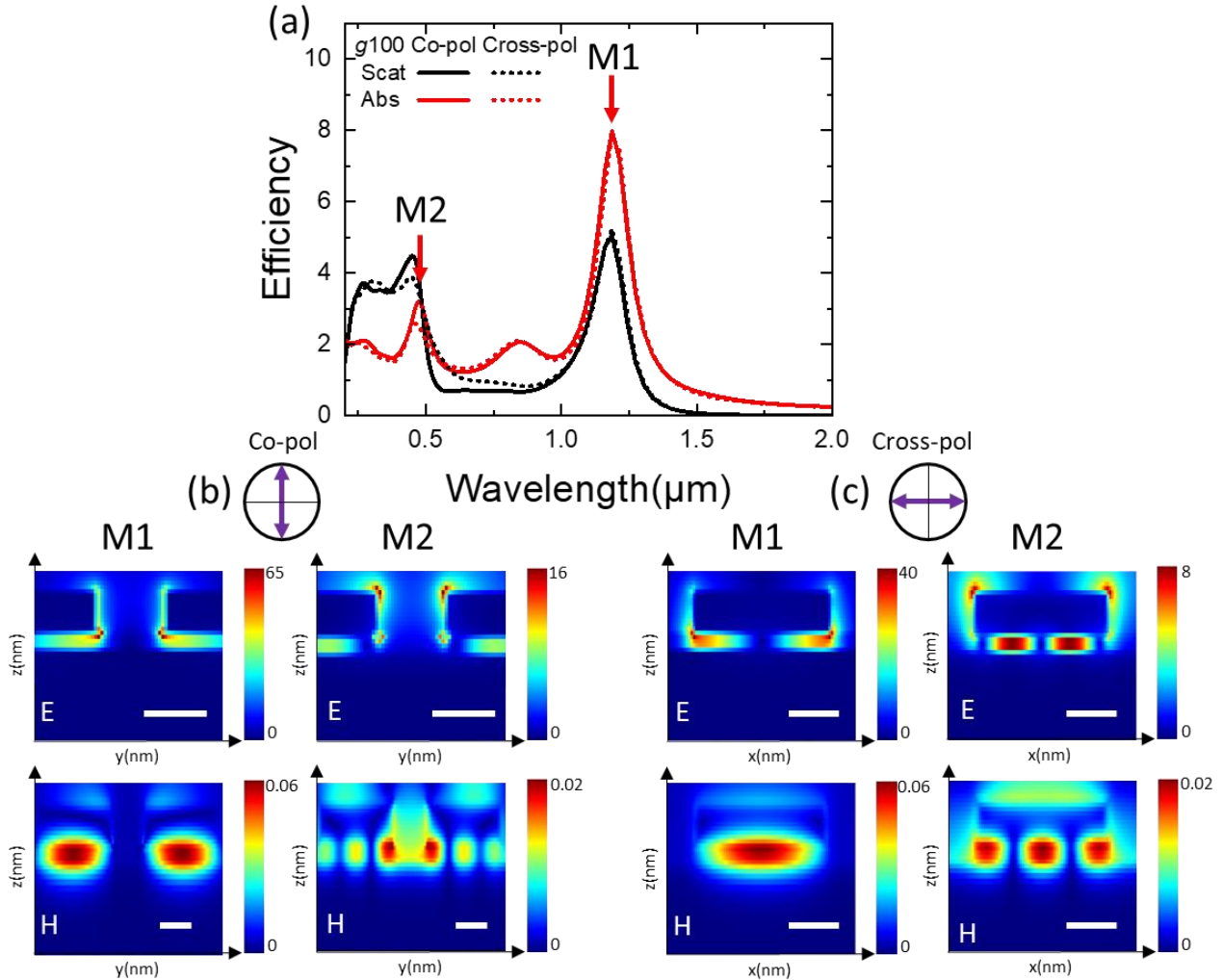


Figure 2. 6. Individual AI BT within a MIM configuration under a co- and cross-polarized light source. The tip-to-tip spacing gap is maintained constant at 100 nm. In the far-field (a), the scattering and the absorption cross-section efficiencies are plotted, showing two distinct modes related to the nanostructure (M1 and M2). In the near-field, the E- and H-fields magnitudes are illustrated in the cross-sectional yz- (for co-pol (b)) and xz-plane (for cross-pol (c)) respectively at $\lambda = 1.186$ and $0.476 \mu\text{m}$ (M1 and M2). All scale bars are 100 nm long. Note the difference of scale for the H-field profile under co-polarized light.

Herein, it is crucial to stress on the gap influence on the far-field response of a BT under both polarizations. For this purpose, the gap is reduced to 20 nm in **Figure 2.6**. As soon as the polarization is triggering a narrower gap, a probable coupling between the closely placed tips becomes highly expected. In principle, this coupling resonance mode is characterized by the

interaction of dipole-like charge oscillations. The inter-particle coupling occurs at lower energy as soon as the triangles are closer. This behavior is described in terms of a plasmon hybridization model: in analogy to atomic and molecular orbitals hybridization principle, their coupling generates new resonances with an energy splitting. At the lower energy, under plane-wave excitation, the bonding mode appears "bright" in spectroscopic measurements as it couples strongly with the incident light through dipole radiation (with some ohmic damping).⁷³ As illustrated in **Figure 2.7a**, under a co-pol, the coupling potentially occurs in the tip-to-tip gap, leading by this to a red-shift of M1, and a blue-shift of M2 while decreasing the g value to 20 nm. Thus, for the smaller gap, the coupling is stronger and its arising M1 is red-shifted. While under a cross-pol, as the corners are triggered (based on **Figure 2.6c**) and no possible coupling occurs, M1 and M2 of the BT are intact even though the tip-to-tip gap is decreased as detailed in **Figure 2.7b**.

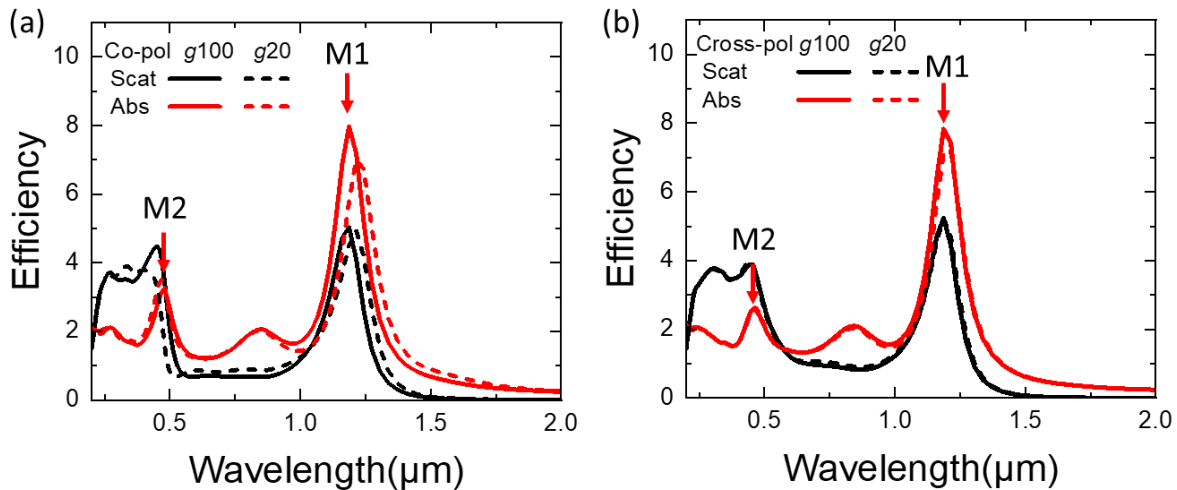


Figure 2. 7. Gap and polarization influence on the individual BT far-field response. (a) The gap influence is studied under a co- and then (b) a cross-polarization. For a $g = 20$ nm, a red-shift is only obtained under a co-pol. Under a cross-pol, the far-field response is unchanged despite the g reduction.

2.1.2.2. Pair of bowties

To imitate a certain periodicity and to better understand the effect of an eventual corner-to-corner interaction, two identical and closely placed BT are introduced inside the source box along the x -axis, as illustrated in **Figure 2.5c**. In the following, the polarization as well as the gap

influence on the features of a pair of BT will be addressed. In this section, the distance between both BT along the x -axis is 20 nm (a corner-to-corner gap of 20 nm). Thus, the tip-to-tip and the corner-to-corner distances, *i.e.* g_y and g_x are equal to 20 nm (check **Figure 2.5d**).

The cross-sectional monitor along the x -axis was elongated to cover both BT bases, and the one in the xy -plane was also extended to cover them both (check **Figure 2.5**). The pair of BT is illuminated under a co-pol, and tip-to-tip zones are technically activated. Absorption efficiencies spectra ($Abs/4 \times A_{triangle}$) are retrieved and compared to those of an individual BT and a single prism in **Figure 2.8**. It is important to note that the cross-section efficiencies depend directly on the surface of the involved triangles, hence, the amplitude of the Abs cross-section efficiency of a prism is higher than the one of a pair of BT where 4 prisms are hosted. In **Figure 2.8**, the response of a BT with a gap of 100 nm is spectrally overlapping with the one of a single prism at the high-wavelengths side, though, an additional red-shift of M1 is noticed for a narrower gap (20 nm). As previously stated, an individual BT with a gap of 100 nm acts indeed as a single prism, so the tip-to-tip coupling is largely weak to be spectrally marked. However, on the low-wavelengths side, a slight blue-shift is observed for M2 while reducing the gap. On this side, the quadrupole mode is arising and it is flowing towards higher energy as soon as the coupling is intensified.¹⁰⁹

As previously mentioned, under a co-pol, M1 is red-shifted for a smaller gap in comparison to a larger gap that is conjoining the single prism energy. Plus, an additional red-shift of M1 is marked for a pair of BT with $g = 20$ nm. Furthermore, at higher energy, a clear blue-shift of M2 is simultaneously observed for this pair of BT. Even though the E-field localization and enhancement at the tip-to-tip gap seems to be very sharp under a co-pol by looking from the top side (xy -plane), it is crucial to look closely throughout the respective yz - and xz - cross-sectional planes. As expected along the cross-sectional yz -plane, a dipole mode is triggered at a lower energy ($\lambda = 1.243 \mu\text{m}$) as the corresponding H-field represents 1 lobe; and 3 lobes appear at higher energy ($\lambda = 0.472 \mu\text{m}$) stressing on the activation of a higher-order mode (quadrupole). However, along the cross-sectional xz -plane, two accompanying modes are trapped at the bases of the BT giving the privilege for an unexpected coupling to occur at the unintentionally triggered corner-to-corner gap. Hence, under a co-pol, both gaps sustain a tangible effect on the coupling as

illustrated in the near-field mappings in **Figure 2.8**. In consequence, this extra coupling in the pair of BT cases is revealed through an extra red-shift of M1 and blue-shift of M2.

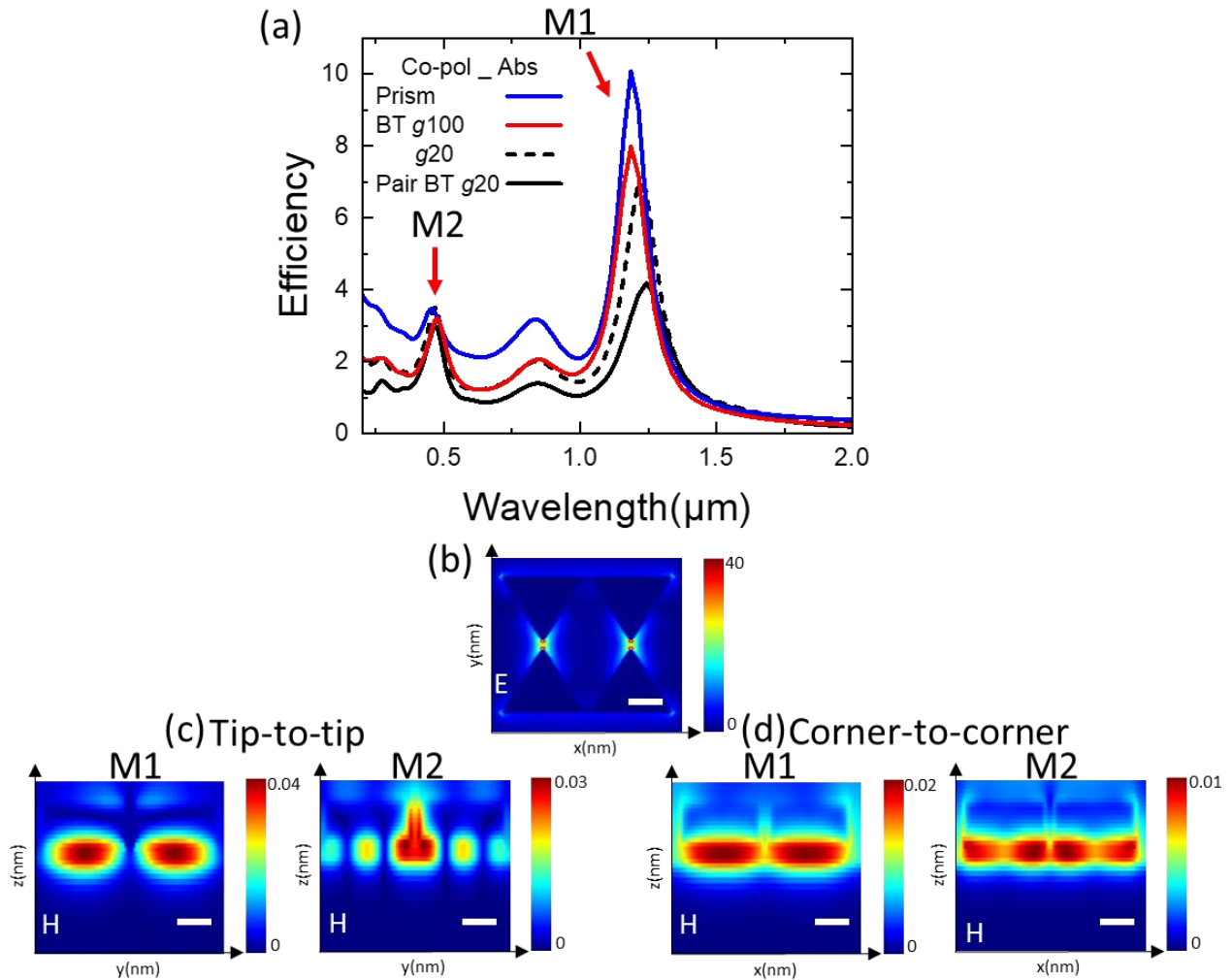


Figure 2.8. Far-field comparison between a prism, a single BT, and a pair of BT under a co-polarized light source (triggering the tip-to-tip gap). (a) The absorption cross-section efficiencies are plotted. Having a large gap, the BT mimics a single prism. For a single BT, the gap value is reduced to 20nm and compared to the response of a pair of BT with $g = 20 \text{ nm}$. On the low-energy side, M1 is red-shifted while decreasing the gap and is more pronounced for a pair of BT. A slight blue-shift of M2 is simultaneously observed on the high-energy side. In the near-field, the gap influence is studied under a co-polarization for a pair of BT having a gap of 20nm. (b) E-field magnitude is presented in the xy -plane at $\lambda = 1.243 \mu\text{m}$. H-field magnitudes are illustrated in the yz -plane for the tip-to-tip area (c) and xz -plane for the corner-to-corner area (d), respectively at $\lambda = 1.243$ and $0.472 \mu\text{m}$ (red arrows). All scale bars are 100 nm long.

To understand the polarization, **Figure 2.9** illustrates the far-field and near-field comparison between the results of a single and a pair of BT, having a gap of 20 nm, and illuminated under both polarized lights. M1 of a pair of BT is red-shifted in respect to the one of a single BT, stating an extra coupling between both BTs.

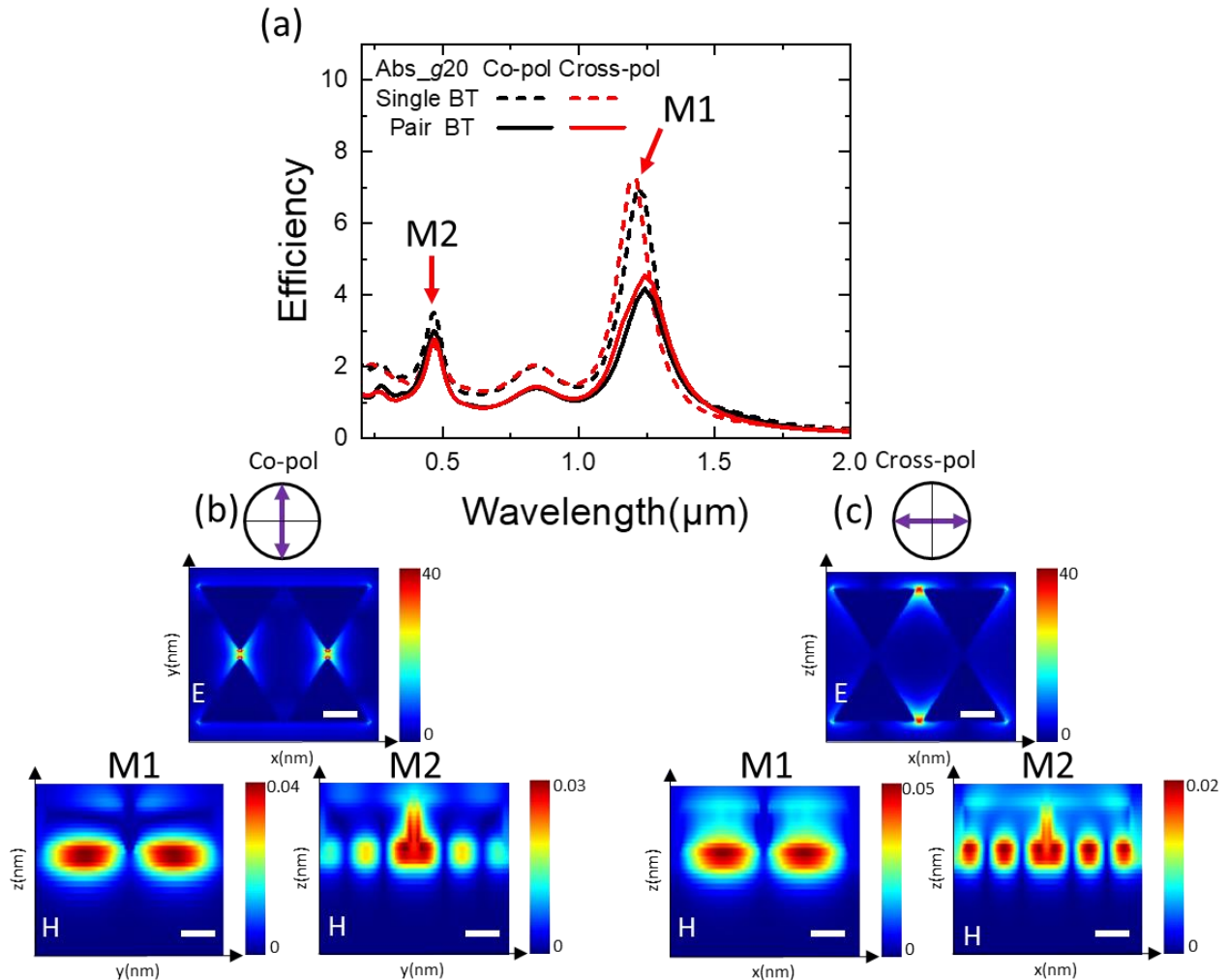


Figure 2.9. Far-field and near-field comparison between a single and a pair of BT, having a gap of 20nm, under both polarized light (a) Absorption cross-section efficiencies are plotted. On the low-energy side, an additional red-shift of M1 is remarked for the pair of BT regardless of the polarization and the responses appear at the same energetic position even for the mode on the high-energy side. In the near-field, the (b) co- and (c) cross-polarization influence on manipulating the E-field distribution is studied. A similar E-field magnitude is presented in the xy -plane at $\lambda = 1.243 \mu\text{m}$ regardless of the polarization direction (b, c). H-field magnitudes within the spacer are illustrated in the cross-sectional yz -plane for the tip-to-tip area (b) and cross-sectional xz -plane for the corner-to-corner area (c), respectively at $\lambda = 1.243$ and $0.472 \mu\text{m}$ (red arrows) showing the presence of 2 different modes (lobes formation). All scale bars are 100 nm long.

Surprisingly, the features of the pair of BT appear to be insensitive to light polarization thanks to the extra-symmetrization of the pair of BT compared to the single BT. At these energies, the correlated modes were retrieved in cross-sectional yz - (under co-pol) and then xz - (under cross-pol) planes. As predicted, the E-field magnitude mapping in the xy -plane shows a strict localization and enhancement at the tip-to-tip or the corner-to-corner sites, respectively for a co- or a cross-pol. Nevertheless, M1 and M2 are respectively related to a dipole and a quadrupole mode, based on the H-field lobe-styles.

In conclusion, under both polarized lights, the MIM configuration and the 3D-sharped prism guarantee a massive influence on the far- and near-field features of a BT, being either isolated or coupled to its neighboring counterpart. Furthermore, a gap-plasmon effect is always present to allowing the E-field trapping at the tips and inside the thin spacer of the MIM structure.

2.2. Plane-wave source

2.2.1. Coupling effects under light polarization for BT within a MIM in a 1D array

In the previous section, the origin of the plasmonic modes was interpreted through TFSF simulations. Dipole and quadrupole modes were manifested at different energy levels in the cases of a free-standing prism up to a pair of BT within a MIM structure. Their far-field a near-field features show a dependency on the polarization as well as on the gap values (where the coupling occurs).

In this section, 1D periodic BT integrated within a MIM are similarly studied under both polarized light sources but using a plane-wave source and collecting the reflectance spectra. The incident beam is navigating through a semi-infinite water medium ($n_{water}= 1.33$ instead of $n_{air}= 1$), the modes are well defined as a better plasmonic impedance (structure-to-environment) is achieved. Note, the LSPR behavior is tested in water in view of a future functionalization. The same LSPR behavior is detected in the air. The tip-to-tip (along y -axis) and the corner-to-corner (along x -axis) distances, *i.e.* g_y and g_x are separately swept to report the corresponding coupling strengths on both modes acquired in reflectance (**Figure 2.10**).

In **Figure 2.10a**, the tip-to-tip coupling is addressed under a co-pol with g_y set at 200 nm, to limit the dipole coupling along the y -direction, and g_x is varied from 20 up to 250 nm. The reflectance spectra show 2 distinct absorption peaks fixed at the same energy despite the variation of g_x values, as the polarization is perpendicular to the coupling direction where the gap decreases. This result agrees with **Figure 2.7b** when the polarization is perpendicular to the gap variation for a pair of BTs.

In **Figure 2.10b**, the tip-to-tip coupling is still addressed under a co-pol with g_x set constant at 200 nm to limit the coupling along the x -axis, *i.e.* corners-to-corners, and the g_y is varied from 20 up to 250 nm. The reflectance spectra show 2 bands of modes, the ones at lower energy red-shift and at higher energy blue-shifts as the gap decreases. The strong coupling along the tips is effectively triggered with a polarization parallel to the coupling axis where the gap decreases. This result agrees with **Figure 2.7a** when the polarization is parallel to the gap variation for a pair of BTs.

In **Figure 2.10c**, under a cross-pol, both modes appear at the same energies despite the variation of g_y . Indeed, the BTs are uncoupled along the cross-pol (x -axis) direction where g_x is fixed at 200 nm. On the contrary, also under a cross-pol, **Figure 2.10d** shows that a strong coupling is provoked along the x -axis by decreasing the g_x from 250 to 20 nm.

In sum, to trigger the strong coupling, the light polarization should be aligned with the decreasing gap direction. This is evidenced by the red and blue shifts of the low and high energy absorption peaks, respectively, in **Figures 2.10b and 2.10d** compared to **Figures 2.10a and 2.10c**, where both modes have constant energy absorption peaks.

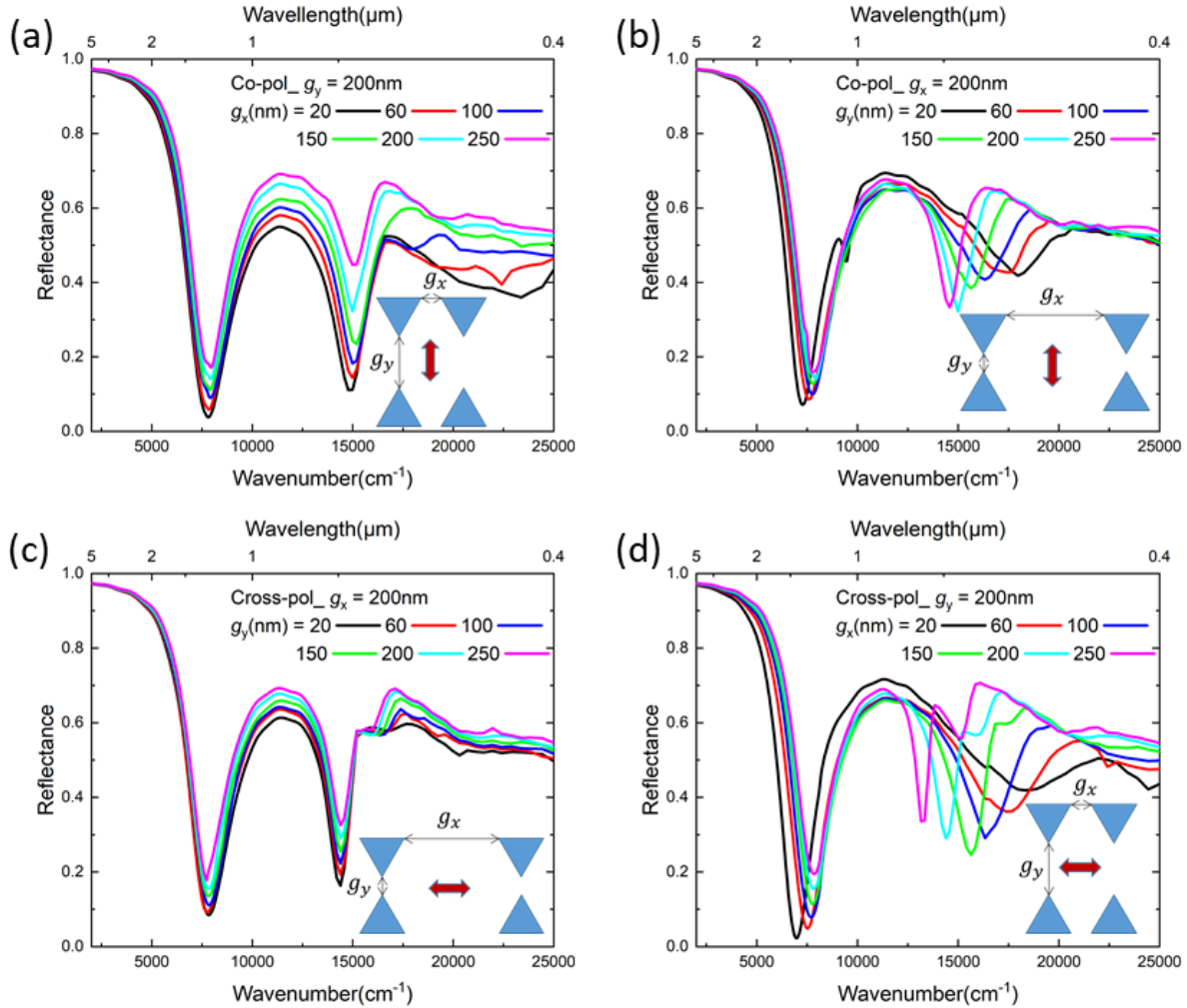


Figure 2. 10. Reflectance of BT within a MIM structure in a 1D-array. Under a co-pol, (a) the tip-to-tip gap (g_y) is fixed and the corner-to-corner (g_x) gap is varied; (b) g_x is fixed, and g_y is varied. Under a cross-pol, (c) g_x is fixed and the corner-to-corner g_y is varied; (d) g_y is fixed and g_x is varied. All gap's fixed value is 200nm and for the gap sweep 20, 60, 100, 150, 200, and 250 nm are selected. The polarization direction triggers the coupling and influences highly the position of both plasmonic modes. When the polarization direction is parallel to the coupling axis, where the BT gap is decreased, the lower energy mode is red-shifting and at higher energy is blue-shifting. In contrast, no special shift is remarked when the polarization is perpendicular to the coupling axis.

2.2.2. Periodic BT arrays with different geometric parameters

Once the identification of the different plasmonic modes is done, we can perform the parametric study of the BT geometry in 2D-arrays to optimize the sensing regions in the EM spectrum. In this part, L and g impacts on the LSPR of the BT will be extensively addressed from the visible (Vis) to

the mid-infrared (MIR). Plane-wave source is herein selected as suitable for the BT 2D-periodic arrays within the MIM structure. However, regarding the long simulation time, it is necessary to improve some simulation conditions, *e.g.* the boundary conditions.

The EM fields through the periodic unit cell of the BT have a plane of symmetry / anti-symmetry in the centre of the structure, as shown in **Figure 2.11**. The boundary conditions will be set as follows to optimize the simulations time. Under co-pol, the E-field is parallel to the y -axis, parallel to the BT main axis, the H-field is along the x -axis. Therefore, the minimum and maximum boundary conditions are set as symmetric along the x -axis, parallel to the E-component, and anti-symmetric along y -axis, parallel to the H-component. This follows the symmetry rules of the EM field where the E-field is considered a vector and H-field a pseudo-vector which is the consequence of the cross-product. Consequently, in the unit cell region, half of the simulation will be automatically shaded in blue (for symmetric) or green (for anti-symmetric), indicating the portion of the simulation regions not to be directly simulated. Selecting these adequate symmetric boundary conditions will preserve periodicity while reducing the computation time needed by about 4 times, as only the uncolored zone will be computed, as shown in **Figure 2.11**.

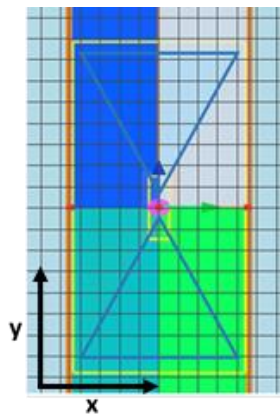


Figure 2. 11. Scheme of the symmetric and anti-symmetric boundary conditions features applied for periodic BT illuminated by a plane wave incident light source. $L = 0.8 \mu\text{m}$ and $g = 100 \text{ nm}$. E-field is parallel to the BT main axis (co-polarized light represented by a blue arrow), so, the lower and upper limits of the x -axis are set as symmetric and those of the y -axis are set as anti-symmetric. Consequently, half of the simulation region will automatically be shaded in blue (for symmetric conditions) or green (for anti-symmetric conditions), keeping on the portion of the simulation region that will be directly simulated (unshaded zone), and preserving the desired periodicity.

2.2.2.1. Side length (L) influence in the LSPR peaks

The triangle side-length (L) is the simplest degree of freedom to span a very wide spectral range from the ultraviolet (UV) to the MIR using the Al-BT as a single building block. Firstly, to address the visible range and the low near-infrared (NIR), Al BTs are simulated under a co- and a cross-polarized light with L equals 0.1, 0.15, 0.2, and 0.3 μm . **Figure 2.12** shows the dipole LSPR maximum absorption with the impact of the gap (g) variation from 20, 60 to 100 nm. Under both polarizations, the LSPR energy position of all Al-BT red-shifts while increasing L and/or decreasing the g value.

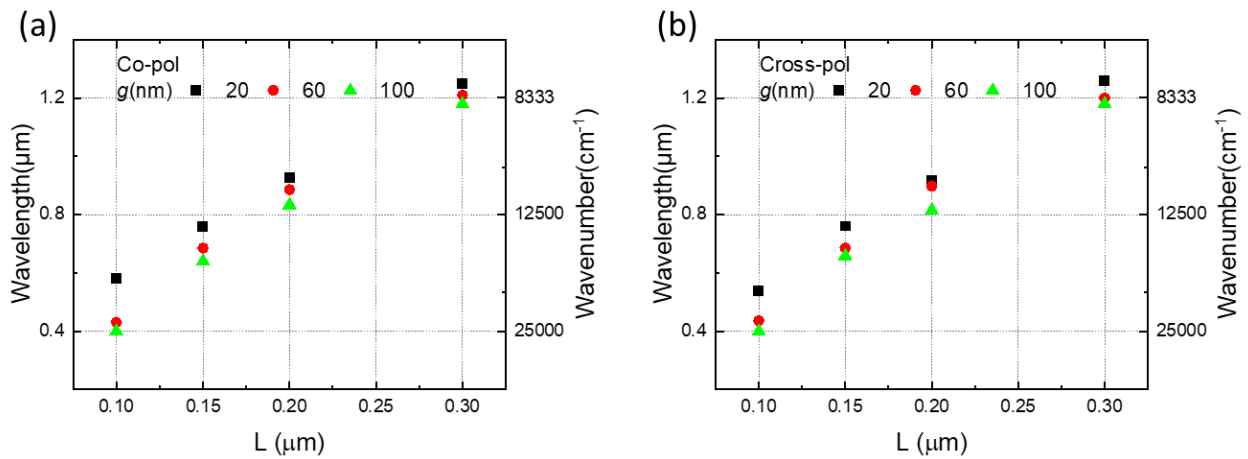


Figure 2. 12. Addressing the visible and the low near-infrared ranges with Al BT. The side length (L) is equal to 0.1, 0.15, 0.2 and 0.3 μm with a separating gap g equals 20, 60, and 100 nm. The BT were simultaneously illuminated under (a) a co- and then (b) a cross-polarized plane-wave light source. Under both polarizations, the LSPR energy red-shifts while increasing L and decreasing the g value.

To drive deeper into the IR range, a broadband plane wave source is selected to analyze and compare the plasmonic features of several nanostructures with variable geometric parameters ($L \geq 0.3 \mu\text{m}$) between $\lambda = 1$ and $10 \mu\text{m}$ ($10\,000$ to $1\,000 \text{ cm}^{-1}$). The complexity of the multi-resonant model influences the energy stability inside the FDTD simulation zone. A huge part of the energy bounces between the triangles and within the MIM. To overcome the simulation instabilities and divergences, appearing as unwanted spectral oscillations, the source limits were slightly expanded from the ones used in the previous simulations to a larger interval ($\lambda = 0.4$ to $1.1 \mu\text{m}$). Yet, the reflectance and the near-field monitors are collecting data in the range of interest ($\lambda = 1$ to $10 \mu\text{m}$). In addition, the incident light is defined as a pulse. So, to avoid zone

edge artifacts the spectral range of the source range is slightly widened compared to the monitors spectral range. Indeed, a lot of oscillations are present at the edge of the Fourier transformation zone, so it is helpful to reduce the working area compared to the total spectral area, to encompass a rather "stable" spectral area.

Figure 2.13 shows numerical results calculated using FDTD simulations in a wide spectral range from the NIR to the MIR using Al-BT 2D arrays. The LSPR wavenumbers are tuned over a wide IR spectral region, thanks to the variation of the Al-BT side length (L) in each zone of arrays within the MIM structure. The BT geometry affects the plasmonic behavior systematically. Fundamentally, for each couple of length and gap for the BT, (L and g), a unique LSPR peak is assigned. For this wide coverage in the IR, L is varied from 0.3 to 2.0 μm with a step of 0.1 μm , and the g value is fixed at 100 nm in **Figure 2.13**. The distance between the antenna rows, Y , is maintained constant at 2 μm . The BTs are illuminated under co-polarized light (E-field parallel to the BT main axis), which provides an effective facing tip-to-tip coupling and supports high field enhancement into that gap. For all BT regions, the first-order plasmonic resonance is always situated at the lowest wavenumber (*i.e.* lowest energy), and then higher orders of the resonance appear at higher wavenumbers (**Figure 2.13a**). In particular, the BTs cover the range from 8 300 to 1 500 cm^{-1} (red-shifting from $\lambda = 1.2$ to 6.5 μm) with a step of $\sim 86 \pm 30 \text{ cm}^{-1}$, by varying L from 0.3 to 2.0 μm with a step of 0.1 μm . This behavior corresponds to the dipolar mode which demonstrates a wavelength red-shift as L increases. This well-known tendency for metallic objects is largely described in the literature.^{73,78,110} Some higher-order radiative (bright) modes are visible only for $L > 0.9 \mu\text{m}$ with a similar tendency.

In analogy to the behavior of a vibrating string, λ is proportional to L (length of the string). λ is inversely proportional to the energy (wavenumbers). As the wavenumbers are proportional to $1/\lambda$, *i.e.* to $1/L$, plotting the wavenumbers in function of $1/L$ shows a linear dependency, likewise when plotting λ in function of L . This behavior is displayed in **Figure 2.13b**. The anticipated linear dependency is confirmed by the automatic linear fit with $R^2 = 0.99$ and a slope coefficient of 0.2523. This slope coefficient is inversely proportional to the effective index of the system.¹¹¹

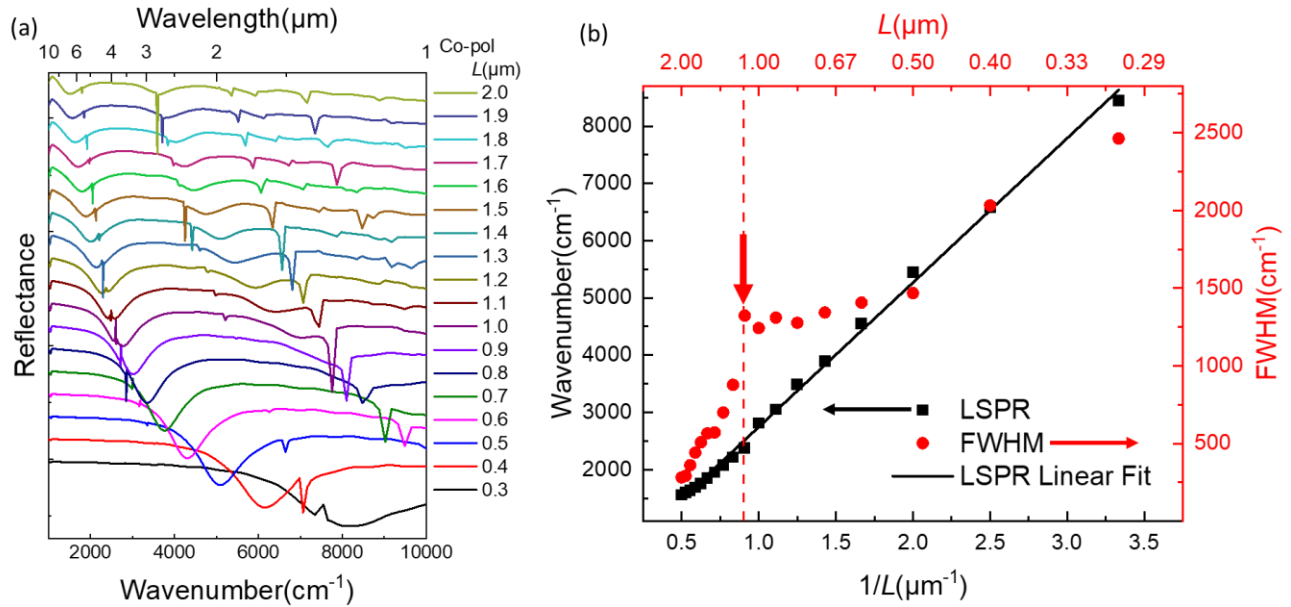


Figure 2.13. Influence of the side length value on the LSPR spectral position. (a) Numerical (FDTD) reflectance results for BT illuminated under co-polarized light, where g is kept constant at 100nm and L is varying from 0.3 to 2 μm with a step of 0.1 μm . Note the spectra are stacked along the reflectance axis for ease of viewing. (b) LSPR wavenumber values are plotted in function of $1/L$ and fitted by a linear fit (black line), and their corresponding width (FWHM) is showing smaller values as the L increases. The black arrow refers to the LSPR wavenumbers scale (to the left). The red arrow refers to the FWHM values scale (to the right).

In **Figure 2.13b**, the full widths at half maximums (FWHM) of the simulated peaks decrease continuously when going deeper in the IR, *i.e.* for bigger BTs (larger L), agreeing with the state-of-art.¹¹² For large BT, $1.4 \mu\text{m} < L < 2.0 \mu\text{m}$, the quality factor (Q-factor) mean value is 4.2 ± 0.9 . It is slightly higher than the one for NAs with $0.3 \mu\text{m} < L < 1.0 \mu\text{m}$, where the Q-factor mean value is reduced to 2.9 ± 0.5 . This reduction of the Q-factor is most likely affected by the Al internal losses (interband transition mode) situated between $\lambda = 0.8$ and $0.9 \mu\text{m}$ (fairly close to $10\,000 \text{ cm}^{-1}$). Al losses are due not only to interband transitions but also to Drude scattering. In both cases, the corresponding Q-factor is considered almost of the same order of magnitude.

However, the obvious increment in the FWHM around $L = 1.1 \mu\text{m}$ (red vertical arrow) is due to a perfect overlap of the LSPR and the array's diffraction peaks. These diffractions result from the periodicity along the y -axis array and correspond to the discrete spikes in the spectra of **Figure 2.13a**. Sometimes, they are referred to as surface lattice resonances (SLR), that arise from the coupling of LSPR and the Rayleigh anomaly. Their spectral position, Λ_y , has been analytically deduced for equilateral triangles in **Equation 2.1** as follows:

$$\Lambda_y = 2 \times L \times \sin 60^\circ + g + Y, Y = 2 \mu\text{m} \quad (2.1)$$

In contrast to LSPR, SLR is associated with a delocalized EM field and its excitation is revealed by considerably narrower spectral features.¹¹³ The wavelength at which SLRs are excited can be tuned by varying the arrangement period, angle of incidence, and geometric parameters of the NAs.¹¹⁴ Indeed, these spikes are affecting also the peak widths of $L = 0.9, 1.0, \text{ and } 1.1 \mu\text{m}$, as the black dot scatters are not following smoothly the global trend. Such a perfect overlapping could be useful for sensing applications.¹¹³

2.2.2.2. Gap (g) influence in the electrical field enhancement

In addition to their behavior in the far-field, BT array resonances are accompanied by outstanding near-field features. Mainly, the sharp edges between each prism of the BT array localize and enhance the E-field at the nanoscale.⁶ In fact, the interaction between the oscillating charges on two sharp-and-aligned structures becomes more significant as soon as they come closer to each other, thus creating a hotspot. Accordingly, under a co-polarized light, the near E-field enhancement and intensity are boosted inside the gap which is formed between the sharp-ends of both coupled triangles facing each other. Here, for a finer simulation resolution, the mesh override pitch is reduced to 2 nm to illustrate the E-field dependency on the gap value. In the far-field, the LSPR is red-shifted by $\sim 13 \pm 8 \text{ cm}^{-1}$ while g is decreased from 100 to 20 nm with a step of 20 nm.

Figure 2.14a shows the simulated local E-field concentrated at the tips when gradually decreasing the tip-to-tip gap value from 100 nm to 20 nm. The E-field enhancement, $|\mathbf{E}|/|\mathbf{E}_0|$, is increasing exponentially (red curve). Consequently, the coupling between the two sharp extremities over a narrow gap creates highly-localized and strongly-enhanced near E-field. **Figure 2.14(b-f)** show the E-field distribution in the xy -plane into the tip-to-tip gap region. Note, the E-field intensity, $|\mathbf{E}|^2/|\mathbf{E}_0|^2$, increases respectively when decreasing the gap based on the accompanying color scale maximum value in the caption. Even though decreasing the gap value will engender a slight red-shift macroscopically according to the inter-prism coupling principle, the LSPR peak position

is nearly situated around $2.96 \mu\text{m}$. At such a wavelength, $|E|^2/|E_0|^2$ rises from 300 to around 1 250 as the gap value decreases from 100 to 20 nm.

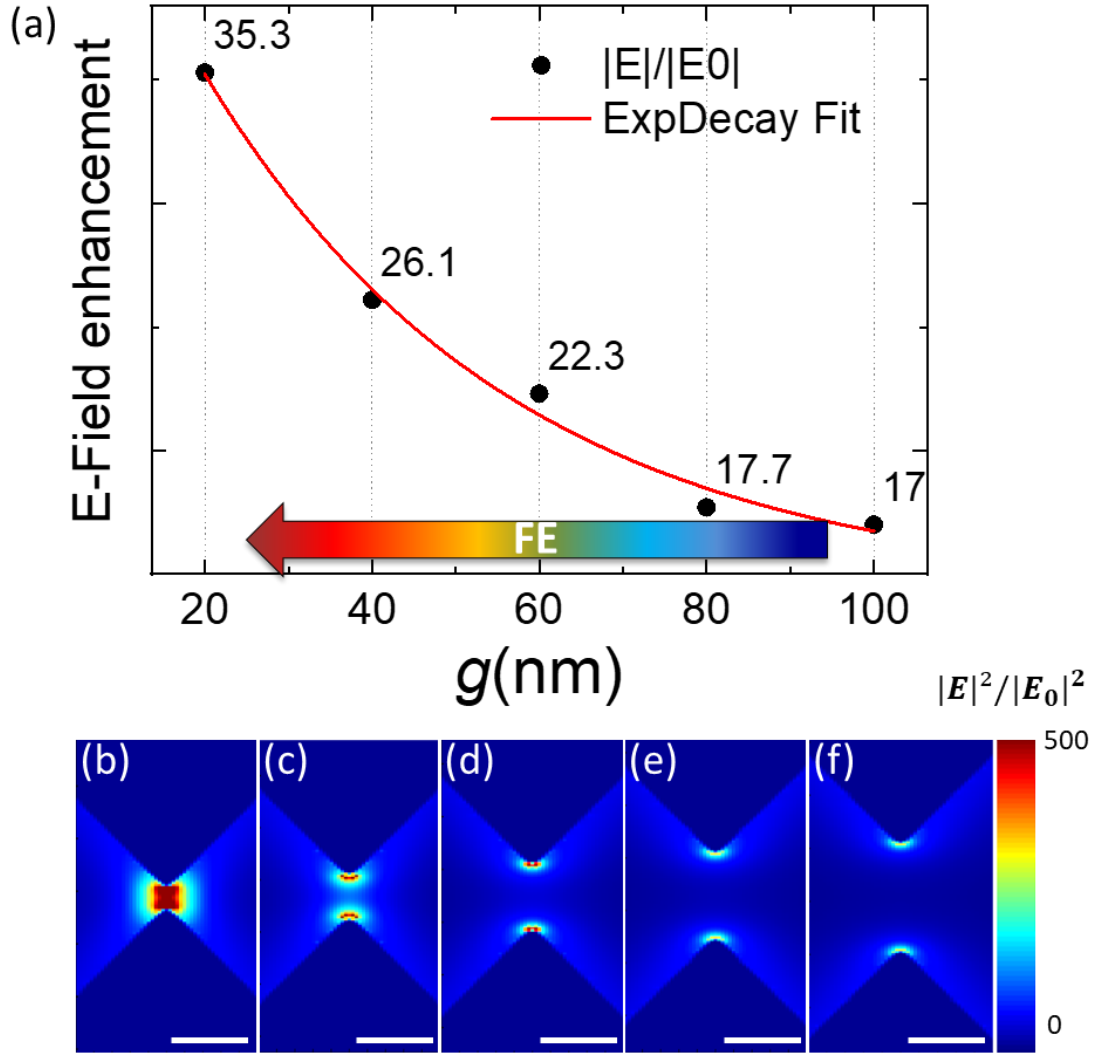


Figure 2. 14. Gap value influence on the local field enhancement and intensity for $L = 0.8 \mu\text{m}$ with g ranging from 100 to 20 nm with a step of 20 nm. (a) E-field enhancement $|E|/|E_0|$ in function of the g exponentially decaying as g increases (red curve), along with the associated enhanced electric field mapping (b-f) calculated at $2.96 \mu\text{m}$ and acquired under co-polarization. The color scale ranging from blue to red indicates the minimum to maximum field intensity $|E|^2/|E_0|^2$, $\max(|E|^2/|E_0|^2)$ equals 1 250, 700, 500, 315, 300 for mapping from **Figure 5b to 5f**. For better contrast, the maximum of the color scale is fixed at 500. All scale bars are 100 nm long.

2.2.3. Compact configuration of Al triangles: Honeycomb-like resonators

In the book Solid State Physics by Charles Kittel, crystallography is introduced as the science of atoms packing in solids. Spheres of equal size can be assembled in a hexagonal close pack (hcp) crystal structure as shown in **Figure 2.15a**. The atoms are stacked in an ABABAB packing sequence which gives rise to the most efficient manner of filling space and the highest packing efficiency.¹¹⁵ In this section, the HC-like resonators will be inspired by the A-layer arrangement (direct lattice), presented in **Figure 2.15b**. Please note that the magnitude of the lattice constants $a_1 = a_2 = a \neq a_3$ and an ideal induced angle γ of 120° is defined between the lattice axis \mathbf{a}_1 and \mathbf{a}_2 , where \mathbf{a}_1 , \mathbf{a}_2 and \mathbf{a}_3 are primitive vectors of the crystal lattice.

In **Figure 2.15c**, the FDTD unit cell of the HC will mimic the Brillouin zone that is defined as the Wigner-Seitz primitive cell in the reciprocal lattice, so-called "*the smallest volume entirely enclosed by planes that are perpendicular bisectors of the reciprocal lattice vectors drawn from the origin.*" Noteworthy for the upcoming polarization effect study in HC arrays, the direct lattice is its own reciprocal but with a rotation of the axis. Hence, the translation and symmetry invariance of this hexagonal building block will help conceive the far- and near-field plasmonic behaviors of our highly-compact triangular patterns.

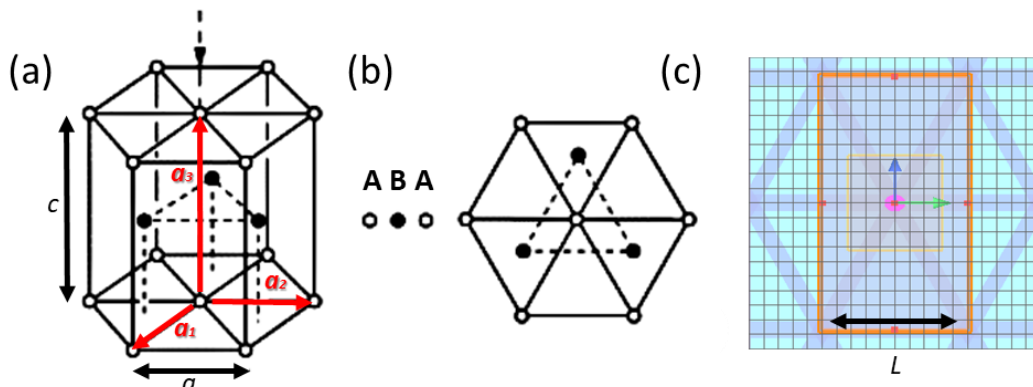


Figure 2.15. The hexagonal close-packed (hcp) structure with an ABA stacking is seen from (a) a side view showing the lattice parameters and the atom's 3D-arrangement and (b) a top view showing both layer configurations. P.S. a is the magnitude of \mathbf{a}_1 and \mathbf{a}_2 and c is the one of \mathbf{a}_3 . The A-layer is our building block to numerically conceive the periodic sequence of honeycomb-like Al NA, its unit-cell is delimited by the orange rectangular box in (c). The value of the hcp lattice constant a is now representing the side length L of each triangle. The Al-BT are illuminated under a co-polarized light (blue arrow) and a finer mesh of 5 nm is introduced at the center of the gathering area of the sharp apexes of 6 triangles.

2.2.3.1. Side length (L) influence in the LSPR peaks

In analogy to the A-layer atoms arrangement of the hcp structure, a HC-like unit-cell is designed in the Lumerical FDTD solver as the first Brillouin zone of a hexagonal lattice structure. Consequently, each predefined atom of the A-layer will represent a potential EM-hotspot. In principle, the center of the unit cell will be reinforced by 6-sharp apexes where the EM-field is strongly localized and enhanced. Note in the FDTD solver, the HC-like pattern is created by generating three groups of periodic lines rotated with a 0° , 60° , and 120° degrees within the 50 nm thick Al layer. These lines are defined as etched material, thus their width w and periodicity p are affecting the sculpted Al prism sizes. The prism's height equals to $L \times \sin 60^\circ$, where L is the side length, and their spacing distance is half of the eventual tip-to-tip gap, g . Hence, the tip-to-tip gap is 2 times bigger than the corner-to-corner gap, defined by single line width. Note this configuration is defined to match the fabrication outcomes that will be further discussed in **Chapter 3**.

Similarly, to the formerly studied Al-BT, the Al-HC are illuminated under a co-polarized plane-wave light source, and the E-field is parallel to the vertical axis of the tip-to-tip facing triangles (blue arrow in **Figure 2.15c**). For more accuracy, a 3D finer mesh of 5 nm is introduced at the center of the assembly region of the sharp apexes of 6 triangles. In the same way, the side length (L) of each triangle is swept from 0.3 to 2.0 μm with a step of 0.1 μm , herein, g is also fixed at 100 nm. The reflectance spectra of various Al-HC are simultaneously collected through an xy-plane-monitor placed above the incident source level. Hence, a wide spectral coverage from NIR to MIR is insured using Al HC from 1 000 to 10 000 cm^{-1} as plotted in **Figure 2.16a**.

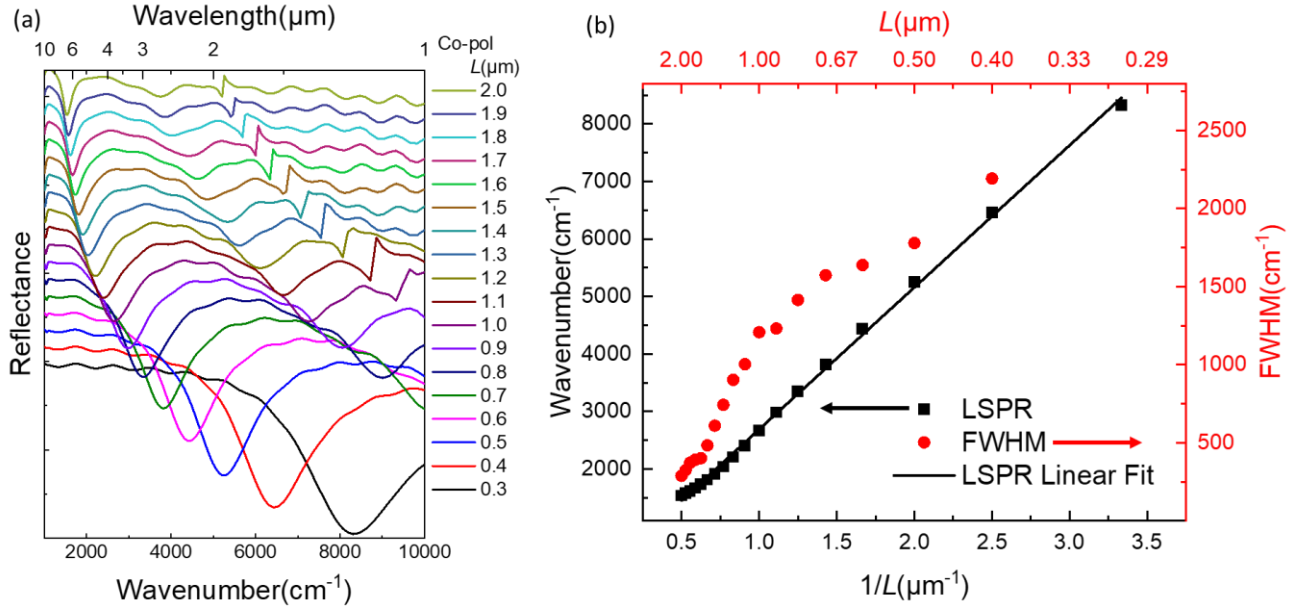


Figure 2. 16. Influence of the side length value on the LSPR spectral position. (a) Numerical (FDTD) reflectance results for HC illuminated under co-polarized light, where g is kept constant at 100 nm and L is varying from 0.3 to 2 μm with a step of 0.1 μm . Note the spectra are stacked along the reflectance axis for ease of viewing. (b) LSPR wavenumber values are plotted in function of $1/L$ and fitted by a linear fit (black line), and their corresponding width (FWHM) is showing smaller values as the L increases. The black arrow refers to the LSPR wavenumbers scale (to the left). The red arrow refers to the FWHM values scale (to the right).

For all HC, the first-order plasmonic resonance is always situated at the lowest wavenumber (*i.e.* lowest energy), and then higher orders of the resonance appear at higher wavenumbers (**Figure 2.16a**). In particular, the HC cover the range between 1.0 to 6.6 μm (*i.e.* 10 000 to 1 540 cm^{-1} with a step of $\sim 70 \pm 30 \text{ cm}^{-1}$), by varying L from 0.3 to 2.0 μm with a step of 0.1 μm . Similar to the results illustrated for BT structures (**Figure 2.13**), as L increases, the main LSPR peaks are losing energy from 8 300 to 1 500 cm^{-1} (red-shifting from $\lambda = 1.2$ to 6.5 μm). This behavior corresponds to the dipolar mode which demonstrates a wavelength shift as L varies. This well-known tendency for metallic objects is largely described in the literature.^{73,78,110} Some higher-order radiative modes are visible only for $L \geq 0.7 \mu\text{m}$ with a similar tendency. The spectral position of the diffraction peaks Λ_y has been analytically deduced for periodic equilateral triangles in **Equation 2.2** as it follows:

$$\Lambda_y = L \times \sin 60^\circ + \sqrt{3} \cdot g. \quad (2.2)$$

The diffraction peaks also exist but are far enough from the dipole LSPR.

In **Figure 2.16b**, the LSPR wavenumbers are represented in function of $1/L$. In analogy to the behavior of a vibrating string, the anticipated linear dependency is confirmed by the automatic linear fit with $R^2 = 0.99$ and a slope of 0.2470. This slope coefficient is inversely proportional to the effective index of the system.¹¹¹ Furthermore, the simulated FWHM are always revealing a decrease while going deeper in the IR, *i.e.* for bigger HC-antennas (with larger L). For large HC, $1.4 \mu\text{m} < L < 2.0 \mu\text{m}$, the Q-factor mean value is 4.2 ± 0.7 . It is higher than the one for smaller NA where $0.3 \mu\text{m} < L < 1.0 \mu\text{m}$ (FWHM mean value is 2.5 ± 0.2). This reduction of the Q-factor is most likely affected by the AI internal losses (interband transition mode) situated between $\lambda = 0.8$ and $0.9 \mu\text{m}$ (fairly close to $10\,000 \text{ cm}^{-1}$). AI losses are due not only to interband transitions but also to Drude scattering. In both cases, the corresponding Q-factors are considered in the same order of magnitude.

Here, a comparison between both NA results is worth mentioning. It is important to note that, for the same L range, the calculated Q-factors are interestingly found constant while using BT or HC. Nevertheless, for a deep comparison, Q-factors for some L values of interest (regarding **Chapter 5**) are investigated. In the BT case, for $L = 2.0 \mu\text{m}$ and $1.4 \mu\text{m}$, the Q-factors are slightly higher (5.5 and 3.4 respectively) than the ones for the HC case (5.3 and 3.1 respectively). Higher quality factors signify narrow resonances due to low losses in the material. Moreover, for the same L value, there's an augmentation of at least 10% of the resonance peak's amplitude when using a HC structure, and this is owing to its compact arrangement compared to the BT arrays. For the same L values, the LSPR of the HC have shown a slight red-shift ($\sim 40 \pm 15 \text{ cm}^{-1}$) compared to those of BT as the interaction between the adjacent triangles is becoming more effective, and thus, arising at lower energy.

Furthermore, inspired by the rotation invariance occurring between the direct and reciprocal hcp lattices, the HC configuration allows obvious 360° -symmetry conservation so that the incident light polarization will affect neither the far- nor the near-field features of the simulated unit-cell. In the far-field, as illustrated in **Figure 2.17** the same HC structures ($L = 2.0 \mu\text{m}$) are illuminated

under a co- and a cross-polarized plane-wave light source and the corresponding reflectance spectra show a perfect overlap under both polarizations for $g = 250$ nm. This underlines the invariance of the physical property of the hexagonal lattice under any E-field polarization direction. Thanks to the symmetry conservation within the unit-cell of the HC, the periodicity impact illustrated by the diffraction peak should be independent of the polarization direction. Indeed, based on **Equation 2.2**, for $L = 2.0$ μm , $\Lambda_x = \Lambda_y = 2.16$ μm . Yet, for $L = 1.0$ μm , the diffraction peak analytically found at $\Lambda_x = \Lambda_y = 1.29$ μm is barely triggered.

The invariance of the HC resonance regardless of the light polarization will be peculiarly useful to improve the signal-to-noise ratio when sensing experiments will be performed.

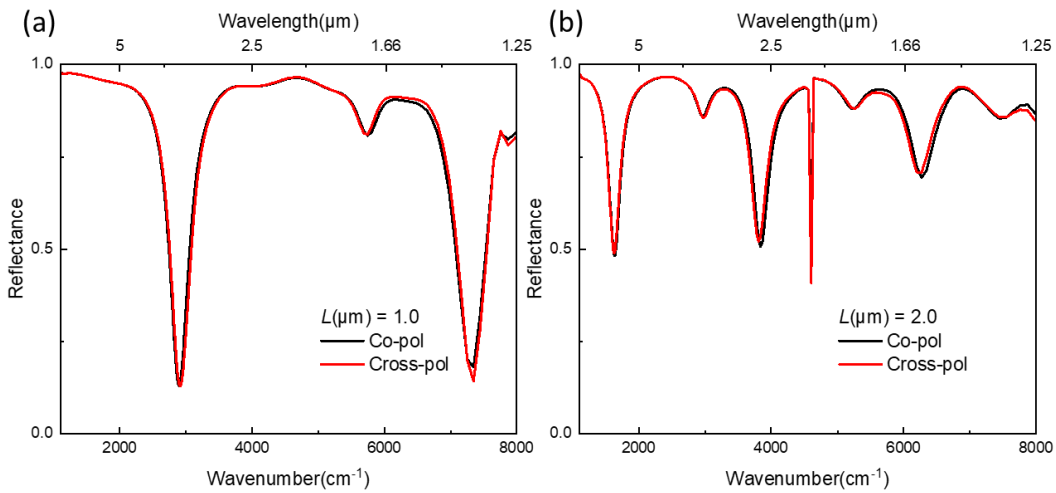


Figure 2. 17. Reflectance of the compact-HC-like unit-cell, g is 250 nm and $L = 1.0$ (a) and 2.0 μm (b), illuminated under both polarized light: co-pol when E-field parallel to the vertical axis of the tip-to-tip facing triangles and cross-pol when it is orthogonal to the former case. In both cases, 2 main separated modes of identical amplitude appear at the same energy to highlight the symmetry conservation in the far-field. Diffraction peak appears clearly for $L = 2.0$ μm , $\Lambda_x = \Lambda_y = 2.16$ μm , seen as a sharp peak.

2.2.3.2. Gap (g) influence in the electrical field enhancement

In the near-field, the gap effect on the field enhancement and distribution is addressed. Once again, it is fundamental to capitalize on the structure and E-field symmetry to optimize the simulation time and memory requirements. Thus, symmetric and anti-symmetric boundary

conditions are respectively selected at the x - and y -limits of the simulation zone of the HC, as represented in **Figure 2.18**.

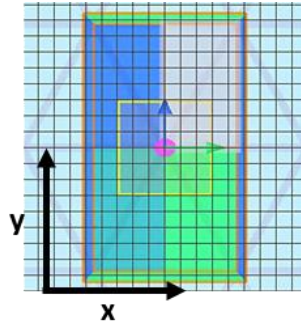


Figure 2. 18. Scheme of the symmetric and anti-symmetric boundary conditions features applied for the unit-cell of the HC, illuminated by a plane wave incident light source. $L = 0.8 \mu\text{m}$ and $g = 100 \text{ nm}$. The E-field is parallel to the tip-to-tip facing triangles of the HC (co-polarized light represented by a blue arrow), so, the lower and upper limits of the x -axis are set as symmetric and those of the y -axis are set as anti-symmetric. Consequently, half of the simulation region will automatically be shaded in blue (symmetric) or green (anti-symmetric), keeping on the portion of the simulation region that will be directly simulated (unshaded zone), and preserving the desired periodicity.

In the following, the gap influence on the Al-HC plasmonic response is investigated under a co-polarized light. The structure's side length is $L = 0.8 \mu\text{m}$ and the gap g are selected to be equal to 100, 60, and 20 nm. In the far-field, the LSPR is red-shifted by $\sim 50 \pm 4 \text{ cm}^{-1}$ while g is decreased from 100 to 20 nm with a step of 20 nm.

To evoke the E-field dependency on the gap value as previously found for a BT, a finer mesh override of 2 nm is adapted instead of 5 nm, especially for better E-field mapping. Likewise, the E-field intensity is collected in the xy -plane and represented in **Figure 2.19**. By promoting the strong interaction between the oscillating charges on closely-placed sharp apexes, the near E-field enhancement and intensity are accordingly improved inside the gap which is formed between the sharp-ends of the coupled triangles (facing each other). Such a coupling is forced to occur along the polarization direction as clearly illustrated in **Figure 2.19a and 2.19b**.

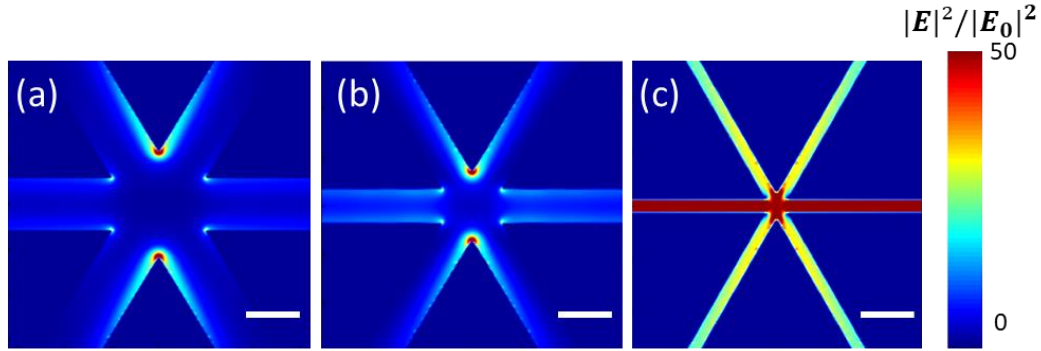


Figure 2.19. Gap value influence on the local field enhancement and intensity for $L = 0.8 \mu\text{m}$ with g equal to 100, 60, and 20 nm. Under a co-polarized light, the enhanced electric field mapping is collected in the xy -plane (a) for $g = 100$ nm calculated at $\lambda = 3.3 \mu\text{m}$, (b) for $g = 60$ nm calculated at $\lambda = 3.37 \mu\text{m}$, (c) for $g = 20$ nm calculated at $\lambda = 3.5 \mu\text{m}$. The color scale ranging from blue to red indicates the minimum to maximum field intensity $|\mathbf{E}|^2/|\mathbf{E}_0|^2$, $\max(|\mathbf{E}|^2/|\mathbf{E}_0|^2)$ equals 250, 233, 216 while decreasing the g value. For better contrast, the maximum color scale is fixed at 50. All scale bars are 100 nm long.

For $g = 100$ nm, $|\mathbf{E}|^2/|\mathbf{E}_0|^2$ equals 250 appears at $\lambda = 3.3 \mu\text{m}$ (red-shifted in respect to the far-field response, *i.e.* reflectance minimum found at $\lambda = 2.97 \mu\text{m}$). In principle, $|\mathbf{E}|^2/|\mathbf{E}_0|^2$ should increase as far as the tip-to-tip spacing decreases. Although, for a gap of 60 nm, LSPR energy appears at $\lambda = 3.05 \mu\text{m}$ and a $\max(|\mathbf{E}|^2/|\mathbf{E}_0|^2)$ equal to 233 is found at a higher wavelength at $\lambda = 3.37 \mu\text{m}$ and is slightly lower than the one found for $g=100$ nm. This result seems illogical until looking at the E-field mapping that shows a considerable redistribution along with the triangle's neighboring edges. This behavior is highlighted when having $g= 20$ nm (**Figure 2.19c**): $\max(|\mathbf{E}|^2/|\mathbf{E}_0|^2)$ of 216 is found at $\lambda = 3.5 \mu\text{m}$ (red-shifted compared to the far-field LSPR found at $\lambda = 3.44 \mu\text{m}$), lower than the one found for a larger gap. In fact, for such a small gap, the near E-field is not only enhanced at the facing tips but also at the edges of the triangles, which is lowering the possibility to be largely enhanced as when it is strictly pinched at the sharp apexes, and creates thus a kind of long-way cavity where the field could be probably delocalized. However, from a far- and near-field perspectives, decreasing the gap from 100 to 20 nm engendered a slight red-shift of both LSPR and the energy supporting the maximum field intensity, according to the inter-triangle coupling principle. In absolute values, the Al-BT structure, for $g = 20$ nm, $|\mathbf{E}|^2/|\mathbf{E}_0|^2$ of 216 is found instead of 1 250, so, in terms of effective E-field enhancement, the BT structure is superior to the HC structure.

However, for such a $g = 20$ nm, the volume where the E-field enhancement is achieved in HC is rather larger in comparison to the BT structure and could play an important role in comparing the detection of the same concentration of molecules in sensing applications, as it will be discussed in **Chapter 5**.

2.3. Conclusion

In this chapter, 3D FDTD numerical simulations were carried out to understand the influence of the shape, size, and distribution of the plasmonic Al metamaterial, starting from a single prism, to isolated, dimmer and periodic array BTs, and finally to a closely packed HC arrangement of equilateral prisms. The impacts of the incident light polarization on the far- and near-field responses of the structures were carefully addressed. To briefly recapitulate, we will state and express the following findings:

- An individual BT acts like a single prism when the tip-to-tip or/and corner-to-corner coupling are excluded.
- The MIM structure promotes an enhanced gap-plasmon mode where the near E-field is pinned at the NA/SiO₂ interface and trapped into the spacer.
- The origin of two resonance modes, namely M1 and M2, are evaluated. The H-field distribution inside the spacer indicates either one or three lobes, so two distinguished mode types, dipole, and quadrupole, are created.
- A strong coupling between BT pairs is triggered when the light polarization is parallel to the coupling axis. So, as the gap is reduced, M1 red-shifts and M2 blue-shifts.
- The dipole LSPR of both simulated NA within the MIM structure is easily tuned from the visible towards the mid-IR by increasing the side length (L).
- The FWHM of the LSPR peaks is always decreased while going deeper in the IR, *i.e.* for bigger antennas.
- HC structures present an outstanding advantage of translational and symmetry invariance. For fixed L and g values, the resonance frequencies under both polarized light cases were found at the same spectral positions.
- By varying L with a step of 0.1 μm , their corresponding LSPR red-shifts by $\sim 86 \pm 30 \text{ cm}^{-1}$ and $\sim 70 \pm 30 \text{ cm}^{-1}$ for BT and HC, respectively.
- Decreasing the gap is accompanied by a further near E-field enhancement as well as a LSPR red-shift. For example, under a co-pol, the LSPR is red-shifted by $\sim 13 \pm 8 \text{ cm}^{-1}$ and by $\sim 50 \pm 4 \text{ cm}^{-1}$ for BT and HC, respectively while g is decreased from 100 to 20 nm with a

step of 20 nm. The shift value is more pronounced for HC where more gaps are triggered producing more active sites for the occurring near-field coupling.

- For the same L values, the arrangement effect is shown as an augmentation of at least 10% of the resonance peak's amplitude when using a HC structure, and this is owing to its compact arrangement compared to the BT arrays. Plus, the LSPR of the HC have shown a global red- shift ($\sim 40 \pm 15 \text{ cm}^{-1}$) compared to those of BT. as the interaction between the adjacent triangles is becoming more effective, and thus, arising at lower energy.
- The maximum near E-field is found always at lower energy than the far-field LSPR energy, because our plasmonic resonators are conceived as damped harmonic oscillators with natural material losses.
- Higher intensity of the local E-field maximum is found for a BT and not for an HC as the former support the E-field effective localization at the sharp apexes, but the latter allows an E-field delocalization along the edges of the triangles, especially for a small spacing, and this large volume where the field is enhanced might be advantageous for further sensing applications.

These numerical results will be supported by a concrete realization of the structures. Indeed, the engaged fabrication processes will be detailed in the upcoming **Chapter 3**, and the optical characterization will be detailed in

Chapter 3: Fabrication of a barcode-like optical transducer

From theory comes out the best practice.

In this chapter, the fabrication approach of metallic nanostructures is presented to accomplish a barcode-like optical transducer from the near-IR to the mid-IR. The main objective is to produce well-defined periodic arrays of bowtie (BT) or highly packed honeycomb (HC) nanoantennas (NA) on the same sample surface. The geometric parameters will be tailored to cover a wide spectral range as detailed in the previous chapter.

Standard photolithography is commonly used to fabricate the plasmonic structures at the micron scale but is limited to medium and large patterns scale and periodicity. However, electron beam lithography (EBL) can go beyond these intrinsic limitations and it is suitable for the fabrication of nanostructures with smaller features. Furthermore, by being a mask-less facility, EBL is more productive when having many different patterns to optimize and produce at once.

The intended geometric parameters, such as pattern's size and spacing, can be directly created and modulated through a numeric Computer-Aided Design (CAD) namely GDSII file that is perfectly created by Python coding without the need to fabricate a physical mask as it is required for photolithography. The Python EBL pattern scripts conceived for this PhD are available on GitHub: <https://github.com/MelissaNajem/Python-Scripts>.

For large area exposure in the minimum of time, photolithography remains an excellent choice, as the EBL operation time is proportional to the exposed area, and a serious compromise is always recommended. Once the pattern is established, nanoimprint lithography (*e.g.* thermal manner by silicon mold) will be a choice for advanced and effective method to define nanostructures with a high throughput capacity at a lower manufacturing equipment cost. It is price-competitive with lower cost for a next-generation tech without the need for small laser sources and optics.

Herein, the fabrication chapter is divided into two main parts:

- A MOS-compatible substrate preparation done at the cleanroom of the Centrale de Technologies en Microélectronique (CTM) of Montpellier.
- An EBL exposure of the NA done at the micro and nanotechnology platform of the Laboratoire d'Analyse et d'Architecture des Systèmes (LAAS-CNRS) in Toulouse, a member of the Renatech French national network. For the BT, the metallization and lift-off steps are finalized at the LAAS; while for the HC, the process finishing is accomplished by an optimized dry etching and a resist cleaning at the CTM.

Our results are the fruit of several fertile discussions and constructive fabrication attempts (detailed in **Annexe 3.1**) that have led to the conception of two different fabrication techniques, one for the BT and the other for the HC. By this, both sophisticated NA are integrated within a metal-insulator-metal (MIM)-configuration as sketched in **Figure 3.1**.

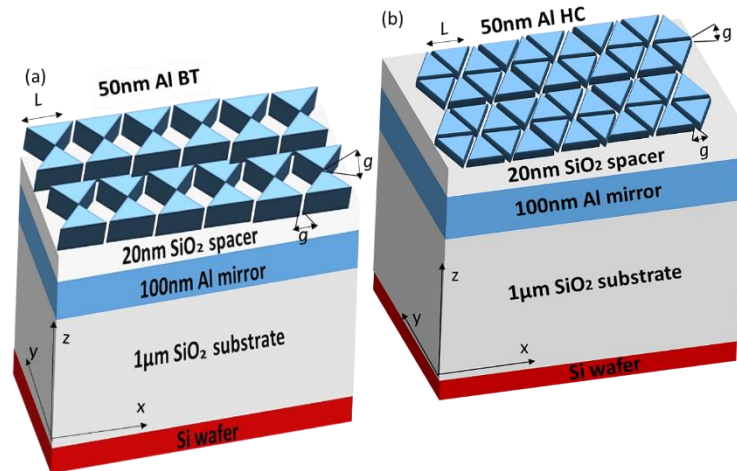


Figure 3. 1. Schematic of the NA arrays (a) Al-BT or (b) Al-HC integrated within nanostructures in a MIM configuration consisting of NA (50 nm)/SiO₂-spacer (20 nm)/Al-mirror (100 nm)), stacked on a MOS-compatible substrate (SiO₂/Si). L is the equilateral triangle side length of a BT; g is the tip-to-tip and corner-to-corner gap. Each BT or hexagonal-HC arrangement is considered a unit cell.

Contents

Chapter 3: Fabrication of a barcode-like optical transducer.....	85
3.1. Main substrate fabrication	88
3.2. Fabrication process of BT based on Metallization and Lift-off.....	92
3.2.1. Dose test sample for all L and g values.....	94
3.2.2. Final BT sample for visible and NIR coverage	96
3.2.3. Final BT sample for a wide IR coverage.....	99
3.3. Fabrication Process of HC with Dry Etching and Plasma Cleaning	101
3.3.1. Argon etching optimization.....	101
3.3.2. Final HC sample for a wide IR coverage	106
3.4. Conclusion	112

3.1. Main substrate fabrication

The desired NA will be integrated within MIM configuration that is MOS-compatible (grown on a Si wafer) and improves the light confinement as presented in the previous Chapter. The main layers stacking is explicitly represented in **Figure 3.2** with the two final technological processes to choose to engineer the final layer in BT or HC NA arrays.

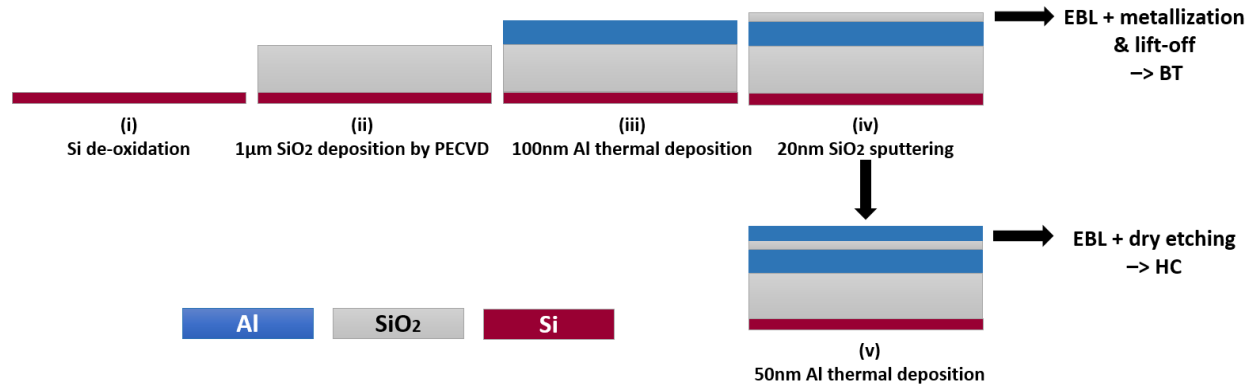


Figure 3. 2. The growth flow of the main substrate starts with (i) premium Si wafer de-oxidation by standard piranha solution combined with a highly diluted HF solution (H₂O:HF/5:1) treatment, followed by (ii) the deposition of a 1 µm thick SiO₂ layer by PECVD and (iii) the thermal evaporation of 100 nm thick Al layer, then (iv) 20 nm thick SiO₂ layer is sputtered. Such a sample is used either for BT fabrication after an EBL patterning with metallization and lift-off or is followed by (v) an extra Al layer deposition of 50 nm for HC fabrication with dry etching after EBL patterning. BT and HC final technological process will be detailed later in the chapter.

The process flow for the main sample fabrication consists of the following steps:

- (i) Premium Si wafer de-oxidation:** immersion for 10 min in a piranha solution (3:1 mixture of sulfuric acid and 30% hydrogen peroxide), rinsed under running water for 5 min, to remove all the piranha residues, and dried by nitrogen flux. This piranha mixture removes organic residues effectively. However, after this surface treatment, about 10 Å of SiO₂ layer will be formed with metallic contamination. A final HF treatment with a highly diluted solution (H₂O:HF/5:1) for 30 s is done and a hydrophobic profile is observed after washing the sample in running DI H₂O for 3 min. In MOS microfabrication devices and applications, the organic and ionic decontamination of Si wafers enables a good deposition quality of the subsequent layers and guarantees good fabrication reproducibility.¹¹⁶

(ii) Layers stacking: (ii) 980 nm-thick SiO₂ layer is deposited at 280°C through Plasma-Enhanced Chemical Vapor Deposition (PECVD, CORIAL), followed by (iii) 100 nm of Al thermal deposition at 1 Å/s, the insulating layer (iv) is 20 nm of SiO₂ sputtered at 0.4 Å/s using a plasma-assisted sputtering machine (PLASSYS, sputtering system). Such a sample is used either for BT fabrication after an EBL patterning with metallization and lift-off or is followed by (v) an extra Al layer deposition of 50 nm for HC fabrication with dry etching after EBL patterning.

Before the final surface engineering, the thin SiO₂ film surface roughness was further investigated with AFM measurements. The surface Roughness Mean Square (RMS) is found at 2 ± 2 nm, which is reassuring as a starting point for a precise NA definition. The BT tailoring begins with an EBL exposure followed by a 50 nm thick Al metallization and a lift-off process. In contrast, in the surface engineering for the HC array fabrication, the 50 nm thick Al layer is directly thermally deposited and EBL exposure defines a mask for a dry etching process. Both technological methods will be detailed later on.

Over the last half-century, EBL has evolved rapidly as one of the key techniques that enable pattern creation at the nanoscale¹¹⁷. EBL has been utilized for a wide variety of device fabrication, going from integrated circuit production to photonic crystals or channels for nanofluidics experiments. Hence, it is widely used thanks to its reliable high-resolution while covering all the scales down to a few nanometers. It is usable in any micro/nanofabrication process step with precise dimensional control in the 10 nm range.

EBL system closely resembles the design of a Scanning Electron Microscope (SEM) used to perform high-resolution images. Their main difference is EBL beam is scanned onto the sample according to the instructions of a pattern generator and following a specific design on a substrate surface covered by an electron-sensitive polymer resist, while in the SEM, the beam is scanned on the sample over the entire field of view to collect secondary electrons and so to form an image. EBL scheme consists of a chamber, an electron gun, and a column. Column and chamber are maintained in a high vacuum by a powerful set of pumps. The column contains the electron optical elements required to create a beam of electrons, accelerate it up to the working voltage,

turn it on and off by the beam blanking plates, focus, and deflect it as it is desired for the exposition of the needed patterns. For more details on the EBL systems, a recommended review by Matteo Altissimo will give the reader a solid understanding of this topic.¹¹⁸

The RAITH150-EBL is used in this PhD project. It has a SEM column (GEMINI) with a micrometric displacement stage supplemented by an interferometer allowing to measure the position of the sample with an accuracy of approximately 2 nm. A piezoelectric system permits to adjust, dynamically, the position of the sample with an overall precision of the order of 10 nm. Schottky-emitter field emission gun (FEG) is employed to expose the patterns. Consequently, the beam locally modifies the resist polymeric sequence: polymer chains are broken in the case of a positive tone, thus, with a suitable developer, it is causing empty areas on the substrate. On the contrary, in a negative tone resist, the irradiated areas are cross-linked, *i.e.* hardened, so the developer will strictly dissolve the unexposed resist.

Technically, for BT and HC lithography, positive tone electron-sensitive resists are implemented. PolyMethylMethAcrylate (PMMA) is the typical resist used across academia and industry for high-resolution tailoring combined with a lift-off process.^{119,120} CSAR is a high-tech resist for EBL which allows the implementation of high-end microelectronics applications, such as for aerospace engineering or high-performance computers. Even extremely small nanostructures (<10 nm) can be realized using CSAR for highly integrated circuits of microchips.¹²¹

In this PhD thesis, PMMA is used for BT and CSAR for HC; and the tactics for the patterns definition are radically different. Indeed, the periodic BT arrays are scanned as equilateral tip-to-tip facing triangles. However, the HC are defined similarly to the "etch material" of the FDTD model in **Chapter 2**, *i.e.* by exposing in-between lines along 0°, 60°, and 120° directions. The corresponding technological parameters will be further provided through this chapter for both fabrication methodologies *i.e.* metallization and lift-off or etching and resist cleaning, for BT or HC respectively. In principle, the NA are tailored to an extent of 100 x 100 μm² to achieve a good signal-to-noise ratio (SNR) for ultimate optical characterizations (see **Chapter 4**).

The fabrication results will be supported by SEM images that offer a way to comment on the morphology, the reproducibility, and the throughput quality of both technological processes, by linking the obtained geometric parameters to those initially desired. Therefore, we used RAITH150 imaging capability at 5 keV (beam current of 10 pA) to make calibrated images of the BT NA. The automatic imaging parameters ($4 \times 4 \mu\text{m}^2$, 2 000 points) lead to a resolution of 2 nm. The focus is regulated at the beginning and cross-checked in the middle of each imaging sequence. Image-J software is used to measure and retrieve the corresponding geometric values that will serve for a statistical study. Besides, as previously mentioned, the HC design exposure is followed by an etching step to transfer the patterns to the 50 nm thick Al layer having the CSAR resist as a mask. However, the etching rate of such a thin metallic layer should be optimized, thus, Atomic Force Microscopy (AFM) analysis is vital to calibrate the required depth. Both softwares, Gwyddion and NanoScope Analysis 1.7, are used not only to measure the eventual depth but also to discover the surface RMS that is normally affected by the native aluminum oxide presence.

3.2. Fabrication process of BT based on Metallization and Lift-off

This process aims to create NA arrays consisting of two closely placed equilateral triangles forming a BT shape with controlled side lengths (L) and spacing (g). This technological process was done completely in the LAAS-Toulouse cleanroom facilities. **Figure 3.3:** (a) shows the EBL machine provided by RAITH150, the insert is its sample holder, monitored through both computer screens, (b) the sample manipulation sites (the hot plate, the spin coater, and the lift-off spot), and (c) displays the electron beam evaporation equipment.

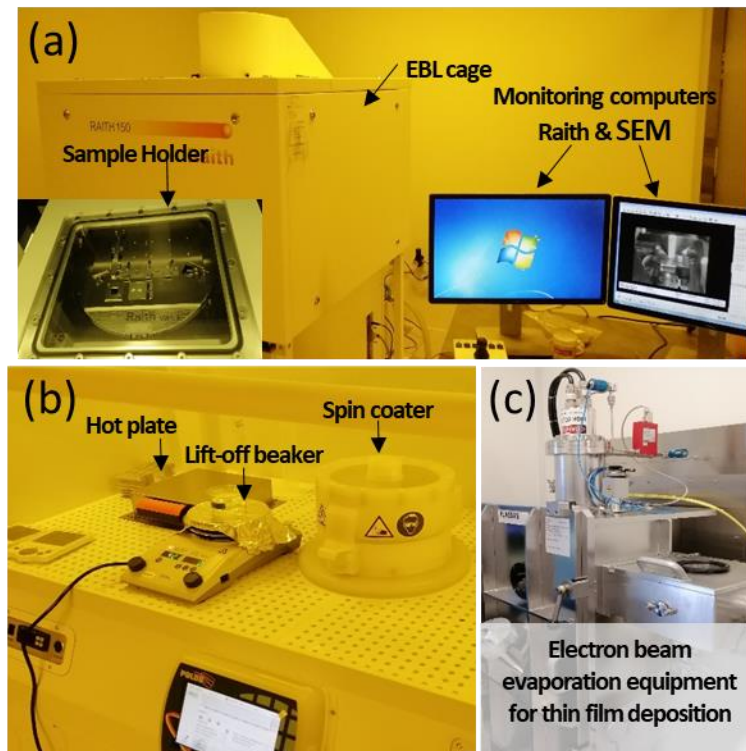


Figure 3. 3. LAAS cleanroom equipment used for the fabrication of the NA. (a) shows the EBL machine (cage) from RAITH150, the insert is its sample holder, monitored through both computer screens. (b) the sample manipulation sites, e.g. the hot plate, the spin coater, and the lift-off spot. (c) displays the metallization instrument, and the electron beam evaporation equipment.

Figure 3.4 presents schematically the fabrication steps of BT arrays based on metallization and lift-off: (i) PMMA positive tone resist spin-coating, (ii) EBL exposure, (iii) exposed-resist development in DMSO, (iv) e-beam evaporation of Al, (v) unexposed-resist lift-off, and (vi) the final structure of 50 nm-thick Al-BT.

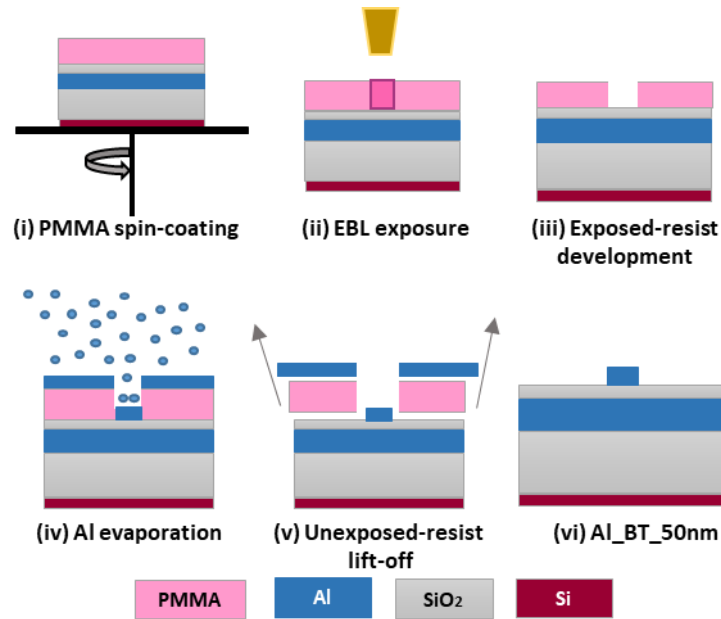


Figure 3. 4. Technological process flow starts with (i) PMMA resist spin-coating, followed by (ii) an EBL exposure and (iii) a standard development, then (iv) a metallization and ending with (v) a lift-off process, to retrieve (vi) the final Al-BT.

The next paragraphs sum up the most important technological details for each step of **Figure 3.4**, after the two first steps previously described in **Figure 3.2**:

- (i) Resist Coating:** Dehydrate the sample surface on a 180°C hot plate for 5 min. PolyMethylMethAcrylate (PMMA) is used as a positive tone versatile organic electron-sensitive resist.^{119,120} The PMMA is prepared from powder (996K as molecular weight brought by Sigma-Aldrich) dissolved in anisole, with a concentration of 38 g/L. The solution conserved away from light and humidity preserves its performance for up to two years. A 140 nm thick layer is obtained at 3 000 rpm for 60 s. To expel the solvent, a bake is performed on the hot plate at 180°C for 1 min.
- (ii) EBL Exposure:** The exposure is done using a FEG-RAITH150 EBL system with a 7.5 μm aperture, operating at 20 keV (optimized beam current of 20 pA), a working distance of 7 mm, and using an exposure step size of 2 nm. Once the sample origin is fixed and the angle correction is done, subsequent contamination dots of ~20 s exposure are used in high magnification to set the focus and correct the stigmatism. To limit stitching errors, a writing field alignment on the contamination dot adjusts the zoom,

rotation, and stigmatism. All these parameters are well-controlled during the exposure thanks to a built-in focus tracking system. The nominal dose value is set to $240 \mu\text{C}/\text{cm}^2$, then a dose factor is applied for each (L, g) combination.

- (iii) Resist Development:** The resist is developed in a Methyl Isobutyl Ketone (MIBK): 2-Propanol (IPA) solution (MIBK:IPA/1:3) for 45 s. After development, the sample is immediately rinsed in IPA (stopper solution) for 30 s. This ensures the best profile for a metallization lift-off with an $\sim 80^\circ$ inclined side-walls. For the nanometric scale patterning by EBL, both the resist profile and thickness are crucial points to master.
- (iv) Al deposition:** A 50 nm thick layer is evaporated from a 99.99% pure aluminum pellets source in a tungsten boat by electron-beam evaporation (PLASSYS MEB550SL) at a $2 \text{ \AA}/\text{s}$ and 10^{-8} mbar. The initial heating power cracks the thin layer of native oxide of the Al pellets. The sample holder is continuously rotated to provide a homogenous deposition. Note, electron beam evaporation is important for a correct lift-off. The resist mask is not reticulated compared to sputtering deposition and the contamination is reduced compared to the thermal deposition.
- (v) Lift-off process:** A Dimethyl sulfoxide (DMSO) remover solution at 80°C is used in a covered beaker to avoid solvent evaporation. A syringe is initially used to send solution bubbles on the deposited metallic layer to ease its shredding, then the beaker is placed into an ultra-sonication bath at 35 kHz for 60 s to guarantee a clean lift-off. The samples are thoroughly rinsed under deionized running water and blown with dry N_2 . Note, this technique is limited by the resist thickness and its edge shape, to allow the solvent to flow to the unexposed resist layer and to remove it together with the unwanted metallic cover.¹²⁰

3.2.1. Dose test sample for all L and g values

For an accurate fabrication technology, it is important to evaluate the dependency of the EBL-applied dose factors on the triangle's side lengths and spacing. The main idea is to define the

optimum dose that gives the most precise triangle's side length and spacing to evaluate the beam current value regarding the exposure precision. An electron dose is usually expressed in $\mu\text{C}/\text{cm}^2$ and it is defined as the number of electrons per unit area required to achieve the desired changes in a resist.¹²² Such investigation is done through a deep SEM images treatment by using Image-J software. For example, to define a BT with $L = 2.0 \mu\text{m}$ and $g = 20 \text{ nm}$ or 100 nm , a dose factor $\times 1.8$ or $\times 2.1$ should be respectively selected. Please refer to **Annexe.3.2** for more details on the antenna's dose test exposure and morphology. Once the perfect dose factors are defined for each (L, g) , as well as the optimal beam current is selected, a complete sample is consequently fabricated for further optical and sensing investigations.

Figure 3.5(a-e) are SEM images of the periodically lithographed BT arrays with $L = 0.8 \mu\text{m}$, featuring variable gap values, which are progressively decreasing from 100 nm to 20 nm with a step of 20 nm with 20 pA . Each pattern is exposed with the right dose factor selected based on the previous results of the dose test. The gap separations g are $99 \pm 2 \text{ nm}$, $81 \pm 4 \text{ nm}$, $61 \pm 4 \text{ nm}$, $38 \pm 5 \text{ nm}$, $22 \pm 3 \text{ nm}$ respectively, measured in a collection of 5 SEM images of 5×7 BT antennas for each zone. According to all collected SEM images, the corners angle and the triangle side length are respectively equal to $59.6 \pm 0.2^\circ$ and $0.799 \pm 0.002 \mu\text{m}$. The pitches along the x-axis, Λ_x , are also measured and their respective values are $0.902 \mu\text{m}$, $0.883 \mu\text{m}$, $0.862 \mu\text{m}$, $0.847 \mu\text{m}$, $0.825 \mu\text{m} \pm 0.002 \mu\text{m}$. Substantially, **Figures 3.5** highlights only a sampling of the high control achieved on the geometric parameters which are tailored at the nanoscale. Remarkably, the constructed triangles are equilateral, manifesting finely sharp and well-defined edges, despite the whole process limitations starting from the control of the multi-stacked layer deposition, followed by a relatively critical EBL writing over a large area, ending with a nanoscale features lift-off step. In sum, the measured values on the whole optical transducer surface are found to be in high conformity with the expected parameters.

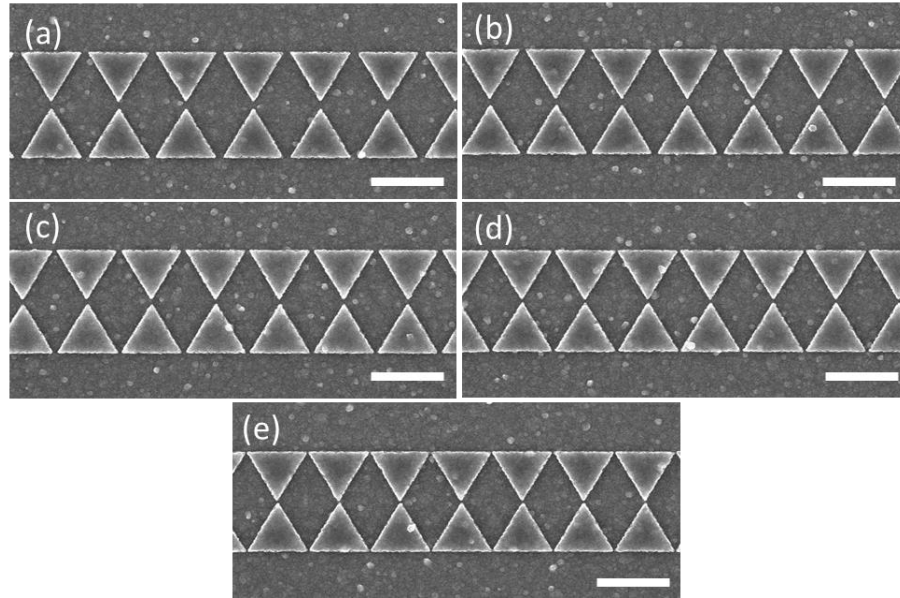


Figure 3. 5. SEM images of the fabricated BT, L equals $0.8\mu\text{m}$ and g is varying (a-e) from 100 nm down to 20 nm with a step of 20 nm. All scale bars are $1\mu\text{m}$ long.

3.2.2. Final BT sample for visible and NIR coverage

3.2.2.1. Exposure pattern and surface distribution

Globally, as the right dose is defined a dose factor is identified for each BT, and a compact Python program is developed using a triple combination [L , g , *dose factor*] to create several $100 \times 100 \mu\text{m}^2$ tailored zones on the same sample. For small sizes $L \leq 0.3 \mu\text{m}$, the dose factor is almost constant at 2.5 and is used to define the smaller BT to address the visible, based on the reflectance simulation of section 2.2 (**Chapter 2**). L is selected to be equal to 0.3, 0.2, 0.15, 0.1 and $0.08 \mu\text{m}$, g values equal to 20, 60 and 100 nm. The patterns organization on the transducer surface is displayed in **Figure 3.6**.

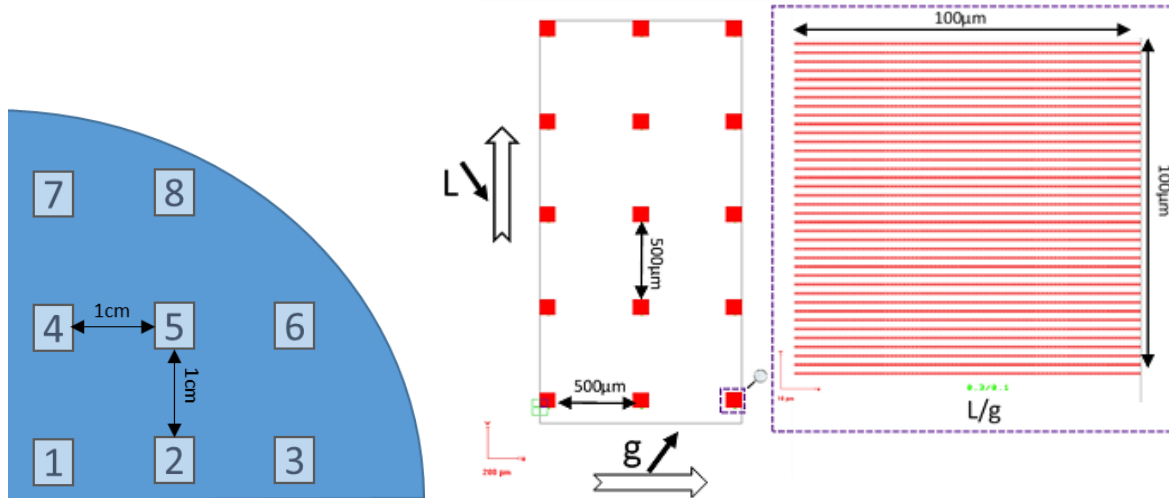


Figure 3.6. A $\frac{1}{4}$ wafer of the main structure with 8 identical sensor transducers. BT EBL- patterns created using a python script, where L is equal to 0.3, 0.2, 0.15, 0.1, 0.08 μm respectively while going vertically up, and g is equal to 0.02, 0.06, 0.1 μm respectively from the left to the right.

In each line, L is maintained constant and g is increased and consequently taking values of 0.02, 0.06, and 0.1 μm ; then L is decreased while traveling from a line up to the following one. Overall, one exposed area is formed of 15 zones and it is repeated 8 times each 1 cm on a quarter substrate wafer as shown in **Figure 3.6**. The 8 zones can be cut into independent sensor transducer surfaces to be exposed to different trial solutions for detection proof-of-concept.

3.2.2.2. Morphology analysis of the sensor transducer

SEM calibrated images are captured automatically at the center of each zone in **Figure 3.6**, by creating a matrix using the RAITH150 program. SEM images are studied over 4 zones (No. 1, 3, 5, and 8) to provide a statistical study of the BT size, L and g , as well as their pitches along x and y, *i.e.*, λ_x and λ_y (please check **Annexe 3.3**). The analysis of the morphology of the sensor transducer ensures the reliability of the technological process and the dose factor and beam current optimization. Indeed, spanning all tailored surfaces, the mean values of L and g are measured for sample No.5. The retrieved values are presented in **Table 3.1** below the corresponding SEM image. For $L = 0.08 \mu\text{m}$ the triangles are closer to being spheres, that's why it was better to represent its diameter, d , instead of L .

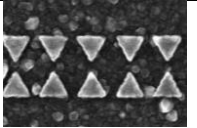
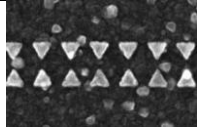
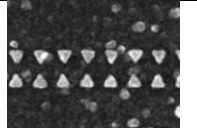
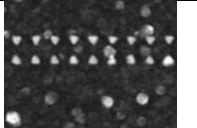
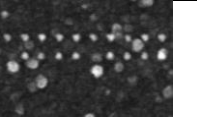
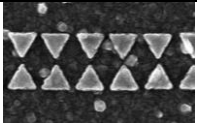
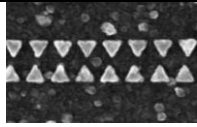
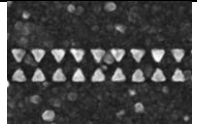
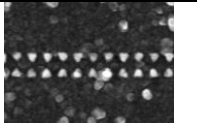
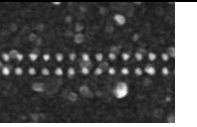
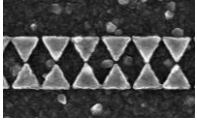
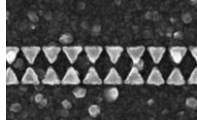
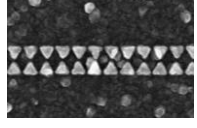
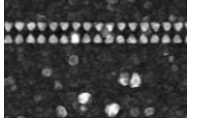
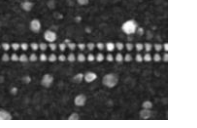
L/g	0.3 μm	0.2 μm	0.15 μm	0.1 μm	0.08 μm
0.1 μm	 L $= 0.295$ ± 0.005 g $= 0.102$ ± 0.001	 L $= 0.195$ ± 0.007 g $= 0.101$ ± 0.006	 L $= 0.145$ ± 0.005 g $= 0.099$ ± 0.005	 L $= 0.096$ ± 0.006 g $= 0.102$ ± 0.007	 d $= 0.087$ ± 0.02 g $= 0.098$ ± 0.008
0.06 μm	 L $= 0.295$ ± 0.009 g $= 0.056$ ± 0.009	 L $= 0.193$ ± 0.007 g $= 0.063$ ± 0.006	 L $= 0.145$ ± 0.005 g $= 0.056$ ± 0.005	 L $= 0.097$ ± 0.003 g $= 0.059$ ± 0.003	 d $= 0.074$ ± 0.002 g $= 0.056$ ± 0.008
0.02 μm	 L $= 0.296$ ± 0.005 g $= 0.019$ ± 0.003	 L $= 0.194$ ± 0.007 g $= 0.024$ ± 0.008	 L $= 0.144$ ± 0.006 g $= 0.025$ ± 0.006	 L $= 0.094$ ± 0.006 g $= 0.023$ ± 0.004	 d $= 0.072$ ± 0.004 g $= 0.019$ ± 0.002

Table 3. 1. BT morphological study. L and g values are in μm . SEM images are provided for each L and g combination. L is varied from 0.3 down to 0.08 μm and the g values are equal to 0.1, 0.06, and 0.02 μm . The calibrated image size is 4 x 4 μm^2 . Geometric parameter values are found based on Image-J treatment. Note that for $L = 0.08 \mu\text{m}$, the triangles are rounded, so the corresponding diameter, d , is measured.

The SEM images of the BT highlight the process stability and effectiveness: despite the comparable size of the Al oxide grains and the nanometric size of the triangles, all the geometric parameters of the fabricated BT are found fairly close to those primarily set in the patterns.

3.2.3. Final BT sample for a wide IR coverage

3.2.3.1. Exposure pattern and surface distribution

According to the dose test results, detailed in **Annexe.3.2**, a Python script is developed to create several $100 \times 100 \mu\text{m}^2$ tailored zones on the same sample separated by $200 \mu\text{m}$ horizontally and vertically; in each of which the $[L, g, \text{dose factor}]$ are kept constant as shown in **Figure 3.7**.

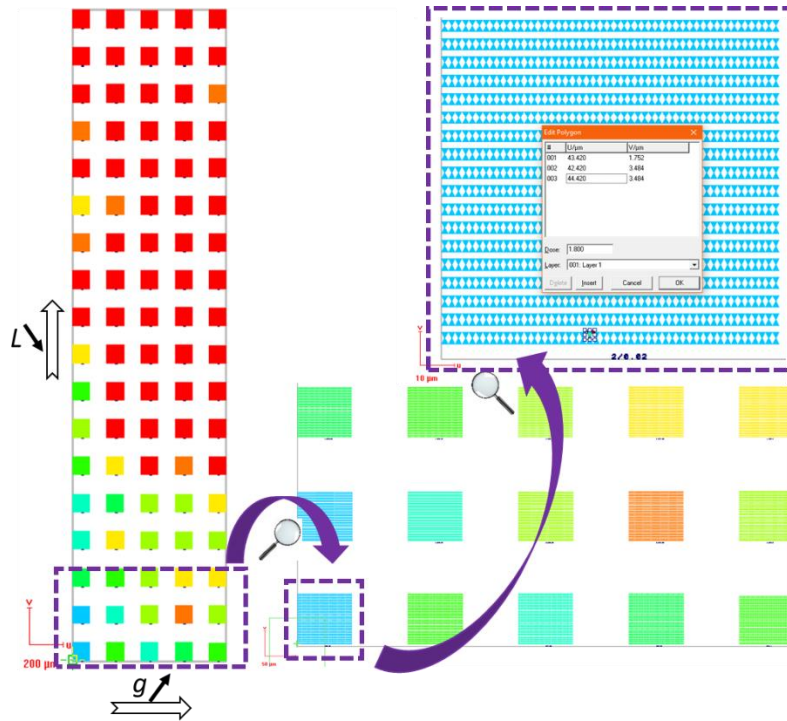


Figure 3. 7. Color-coded patterns with adequate dose factors for each BT zone. The dose factor variation for PMMA is visualized in a color palette from light blue to red denoting a factor of $\times 1.8$ to $\times 2.5$. From the left to the right, g value increases from 0.02 to $0.1 \mu\text{m}$ with a step of $0.02 \mu\text{m}$; from the bottom to the top, the L value decreases from 2.0 to $0.3 \mu\text{m}$ with a step of $0.1 \mu\text{m}$.

This figure represents the total view of the colored matrix representing the dose factor variation: it is visualized using a color palette gradually varying from light blue to red for respective factors ranging from $\times 1.8$ to $\times 2.5$. In each line, L is constant, while from the left to the right, g is increased

from 0.02 nm to 0.1 μm with a step of 0.02 μm . From one column up to the other, L decreases from 2.0 μm up to 0.3 μm with a step of 0.1 μm .

3.2.3.2. Morphology analysis of the sensor transducer

Figure 3.8(a-e) are SEM images of the periodically lithographed BT arrays with $L = 2.0 \mu\text{m}$, featuring variable gap values, which are progressively decreasing from 100 nm to 20 nm with a step of 20 nm. The g values are equal to $111 \pm 6 \text{ nm}$, $83 \pm 7 \text{ nm}$, $68 \pm 5 \text{ nm}$, $36 \pm 6 \text{ nm}$, $27 \pm 4 \text{ nm}$ respectively, measured in a collection of 5 SEM images of 5×7 BT antennas for each zone. According to all collected SEM images, the corners angle and the triangle side length are respectively equal to $61.6 \pm 0.4^\circ$ and $2.008 \pm 0.017 \mu\text{m}$. The pitches along the x-axis, λ_x , are also measured and their respective values are 2.112 μm , 2.096 μm , 2.064 μm , 2.203 μm , $2.037 \pm 0.002 \mu\text{m}$. Substantially, **Figure 3.8** highlights only a sampling of the high control achieved on the geometric parameters which are tailored at the nanoscale. Remarkably, the constructed triangles are equilateral, manifesting finely sharp and well-defined edges, despite the significant roughness of the sample that was cleaved at the edge of the Si-based main substrate. (RMS = $14.3 \pm 1.1 \text{ nm}$ and the diameter of the oxide grains is around $140 \pm 20 \text{ nm}$).

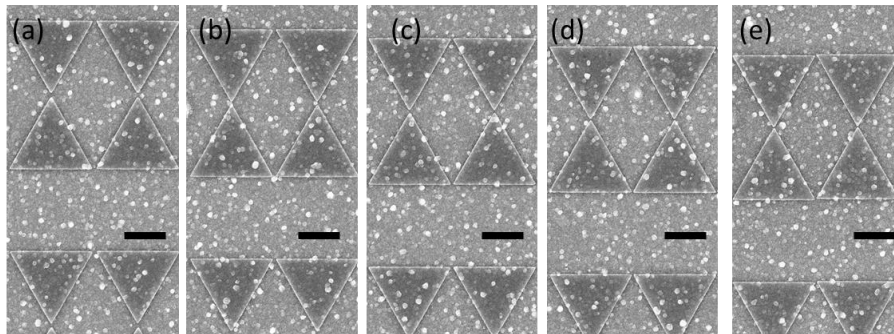


Figure 3. 8. SEM images of the fabricated BT, L equals 2.0 μm and g is varying (a-e) from 100 nm down to 20 nm with a step of 20 nm. All scale bars are 1 μm long.

Here, it is important to note that the excess of oxide beads on this sample's surface is due to skipping the piranha step from the Si wafer de-oxidation treatment. Indeed, the skated layers were growing locally around the Si oxide beads provoking bigger oxide grains construction.

3.3. Fabrication Process of HC with Dry Etching and Plasma Cleaning

In this section, the fabrication approach of the metallic Honeycomb (HC) nanostructures on a MOS-compatible substrate is detailed. On the same sample, several well-defined aluminum (Al) HC with different triangle side lengths L and spacing g are fabricated. The intended geometric parameters are directly created and modulated through a GDSII file that is created by python coding. The technological process is also interchanged between *Montpellier* and *Toulouse* within the *framework* of the *Renatech* network: the definitive HC patterns exposure is done in the clean room of the LAAS in Toulouse and the process finishing is accomplished by an argon etching and a resist cleaning at the CTM of Montpellier.

3.3.1. Argon etching optimization

To optimize the etch of the 50 nm-thick layer of Al, it is crucial to try both etching routes: the wet and the dry etching. For more details, please refer to **Annexe 3.4**. The wet chemical etching was massively accompanied with clear surface oxidation residues, hence, it was avoided. A precise study of the physical etch rate is proceeded in the following sections for the configuration of interest, *i.e.* a positive tone resist covering a MIM structure, as an Argon (Ar) sputtering is applied to transfer the patterns to a 50 nm thick Al layer.

3.3.1.1. Lines Exposure and Dry Etching on a MIM Configuration

This section is the starting point of the final technological process of HC. Indeed, to overcome the anticipated proximity effects while exposing the triangles and the limitation of the lift-off process (**Annexe 3.1**), the conception of the hexagonally organized triangles has been upgraded: instead of scanning the triangles on a negative tone resist, the same triangles are herein defined as the contrast of scanning their in-between lines as illustrated in **Figure 3.9**. Hence, their L and g are defined by the periodicity, p , and width, w , of the line. This idea will be further detailed in the upcoming parts.

Firstly, to test the recipe of the ICP-150 W Ar etching of a thin Al layer using a positive tone resist as a mask for the triangles, one sequence of samples was lithographed on an industrial PMMA- A4 (at the CTM) and another one on a CSAR resist (at the LAAS) and the etching rate was evaluated.

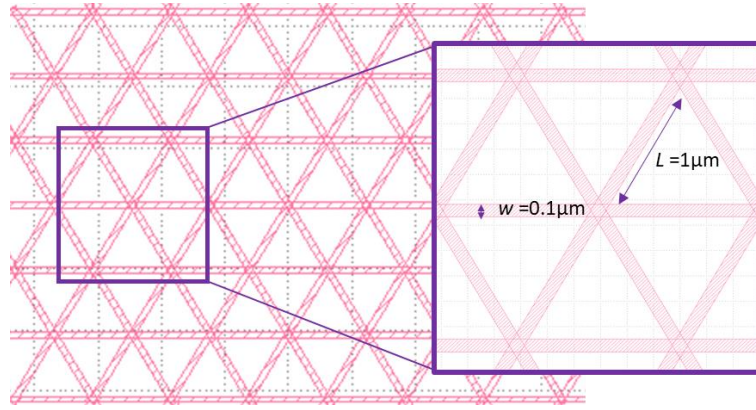


Figure 3.9. Patterns to define the hexagonally placed triangles. The lines are exposed on a positive tone resist and then transferred to the Al layer through Ar etching, to define the consequent Al triangles with $L = 2.0 \mu\text{m}$ and $w = 0.1 \mu\text{m}$.

It is important to note that in both cases, the resist was present just after the etching process and it was manifested under an optical microscope. In fact, the nominal thickness of the PMMA and the CSAR are 180 and 150 nm after EBL exposure, so both resist thicknesses are enough to protect the unpatterned surface while the 50 nm Al layer is etched.

PMMA-A4 as a Mask onto the Triangles

- **Resist Coating:** Dehydrate the sample surface on a 150°C hot plate for 5 min. The industrial PMMA-A4 is spin-coated with 6 000 rpm for 60 s, and baked for 60 s at 180°C, giving a thickness of 180 nm.
- **EBL Exposure:** The patterns of **Figure 3.9** are lithographed using a beam current of 22 pA (spot size of 30) in a 10 x 10 μm^2 extension (for time's sake). The dose factor is evaluated and varied from x 0.9 to x 1.4 for a nominal dose of 300 $\mu\text{C}/\text{cm}^2$.
- **Resist Development:** The resist is developed in a diluted MIBK solution (MIBK:IPA/1:3) for 30 s and then rinsed in a stopped solution of IPA for 30 s.

- **Argon etching:** The PMMA acts as a mask to transfer the patterns onto the metal layer. The sample is etched under an Ar sputtering for 115 s (based on several optimizations and proof firstly done on a large surface and knowing that the 180 nm PMMA layer will resist until 6 min and 30 s under Ar etching, etching rate equals 0.46 nm/s). It is worth noting that the etching rate strongly depends on the open area size through which the etchant attacks the metallic layer.
- **Residual resist cleaning:** At the end, the unexposed resist is cleaned following the 3 min acetone/3 min IPA /N₂ drying sequence.

Following the Ar etch, SEM images were hardly retrieved before the resist cleaning step (the resist presence causes a huge charging effect even under low vacuum mode). However, the SEM images at the end of the process (after the resist cleaning) show a good definition of the triangles, even though the parameter values were smaller than the aimed ones (**Figure 3.9**). **Figure 3.10a and 3.10b** show respectively the SEM and the AFM images of the patterns with a dose factor x1. The Al triangles are well transferred to the Al layer following the etching step of the open lines, yet, a re-deposition of the Al atoms and pencil-like structures are remarked as typified in **Figure 3.10b**. Plus, the depth is found to be equal to 170 nm. So, unwanted etching occurs through the SiO₂ layer, and thus the etching time should be optimized. After many tests, it is found that, on large surfaces, the etching rate of Al and SiO₂ are respectively equal to 0.5 nm/s and 0.8 nm/s, respectively. Hence, a critical selectivity is blocking the precision of the etch depth for such a process.

Till now, the shape, size, and thickness of the HC structures are not perfectly controlled. Therefore, the line-exposure methodology is tested at the LAAS using a high-tech resist, namely CSAR, and the process finishing is accomplished by an Ar etching and a resist cleaning at the CTM.

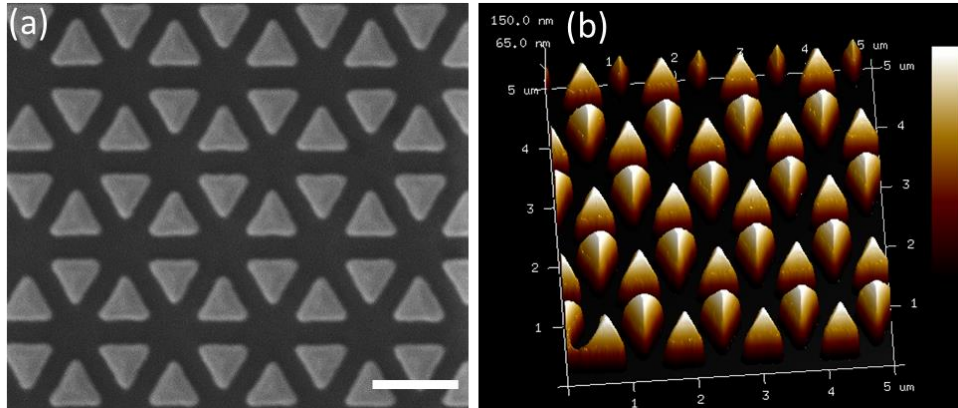


Figure 3. 10. HC-like triangles were transferred to the Al layer by Ar etching of the in-between lines for 115 s. (a) SEM image of the structures after the resist mask cleaning. The bar scale is 1 μm long. (b) A 3D representation of the topography of the structure (tilted AFM image) representing a pencil-like definition of the triangles. The color scale intensity is varying between -20 and 150 nm for better height visualization.

CSAR as a Mask onto the Triangles

The process flow will be detailed in the coming section which is dedicated to the complete sample fabrication with the perfectly selected dose factors. Noteworthy, the exposure parameters, *i.e.* the beam current, the working distance, the nominal doses, and the step sizes, will remain unchangeable for any HC patterns exposure. The dose factors are varied from x1 to x8.6 for all the line widths swept from 20 to 100 nm. After a standard development, SEM images are collected, showing a slight difference in terms of line width between the differently oriented lines (**Figure 3.11**) as the beam displacement is unique along each direction (scanning horizontally or diagonally). However, the lines are finely defined for specific dose factors. The latitude of the process seems to be linear: line width increases as the dose factor increases. Furthermore, based on the SEM images, we can see the grains of the Al top layer of the substrate via the "open lines" which evidence a perfect resist development.

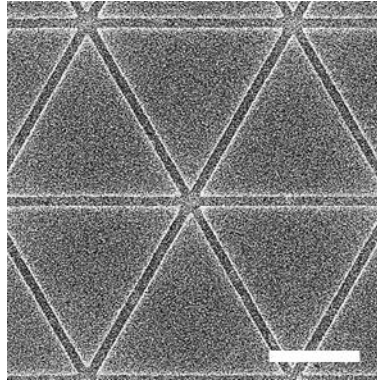


Figure 3. 11. SEM image of HC patterns after the CSAR resist development. $L = 2.0 \mu\text{m}$ and $w = 91 \text{ nm}$, dose factor is $\times 5.8$. The triangles are well defined. The observation of grains through the lines witnesses their perfect opening. The bar scale is $1 \mu\text{m}$ long.

Regarding the etching process, one can assume that:

- the opening dimensions will highly influence the etching rate,
- Al-oxide grains would resist the upcoming Ar etching.

So far, to etch a 50 nm-thick Al through a slit of 200 nm (PMMA as a mask), a pre-calibrated etch time of 115 s is established. Practically, the HC dose test sample (CSAR as a mask) is etched for 115 s and the resist is cleaned under a 100 % Plasma O_2 flux for 5 min. The etching results through an opening of 100 nm are evaluated through AFM analysis as presented in **Figure 3.12a** and a depth of 33 nm is retrieved. Thus, the etching time has to be re-optimized, and the 2nd HC dose test sample is etched for 175 s (**Figure 3.12b**). A depth of 50 nm was nicely observed on AFM image in **Figure 3.12b**. Nevertheless, an Al re-deposition is observed on the perimeter of the triangle because the Ar sputtering is anisotropic and the etch is taking place through narrow openings. Plus, inside the chamber, the created plasma was not stable: the RF forwarded and reflected powers curves were unsteady. These parameters are uncontrollable during the etch (machine limitation).

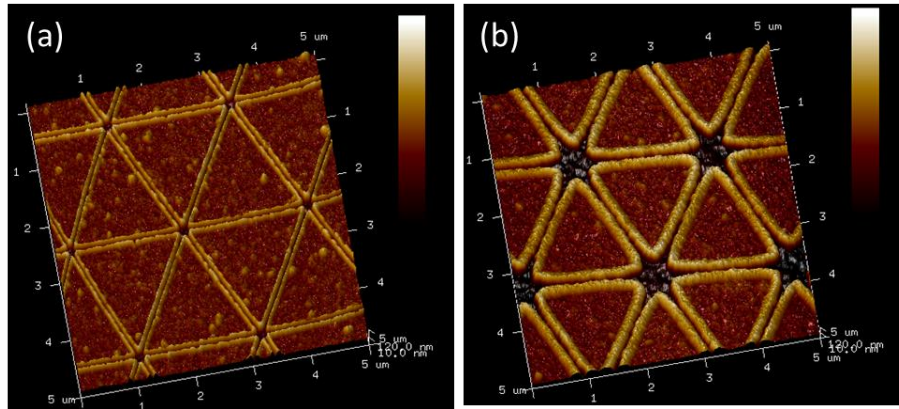


Figure 3.12. AFM images at the end of the process. Ar etching time was set to (a) 115 s and (b) 175 s. Color scale intensity varied between 120 and -100 for better visualization. An obvious Al re-deposition is remarked at the outlines of the HC-like triangles upon their transference to the Al film.

At this stage, the development and the etching results will lead us to select the perfect dose factors for the final and complete HC sample as will be detailed in the coming section. It is crucial to anticipate the Al re-deposition on the boundaries of the Al triangles that plug the openings by selecting a dose factor that gives line widths slightly larger (+2 nm to +5 nm) than those expected.

3.3.2. Final HC sample for a wide IR coverage

The complete technological process flow is summarized in **Figure 3.13** as the following:

- (i) **Resist Coating:** Dehydrate the sample surface on a 150°C hot plate for 5 min. CSAR 62 resist (CSAR:Anisol/1:2) is used as a positive tone versatile electron-sensitive resist. A 150 nm thick layer is obtained at 3 000 rpm for 60 s. To expel the solvent, a bake is performed on the hotplate at 180°C for 1 min.
- (ii) **EBL Exposure:** The 3D-exposure of the lines with angles of 0°, 60°, and 120° is done with a 10 μm aperture, operating at 20 keV (beam current of 40 pA), a working distance of 7 mm, and using an area step size of 4 nm, an area nominal dose of 50 μC/cm²; and a line step size of 2 nm, a line nominal dose of 100 pC/cm². Once the sample origin is fixed and the angle correction is done, subsequent contamination dots of ~20 s exposure are used in high magnification to set the focus and correct the

stigmatism. To limit stitching errors, a writing field alignment on the contamination dot adjusts the zoom, rotation, and stigmatism. All these parameters are well-controlled during the exposure thanks to a built-in focus tracking system.

- (iii) Resist Development:** The resist is developed in an Amyl Acetate solution for 60 s, then the sample is dropped in a stopper solution of IPA, ensuring thus the best sidewalls profile for the upcoming dry etch.
- (iv) Argon etching:** The CSAR acts as a mask to transfer the patterns onto the metal layer: the 50 nm-thick Al layer is etched via the opened zones (*i.e.* lines) using argon (Ar) sputtering (150 W as Rf and 200 W as Lf, with a voltage bias of 170 V) for 180 s.
- (v) Residual resist cleaning:** At the end, the unexposed resist is cleaned by an inductive plasma O₂ (100% O₂) for 5 min.

Following this process, we created nanostructure arrays consisting of hexagonal and closely placed equilateral triangles forming a HC shape with controlled side lengths and spacing.

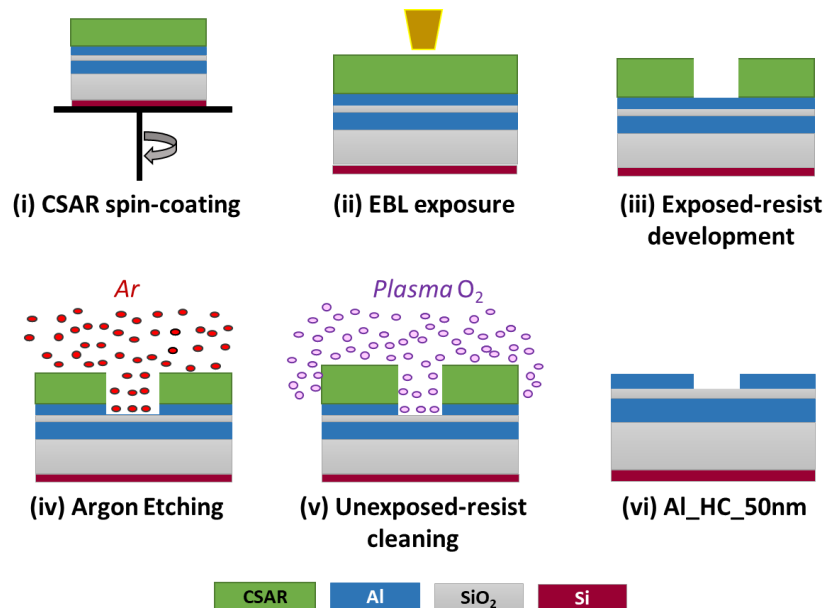


Figure 3. 13. Technological process for HC starts from (i) CSAR resist spin-coating, followed by (ii) an EBL exposure and (iii) a standard development, then (iv) an argon etching and ending with (v) a resist pure plasma O₂ cleaning process, to retrieve (vi) the final Al-HC.

3.3.2.1. Exposure pattern

The HC are defined as the contrast of 3D-exposed lines with angles of 0° , 60° , and 120° , once the linear openings are transferred by etching to the 50 nm thick Al layer. The created patterns are shown in **Figure 3.14**. Based on the previously done dose tests, adequate dose factors for CSAR are defined for each zone as visualized in a color palette in **Figure 3.14** from blue to light red denoting a factor of $\times 4.2$ to $\times 8.2$. From the left to the right, L value decreases from 2.0 to 1.0 μm with a step of 0.1 μm ; from the bottom to the top, the g value increases from 0.02 to 0.1 μm with a step of 0.02 μm . Plus, on the same sample, two exposure modes are tested (concentric and linear modes) for the whole HC palette to optimize the line's definition. Note that the effect of both exposure modes on the HC structures will be optically evaluated in **Chapter 4**.

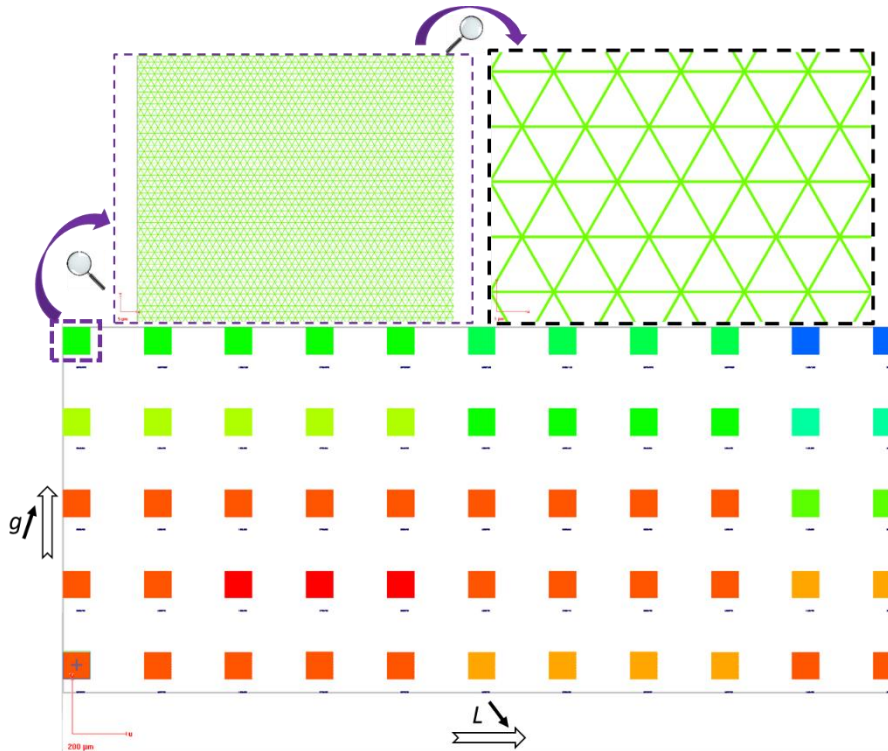


Figure 3. 14. Color-coded patterns with adequate dose factors for each BT zone. The dose factor variation for CSAR is visualized in a color palette from blue to light red denoting a factor variation from $\times 4.2$ to $\times 8.2$. From the left to the right, L value decreases from 2.0 to 1.0 μm with a step of 0.1 μm ; from the bottom to the top, the g value increases from 0.02 to 0.1 μm with a step of 0.02 μm . The hexagonally placed triangles are defined as the contrast of the periodic and 3D-exposed lines with angles of 0° , 60° , and 120° , upon their transference to the 50 nm thick Al layer through the etching of the linear openings.

3.3.2.2. Morphology analysis of the sensor transducer

At the end of the technological process, AFM analysis is done to prove that the desired depth of 50 nm is achieved with Ar etching for necessarily large openings (larger than 40 nm). 3D-AFM images for $L=2.0\ \mu\text{m}$ and opening of 100 and 20 nm are represented in **Figure 3.15a** and **3.15b**. **Figure 3.15a** underlines the verticality of the triangle's profiles following the etching step by Ar sputtering. Based on **Figure 3.15c** and **3.15d**, the RMS values of the triangle's surface are alike for both cases and respectively equal $2.5 \pm 0.3\ \text{nm}$ and $2.6 \pm 0.7\ \text{nm}$. In **Figure 3.15c**, $L = 1.99 \pm 0.04\ \mu\text{m}$, and the opening widths are doubled up because of the anisotropic etching. In **Figure 3.15d**, $L = 1.9 \pm 0.2\ \mu\text{m}$ and the lines are not perfectly opened.

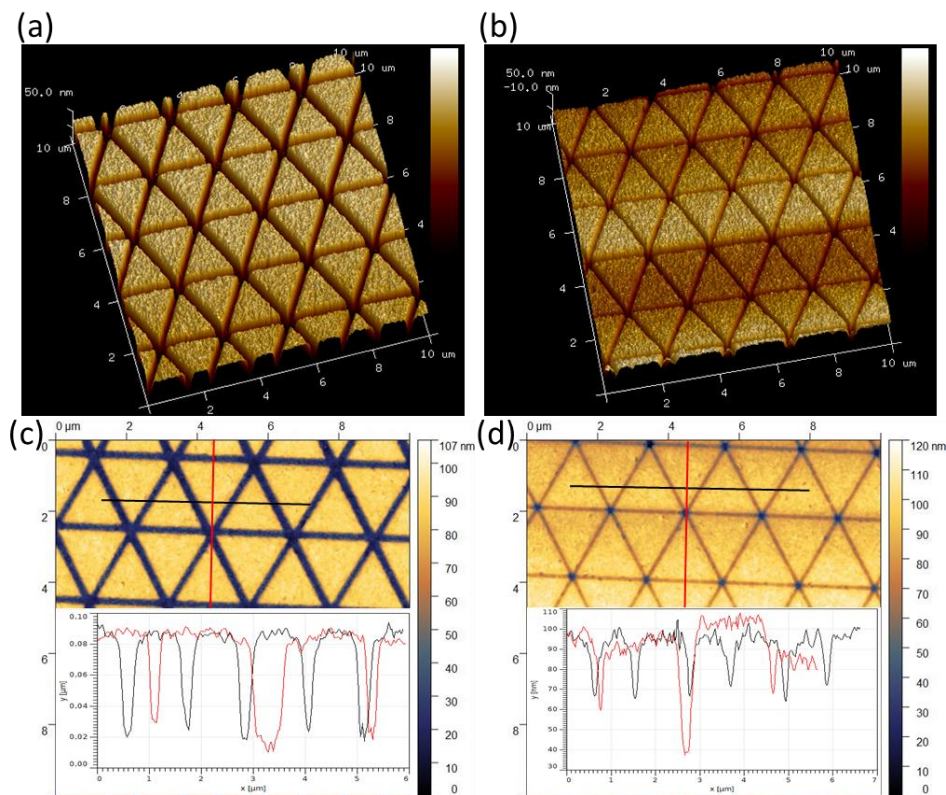


Figure 3. 15. AFM images at the end of the process for $L = 2.0\ \mu\text{m}$ and g equal to (a, c) 0.1 and (b, d) $0.02\ \mu\text{m}$. Ar etching time was set to 180 s. Color scale intensity is varied between 50 and -70 in (a) and (b) for better visualization. The surface of the Al triangles is normalized likewise in both cases, and the lines definition in (a) is stating a very clean and directional etch. The depth in (c) is standardized around $55 \pm 2\ \text{nm}$, but in (d) a deeper etch occurs at the triply etched sites, and the lines are not perfectly open.

Furthermore, to evaluate the etching depth in **Figure 3.15c** and **3.15d**, two cross-sections are sketched in the insets curves along (in red) and across (in black) the tip-to-tip facing triangles. In

Figure 3.15c, a global depth value is found around 55 ± 2 nm through the in-between lines, and a slightly deeper value is found at the intersection point. However, for a smaller opening (**Figure 3.15d**), the expected depth is only found at the intersection point. In principle, at the intersection of the exposed line, the width of the opening is wider than that of the lines in between the triangles, and this is due to the triply exposed resist at these sites. Except for these sites, the depth was found around 27 ± 2 nm. Hence, it would have been better to separate the large and the small opening on two different samples and to etch the small openings for a longer time.

In conclusion, these results underline the opening effect on the etching rate as previously stated. Noteworthy, as revealed in **Figure 3.15a and 3.15c**, the Al components were etched and correctly evacuated from the surface, so no Al re-deposition is perceived at the perimeter of the triangle (as obtained in **Figure 3.12b** for a similar etching time) and this is thanks to the high stability of the plasma environment that was created inside the chamber.

The second hypothesis regarding the oxide grain's reaction against the Ar flux is also emphasized in **Figure 3.16**. SEM images are collected using a Hitachi S4800 at the IEM (European Institute of Membrane) at a voltage of 10 kV, with a working distance of 12.6 mm, and a magnification of x 40.0k (**Figure 3.16a**) and x 20.0k (**Figure 3.16b and 3.16c**).

In detail, as revealed in the SEM images (**Figure 3.16a**), a damaged etch occurs due to the oxide grain's resistance against the Ar bombardment by redirecting the Ar ions towards the side walls of the Al triangles. Moreover, SEM images are collected for two similar patterns that were exposed using two different modes, namely, the linear (in **Figure 3.16b**) and concentric modes (in **Figure 3.16c**) for L and g theoretically equal $0.8 \mu\text{m}$ and $0.1 \mu\text{m}$, respectively. The patterns of **Figure 3.16a** are linearly exposed. A clear imperfection is detected for the triangle sizes and their final distribution for the part that is exposed with a concentric mode. This might be related to the strong proximity effects at the triply overdosed resist at lines intersection zones, generating larger open spots (locally larger lines width) and thus smaller triangles, keeping in mind that the triangle height (and side length) is defined and directly affected by the periodicity and width of the line.

This result will be optically evaluated in **Chapter 4**, to underline the influence of such an imperfection on the HC reflectance measurements.

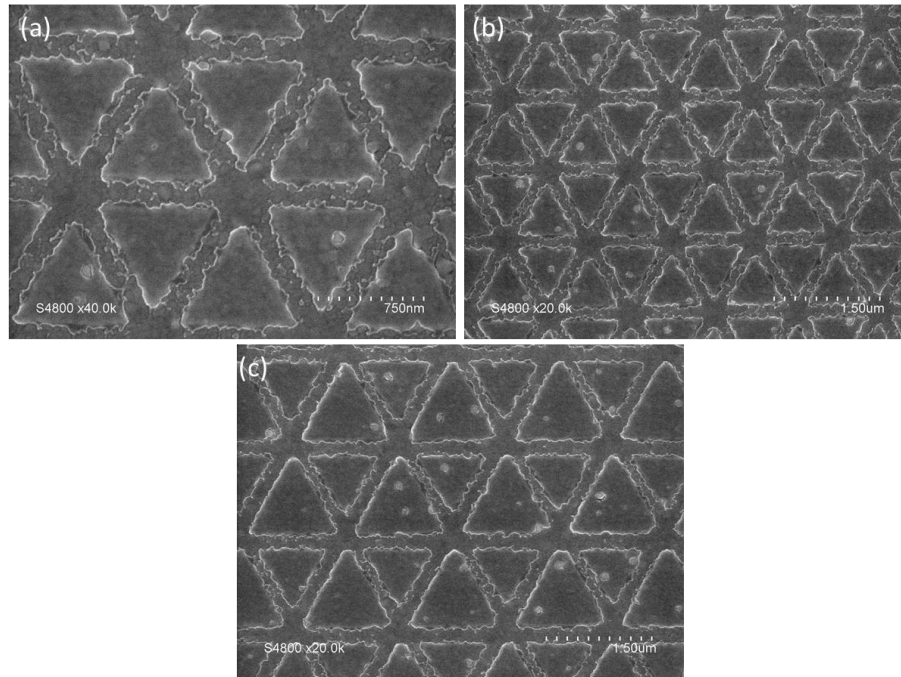


Figure 3. 16. SEM images of the patterns exposed (a, b) in a linear mode and (c) in a concentric mode. In both (a, b), $L = 1.0 \mu\text{m}$ and $g = 0.1 \mu\text{m}$, but the magnification is changed from x 40.0k (a) to x 20.0k (b). Besides the corroded triangles finishing, the distribution of their size seems extremely homogenous in comparison to (c), where $L = 0.8 \mu\text{m}$ and $g = 0.1 \mu\text{m}$.

In front of such damaged triangles, the highlight question is: will these structures be able to resonate under a suitable illumination, *e.g.* to be activated for spectroscopic analysis?

To be discussed in **Chapter 4**.

3.4. Conclusion

In this chapter, we have defined well-controlled procedures for creating matrices of Al BT and HC NA with different side lengths, L , and gaps, g , using electron-beam lithography combined with lift-off or physical etching techniques. The resulting geometric parameters of the NA, *i.e.*, L and g were studied in details. For the BT NA, L was overall varied from 0.08 μm to 2.0 μm , to build a wide-band transducer active from the visible to the MIR as previously simulated. For the HC, L was mainly varied from 1.0 μm to 2.0 μm for an IR spectral coverage. For both NA, the gap was tailored from 100 nm down to 20 nm.

To achieve such a precise fabrication, a collaboration was held between the CTM and the LAAS, where the ultimate lithography of both structures was mainly achieved using a high-tech EBL machine. Schottky-emitter FEG was set to 20 pA using a 7.5 μm aperture for BT exposure and to 40 pA using a 10 μm aperture for HC (lines) exposure.

The fabrication key process requires a neat control of the MIM multi-stacked layer deposition as presented. Moreover, it is important to define and master the relatively critical EBL writing over a large area with different geometry and doses. For the BT, the prisms are equilateral after the lift-off, manifesting finely sharp and well-defined edges which lengths were found to be in high conformity with the expected parameters. For $L < 0.3 \mu\text{m}$, the BT were defined, although their features were comparable to the surface oxide grains diameter.

For HC, a physical etching with an EBL patterned mask was implemented to transfer the lithographed the NAs into the 50 nm thick Al layer, through narrow openings and using a positive tone resist covering the triangles. Subsequently, the anticipated etched depth was achieved, though, the hexagonally placed triangles were corrosively etched as a consequence of the presence of the aluminum oxide grains that massively redirected the Ar attack towards the sidewalls of the Al triangles.

The NAs are successfully fabricated within the surface of the MIM structure, their plasmonic behavior will be presented in the next chapter.

Chapter 4: Optical characterization of a barcode-like optical transducer

When the experiment matches the theory.

In the previous chapters, the optical properties of the plasmonic nanoresonators were modeled through FDTD simulations. Then, the technological process flows for the fabrication and the integration of the BT and the HC nanostructures in a MIM configuration were presented in details. The following step is to optically characterize both NA and to compare the results with the numerical ones. In this chapter, the optical properties of the structures simulated in **Chapter 2** and fabricated in **Chapter 3** are addressed in their corresponding range of resonance, namely the visible and the IR range. The influence of the light polarization as well as the geometric parameters, *e.g.* L and g , will be evaluated for the BT and the HC. The NA geometry affects the plasmonic properties systematically. Fundamentally, for each side length and gap (L and g), a unique LSPR peak is assigned for each NA. The chapter begins with an overview of both experimental setups implemented for the measurements in the visible and the IR ranges, then the obtained spectral results will be presented for both of the plasmonic resonator structures.

Contents

Chapter 4: Optical characterization of a barcode-like optical transducer ...	113
4.1. The experimental setups	115
4.2. BT Optical Transducer properties.....	117
4.2.1. BT covering the visible and the NIR ranges.....	117
4.2.2. BT covering the IR.....	119
4.3. HC Optical Transducer properties	125
4.3.1. Side length (L) effect	125
4.3.2. Gap (g) effect.....	127
4.3.3. Polarization effect	128
4.3.4. Comparison of both EBL exposure modes	129
4.4. Conclusion	131

4.1. The experimental setups

The optical response of the fabricated resonators is mainly characterized in the IR through a Hyperion 3000 microscope coupled to a Fourier Transform InfraRed (FTIR) spectrometer (Bruker Vertex 70), illustrated in **Figure 4.1a**.

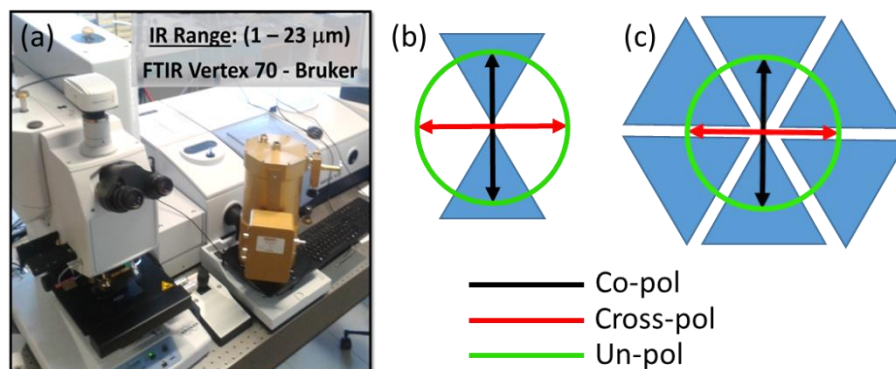


Figure 4. 1. (a) Hyperion 3000 microscope coupled to a Fourier Transform InfraRed (FTIR) spectrometer (Bruker Vertex 70) with mounted 15 x objective. For micro-FTIR measurements, a wide band IR (1-23 μm) mercury-cadmium-telluride (MCT) detector is implemented. Imaging of sample surfaces is possible due to a focal plane array (FPA) detector. Light illumination is illustrated in (b) for BT and (c) for HC structures. A co-polarized (black arrow), cross-polarized (red arrow) light can be implemented: the former defines an E-field direction parallel to the BT main axis (tip-to-tip triangles direction) and the latter expresses an E-field direction perpendicular to it. An un-polarized (green circle) light is achieved by removing the polarizer completely from the optical path.

A broadband IR light source, namely Globar (silicon carbide SiC-based-MIR source) with potassium bromide (KBr) beam splitter is implemented for the measurements. The light is focused on the sample through a 36 × / 15 × Cassegrain objectives (numerical aperture N.A. = 0.5 / N.A. = 0.4) and collected onto a liquid N₂-cooled mercury cadmium telluride detector (MCT or Hg:Cd:Te) with a single element detector or with a focal plane array (FPA) of 64 × 64 pixels. The accessible spectral band is ranging between 400 to 8 500 cm⁻¹ and 800 to 3 800 cm⁻¹, respectively. The acquired spectra are normalized to the spectrum of a gold mirror serving as background. Typically, background and spectral measurements are systematically executed using single element and FPA configurations with a resolution of 4 cm⁻¹. The interferograms are averaged to obtain one background-corrected spectrum, achieving a high signal-to-noise ratio, with 1 000 and 100 scans, respectively. As illustrated in **Figure 4.1b** and **4.1c**, a co- or cross-polarized illumination is introduced (parallel or perpendicular to the BT main axis) as a 0° (or 90°) angle is read on the

polarizer goniometer. An un-polarized light is achieved as well by simply removing the polarizer from the optical path of the incident light.

For the visible range measurements, the experimental set-up is provided by the Nano-optics lab at Politecnico di Milano. It consists of a stabilized Tungsten-Halogen lamp ([Thorlabs, SLS201/M](#)) to generate the excitation. Light is linearly polarized by a Glan-Taylor calcite polarizing prism ([Thorlabs, GL10-B](#)), which has a broad wavelength range compared to absorptive polymer-matrix polarizers. The sample is mounted facing down on a xyz piezoelectric stage (Physik Instrumente, P-517.3CL) which enables fine positioning of the sample. H/V polarization on the table = x/y on the sample = parallel / perpendicular to the BT main axis (*i.e.* co-pol/ cross-pol) are obtained for a 82°/172° reading of the goniometer. Light is focused onto the sample through an air microscope objective (Nikon, CFI Plan Fluor 60XC) with N.A. = 0.85 as numerical aperture, and is collected through the same objective. The excitation and detection path are separated by a non-polarizing beam splitter cube ([Thorlabs, BS022](#)). Spectrally-resolved measurements are performed with an imaging spectrometer (Andor, Shamrock SR-303i) equipped with a 150 grooves/mm ruled diffraction grating blazed at 500 nm and a back-illuminated charge-coupled device (CCD) camera (Andor, iKon-M DU934P-BV). The exposure time was typically set to 80 ms, to use its full dynamic range without approaching saturation. 100 accumulations are typically implemented for reducing shot noise, which is especially visible on the blue side of the spectrum where the lamp is very weak.

4.2. BT Optical Transducer properties

4.2.1. BT covering the visible and the NIR ranges

Firstly, the LSPR of the BT NA with $0.2 \mu\text{m} \leq L \leq 0.3 \mu\text{m}$ are measured in the NIR range. To address the NIR range, between $2\,000$ to $10\,000 \text{ cm}^{-1}$ (1 to $5 \mu\text{m}$), the NIR source of the FTIR (illustrated in **Figure 4.1b**) is used with a calcium fluoride (CaF_2) beam splitter and a $36 \times$ IR objective. The measured spectra are presented in **Figure 4.2a and 4.2b** under a co-and cross-pol, respectively. Note, the global red-shift of the measured spectra in comparison to those simulated by FDTD is around 600 cm^{-1} for $L = 0.3 \mu\text{m}$ and around 800 cm^{-1} for $L = 0.2 \mu\text{m}$. The mismatch is more dramatic for the smallest L values because of the technological limits as presented in **Chapter 3**, where the tips of the triangles become rounded and their size becomes comparable to the surface oxide beads (check **Table 3.1**). The low quality of the deposited layers is also expressed through a decrease of the spectra amplitude of around 40%. Nevertheless, the anticipated spectral tendency is confirmed under both light polarizations: the LSPR red-shifts as soon as L increases from 0.2 to $0.3 \mu\text{m}$, or when g decreases from 100 to 20 nm . This behavior is displayed in **Figure 4.2c**. Besides, for the same L and g values, the LSPR of the BT is found almost insensitive to the light polarization, except for $L = 0.3 \mu\text{m}$ and $g = 20$, as the fabricated structures were not perfectly defined. Furthermore, back to the response of $L = 0.3 \mu\text{m}$ in **Figure 4.2a**, one can remark the appearance of a second mode at higher energy. However, the detection limit for the implemented FTIR is limiting the extension of the measurements. To overcome this restriction, additional measurements were done at the Nano-optics lab in Politecnico di Milano in the visible range for $L = 0.3 \mu\text{m}$ as presented in **Figure 4.2d**. The "FTNIR" spectra are more pronounced and are following the spectral tendency while varying g . Yet, at higher energy, the searched peak seems to shyly appear. Systematic measurements are also done in different zones where $L = 0.15 \mu\text{m}$ and $g = 20, 60$ and 100 nm . Similarly, for $L = 0.15 \mu\text{m}$ in **Figure 4.2e**, the peak red-shifts in the visible when decreasing the g as displayed in **Figure 4.2f**.

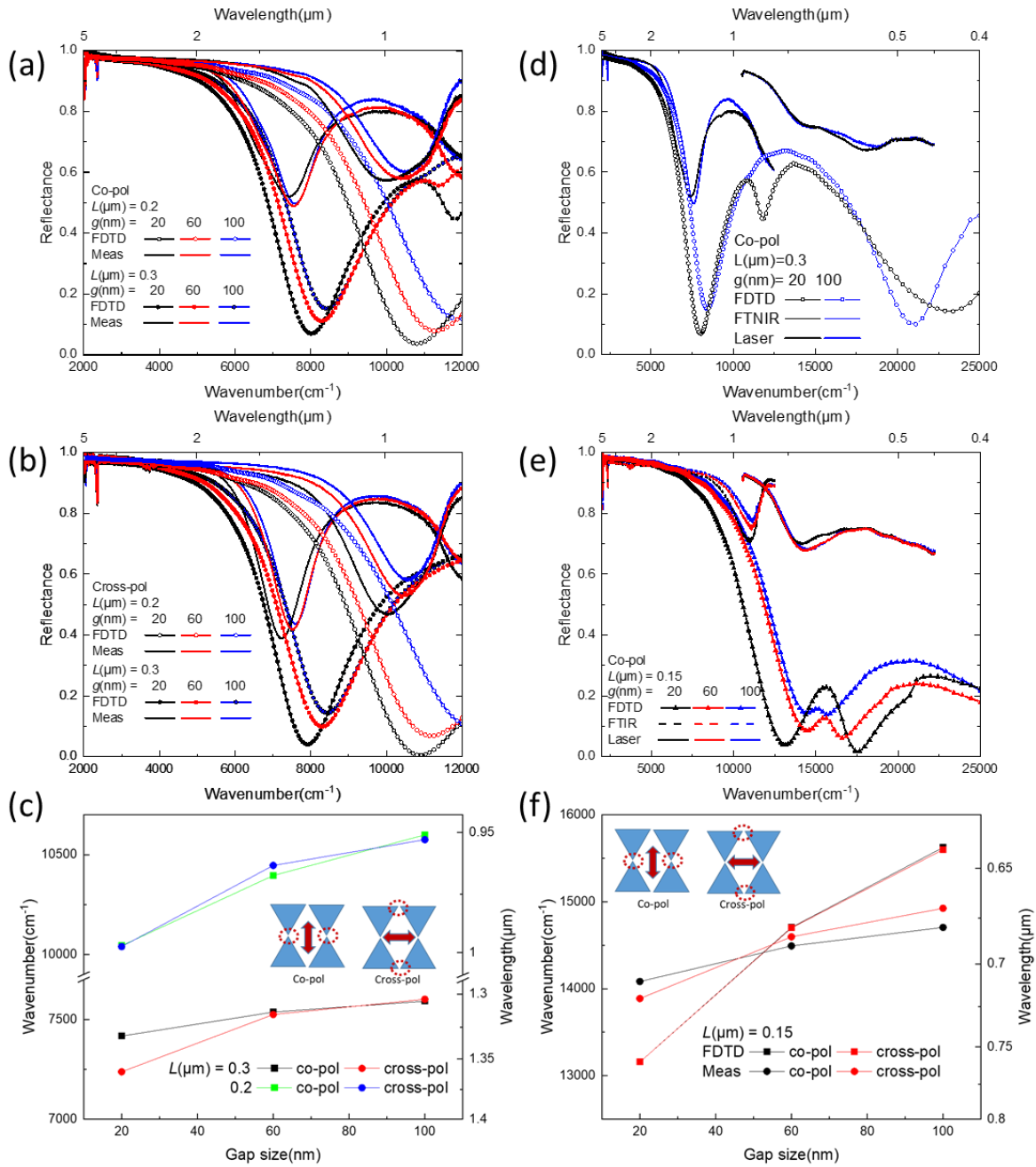


Figure 4. 2. The reflectance measurements of Al BT covering (a) the NIR with $L = 0.2$ and 0.3 μm under a co-pol and (b) under a cross-pol. The spectral tendency to red-shift is revealed in (c) for the respective L and g variations, regardless of the light polarization. The numerical and experimental results are in good agreement. The inset shows the light polarization as well as the activated sites of the occurring coupling. The measurements are extended to the visible for $L = 0.3$ μm in (d) and for $L = 0.15$ μm in (e). The reflectance spectra which are presented in the visible are also background corrected. The spectral influence of g on the LSPR for $L = 0.15$ μm is shown in (f) and further studies are continuing on these results in the visible range.

Here, it is crucial to underline the fact that it is challenging to connect both spectral information as the measurements in the NIR and the visible are achieved using two completely different approaches and setups. Plus, in both methods, the studied plasmonic features are situated at the detection limits of both systems. Nevertheless, the analyzes of these spectra are still under examination, though, they are challenging and might require careful optimizations. However, the peak energies in the visible are coherent with the FDTD simulation even if they are not as well defined as in the NIR.

4.2.2. BT covering the IR

In this part, the effect of each of the geometric parameters and the light polarization on the optical response of the BT is continued but detailed in the broad IR range.

4.2.2.1. Side length (L) effect

Figure 4.3 shows reflectance spectra in a wide spectral range from the mid-IR to the near-IR using a single optical transducer surface of BT. The LSPR wavelength is tuned over a wide IR spectral region, from 1 000 to 10 000 cm^{-1} , thanks to the size of the Al-BT in each zone of arrays. For this wide coverage in the IR, L is varied from 0.3 to 2.0 μm with a step of 0.1 μm , and g is swept from 100 nm down to 20 nm with a step of 20 nm. The distance between the antenna rows, Y , is maintained constant at 2 μm . The BTs are illuminated under co-polarized light (E-field parallel to the BT main axis), which provides an effective facing tip-to-tip coupling and supports high field enhancement into the gap as proven in **Chapter 2**.

Figure 4.3a shows the experimental reflectance spectra of each structured zone under a microscope coupled to a FTIR spectrometer using a single element MCT detector. For all BT regions, the first-order plasmonic resonance is always situated at the lowest wavenumber (*i.e.* lowest energy), and then higher orders of the resonance appear at higher wavenumbers. As L increases, the main LSPR peaks are gradually losing energy from 8 300 to 1 500 cm^{-1} (red-shifting from 1.2 to 6.5 μm). This behavior corresponds to the dipolar mode which demonstrates a

wavelength shift as L varies. This well-known tendency for metallic objects is largely described in the literature.^{73,78,110} In detail, LSPR is red-shifted by $\sim 80 \pm 30 \text{ cm}^{-1}$ when L is increased with a step of $0.1 \text{ }\mu\text{m}$. Some higher-order radiative modes are visible only for $L > 0.9 \text{ }\mu\text{m}$ with a similar tendency.

Figure 4.3b represents the numerical results calculated using FDTD simulations. Similarly, one main resonance peak is attributed to each L value. Accordingly, LSPR peaks are shifted towards a lower wavenumber as L is increased. Furthermore, the simulated peak widths decrease continuously along with the simulated spectral range as the peak shifts to lower energies, likewise for the experimental ones (**Figure 4.3a**), as detailed in **Chapter 2**, agreeing with the state-of-art.¹¹²

In addition, the Q-factor for $1.4 \text{ }\mu\text{m} < L < 2.0 \text{ }\mu\text{m}$ is considered constant at around 8, slightly higher than the value found in the simulation. Please note that the material data in the simulation are barely matching those of the fabricated NA, so the FWHM might be higher for the simulated spectra which are strictly considering the real and the imaginary part of each of the MIM materials. Still, the agreement between numerical and experimental results is almost perfect.

Despite their resemblance, the numerical results show sharp peaks identified as BT array's diffraction peaks resulting from the periodicity which is triggered along the y -axis. Their spectral position, Λ_y , has been analytically deduced for equilateral triangle's dimension as discussed in **Chapter 2**. However, these spiky diffraction peaks are latent under the FTIR detector having a wide N.A. objective in the microscope. Indeed, diffraction peaks are attenuated in FTIR measurements since the light source of the commercial FTIR is not perfectly collimated as for the simulation (perfect normal incidence), so the measured reflectance spectrum will be an integration over at least 15° of incident angles of all the spectra.

Moreover, in **Figure 4.3a** the surrounding environment concrete effects are observed since the optical measurements are acquired in an N_2 medium and not in vacuum. Indeed, absorption lines of water and CO_2 are manifested in the FTIR results. In **Figure 4.3a**, the signature of weak oscillations spanning between $1\ 090$ and $1\ 800 \text{ cm}^{-1}$, $3\ 500$ and $3\ 900 \text{ cm}^{-1}$, and above $5\ 000 \text{ cm}^{-1}$ corresponds to water lines. The ro-vibrational modes of CO_2 are centered around $2\ 350 \text{ cm}^{-1}$.

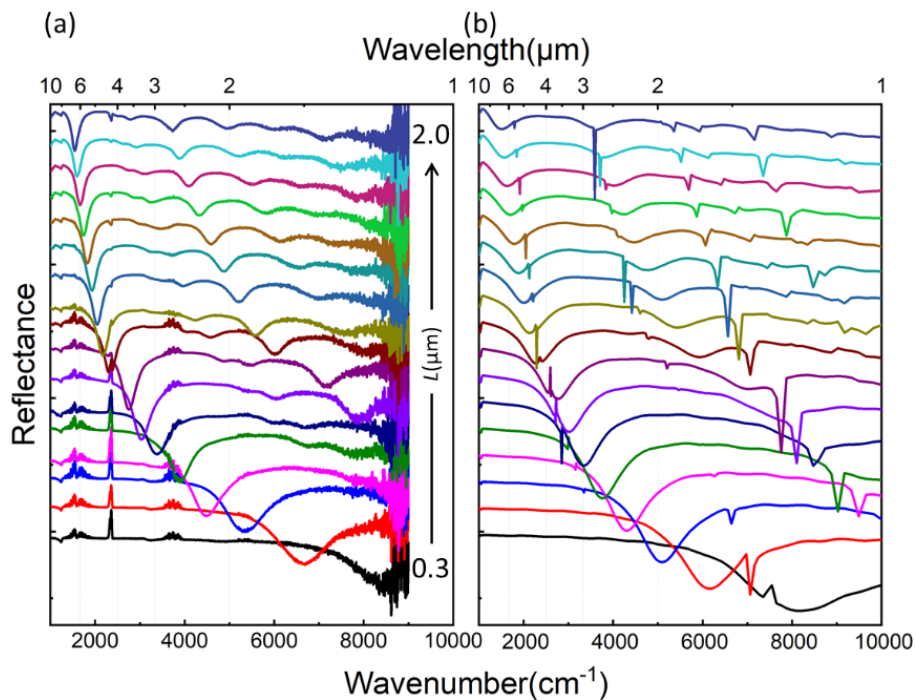


Figure 4. 3. Optical transducer plasmonic modulation over a wide range in the IR according to the side length of the BT in each array zone. (a) Experimental (FTIR) vs (b) numerical (FDTD) reflectance results for BT arrays illuminated under co-polarized light (E-field parallel to the BT main axis), where g is kept constant at 100 nm and L is varying from 0.3 to 2 μm with a step of 0.1 μm . Note the spectra are stacked along the reflectance axis for ease of viewing.

The NA are perfectly fabricated and this is translated into the minor spectral difference of their simulated and measured LSPR by $\sim 50 \pm 20 \text{ cm}^{-1}$. This is owing to the mismatch of the material definition in FDTD in comparison to the real deposited material quality.

4.2.2.2. Gap (g) effect

The combination of an FPA detector with conventional FTIR systems allows a concurrent and rapid collection of thousands of infrared spectra over large areas of a sample, which has been particularly useful in surface chemical analysis.^{123–125} **Figure 4.4** presents the high potential of the FPA to detect geometry differences at the microscale range on a nanoengineered surface with multiple BT array zones. **Figure 4.4a** is a real shot of the sample surface with two different triangle sizes, $L = 0.8 \mu\text{m}$ and $L = 0.9 \mu\text{m}$, and 5 gaps from 100 to 20 nm with a step of 20 nm, with colored pixels and indexed by the L and g values corresponding to each zone. **Figure 4.4b** represents the

reflectance spectra of only two single pixels ($2 \times 2 \mu\text{m}^2$) on each BT array zone showing the effect of L on the LSPR position and a pixel on the bare substrate. **Figure 4.4c** is the so-called pixelated surface chemical image showing a color contrast between different BT array zones. Finally, in **Figure 4.4d**, the reflectance of each colored-pixel of **Figure 4.4a** stacked together highlights the gap effect on the LSPR position for the BT arrays with a constant L .

The FPA image chemical contrast is defined by the hatched areas of the integrated zone in **Figure 4.4b**. The integration area is delimited by the spectrum curve and black lines drawn between the intensity (reflectance) values of the two pre-defined wavenumber limits (gray dashed lines). The hatched areas of **Figure 4.4b** contain the spectral intensity of each detected pixel within the selected wavenumber range. A larger area implies a stronger activation of the pixel in the integrated zone. The numerical treatment in a pre-defined integrated zone of all the pixels ($340 \times 340 \mu\text{m}^2$) is translated by a color-coded pixel's excitation for the involved hatched area as shown in **Figure 4.4c**. The contrast intensity (color scale of **Figure 4.4c**) is strongly negative whenever the hatched zone is situated below the straight black line of the integration, and it is positive in the opposite case. As the integration area in **Figure 4.4b** is encompassing a notable part of BT arrays with $L = 0.9 \mu\text{m}$ resonances, and the hatched area is largely situated below the straight black line, the boxes of those BT arrays are mainly activated in dark blue in **Figure 4.4c**, while those of $L = 0.8 \mu\text{m}$, are less activated and represented in pink (positive contrast as the hatched area is above the straight black line), and the bare substrate is mainly activated in yellow (intensity near 0) as the involved area is negligible. **Figure 4.4c** digitalizes the authentic homogeneity of the fabricated surface and reveals real defect areas, *i.e.* here a dust, on the sample surface as observed in the BT array zone corresponding to $L = 0.8 \mu\text{m}$ and $g = 80 \text{ nm}$ through pixel disarrangement (**Figure 4.4a**).

Finally, in **Figure 4.4d**, the gap effect on the LSPR position for the BT arrays with a constant L is the main feature of the stacked reflectance for each colored-pixel of **Figure 4.4a**. A similar effective energetic displacement of the LSPR positions is measured, following the black dots labeled FPA, and simulated, following the black curves labeled FDTD. Both tendencies agree with the previously-cited coupling theory.⁶⁸ Based on the FPA measurements, LSPR of the BT is red-shifted by $\sim 10 \pm 5 \text{ cm}^{-1}$ when g is decreased of 20 nm, compared to $\sim 13 \pm 8 \text{ cm}^{-1}$ based on

FDTD. Though, a slight spectral shift of $\sim 130 \pm 8 \text{ cm}^{-1}$ is separating the FTIR-resonance positions and the ones retrieved by FDTD. Actually, in FDTD the materials are usually pre-defined in perfect conditions. Even though some modifications could be applied to match the concrete quality of the deposited materials, such tangible mismatch (not only counting the material optical properties but also the surface oxidation and roughness) is displayed in a collective red-shift of the experimental results compared to the analytical ones.⁶¹

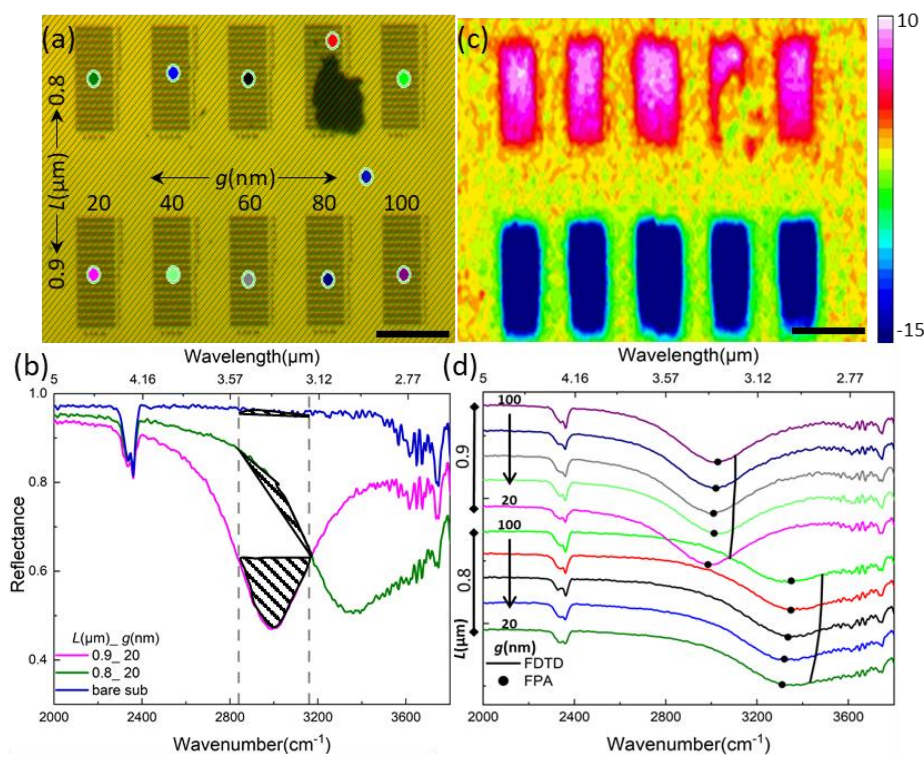


Figure 4. 4. Surface response investigation of BT arrays with $L = 0.8 \mu\text{m}$ and $0.9 \mu\text{m}$ with variable gap values under Focal Plane Array detector. (a) real image of the sample with colored pixels for each L (μm) _ g (nm) fixed couple, (b) for $g = 20 \text{ nm}$, plasmonic resonances ω_{res} of BT arrays with $L = 0.8 \mu\text{m}$ and $0.9 \mu\text{m}$ are centered in $2.95 \mu\text{m}$ and $3.32 \mu\text{m}$, respectively; after the integration of the hatched areas (c) is the activated color-coded chemical image; (d) spectra plotted in a stack for all the colored pixel of (a) showing theoretical (lines) versus experimental (dots) results. All scale bars are $50 \mu\text{m}$ long.

4.2.2.3. Polarization effect

In this section, the influence of polarization on the LSPR is addressed. The BT zone is tailored in a $100 \times 100 \mu\text{m}^2$ extend and selected with $L = 2.0 \mu\text{m}$ and $g = 100 \text{ nm}$. This zone is illuminated under a co-pol, a cross-pol, and an un-polarized light source (check **Figure 4.1b** and **4.1c**).

Figure 4.5 illustrates the insensitivity of the dipole (at $1\,550\text{ cm}^{-1}$) and the quadrupole mode (at $2\,788\text{ cm}^{-1}$), as a weak coupling occurs for such a gap. This result agrees well with the FDTD findings detailed in **Chapter 2**. Note that the LSPR spectrum under an un-polarized light is situated between the co-pol and cross-pol spectra as it is showing a mean situation of the reflectance.

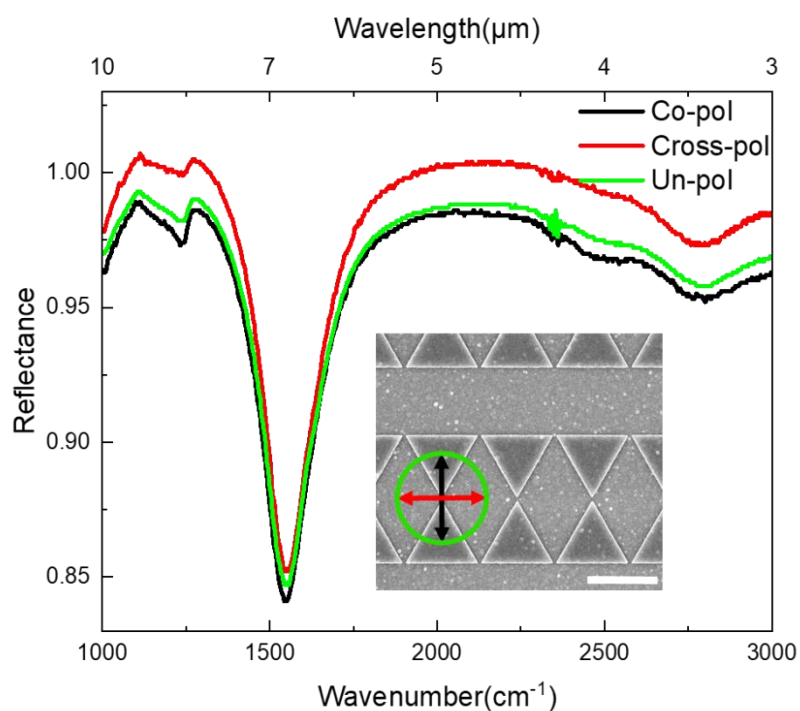


Figure 4. 5. Polarization influence on the reflectance spectra of the BT NA illuminated under a co-pol, cross-pol, and un-pol light source. The inset shows the SEM image of the fabricated BT with $L = 2.0\ \mu\text{m}$ and $g = 100\ \text{nm}$, as well as the direction of the E-field in each case. The scale bar is $2.0\ \mu\text{m}$ long.

As discussed in **Chapter 3**, the surface of the sample presented in the inset of **Figure 4.5** is rough compared to the previously fabricated samples (**Figure 3.5**). This high roughness is caused by skipping the piranha cleaning step of the Si wafer. Indeed, the roughness of the sample, covered by a thin layer of native oxide, is seen as a spectral shift of LSPR by $\sim 160 \pm 4\ \text{cm}^{-1}$ for this set of BT arrays, compared to those of the previously fabricated BT on a smoother sample as represented in the SEM of **Figure 3.5**.

4.3. HC Optical Transducer properties

4.3.1. Side length (L) effect

Figure 4.6 shows reflectance spectra of the barcode-like plasmonic transducer in a wide IR spectral range. The LSPR wavelength are tuned over a wide IR spectral region, from 1 000 to 10 000 cm^{-1} , thanks to the L sweep of each Al-HC zone. The HC geometry affects the plasmonic behavior systematically. Fundamentally, for each HC array, *i.e.* for each couple length and gap (L and g), a unique LSPR peak is given. For this wide coverage in the IR, L is varied from 1.0 to 2.0 μm with a step of 0.1 μm , and g is swept from 100 nm down to 20 nm with a step of 20 nm. Regarding the critical technological process presented in **Chapter 3**, the g of 100 nm is guaranteed and fixed in the following study in **Figure 4.6**. Herein, the HCs are illuminated under co-polarized light which provides an effective facing tip-to-tip coupling and supports high field enhancement at these sharp apexes.

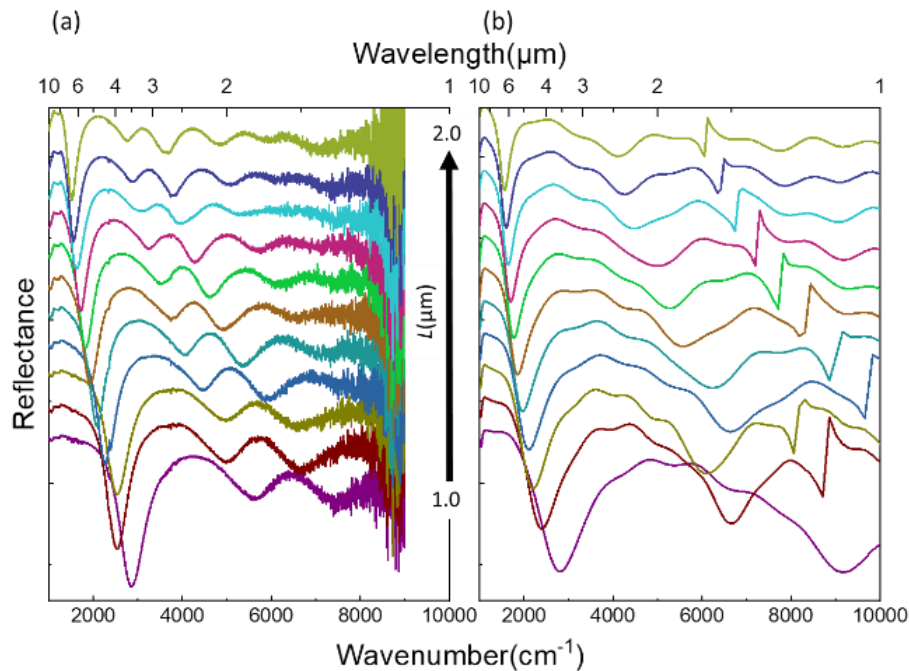


Figure 4.6. Plasmonic activation of the optical transducer over a broad spectral band in the IR according to the side length of the hexagonally placed equilateral triangles in each HC array zone. (a) Experimental (FTIR) vs (b) numerical (FDTD) reflectance results for HC arrays illuminated under co-polarized light (E-field parallel to the axis of the tip-to-tip facing triangles), where g is kept constant at 100 nm and L is varying from 1.0 to 2.0 μm with a step of 0.1 μm . Note the spectra are stacked along the reflectance axis for ease of viewing.

Using the single element mode detector of a FTIR spectrometer, the experimental reflectance spectra of each HC-structured region are analyzed and displayed in **Figure 4.6a**. For all HC regions, the first-order plasmonic resonance is always situated at the lowest wavenumber (*i.e.* lowest energy), and then higher orders of the resonance appear at higher wavenumbers. As the side lengths, L , of the hexagonally placed triangles increase, the energy of the main LSPR peaks is progressively reduced from 2 800 to 1 500 cm^{-1} (red-shifting from 3.57 to 6.6 μm). This behavior agrees with the dipolar mode which demonstrates an energy modification as the antenna's size varies as it is well-known for metallic objects.^{73,78,110} In particular, While changing the L with a step of 0.1 μm , the LSPR is red-shifted by $\sim 100 \pm 50 \text{ cm}^{-1}$ for HC. Some higher-order radiative modes are noticeable with a similar shift tendency. Though, a slight spectral shift of $\sim 60 \pm 20 \text{ cm}^{-1}$ is separating the FTIR-resonance positions and the ones retrieved by FDTD. This shift is mainly due to the deposited material quality.

The numerical results calculated using FDTD simulations are as well represented in **Figure 4.6b**. Likewise, one main resonance peak is attributed to each L value. Accordingly, LSPR peaks are shifted towards a lower wavenumber as L is increased. Furthermore, as stated in the literature,¹¹² the widths of the simulated and the experimental peaks decrease continuously along with the simulated spectral range as the LSPR shifts to lower energies as discussed in **Chapter 2**. The agreement between numerical and experimental results is almost perfect.

Despite their similitude, the numerical results (**Figure 4.6b**) show sharply discontinuous peaks at the highest energy part of the spectrum for $L \geq 1.1 \mu\text{m}$. These features are recognized as the triangle's diffraction peaks resulting from their periodic arrangement which is triggered herein along the y -axis. Their spectral position, λ_y , has been analytically deduced for equilateral triangles as discussed in **Chapter 2**. However, these spiky diffraction peaks are suppressed under the FTIR detector having a wide N.A. objective in the microscope.

Moreover, in **Figure 4.6a** the tangible belongings of the nearby environment, *e.g.* absorption lines of water and CO_2 , are witnessed since the optical measurements are acquired in an N_2 medium and not in vacuum. The signature of weak oscillations spanning between 1 090 and 1 800 cm^{-1} , 3 500 and 3 900 cm^{-1} , and above 5 000 cm^{-1} corresponds to water lines. The ro-vibrational modes

of CO₂ are determined around 2 350 cm⁻¹, and barely envisaged unless it is perfectly intersecting with the resonance of $L = 1.3 \mu\text{m}$ situated at 2 283 cm⁻¹.

4.3.2. Gap (g) effect

Following the critical technological process presented in **Chapter 3**, only the gaps of 100 and 80 nm were well-defined due to the limitation of the dry etching step and its high dependency on the slit dimension through which the etch occurs. In fact, for smaller gap values, the LSPR spectra lose their features ($g = 60$ nm) and resemble more an Al mirror with a flat reflectance spectrum, as for a $g = 40$ and 20 nm. These results are plotted for $L = 2.0 \mu\text{m}$, and the HC are illuminated under a co-pol (**Figure 4.7a**) and a cross-pol (**Figure 4.7b**). Nonetheless, the gap effect is detected while g is reduced from 100 to 80 nm: accordingly, the LSPR is red-shifted by $\sim 60 \pm 10 \text{ cm}^{-1}$, stating a stronger coupling arising for a smaller gap.

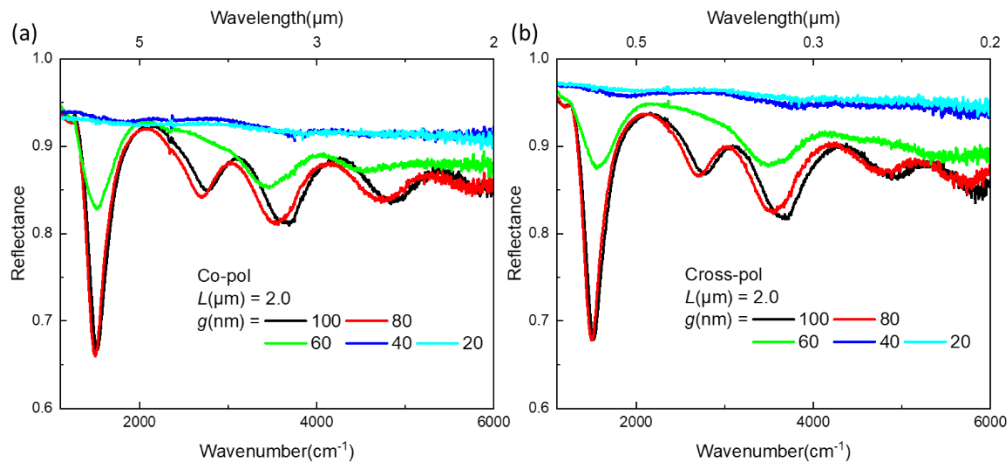


Figure 4. 7. Gap influence on the HC optical measurements under both light polarizations, *i.e.* co-pol (a) and cross-pol (b). L equals 2.0 μm and g is varied from 100 nm down to 20 nm. The gap effect is clearly when g decreases from 100 nm to 80 nm, and a red-shift of $60 \pm 10 \text{ cm}^{-1}$ is retrieved. For $g = 60$ nm, the HC structure is not perfectly defined and its spectrum loses gradually its features. For g smaller than 60 nm, the HC structures act like a mirror as the in-between lines are not successfully etched.

4.3.3. Polarization effect

In this section, the influence of polarization on the LSPR is addressed. The HC zone is tailored in a $100 \times 100 \mu\text{m}^2$ extend and selected with $L = 2.0 \mu\text{m}$ and $g = 100 \text{ nm}$. This zone is illuminated under a co-pol, a cross-pol, and an un-polarized light source (check **Figure 4.1b** and **4.1c**). **Figure 4.8** illustrates the insensibility of the dipole (at 1535 cm^{-1}) and the quadrupole mode (at 2755 cm^{-1}). Indeed, inspired by the rotation invariance occurring between the direct and reciprocal hexagonal close-packed lattices, the HC configuration allows obvious 360° -symmetry conservation so that the incident light polarization will not affect their corresponding reflectance while varying the light polarization direction. This result agrees well with the FDTD findings detailed in **Chapter 2**. Note that the LSPR spectrum under an un-pol light slightly exceeds the spectra under a co-pol and a cross-pol. This is due to the fabrication imperfection shown in the inset of **Figure 4.8**.

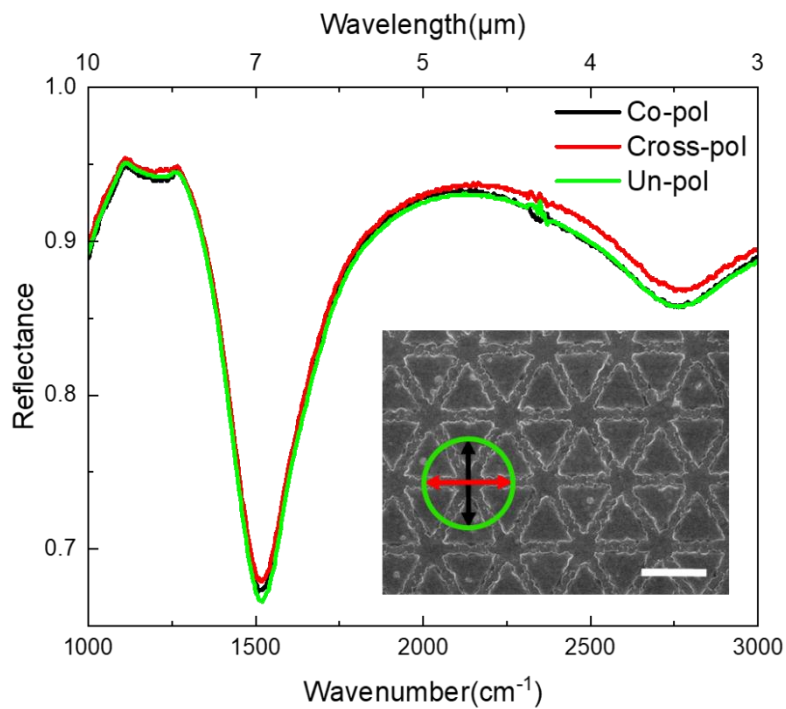


Figure 4. 8. Polarization influence on the reflectance of the HC NA illuminated under a co-pol, cross-pol, and un-pol light source. The inset shows the SEM image of the fabricated BT with $L = 2.0 \mu\text{m}$ and $g = 100 \text{ nm}$, as well as the direction of the E-field in each case. The scale bar is $2.0 \mu\text{m}$ long.

Here, it is crucial to highlight the advantage of the NA organization using HC in comparison to the BT. In **Figure 4.9**, for the same L and g values, for a HC compact arrangement of the triangles, one can remark that the reflection amplitude of the LSPR is improved by 20% compared to BT simple tip-to-tip triangle arrays. Moreover, the compact arrangement is translated into a slight red-shift as the interaction between the adjacent triangles is becoming more effective, and thus, arising at lower energy. The response of the HC has shown a slight red-shift ($\sim 20 \pm 4 \text{ cm}^{-1}$) compared to the BT resonance for the same L and g values.

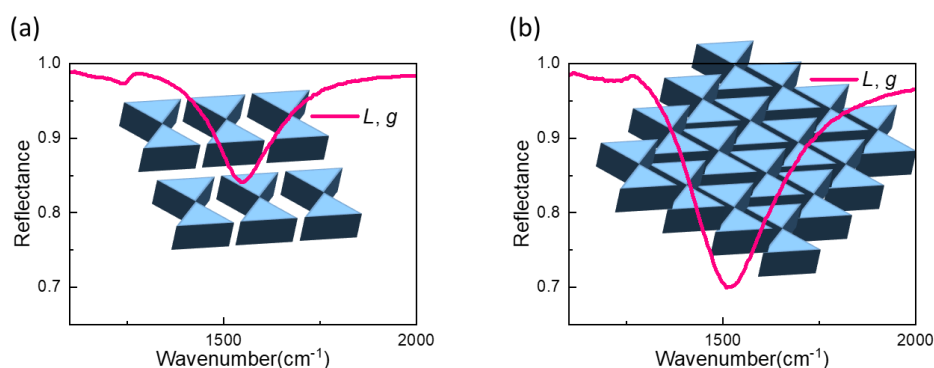


Figure 4.9. The arrangement influence on the reflectance of (a) the BT and (b) the HC NA (insets), illuminated under a co-pol light source. In both cases, L and g are respectively fixed at $2.0\mu\text{m}$ and 100 nm . For a compact arrangement, the LSPR is more pronounced in terms of amplitude and it is slightly red-shifted compared to the one of the BT, as more resonators are interacting.

4.3.4. Comparison of both EBL exposure modes

As suggested in **Chapter 3**, two different exposure modes are tested while scanning the lines that define the HC structures. Moreover, SEM images are collected for some sampling patterns that were exposed using both modes, namely, the concentric (in **Figure 4.10a**) and the linear (in **Figure 4.10b**) modes. As a clear imperfection is detected for the triangle sizes and their final distribution for the lines that are exposed with a concentric mode. Such imperfection is mainly due to the proximity effects during the exposure, especially at the intersection of the lines. The resist in this zone is overdosed and this influences the triangle's final definition. Here, we want to prove that this fabrication imperfection could be optically detected under the FTIR. For this purpose, the same reflectance measurements are acquired under a co-pol (**Figure 4.10c**) and then

a cross-pol (**Figure 4.10d**) for patterns with L and g theoretically equal to $2.0\ \mu\text{m}$ and $100\ \text{nm}$. The spectra of the HC defined by a concentric-line exposure presents a wider LSPR peak ($\Delta\text{FWHM} \sim 20\ \text{cm}^{-1}$) and a slightly attenuated modes at the higher energy side in comparison to the spectra of the HC defined by a linear-line exposure. Moreover, and under both polarizations, the amplitude of the LSPR peaks is reduced by 10% for a concentric exposure. Nevertheless, despite the fabrication imperfection, under both polarizations, the reflectance spectra perfectly overlap for both exposure cases (**Figure 4.10d**). This means that the symmetry invariance is saved. In sum, the fabrication imperfection can be seen through the broadening and the reduction of the LSPR peak for a fixed polarization. The LSPR insensitivity to the light polarization persists even though the HC structures are defective.

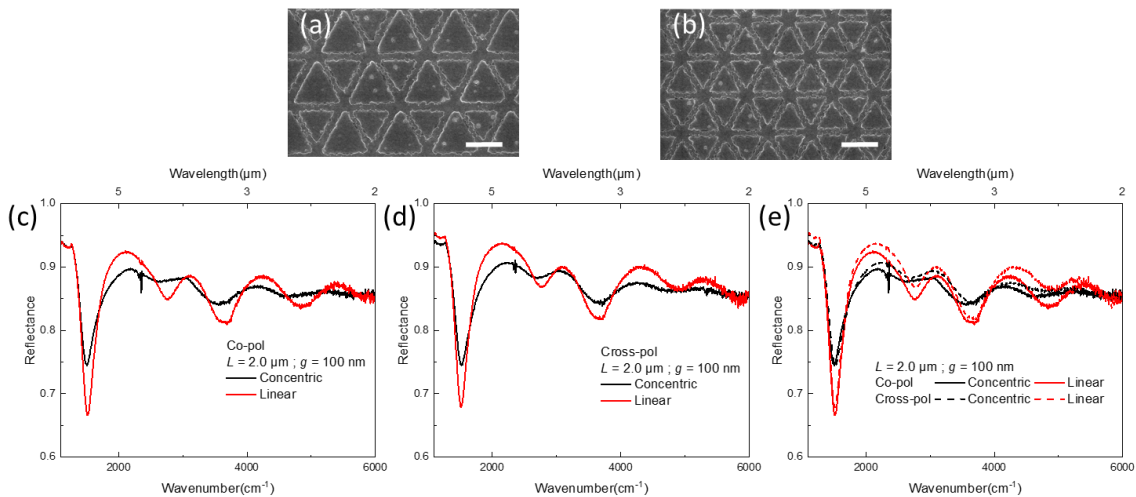


Figure 4.10. Comparison between the optical measurements of HC that are defined either by a concentric mode (a) or by a linear mode (b). Note that SEM images are of a sampling zone, showing the final fabrication results. Theoretically, the g is fixed to $100\ \text{nm}$ while L equals $1.0\ \mu\text{m}$ in (a) and $0.8\ \mu\text{m}$ in (b). The scale bars are $1.0\ \mu\text{m}$ long. The FTIR measurements in (c-e) are acquired for $L = 2.0\ \mu\text{m}$ and $g = 100\ \text{nm}$, under both polarizations to evaluate the fabrication imperfection results in (c, d) and the invariance of the HC to the polarization in (e).

4.4. Conclusion

In this chapter, the optical characteristics of BT and HC are evaluated while varying their triangles side lengths, L , and gap values, g . In line with this, visible to NIR bands are accessed if $L \leq 0.2 \mu\text{m}$; and a wide IR spectral range is activated using BT structures only by varying the L from 0.3 to 2.0 μm and HC while sweeping L from 1.0 to 2.0 μm with a step of 0.1 μm .

- For each L value, one main LSPR is assigned. It red-shifts as soon as L is increased. The LSPR shift values and tendency are agreeing well with the FDTD results. Though, a slight spectral shift is separating the FTIR-resonance positions and the ones retrieved by FDTD by $\sim 50 \pm 20 \text{ cm}^{-1}$ for BT and $\sim 60 \pm 20 \text{ cm}^{-1}$ for HC.
- The spacing g offers a new degree of freedom to red-shift the LSPR by reducing the g value. The shift values for both NA while varying each parameter are in good agreement with those found using FDTD (**Chapter 2**).
- The LSPR of both NA, with a g around 100 nm, are found insensitive to light polarization. This invariance is owing to the weak coupling for BT and certain symmetry conservation for HC.
- The fabrication imperfection of HC is evaluated through simple FTIR measurements. It is seen as a broadening and reduction of the LSPR peak for a fixed polarization. The LSPR insensitivity to the light polarization persists despite of the HC fabrication defects.

In conclusion, the spectral findings of both BT and HC NA are already reached in simulation as presented in **Chapter 2** and are successfully proved experimentally in the actual **Chapter 4** through optical characterizations. The main discrepancies between experiments and simulations are the materials optical quality and the final shape of the fabricated NA. Both are definitely influencing the energy and the FWHM of the resulting LSPR. Although a minor spectral shift is noticed between the FDTD and the FTIR results for both NA, the tendencies of the corresponding LSPR in function of L and g are in fair agreement. This highlights the robustness and accuracy of

Chapter 4: Optical characterization of a barcode-like optical transducer

the fabrication processing. Hence, the finely fabricated NA, presented in **Chapter 3**, demonstrates a promising behavior of a multi-resonant plasmonic transducer, active in a wide spectral range and ready to serve as a sensor transducer to detect the species of interest by simply selecting the adequate L and g to tune the LSPR and the molecular vibrations frequencies. The detection details and results via BT and HC NA will be provided and discussed in **Chapter 5**.

Chapter 5: SEIRA sensing investigation using Aluminum metasurfaces

It is always unachievable until proven otherwise.

This chapter focuses on the demonstration of the SPR and the SEIRA sensing using the Al-based MIM plasmonic structures deposited on a Si substrate. Periodic arrangements of both types of nanoantennas (NA), Bowties (BT), and Honeycomb (HC) were studied formerly through the actual manuscript. Herein, they are assessed in sensing experiments using a trial molecule, an aromatic compound, vanillin. The hybrid coupling between the vibrational lines and various plasmonic resonances covering a wide IR range is evaluated as a Fano-like modulation that indicates the strength of the occurring coupling. In the following, experimental and analytical results concerning the sensing performance are detailed. Plus, a promising perspective regarding the CO₂ vibration enhancement is provided. These results are extremely encouraging for a simple sensing application as it is only required to tune the plasmonic resonances of the transducer's antennas to the molecular vibrations of interest.

Contents

Chapter 5: SEIRA sensing investigation using Aluminum metasurfaces	133
5.1. Oxide stability	134
5.2. SEIRA Sensing proof	135
5.2.1. Al-Bowties for SEIRA demonstration.....	136
5.2.2. Al-Honeycombs for SEIRA demonstration	150
5.2.3. Gas-SEIRA sensing	157
5.3. Conclusion.....	162

5.1. Oxide stability

Before launching any spectroscopic investigation, it is crucial to identify the influence of the oxide on the Al-BT resonances. These samples were fabricated one year and a half before starting the SEIRA measurements and set aside in standard laboratory boxes outside of the controlled environment of the cleanroom and without any other specific protection layer. In fabrication technology, the instant Al oxidation is a limiting aspect for optoelectronic devices and ultimately affects the transducer surface. However, such a native oxide is stable upon its creation but the threat of a continuously growing oxide that will ruin the plasmonic resonance of BT is not yet discarded.^{64,126} This hypothesis is rejected by comparing the reflectance spectra for $L = 2.0$ to $1.4 \mu\text{m}$ with a step of $0.2 \mu\text{m}$, acquired in 2022 (**Figure 5.1b**) to those dating one year back (in 2021, **Figure 5.1a**). The stability of the Al-engineered surfaces is conclusive.

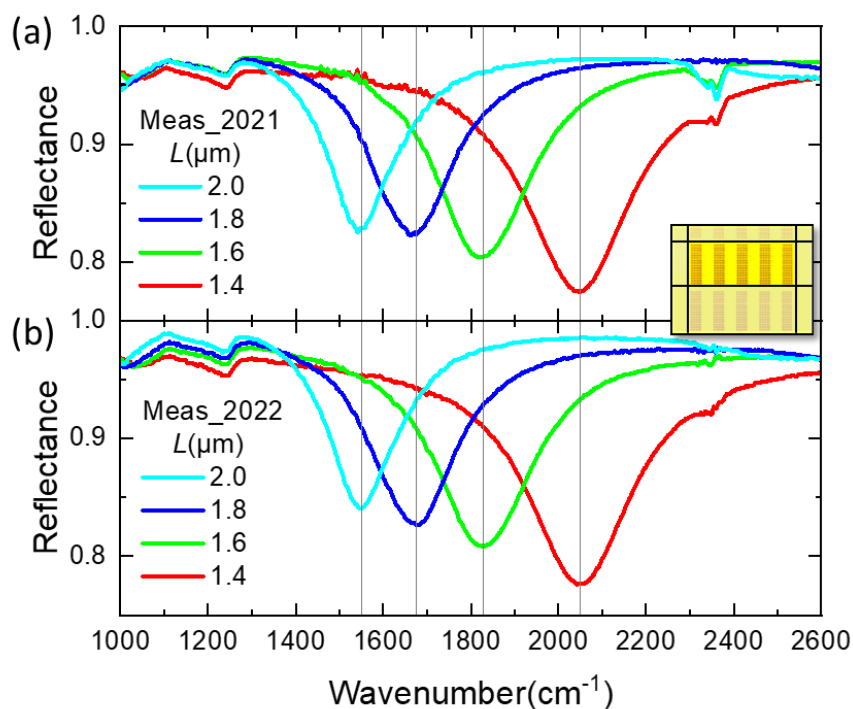


Figure 5. 1. Oxide impact on the LSPR of Al-BT. L is varied from 2.0 to $1.4 \mu\text{m}$ with a step of $0.2 \mu\text{m}$. Reflectance measurements are done in march of 2021 (a) and 2022 (b) under the same experimental conditions. The BT corresponding resonances appear at the same energies and peak amplitudes and the same FWHM values regardless of the time delay, highlighting the oxide stability upon its creation. The inset shows an FPA image of the 5 zones of Al-BT selected by a manual knife-edge covering $230 \mu\text{m} \times 90 \mu\text{m}$.

For a proof of principle, reflectance measurements were collected using the micro- FTIR setup with a sampling zone of $230 \times 90 \mu\text{m}^2$ (inset of **Figure 5.1**), a resolution of 4 cm^{-1} , and 1 000 scans, under a co-polarized MIR illumination (along the BT main axis). The measured signals are normalized to the signal obtained from a gold mirror serving as a reference. Similarly, as illustrated in **Figure 5.1**, for all the tested BT side lengths supporting tunable LSPR, their corresponding resonances remain at the same energetic position with the same amplitude and present a similar full width at half maximum value (FWHM) despite the time delay between both measurement sequences. Such a result confirms the oxide stability and it supports the introduction of Al-based resonators to a prospective world of mass fabrication and integration of low-cost and reliable SEIRA sensors thanks to their CMOS compatibility and their stability. Precisely, the omnipresent 2–4 nm thick oxide layer, spontaneously formed upon its exposure to the atmosphere, passivates the antenna structure against further oxidation and enables a broader range of covalent binding schemes for molecules to the antenna than Au or Ag.⁶⁵ Based on FDTD simulations, a 2 nm thick oxide layer could engender a spectral red-shift of the proper plasmonic resonance by 20 cm^{-1} .

5.2. SEIRA Sensing proof

In this part, the SEIRA demonstration is verified using BT metasurfaces, while in the next part, HC metasurfaces will be the kit tool to prove the SEIRA phenomena. The tailored surfaces might differ, yet the selected side lengths, L , of the involved antennas remain the same in both scenarios.

To demonstrate the SEIRA behavior using a barcode-like plasmonic transducer, vanillin (4- hydroxy-3-methoxybenzaldehyde) is selected as a test molecule, grown naturally in vanilla beans, and chemically synthesized for mass production.¹²⁷ It is one of seven phenolic compounds considered for their defensive properties against "hydrogen peroxide-induced DNA damage" in human peripheral blood lymphocytes.¹²⁸ Besides, Vanilla is one the most universal and popular flavors, thanks to its floral-fruity fragrance combined with a deep aromatic body, it can be largely convenient for food, beverages, pharmaceuticals, and perfumery uses.¹²⁹ The most

noteworthy aspect is that vanillin is recently engaged as a perfect inhibitor towards the corrosion of Al in hydrochloric acid solutions that are traditionally used for Al chemical etching.¹³⁰ Thus, Al corrosion resistance will be fortified by the physisorbed film of vanillin at the Al nanoresonators surface.

To evaluate the SEIRA spectroscopic features, vanillin is dissolved in ethanol with a concentration of 2 mg/ml. Then, a droplet of 1 μ l is deposited on the plasmonic transducer. Around 10 nmol are hence released on the whole sample surface, the molecular mass of vanillin being 152.1 g/mol. The adsorption of vanillin on Al follows a Langmuir isotherm model: the adsorbed molecules do not interact and the energy of adsorption is equivalent for all sites, hence, each of which can hold at most one molecule. In this sense, a mono-layer coverage could be assumed once the vanillin is placed on the Al antenna's surface.¹³⁰ Thus, the distribution of vanillin molecules is supposed to be homogenous on the transducer surface of approximately 1 cm². Five IR absorption lines of vanillin interfere simultaneously within the selected plasmonic resonances of the optical transducer. The overlap between the plasmonic resonances and the vibrational frequencies produces different vibrational signal enhancements coherent to the ratio of both frequencies.

5.2.1. Al-Bowties for SEIRA demonstration

The characterized surface for the BT case is illustrated in the inset of **Figure 5.1**. Accordingly, 0.4 nanograms of vanillin are located within the zone of 230 \times 90 μ m², where 5 zones of Al-BT arrays are designed in areas of 25 \times 90 μ m² each, separated by 25 μ m, with the same length, L , and five different gaps, g (see the red square in **Figures 5.2a and 5.2d** as an example). To evaluate the immediate surface sensing, Focal Plane Array mode (FPA) would be a challenging but compelling method to attempt, more concretely thanks to its chemical image treatment under a 15 \times IR objective, 100 scans with 4 cm⁻¹ of resolution are selected to collect the most reliable spectra as the vanillin/ethanol droplets are time-sensitive.

5.2.1.1. FPA for SEIRA demonstration

The first SEIRA investigation is done using the FPA and summarized in **Figure 5.2**. **Figure 5.2a and 5.2d** are the real images of the sample zone consisting of BT with L equals to 2.0, 1.9, and 1.8 μm , before and after the deposition of vanillin/ethanol droplets. The assumed homogenous distribution of vanillin molecules is experimentally demonstrated in **Figure 5.2d** (small roundish spots). Each colored dot is selected for a gap value. A reflectance collection for three gap values is respectively plotted in **Figure 5.2b and 5.2e**. For further investigations, purple and magenta dots are selected as references to the bare substrate and the spot of vanillin molecules, respectively. For all the plasmonic areas, the spectral resonances red-shift $\Delta\omega_{res} \sim 40 \text{ cm}^{-1}$ in presence of vanillin/ethanol solution, as found by comparing **Figure 5.2b and 5.2e**. In other words, the SPR sensing is noticed directly by the FPA in each pixel with a sensitivity of $\sim 185 \text{ nm/RIU}$ ($\sim 10^2$ as reported by Mayer *et al* for metallic nanoparticles).³¹ Moreover, in **Figure 5.2e**, the absorption signatures appearing at 1 509, 1 587, and 1 665 cm^{-1} , correspond to certain vibration frequencies of vanillin (gray lines). Indeed, the modifications in the reflectance spectra, *i.e.*, the Fano-like asymmetric features of the SEIRA sensing, correspond to the perfect spectral matching between Al-BT resonances and several vibration frequencies. Therefore, FPA offers a unique advantage to assess qualitatively the SEIRA activation. In **Figure 5.2b and 5.2e**, an integration zone (delimited within dashed blue lines) is framing the absorption signature of vanillin situated at 1 509 cm^{-1} that matches the plasmonic resonance of $L = 2.0 \mu\text{m}$. Consequently, in **Figure 5.2c**, the boxes of BT arrays with $L = 2.0 \mu\text{m}$ are mainly activated in dark blue, while those of $L = 1.9$ and $1.8 \mu\text{m}$, are less activated and represented in cyan blue. In **Figure 5.2f**, the SEIRA signature integration is promisingly pronounced in the BT arrays zones, where small red spot areas show a high contrast in comparison to the large green ones. This color activation underlines the aptitude of the tailored tip-to-tip plasmonic BT to indicate the location of the arising SEIRA.

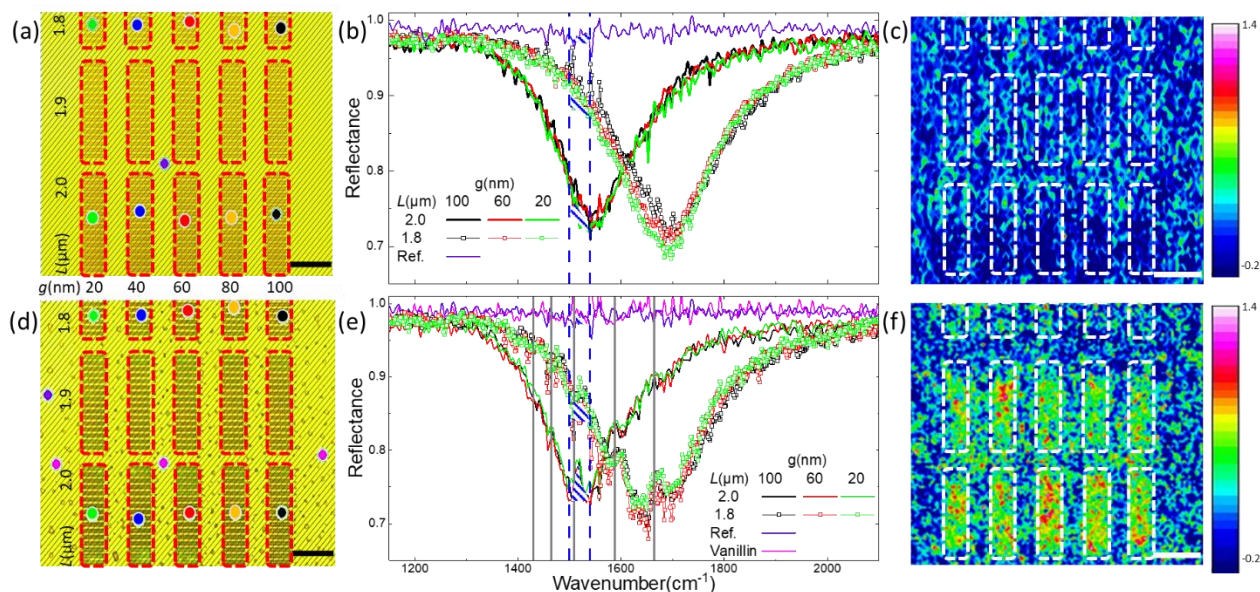


Figure 5. 2. Surface response investigation under a co-polarization of BT arrays with $L = 2.0, 1.9,$ and $1.8 \mu\text{m}$ with variable gap values going from 20 to 100 nm through a Focal Plane Array detector. (a-c) illustrate the results before vanillin deposition, and (d-f) represent the inquiry after vanillin deposition. (a, d) real images of the sample with color pixels for each gap value. Purple and magenta dots stand for bare substrate and vanillin spots, respectively. A homogenous coverage is illustrated in (d). Plasmonic resonances are collected pixel by pixel and represented in (b, e) for the color-corresponding BT as well as for the vanillin spots (magenta) and the bare substrate spots (purple). The resonances in (e) are red-shifted in comparison to (b) and the Fano-line shapes of the vibrational features spectrally covered by the broad LSPR evidence the coupling between the LSPR and the narrow vibrational lines, through asymmetric features (gray lines). The hatched areas around an absorption line of vanillin show the contrast of amplitude between both resonances without and with vanillin, then the color-coded chemical images (c, f) are activated after integration (dashed blue lines), highlighting the induced SEIRA that is mainly arising from the BT arrays. All scale bars are $50 \mu\text{m}$ long.

Moreover, the near-field theory, which is presented through the E-field mappings in **Chapter 3**, demonstrates the influence of the gap value on the near-field enhancement and consequently on the expected SEIRA effect. The highest electric field enhancement corresponds to $g = 20 \text{ nm}$. Therefore, it is the most sensitive to the surrounding molecules, as recalled in **Figure 5.3a**. The SEM image shows the fabricated BT with a gap of 20 nm and the simulated near-field distribution inside such a gap, the field intensity $|E|^2/|E_0|^2$ is found up to 10^3 . **Figure 5.3b** illustrates the gap spectral influence on the plasmonic ω_{res} position (check **Figure 5.3c**), and their possible coupling to the discrete absorption line of vanillin, marked by vertical lines. Herein, the curves of **Figure 5.2e** are plotted for $L = 2.0 \mu\text{m}$ but with a vertical offset for a clear view of the spectral dependence of the position of ω_{res} as well as the amplitude of ω_{vib} modulation on the gap value.

In **Figure 5.3b**, the vibrational signals are obtained by the normalization of the reflectance for each BT array to the baseline (BL, dashed lines in **Figure 5.3b**) calculated by Euler's least square smoothing algorithm.¹³¹ Please refer to **Annexe 5.1** for more details. This hybrid coupling efficiency is interpreted through the strength (peak-to-peak value) and the shape of the Fano-like signals and is modulated by a tuning ratio $\omega_{vib}/\omega_{res}$. As previously detailed in **Chapter 2 and 3**, the variation of ω_{res} with respect the gap value is presented in **Figure 5.3c** : ω_{res} red-shifts as soon as the gap value is decreased from 100 to 20 nm, exhibiting a stronger tip-to-tip coupling.

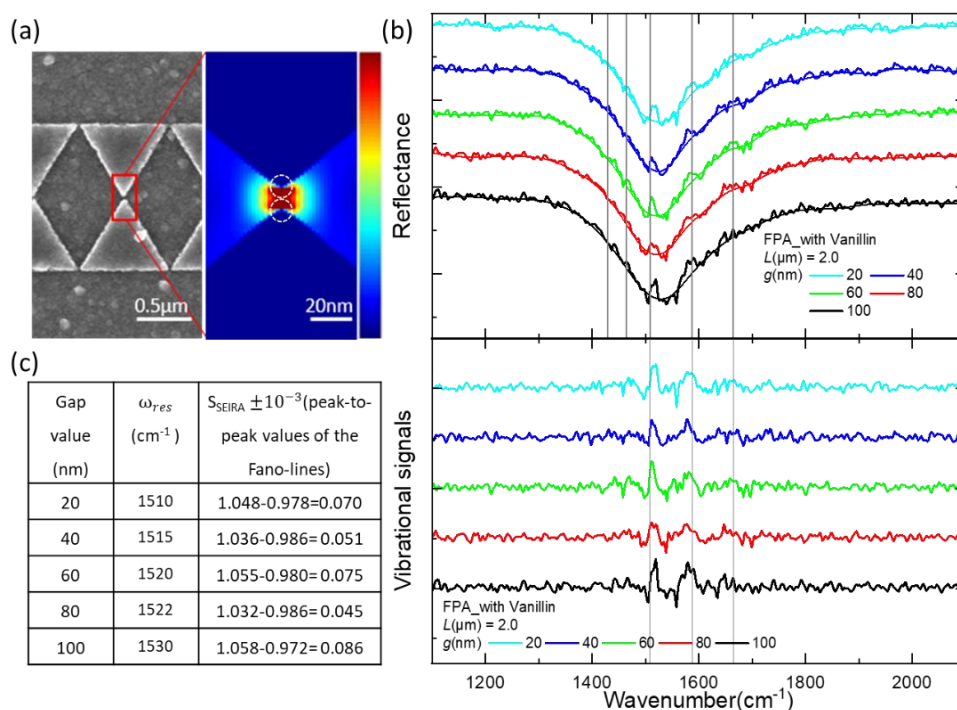


Figure 5.3. Gap influence on the SEIRA analysis. (a) SEM image of the fabricated BT NA with a gap of 20 nm and the resulting near E-field localization and enhancement under a co-polarized light. The dotted circles (radius = 8 nm) give a better visualization of the activated zones where the molecules are strongly coupled. (b) FPA results show the gap spectral influence on the ω_{res} of BT arrays with $L = 2.0 \mu\text{m}$ during the SEIRA sensing, and (c) the resulting background-corrected vibrational signals for each vanillin vibrational mode vertical line. ω_{res} are defined for each gap value and S_{SEIRA} is calculated for $\omega_{vib} = 1509 \text{ cm}^{-1}$.

Plus, the table in **Figure 5.3c** shows that for $\omega_{vib} = 1509 \text{ cm}^{-1}$, the strongest asymmetric profile of the vibrational signals for a gap of 100 nm ($\omega_{res} = 1530 \text{ cm}^{-1}$) with a tuning ratio of 0.98. For such a gap value, we conclude a perfect overlap condition between ω_{res} and ω_{vib} , and assume a better distribution of the molecules in the proximity to the enhanced tips. However, our first intuition is

to identify in **Figure 5.2f** the red spots as enhancement of the vanillin line situated at $1\,509\text{ cm}^{-1}$, around which the integration is done in **Figure 5.2e**. Hence, strong activation of the BT array region is observed where $g = 60\text{ nm}$ ($\omega_{res} = 1\,520\text{ cm}^{-1}$). We also remark in **Figures 5.3b and 5.3c** that a similar strong asymmetric profile is obtained as well for $g = 60\text{ nm}$. Thus, for a 60 nm gap value, the spectral overlap between the ω_{res} and ω_{vib} seems to be as well perfectly adapted to produce a strong enhancement of the pre-mentioned absorption line.

In sum, to produce the strongest intended S-shape profile, characteristic of the Fano resonance, the corresponding ω_{res} should imperatively be finely tuned to be suitable to enhance the ω_{vib} . Whereas, the tuning factor will also change with the gap, as the ω_{res} is changing with the gap value. Moreover, a phase change of the Fano-type interaction can also occur as the ω_{res} peak shifts with the gap variation. Such a spectral dependency is rendering it extremely difficult to finely compare the amplitude of the resulting asymmetric lines and to deduce the most adequate BT gap to perfectly trigger the selected absorption line using FPA. The resolution of the absorption signatures is spectrally limited as well, due to a low signal-to-noise ratio (SNR) of the FPA spectrum from single pixels in these measurement conditions.

5.2.1.2. MCT single element for SEIRA demonstration

To overcome the low SNR of FPA, complementary far-field measurements are done using the MCT single element detector under a $36 \times$ IR objective (N.A. = 0.5). The reflectance area of the optical transducer is selected by a manual knife-edge aperture corresponding to only 5 zones of Al-BT of the same length with different gap sizes from 20 to 100 nm. **Figure 5.4** presents the performed reflectance measurements on the same sample position without (**Figure 5.4b**) and with (**Figure 5.4c**) the vanillin/ethanol (2 mg/ml) droplet and the retrieved vibrational signals (**Figure 5.4d**).

Figure 5.4a gives a reference for the vanillin absorption lines from $1\,100$ to $2\,100\text{ cm}^{-1}$, obtained from a transmittance measurement of a highly-concentrated vanillin solution (50 mg/ml) in ethanol, deposited on an IR-transparent KBr crystal. Below $1\,400\text{ cm}^{-1}$, the IR absorption lines of the vanillin are not accessed with the plasmonic resonances of the fabricated BT arrays

(**Figure 5.4c**). However, five narrow IR absorption lines of the vanillin for wavenumbers higher than 1400 cm^{-1} are interfering within large plasmonic resonances, corresponding to Al-BT arrays of L from 2.0 to $1.4\text{ }\mu\text{m}$ with a step of $0.1\text{ }\mu\text{m}$. The five absorption features of vanillin are situated at $1\ 430$, $1\ 464$, $1\ 509$, $1\ 587$, and $1\ 665\text{ cm}^{-1}$ (see the vertical gray lines in **Figure 5.4**). These lines correspond closely to C=O, CH, CC, CO, and CH₃ stretching, in-plane bending, and asymmetric deformation vibrational lines.¹³² The experimentally found vibrational lines are slightly shifted compared with the analytical ones stated by Balachandran *et al.* due to the interaction of the molecules with the substrate and their medium (solid, liquid) which is directly affecting their binding energy. For each of these five IR lines, asymmetric line shapes (Fano-type) highlight the corresponding hybrid coupling between large plasmonic resonances ω_{res} and narrow vibrational mode ω_{vib} frequencies (**Figure 5.4c**).

In **Figure 5.4d**, the vibrational signals are obtained by the normalization of the reflectance for each BT array to their corresponding baseline (BL, dashes lines in **Figure 5.4c**) calculated by Euler's least square smoothing algorithm, detailed in **Annexe 5.1**.¹³¹ The efficiency of this hybrid coupling is interpreted through the strength and the shape of the Fano-like signals and is modulated by a tuning ratio $\omega_{vib}/\omega_{res}$. As plotted in **Figure 5.4d**, for each L value, when $\omega_{vib}/\omega_{res} \approx 1$ (typically around the colored vertical lines), the vibrational signal amplitude (peak-to-peak value) reaches its maximum, thus, stating the best spectral overlap between ω_{vib} and ω_{res} . The shape of the vibrational signals for each ω_{vib} are also impacted by the tuning ratio, *i.e.* by their position compared to ω_{res} . Herein, the Fano-like profiles are compared for $\omega_{vib} = 1\ 665\text{ cm}^{-1}$ in function of the tuning ratio $\omega_{vib}/\omega_{res}$. For a coupling tunings above 1 (**Figure 5.4d**, *e.g.* black Fano-line), the line shape keep on their asymmetric outlines but with inverted minimum and maximum compared to those found at tunings below 1 (**Figure 5.4d**, *e.g.* green Fano-line).⁴⁶

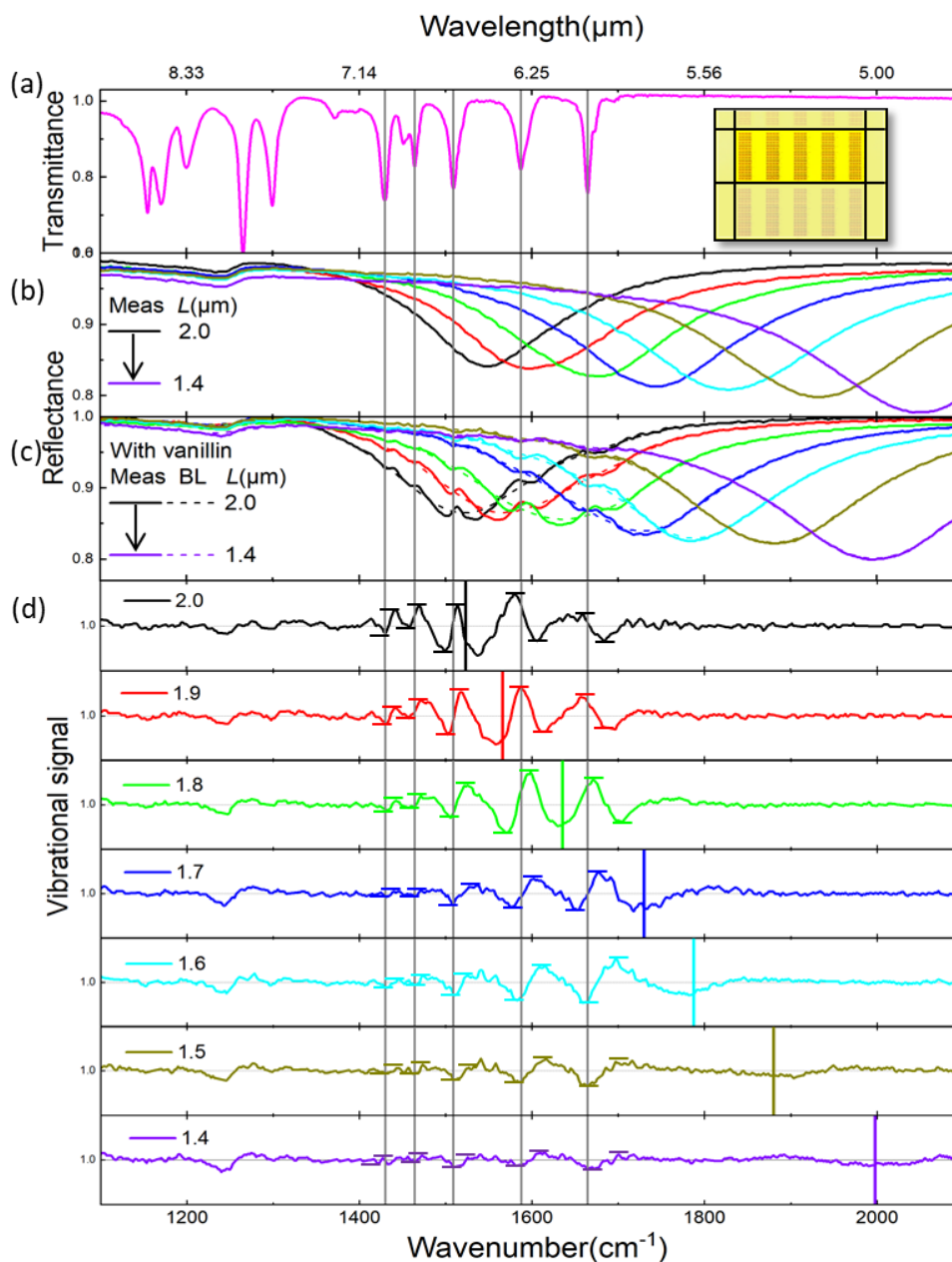


Figure 5. 4. Resonant SEIRA sensing demonstration of vanillin using Al-BT. (a) Transmittance spectrum of vanillin (50mg/ml) normalized to the one of cleaned KBr platelet, shown as a reference. Gray vertical lines eye-guide the IR absorption lines of vanillin. The inset shows an FPA image of the 5 zones of Al-BT selected by a manual knife-edge covering $230 \mu\text{m} \times 90 \mu\text{m}$. Reflectance spectra of the Al-BT of different side lengths L varying from 2.0 to 1.4 μm with a step of 0.1 μm , covering accordingly a wide spectral range from 1 400 to 2 100 cm^{-1} are acquired before (b) and after (c) the deposition of vanillin. The dashed curves are the corresponding baseline (BL) fitted using Euler's smoothing algorithm, excluding the vibrational features (Fano-type).¹³¹ (d) Vibrational signals normalized by the BL for each BT array (side length L given in microns). The plasmonic resonance positions ω_{res} are marked with thick colored vertical lines. The signal strengths of the enhanced molecular vibrational modes (S-shape) are obtained as a peak-to-peak value, delimited by the horizontal ticks. Note the signal strength and the line shape of a given vibrational mode change depending on its frequency compared to ω_{res} .

Similar results are achieved under cross-polarized light (across the BT tip-to-tip axis) as illustrated in **Figure 5.5**.

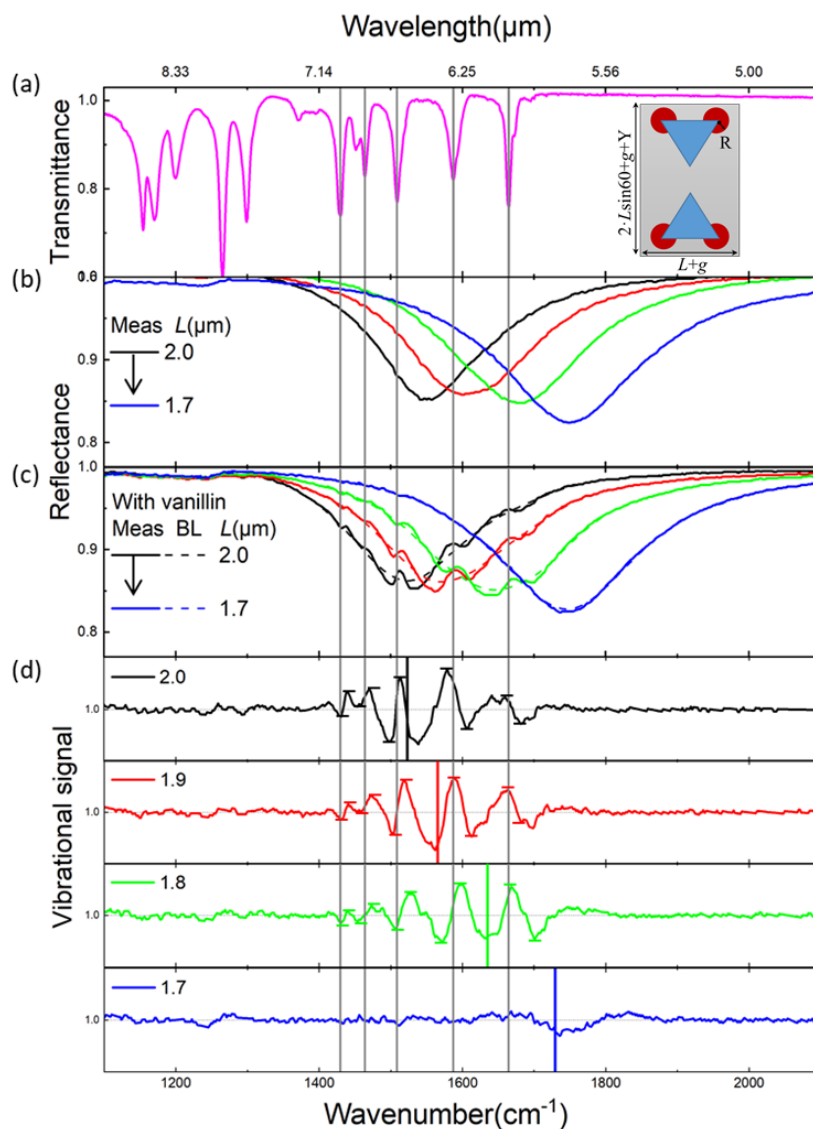


Figure 5. 5. Resonant SEIRA sensing demonstration of vanillin using Al-BT under cross-polarized light. (a) Transmittance spectrum of vanillin (50mg/ml) normalized to the one of cleaned KBr platelet, shown as a reference. Gray vertical lines eye-guide the IR absorption lines of vanillin. Reflectance spectra of the Al-BT of different side lengths L varying from 2.0 to 1.7 μm with a step of 0.1 μm , covering accordingly a wide spectral range from 1 400 to 1 800 cm^{-1} are acquired before (b) and after (c) the deposition of vanillin. The dashed curves are the corresponding BL fitted using Euler's smoothing algorithm, excluding the vibrational features (Fano-type).¹³¹ (d) Vibrational signals normalized by the BL for each BT array (side length L given in microns). The plasmonic resonance positions ω_{res} are marked with thick colored vertical lines. The signal strengths of the S-shape are obtained as a peak-to-peak value, delimited by the horizontal ticks. Note the signal strength and the line shape of a given vibrational mode change depending on its frequency compared to ω_{res} . BC of $L= 1.7 \mu\text{m}$ witnesses the time-dependence of the experiment, the vanillin is crystallized upon the ethanol evaporation. The inset shows the corner's activation under cross-polarized light.

For the sake of characterization time, only 3 values of L were selected, varying from 2.0 to 1.7 μm with a step of 0.1 μm . Likewise, once the spectral overlapping condition is fulfilled, Fano-like profiles appear and are modulated by their position regarding ω_{res} . For example, as illustrated in **Figure 5.5d** the Fano-signal of $\omega_{vib} = 1587\text{ cm}^{-1}$ inverts its minimum and maximum in dependence on its relative position compared to the respective ω_{res} of $L = 2.0\text{ }\mu\text{m}$ (black Fano-line at 1523 cm^{-1}) and $L = 1.8\text{ }\mu\text{m}$ (green Fano-line at 1645 cm^{-1}).

Remarkably, the results of $L = 1.7\text{ }\mu\text{m}$ underline the time-dependency of the test solution as the corresponding measurements were acquired after 30 min following the droplet deposition. By looking through the microscope, we can observe complete evaporation of the vanillin/ethanol droplets and crystallization of vanillin molecules on a spot of the sample surface aside from the tailored zones. As a consequence of this, for $L = 1.7\text{ }\mu\text{m}$, ω_{res} is retrieved at almost the same spectral position (blue curves of **Figures 5.5b and 5.5c**), and the resulting blue vibrational signal in **Figures 5.5d** remains flat along the range of interest. Note that, previous measurements were systematically acquired within 10 min for each zone.

To evaluate the SEIRA sensitivity of the Al-BT arrays, **Figure 5.6** summarizes the enhancement factor, EF, for the five IR lines of the vanillin according to the spectral tuning ratio under co-polarized light compared to the state-of-art in metallic with and without a MIM structure. Let us begin with the definition of EF by the expression of **Equation 5.1** as:

$$EF = \frac{S_{SEIRA}}{S_0} \times \frac{A_0}{A_{SEIRA}} \quad (5.1)$$

where S_{SEIRA} and S_0 are the enhanced and unenhanced signal strengths, respectively. From the measurements on a metallic surface, the unenhanced signal strengths, S_0 , are found in the order of $2\text{-}5 \times 10^{-3}$ for the absorption lines. The signal strengths of the enhanced molecular vibrational modes (S-shape) are obtained as a peak-to-peak value, delimited by the horizontal ticks. The signal strengths, S_{SEIRA} , are in the order of 2×10^{-2} , as measured in **Figure 5.4**. A_{SEIRA} and A_0 denote the areas covered with molecules in SEIRA and the reference measurements, respectively (see the insets in **Figure 5.5 and 5.6**). The A_0 is defined in analogy to the FDTD unit cell, *i.e.* the

repetitive surface accessible to the molecules at the BT surface. The surface is analytically calculated as developed in **Equation 5.2**:

$$A_0 = (2 \times L \times \sin 60 + g + Y) \times (L + g) \quad (5.2)$$

In the following, the gap is considered equal to 100 nm for the 5 zones as the worst-case scenario for a low near-field enhancement, regarding the near E-field mapping of **Chapter 3**. The total antenna surface area, A_0 , yields 0.4 picograms per BT antenna. For a completely covered antenna, 15×10^8 molecules per BT antenna are expected. However, the probed molecules are traced in the antenna's intense near-field hotspots, specifically at the sidewalls of the activated tips (see **Figure 5.3a**). As the SEIRA signal originates essentially from these molecules, an effective area, A_{eff} , that is accessible to the analyte is defined as the 5/6 of an 8 nm-radius circular surface centered around the BT tip, where the local EM field is intensified, excluding thus the internal area of the equilateral triangle tip.

Under a co-polarization, as the E-field is localized and enhanced at both inner BT tips, A_{SEIRA} is counting twice the A_{eff} . A_{SEIRA} represents 0.04 ‰ of the unit cell area A_0 . Therefore, 5×10^4 molecules are located at both inner tips (A_{SEIRA}), hence, approximately 2.5×10^4 molecules per tip (A_{eff}). Under a cross-polarized light, A_{SEIRA} is counting four times the A_{eff} . A_{SEIRA} represents on average 0.08 ‰ of the unit cell area A_0 . Therefore, 9.8×10^4 molecules are located at the outer-corners of the BT (A_{SEIRA}), hence, approximately 2.5×10^4 molecules per tip (A_{eff}).

On one hand, the number of molecules per tip will reasonably persevere its value as the involved parameters, *i.e.* number of released molecules, A_0 , and A_{eff} are unchangeable. On the other hand, the total number of trapped molecules should be proportional to the number of hotspots (A_{SEIRA}). In line with this, under a cross-pol, the number of molecules per A_{SEIRA} is twice the one found under a co-pol, yet always remains in the same order of magnitude (10^4).

The retrieved number of molecules is three orders of magnitude lower than the value reported by Barho *et al.* for vanillin detection ($\sim 5 \times 10^7$ molecules per antenna) with highly doped semiconductor periodic rectangular nanoantenna arrays, where the E-field is only localized at the resonator corners. Interestingly, $\sim 10^4$ molecules are in the same order of magnitude as the best-

reported values so far for the detection of self-assembled monolayers (SAM) of stearic acid (also known as octadecanoic acid) using asymmetric Al cross-antennas ($\sim 3.6 \times 10^4$ molecules at the tip region of the antenna) and octadecanethiol (ODT) with a gold nanorod antenna ($\sim 1.5 \times 10^4$ molecules per antenna), respectively reported by Halas *et al.*⁶⁵ and Neubrech *et al.*⁴³ Furthermore, using a MIM structure with Fan-like Au NA in a 3×3 array, Brown *et al.* achieved the detection of $\sim 0.5 \times 10^4$ molecules per antenna of ODT,⁸⁵ and Dong *et al.* detected ~ 500 molecules of 4- nitrothiophenol per antenna.⁸⁷

Subsequently, **Figure 5.6** shows the evolution of the enhancement factor EF versus the ratio of molecular and plasmonic resonance frequencies $\omega_{vib}/\omega_{res}$ for these results in comparison to the state-of-art in the literature.

EF is established for the signal strength and the active area of BT arrays from $L = 1.4$ to $2.0 \mu\text{m}$, under co-polarized light. The order of magnitude of the EFs is $\sim 10^7$ as shown in the left y-axis of **Figure 5.6**. On the right y-axis of **Figure 5.6**, EFs values are provided for different antenna sizes, shapes, and compositions, as reported by Brown *et al.* and Vogt *et al.*. Note that the error propagation is calculated for each EF value as detailed in **Annexe 5.2**. Typical EFs stated in the literature according to Neubrech *et al.* are ranging from 10^3 to 10^5 depending on the antenna shape, material, and organization.⁴³

The EF maximum value is 1.8×10^7 found for a tuning ratio $\omega_{vib}/\omega_{res} = 0.99$. Thus, the strongest enhancement is achieved for the absorption line ω_{vib} situated at 1509 cm^{-1} with a BT array of $L = 2.0 \mu\text{m}$, resonating at a $\omega_{res} = 1524 \text{ cm}^{-1}$. Similar results are found under cross-polarized light (under un-polarized light, max EF is found at 6×10^6 with the same tuning ratio). It is four orders of magnitude higher than the reported value by Vogt *et al.* for IR sensing (EF $\sim 10^3$ using Au nanorods).⁴⁶

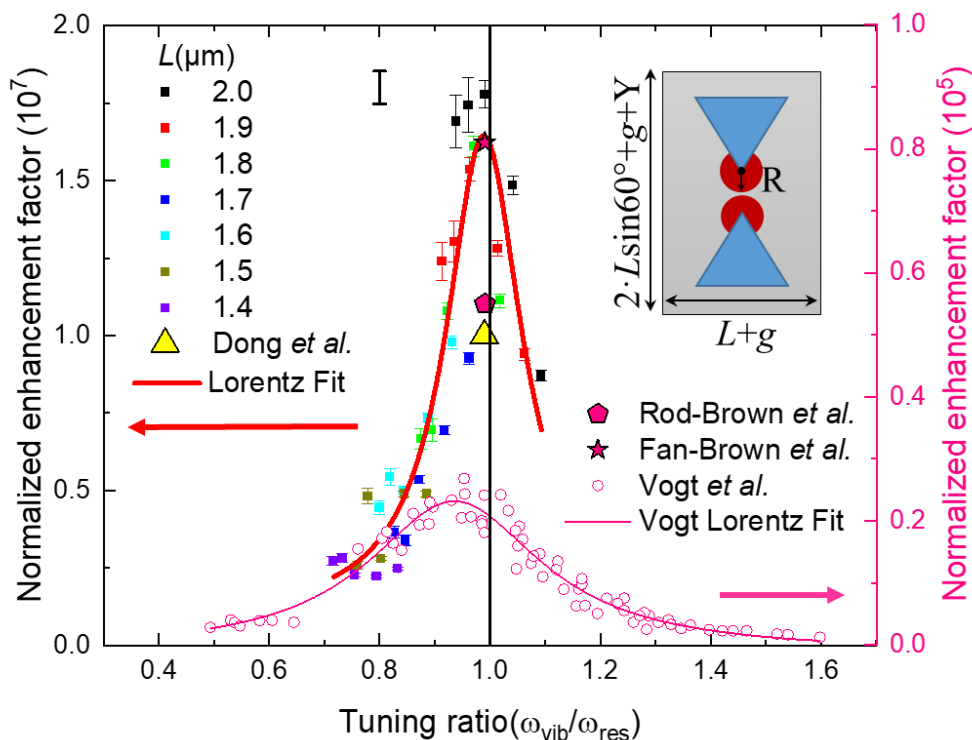


Figure 5.6. Normalized enhancement factor (EF) of the five enhanced absorption modes of vanillin in the considered spectral fingerprint range versus the ratio of molecular and plasmonic resonance frequencies ($\omega_{vib}/\omega_{res}$). The inset shows the A_0 and A_{SEIRA} with a 100 nm gap for all the BT arrays of the same length. The vibrational signal enhancement is generally maximized below $\omega_{vib}/\omega_{res} = 1$ (black line) as found with a Lorentz curve (thick red curve), declaring the perfect overlap between vibrational modes and plasmonic resonances. The thick error bar represents the systematic error related to A_{SEIRA} estimation, to be introduced to the maximum EF value, as detailed in **Annexe 5.2**. Vogt *et al.* data is plotted in pink circles as well as their Lorentz fit (thin pink curve) for further comparison. Brown *et al.* and Dong *et al.* data are plotted as specific symbols (see the legends). Note the difference of the y-axes scales corresponding to each legend.

In **Figure 5.6**, the data of Vogt *et al.* are plotted on the same graph (pink circles) to underline the improvement of the EF achieved using AI-BT as well as their constantly global tendency to be maximized for $\omega_{vib}/\omega_{res}$ below 1 as fitted by a Lorentz curve (red curve) with a maximum centered around 0.98 and 0.16 as the full width at half maximum (FWHM). This result agrees well with the fact that the optimal enhancement is established at a tuning ratio slightly lower than 1 between the vibrational line and the antenna plasmonic resonance frequencies, as reported by

Alonso-Gonzalez *et al.*,⁴⁹ and consistently with Wallace *et al.* SEIRA measurements of 4-nitrothiophenol-functionalized gold dendritic fractals,⁹⁰ and Vogt *et al.* findings (see in **Figure 5.6** the Lorentz fit with a pink curve).⁴⁶ The smaller FWHM indicates fewer losses and consequently a higher EF. This is most probably due to the higher energy confinement within the Al-BT MIM configuration as well as to the reduced effective area of the near E-field distribution compared to the previously mentioned Au nanorods.

Finally, in **Figure 5.6** the resulting EFs are two orders of magnitude higher than those reached with 20-nm gaps in Fan-like Au NA with MIM structures, as reported by Brown *et al.*⁸⁵ However, the EFs are similar to the values reported by Dong *et al.* achieved with a 3-nm gap BT antennas in a MIM structure with an insulator spacer of 300 nm.⁸⁷ The similar EF is achieved with a drastic reduction of the A_{SEIRA} involved in the EF (see **Equation 5.1**). In sum, the difference in the EF values from Brown *et al.* is attributed to a larger E-field confinement gained thanks to the reduced thickness of the SiO₂ insulator layer (20 nm), creating thus a gap-plasmon effect, in comparison to their ~ 300 nm insulator layer, defining an optical cavity.

5.2.1.3. Polarization effect and SPR analysis

In this section, the polarization effect on the plasmonic resonances is investigated during the SEIRA demonstration as illustrated in **Figure 5.7**. A set of selected BTs ($L = 2.0, 1.9,$ and $1.8 \mu\text{m}$) are illuminated under a co- then cross-pol, before and after the deposition of vanillin. The spectrum of vanillin is cropped, showing the spectral window of interest (**Figure 5.7a**). As presented in **Figure 5.7b**, the polarization does not affect the measured resonances. Regardless of the polarization, for a specific absorption feature of vanillin, the corresponding asymmetric line shapes appear with the same strength at the same spectral positions. Note that the reflectance curves under both polarizations do not perfectly overlay in terms of amplitude due to the environmental measurement conditions which are not impeccably controlled.

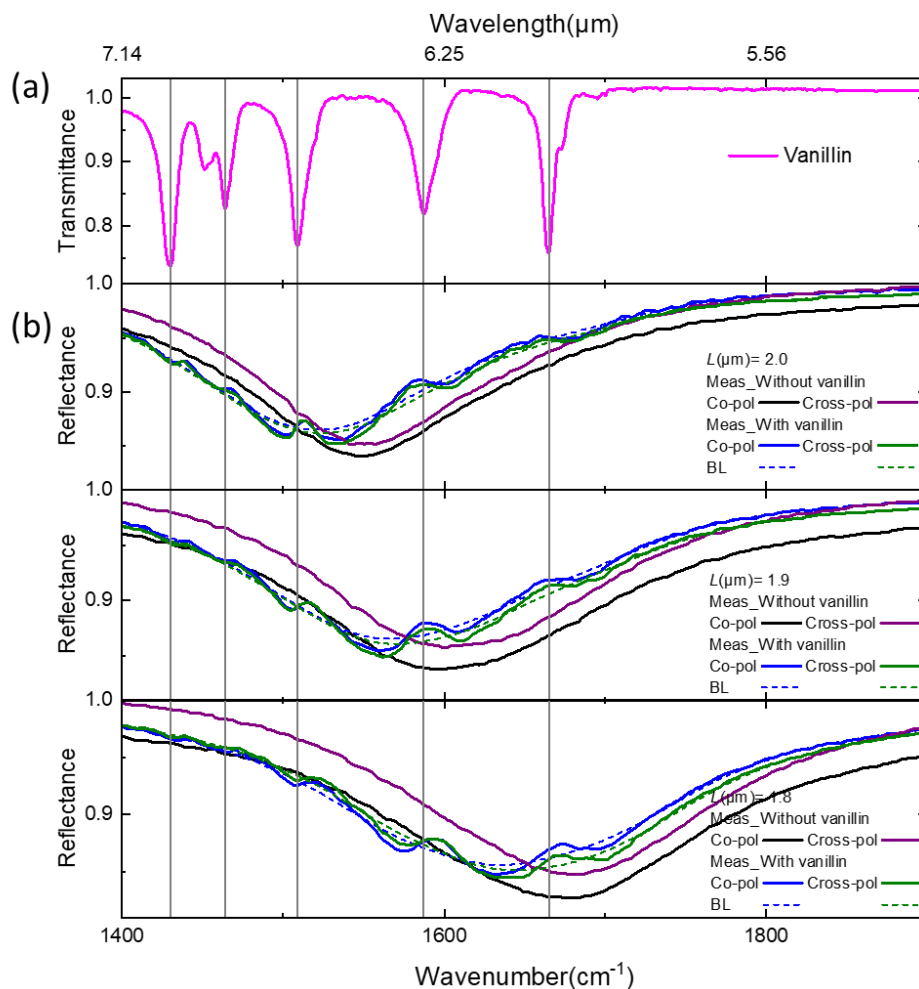


Figure 5. 7. SPR sensing demonstration under co-and cross-polarized light. (a) Transmittance spectrum of vanillin focuses on the accessible absorption lines of vanillin between 1 400 and 1 900 cm^{-1} . (b) Reflectance spectra of BT with respective L values of 2.0, 1.9, and 1.8 μm , before and after vanillin deposition and under both polarized light. The dashed curves are the corresponding BL generated by Euler's smoothing algorithm.

Globally, the optical sensitivity is around 245 nm/RIU . This stresses the invariance of the ω_{res} under both polarization for such a gap value of 100 nm and the same L value, as discussed in **Chapter 3 and 4**. However, spanning the spectral range and for the tuning ratios between ω_{res} and ω_{vib} of interest, some vibrational signals are probably more enhanced than others.

5.2.2. Al-Honeycombs for SEIRA demonstration

Similar measurements are done to prove the SEIRA-sensing singularities using a more compact arrangement of equilateral triangles, *i.e.* a 100 μm x 100 μm of honeycomb-like (HC) tailored metasurface. As formerly proved by simulations and optical characterizations, the HC structure offers an invariance to light polarization. In line with that, the sensing demonstration is done under a co-polarized and un-polarized light to evaluate and demonstrate the advantage of such an optical characteristic using a single-element MCT detector.

Using the same measurement parameters, 36 \times IR objective (N.A. = 0.5), SEIRA experiments are carried out. However, the reflectance area of the optical transducer is now selected by a manual knife-edge aperture corresponding to a 100 μm x 100 μm zones enclosing the compact Al-HC where the side length, L , and the gap, g , values are constant. Herein, the g value is set to 100 nm. The SEIRA demonstration is detailed under a co-polarized light in **Figure 5.8** and is compared to the SEIRA findings using un-polarized light.

Figure 5.8 presents the executed reflectance measurements on the same HC-sample position without (**Figure 5.8b**) and with (**Figure 5.8c**) the vanillin/ethanol (2 mg/ml) droplet and the retrieved vibrational signals (**Figure 5.8d**). Similarly, five narrow IR absorption lines of the vanillin are successively coupled to large plasmonic resonances, corresponding to Al-HC arrays of L from 2.0 to 1.4 μm with a step of 0.1 μm . The asymmetric line shapes for each vibrational line evidence the corresponding coupling between ω_{res} and ω_{vib} . As previously detailed, the strength and the shape of the Fano-like signals are modulated by a tuning ratio $\omega_{vib}/\omega_{res}$.

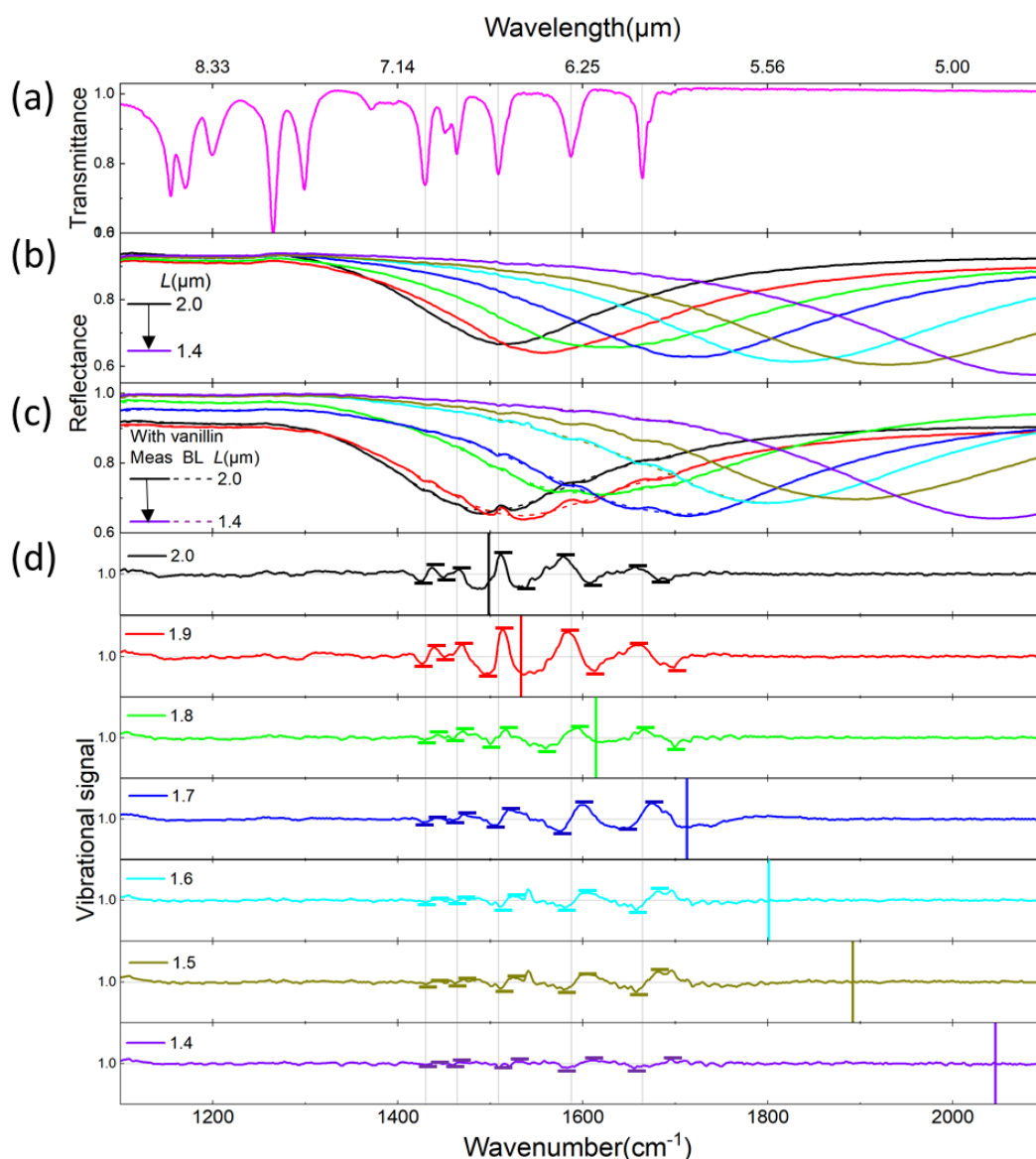


Figure 5. 8. Resonant SEIRA sensing demonstration of vanillin using Al-HC under a co-polarized light. The gap value is fixed at 100 nm. (a) Transmittance spectrum of vanillin (50 mg/ml) normalized to the one of cleaned KBr platelet, shown as a reference. Gray vertical lines eye-guide the IR absorption lines of vanillin. Reflectance spectra of the Al-HC of different side lengths L varying from 2.0 to 1.4 μm with a step of 0.1 μm , covering accordingly a wide spectral range from 1 400 to 2 100 cm^{-1} are acquired before (b) and after (c) the deposition of vanillin. The dashed curves are the corresponding baseline (BL) fitted using Euler's smoothing algorithm, excluding the vibrational features (Fano-type). (d) Vibrational signals are normalized by the BL for each HC array (side length L given in microns). The plasmonic resonance positions ω_{res} are marked with thick colored vertical lines. The signal strengths of the enhanced molecular vibrational modes are obtained as a peak-to-peak value, delimited by the horizontal ticks.

A global spectral red-shift of $\Delta\omega_{res} \sim 30 \text{ cm}^{-1}$ is obtained in presence of vanillin/ethanol solution, by comparing **Figure 5.8b and 5.8c**. Hence, the SPR sensing is noticed with a sensitivity of $\sim 182 \text{ nm/RIU}$ ($\sim 10^2$ as reported by Mayer *et al* for metallic nanoparticles).³¹

To evaluate the SEIRA sensitivity of the Al-HC arrays under co-polarized light, **Figure 5.9** summarizes the enhancement factor, EF, for the five IR lines of the vanillin according to the spectral tuning ratio. The signal strengths, S_{SEIRA} , are in the order of 2.5×10^{-2} , as measured in **Figure 5.8**. This value is slightly higher than the retrieved values for Al-BT under a co-polarized light (S_{SEIRA} in the order of 2×10^{-2}), and it is related to a signal improvement thanks to compacting the NA into the characterization zone. Under un-polarized light, S_{SEIRA} are in the order of 4×10^{-2} , two times greater than the S_{SEIRA} values measured under a co-polarized light, and it is due to the improved SNR achieved once the totality of the incident illumination intensity reaches the zone of interest onto the sample without being attenuated by a factor of 1/2 upon traversing a polarizer. A_0 is defined as the repetitive surface entity (antenna) accessible to the molecules and is analytically calculated as developed in **Equation 5.3**:

$$A_0 = 3 \frac{\sqrt{3}}{2} \times a^2 ; a = L + \sqrt{3} \times g \quad (5.3)$$

In the following, the gap is considered equal to 100 nm. The total antenna surface area, A_0 , yields 0.2 picograms per HC antenna, the half of the mass that is covering the A_0 for BT, as the characterized surface of HC is half of the BT's one ($S_{\text{objective, HC}} = 100 \times 100 \mu\text{m}^2 < S_{\text{objective, BT}} = 230 \times 90 \mu\text{m}^2$). For a completely covered antenna, 7×10^8 molecules per antenna (lower than 15×10^8 molecules per BT antenna) are estimated. However, the probed molecules are outlined in the antenna intense near-field hotspots, triggered by the light polarization (see the inset of **Figure 5.10**). Under a co-polarized light, A_{SEIRA} is counting six times the A_{eff} . A_{SEIRA} represents 0.12 ‰ of the unit cell area A_0 . Therefore, approximately 1.3×10^4 molecules are triggered per tip (A_{eff}). Under a non-polarized light, the same amount of molecules is retrieved per tip, yet, A_{SEIRA} is counting eighteen times the A_{eff} . A_{SEIRA} represents 0.37 ‰ of the unit cell area A_0 . Despite of the difference in A_0 definition and A_{SEIRA} quantification, the retrieved numbers of triggered molecules using HC antennas are in the same order of magnitude as for the BT antennas.

It is successfully matching the state-of-art as reported by Halas *et al.*⁶⁵, Neubrech *et al.*⁴³, and Brown *et al.*⁸⁵

Moreover, the evolution of the normalized enhancement factor EF versus the tuning ratio $\omega_{vib}/\omega_{res}$ is illustrated in **Figure 5.9** for all the selected L values. EF is higher than $\sim 10^7$ as shown in the y -axis of **Figure 5.9**. Note that the error propagation is calculated for each EF value as detailed in **Annexe 5.2**. It is identical to the order of magnitude achieved with the BT antennas and it is agreeing with the greatest stated value reported by Dong *et al.* using a 3-nm gap MIM BT antennas.⁸⁷ The EF maximum value of 1.2×10^7 is found for a tuning ratio $\omega_{vib}/\omega_{res} = 0.98$. The strongest enhancement is achieved for the absorption line ω_{vib} situated at 1587 cm^{-1} with a HC array of $L = 1.9 \text{ }\mu\text{m}$, resonating at a $\omega_{res} = 1533 \text{ cm}^{-1}$. Under a non-polarized light, maximum EF is found around 3×10^6 (black dot). It is attained once the HC array of $L = 2.0 \text{ }\mu\text{m}$, resonating at a $\omega_{res} = 1504 \text{ cm}^{-1}$, enhances the absorption line ω_{vib} situated at 1509 cm^{-1} . On one hand, from a near-field point of view, this result seems to correlate with **Equation 5.1**, as the EF is inversely proportional to the A_{SEIRA} . The maximum EF is reduced under an un-polarized light (triggering 18 tips) versus the one retrieved under a co-polarized light (triggering 6 tips). On the other hand, from a far-field point of view, the result seems confusing especially as the light polarization or non-polarization should not affect the ω_{res} for a fixed L value, and same vibrational signal enhancement should occur with the same antenna size. Hence, the maximum EF should be also obtained with $L = 2.0 \text{ }\mu\text{m}$ under a co-polarized light. However, under a fixed polarization case, HC arrays are enhancing a certain ω_{vib} with a different tuning ratio. For example, under a co-polarized light, ω_{vib} situated at 1509 cm^{-1} is enhanced by the HC of $L = 2.0 \text{ }\mu\text{m}$ and producing a maximum EF of 1.07×10^7 , which is close to the greatest achieved value of 1.2×10^7 . However, the tuning ratio is not the same for both EF values, and it is massively influencing the maximum EF value selection, as it should be lower than 1. This condition is thus fulfilled with $L = 1.9 \text{ }\mu\text{m}$ and not with $L = 2.0 \text{ }\mu\text{m}$.

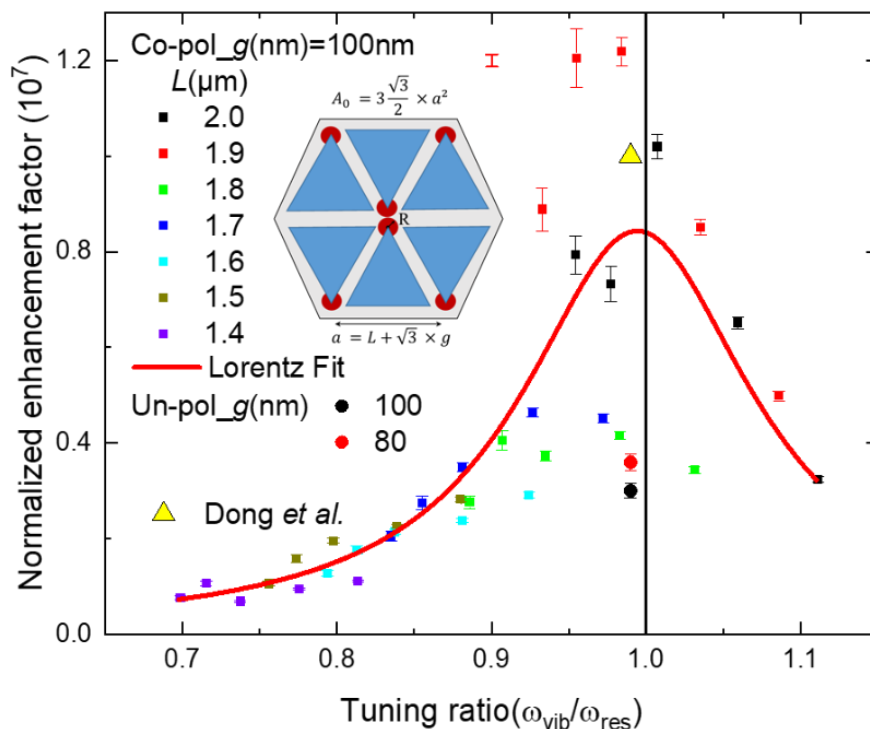


Figure 5.9. Normalized enhancement factor (EF) of the five enhanced absorption modes of vanillin in the considered spectral fingerprint range versus the ratio of molecular and plasmonic resonance frequencies ($\omega_{vib}/\omega_{res}$). The inset shows the A_0 and A_{SEIRA} under a co-polarized light. The vibrational signal enhancement is generally maximized below $\omega_{vib}/\omega_{res} = 1$ (black line) as found with a Lorentz curve (thick red curve), declaring the perfect overlap between vibrational modes and plasmonic resonances. The thick error bar represents the systematic error related to A_{SEIRA} estimation, to be introduced to the maximum EF value, as detailed in **Annexe 5.2**. The maximum EF values retrieved under un-polarized light are also included as black and red dots for a respective gap of 100 nm and 80 nm. The maximum EF is reduced by a factor of 3 under un-polarized light which is also inversely proportional to the A_{SEIRA} prompted by the light polarization.

Moreover, using un-polarized light, the achieved value $\sim 10^6$ is one order of magnitude lower than the reported value for the same gap value but under co-polarized light $\sim 10^7$. Indeed, despite of the SNR improvement when removing the polarizer, the anticipated results under a cross-polarized light should be taken into consideration, as the non-polarized light is embracing both polarization cases. Here, the hypothesis reclaims a drop-off in the EF values under cross-polarized light that is translated into a total defeat of those under un-polarized light. Based on the simulation, one can remark that under cross-polarized light, the near E-field intensity, where the

SEIRA mainly occurs, is about half of the intensity value triggered by a co-polarized light. This near-field result supports the previous hypothesis and justifies the EF slight dropping under an unpolarized light condition.

After the polarization effect study, it is interesting to underline the influence of the gap reduction on the far-field and the near-field SEIRA results. The measurement results are plotted in detail in **Figure 5.10**. Thanks to the spectral red-shift engendered by the gap value reduction from 100 nm to 80 nm, a new set of HC antennas with smaller L could be engaged to trigger some vanillin lines. The spectral resonances red-shift with a mean value of $\Delta\omega_{res} \sim 50 \text{ cm}^{-1}$ when decreasing the gap value is authorizing the HC of $L = 1.5$ and $1.4 \mu\text{m}$ to couple and enhance several vibrational lines as displayed in **Figure 5.10d**. Hence, besides the size of the antenna, their spacing is presenting a new spectral degree of freedom to modulate the SEIRA coupling. Given the near-field SEIRA interpretation, the EF is retrieved at 3.6×10^6 for a gap of 80 nm and it is achieved once the HC array of $L = 1.9 \mu\text{m}$, resonating at a $\omega_{res} = 1510 \text{ cm}^{-1}$ (a wavenumber lower than the one marked for the same antenna's size, but with larger spacing), enhances the absorption line ω_{vib} situated at 1509 cm^{-1} (please check the red circle in **Figure 5.9**).

To conclude, both antenna structures are well-adapted for an accurate vibrational SEIRA sensing demonstration. Indeed, the far-field and near-field results are matching the state-of-art. Nevertheless, the arrangement of the antennas affected the reflectance amplitude, and in consequence, the vibrational signal S_{SEIRA} amplitude. In fact, under co-polarized light, for the compact-HC case, the amplitude of the S_{SEIRA} are upgraded by a factor of 1.25 compared to those retrieved for the BT case. The influence of the antenna's arrangement is drastically manifested in the estimation of the EF parameters and precisely while defining the A_{SEIRA} that is reflecting the number of the involved hotspots (active sites for SEIRA). A_{SEIRA} is 3 times higher for HC (0.12 ‰ of A_0) than for BT (0.04 ‰ of A_0), thus, the EF is 3 times lower in HC case than in BT case, as it is inversely proportional to A_{SEIRA} . Still, the spectral influence of the gap value detected using the HC has presented a promising degree of freedom for an extended SEIRA study.

Hence, it is always crucial to be aware of the effect of each parameter on the estimated EF and to compromise the design of the antenna to optimize the SEIRA output.

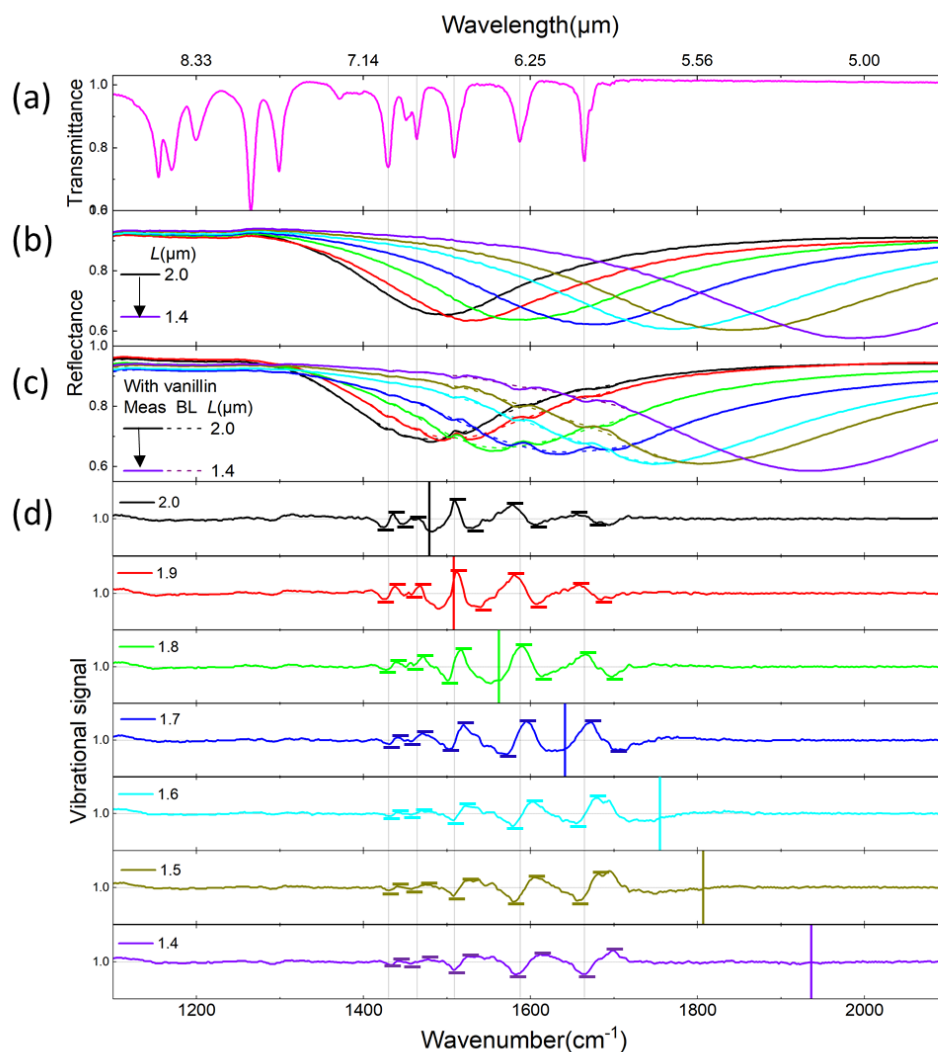


Figure 5.10. Resonant SEIRA sensing demonstration of vanillin using Al-HC under un-polarized light. The gap value is fixed at 80 nm. (a) Transmittance spectrum of vanillin (50 mg/ml) normalized to the one of cleaned KBr platelet, shown as a reference. Gray vertical lines eye-guide the IR absorption lines of vanillin. Reflectance spectra of the Al-HC of different side lengths L varying from 2.0 to 1.4 μm with a step of 0.1 μm , covering accordingly a wide spectral range from 1 400 to 2 100 cm^{-1} are acquired before (b) and after (c) the deposition of vanillin. The dashed curves are the corresponding baseline (BL) fitted using Euler's smoothing algorithm, excluding the vibrational features. (d) Vibrational signals are normalized by the BL for each HC array (side length L given in microns). The plasmonic resonance positions ω_{res} are marked with thick colored vertical lines. The signal strengths of the enhanced molecular vibrational modes are obtained as a peak-to-peak value, delimited by the horizontal ticks. The smallest HC antennas are more likely to enhance the ω_{vib} of the vanillin thanks to the spectral shift induced by decreasing the gap value from 100 nm to 80 nm.

5.2.3. Gas-SEIRA sensing

In the same spirit, the Al NA transducer opens the way to one of the most optimistic perspectives: the enhancement of gas absorption features. Away from the absorption features of vanillin, the well-known absorption line of carbon dioxide (CO_2) that is situated at 2353 cm^{-1} is assessed. It is enhanced thanks to the tailored surface upon its illumination under a co-polarized light. Indeed, by considering a steady environmental concentration of CO_2 inside the measurement room (400 ppm), a SEIRA-like signal is observed via the Al-BT and is especially enhanced by $L = 1.2\ \mu\text{m}$, as illustrated in **Figure 5.11**.

Thanks to an optimum spectral tuning, the inquired ω_{vib} is enhanced by ω_{res} of $L = 1.2\ \mu\text{m}$, compared to the detuning cases observed with $L = 1.3$ and $1.0\ \mu\text{m}$. Such enhancement is directly concluded from the baseline corrected (BC) line, which is mainly flat apart from the vibrational enhanced signal of CO_2 . For an ambient environment, the CO_2 concentration is taken as 400 ppm. A simulated spectrum is obtained from Hitran program with a plot increment of 0.5 cm^{-1} , under P_{atm} and room temperature ($T = 296\text{ K}$) on a path length of 10 cm (the assumed distance between the sample and the detector).

Analytically, the number of sensed CO_2 molecules can be estimated inside the gap volume as well as at the $A_{SEIRA} = 2 \times A_{eff}$ of the Al-BT. Thus, 5 400 molecules are expected into the gap volume of 10^6 nm^3 , and 22 molecules at the A_{SEIRA} , which is equivalent to 1 zeptogram.

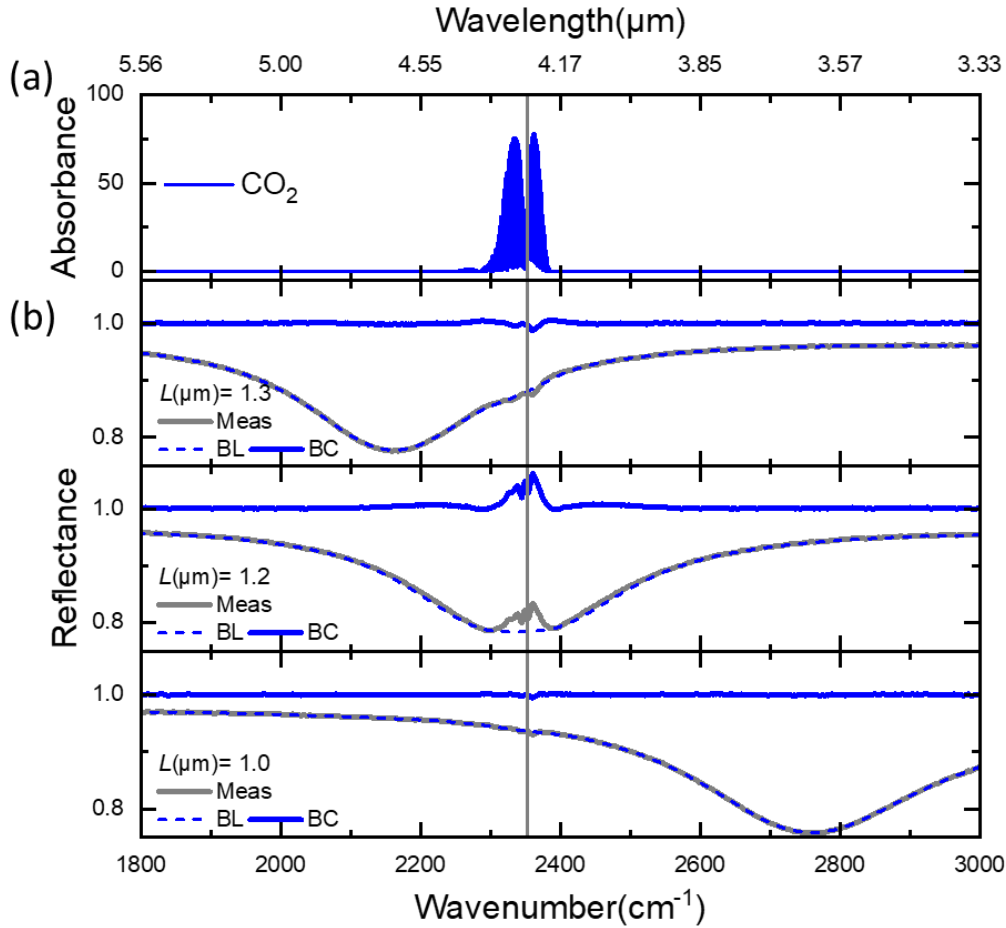


Figure 5.11. CO_2 signal enhancement in the ambient environment. (a) CO_2 synthetic absorption (%) spectrum generated by Hitran program, with a plot increment of 0.5 cm^{-1} , under P_{atm} and room temperature ($T=296\text{K}$) on a path length of 10 cm (assumed distance between the sample and the detector). (b) Reflectance spectra of Al-BT with different side lengths L varying from 1.3 to $1.0 \mu\text{m}$ with a step of $0.1 \mu\text{m}$, covering accordingly a wide spectral range from 1800 to 3000 cm^{-1} (gray curves). The dashed blue curves are the corresponding baseline (BL) fitted using Euler's smoothing algorithm, excluding the vibrational features. The blue lines are the relative baseline corrected reflectance spectra (BC) of the selected BT arrays. BC represents the vibrational signal strength of the CO_2 absorption peak whose position is denoted by the gray vertical line at 2353 cm^{-1} .

Similarly, HC compact antennas enhance the well-known CO_2 absorption line. The proof of principle is illustrated in **Figure 5.12** with various sets of L and g . The Fano-like SEIRA signals are observed and particularly enhanced by $L = 1.3 \mu\text{m}$ and a $g = 100 \text{ nm}$ and $L = 1.2 \mu\text{m}$ and a $g = 80 \text{ nm}$ thanks to a perfect coupling between their corresponding ω_{res} and the ω_{vib} of interest, compared to the detuning cases observed with the rest of the geometric parameters combinations.

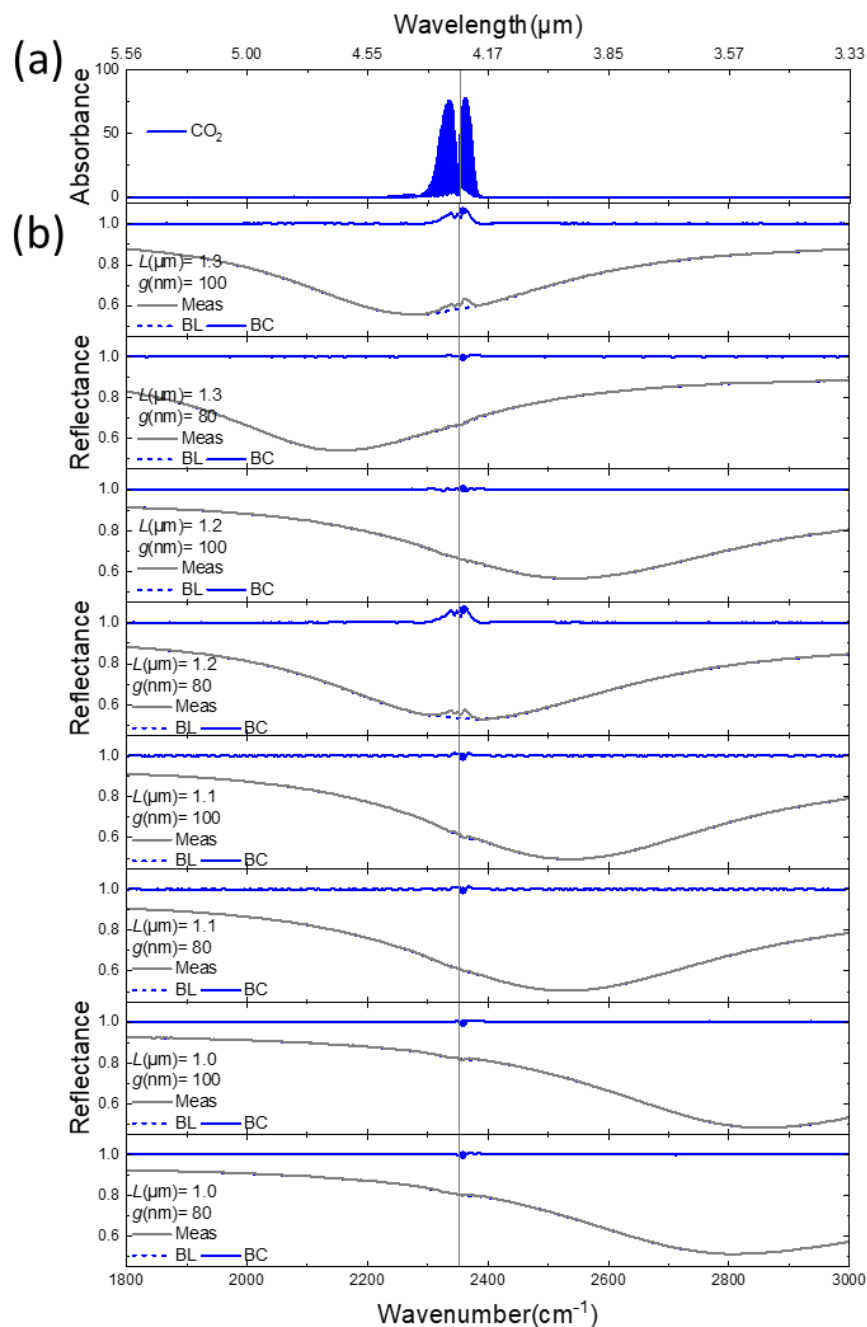


Figure 5. 12. CO_2 signal enhancement in the ambient environment using HC antennas under co-polarized light. (a) CO_2 synthetic absorption (%) spectrum generated by Hitran program, with a plot increment of 0.5 cm^{-1} , under P_{atm} and room temperature ($T = 296\text{K}$) on a path length of 10 cm (assumed distance between the sample and the detector). (b) Reflectance spectra of Al-HC with different side lengths L varying from 1.3 to 1.0 μm with a step of 0.1 μm , covering accordingly a wide spectral range from 1 800 to 3 000 cm^{-1} (gray curves). An extra spectral tuning is prompted by the gap value variation between 100 and 80 nm. The dashed blue curves are the corresponding BL fitted using Euler's smoothing algorithm, excluding the vibrational features. The blue lines are the relative baseline corrected reflectance spectra (BC) of the selected HC arrays. BC represents the enhanced vibrational signal strength of the CO_2 absorption peak whose position is denoted by the gray vertical line at 2 353 cm^{-1} .

Herein, the number of detected molecules slightly depends on the gap size, *i.e.* accessible volume, but same number is achieved per A_{SEIRA} . The activated gap of 100 nm yields 16 200 molecules in the six activated hotspots volume of $3 \times 10^6 \text{ nm}^3$, *i.e.* 135 molecules per A_{SEIRA} . Note that the number of the estimated molecules in the HC with a gap of 100 nm is 3 times higher than the previously retrieved value for the BT with the same gap value, as the activated area A_{SEIRA} is counting 3 times a BT-like tip-to-tip gap under co-polarized light. Though, for a gap of 80 nm, 8 100 molecules are detected in a volume of $80 \times 80 \times 80 \times 10^6 \text{ nm}^3$, yet 130 molecules per A_{SEIRA} . Hence, for both gap values, 10 zeptograms of ambient CO₂ are sensed.

The EF is also evaluated for CO₂ detection using both antennas, as presented in the **Figure 5.13**. EF is calculated for BT and HC based on **Equation 5.1**. Note that EF are strictly calculated for the best (L, g) combination giving the ideal frequencies tuning, as plotted in **Figure 5.11 and 5.12**. The highest value is found at $\omega_{vib}/\omega_{res} = 0.99$ using BT ($L = 1.2 \text{ }\mu\text{m}$ and $g = 100 \text{ nm}$) owing to the optimal achieved spectral coupling. The EF value is decreased using HC because of the number of the activated A_{SEIRA} as previously detailed in SEIRA proof using vanillin (**Chapter 5**). Still, EF remains in the same order of magnitude (10^5) regardless of the NA's shape. This value is matching the state-of-art for molecule detection, reported by Brown *et al.* and Vogt *et al.*. However, it is two orders of magnitude higher than the stated value by Chong *et al.* for CO₂ detection using silicon nitride nanomembrane on top of which plasmonic nanopatch of Au antennas are integrated with a metal-organic framework (MOF) to enable the CO₂ adsorption owing to its nanoporous structure.¹² In fact, the EF estimation of 1 800 was taking into consideration the metal–MOF interfaces to achieve strong optical field enhancement across the entire thick MOF film, unlike the conventional SEIRA sensing investigation detailed by Neubrech *et al.*⁴³ This value could be possibly better estimated by relying on highly localized hotspots (A_{SEIRA}) of the plasmonic NA.

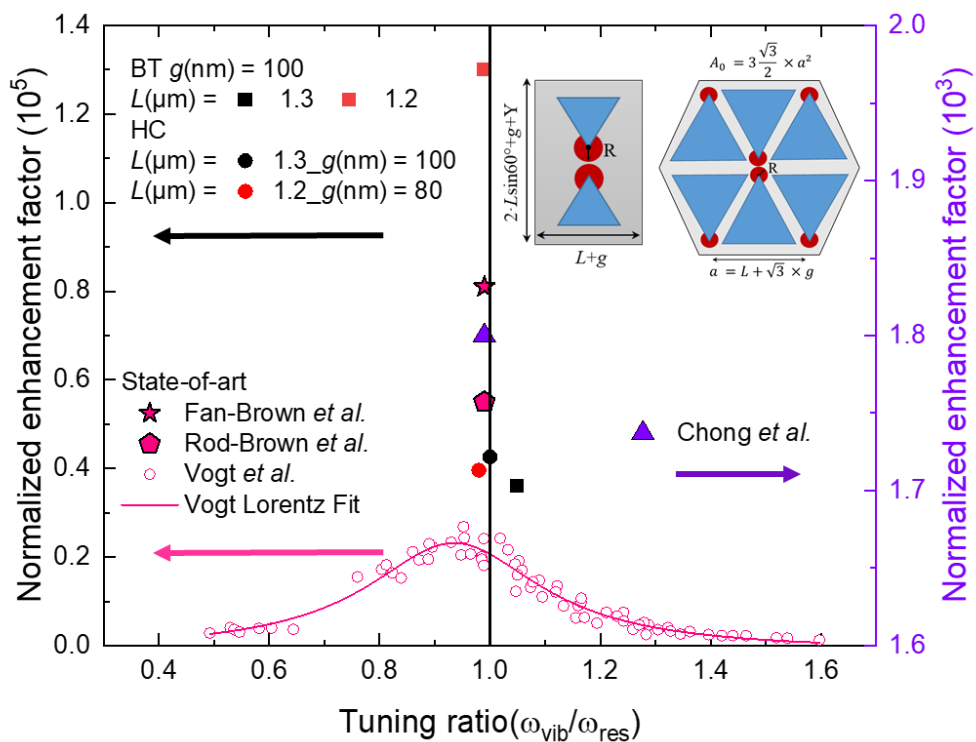


Figure 5. 13. Normalized enhancement factor (EF) For CO₂ detection using both BT and HC versus the tuning ratio ($\omega_{vib}/\omega_{res}$). For BT, L values are varied from 1.3 to 1.2 μm , the g value is fixed at 100 nm. Similarly, for HC, the g value is decreased from 100 to 80 nm. The error bars are in the size of the data points, so are not included. The inset shows the corresponding A_0 and A_{SEIRA} under a co-polarized light. The vibrational signal enhancement is generally maximized below $\omega_{vib}/\omega_{res} = 1$ (black line).

Ultimately, for a better estimation of the occurring SEIRA behavior obtained for an ambient CO₂ concentration (400 ppm), these results should be sequentially linked with supplementary measurements to be executed in a well-controlled chamber in which the flux (concentration) of CO₂ and/or the one of N₂ could be finely modulated.

5.3. Conclusion

In summary, the sensing peculiarity of a barcode-like plasmonic transducer was demonstrated in a wide spectral band ranging from 1 100 to 2 100 cm^{-1} . Thanks to the tunability of LSPR achieved by varying the geometry, several proof-of-principle experiments were presented to evaluate the performance of both suggested designs, *i.e.* bowties and honeycombs, for resonant SEIRA spectroscopy. The evaluation of Al oxide stability was required to reassure and provide a supportive environment for the development of SEIRA implementation using Al. Indeed, the plasmonic responses of Al-BT were undamaged after 2 years of being exposed to the atmosphere without any particular protection. Consequently, Al-BT arrays were illuminated under co- (or cross-) polarized light, offering by this a near-field distribution onto the inner (or the outer) tips of the BT. The LSPR of the Al-HC arrays, illuminated under a co-and un-polarized light, are fixed thanks to the geometry symmetric invariance. Regardless of the polarization, the number of 2.5×10^4 molecules per tip is similarly found, and in the same order of magnitude as the retrieved number of triggered molecules using HC antennas. This number is three orders of magnitude lower than the value reported by Barho *et al.* for vanillin detection ($\sim 5 \times 10^7$ molecules at the corners) with highly-doped semiconductor periodic rectangular. It is successfully matching the state-of-art as reported by Halas *et al.*⁶⁵, Neubrech *et al.*⁴³, and Brown *et al.*⁸⁵. Furthermore, in line with its dependency on the spectral tuning ratio, the size and shape of the Fano-like vibrational signals were evaluated.

By combining the vibrational signal strength with the plasmonic near-field investigation, the resulting enhancement factor was considered for all the involved illumination. Enhancement factors, EF, higher than 10^7 are found and perfectly match the state-of-art of SEIRA. The maximum EF is revealed for a tuning ratio slightly lower than 1, stating the pre-established behavior of a damped harmonic oscillator.

Moreover, the Al plasmonic transducer has shown promising particularity to identify the atmospheric carbon dioxide by SEIRA-stimulating its absorption line at $2\,353\text{ cm}^{-1}$ through both proposed metasurfaces and assuming a low gas concentration of a few hundreds of molecules

into the gap. A maximum EF of 10^5 is achieved using BT antennas with a tuning ratio below 1, matching the Vogt *et al.* findings.⁴⁶

Ultimately, to improve the SEIRA readout, smaller gaps can be finely designed, offering larger near-field enhancement inside the gap region as we have proved theoretically. Yet, in the far-field, the spectral influence of the gap value using the HC has presented a promising degree of freedom for an extended SEIRA study. In addition, a stronger near E-field intensity will in turn lead to a higher signal enhancement. Thus, an extremely propitious broadband sensitivity goes one step forward to building compact and low-cost bio-sensing devices for sensitive IR detection based on the trendy Si-technology.

General Conclusions and Perspectives

The main target of this research project is to associate the conception, the fabrication and the experimental characterization of advanced plasmonic nanostructures integrated within a MIM configuration and that sustain the lightning-rod and the gap-plasmon effects. To achieve these goals, a circular research methodology was followed and ended with a plasmonic-based sensing demonstration using the developed optical transducer. Periodic bowties and compact honeycomb nanoantennas were made of Al and implemented to cover a wide IR range, by sweeping their geometric features, namely, the side length of the equilateral triangles, L , and spacing, g .

The FDTD numerical studies on the geometric parameters of the nanostructures allowed to predict and control the spectral position of their corresponding plasmonic resonance frequencies. On the far-field spectral level, a red-shift of the plasmonic resonance is achieved as soon as L increases, in accordance with the antenna theory; and as the g decreases, agreeing with the atomic and molecular orbital hybridization principle. By this, a wide spectral range is effectively covered using BT from 0.9 to 6.6 μm (*i.e.* 11 200 to 1 500 cm^{-1} with a step of $\sim 86 \pm 30 \text{ cm}^{-1}$), by simply varying L from 0.2 to 2.0 μm with a step of 0.1 μm . While the HC cover the range between 1.0 to 6.6 μm (*i.e.* 10 000 to 1 540 cm^{-1} with a step of $\sim 70 \pm 30 \text{ cm}^{-1}$), by varying L from 1.0 to 2.0 μm with a step of 0.1 μm . Furthermore, g values are decreased from 100 nm down to 20 nm with a step of 20 nm and the LSPR is red-shifted $\sim 13 \pm 8 \text{ cm}^{-1}$.

On the near-field level, FDTD simulations have shown a stronger coupling between the closely placed tips where narrower gaps are triggered. An outstanding enhancement of the local E-field up to 10^3 is reached for $g = 20 \text{ nm}$. Such an enhancement is highly appealing for a sensitive molecule recognition at these advanced hotspots. Additionally, the influence of light polarization on both structures is evaluated. For a large gap, *i.e.* $g > 20 \text{ nm}$, the plasmonic resonances for a specific L are found intact regardless of the light polarization. However, the near EM-field is drastically driven by the polarization direction. It is strongly enhanced at the tip-to-tip facing triangles or at the corner-to-corner facing triangles under a respective polarization along or across the antenna axis (parallel to the height of the tip-to-tip facing triangles). The near EM-field

localization is a key parameter for the evaluation of SEIRA characteristics such as the number of sensed molecules per activated tip and the subsequent enhancement factor.

Following the conception, a cleanroom process was followed to fabricate the main substrate as well as to design both nanoantenna types. The main substrate is a Si-based MIM structure consisting of a 100 nm thick Al mirror, then a 20 nm thick SiO₂ layer as a spacer. At this stage, the BT tailoring begins with an EBL exposure of the triangles followed by the sputtering of a 50 nm thick Al layer. The sputtering method is appropriate for the upcoming lift-off step. However, the surface engineering of the HC array was defined in contrast to the exposed patterns thanks to a following etch. Indeed, on top of the SiO₂ spacer, a 50 nm thick Al layer is thermally deposited, and the MIM configuration is thus completed. Then, an EBL exposure defines linear openings for the following dry etching process and resist cleaning. Note that in both technological methods, a positive tone resist is implemented taking into consideration not only the lithography resolution but also the framework of the whole technology. In particular, PMMA is more suitable for a lift-off process that defines the BT structures thanks to its natural inclined side-definition. CSAR is adopted for a critical definition of the HC by exposing the nanolines horizontally (along 0°) then with a deviation of a 60°, and 120° from the horizontal. CSAR is well adapted for the dry-etching step. Based on SEM images, the geometric parameters of the fabricated structures were in good agreement with the estimated nominal values, this underlines the adeptness of both conceived technologies.

Experimental characterizations using a FTIR spectrometer have confirmed the far-field behavior of both nanoantenna types. While changing the L with a step of 0.1 μm , the LSPR was shifted by $\sim 80 \pm 30 \text{ cm}^{-1}$ for BT and $\sim 100 \pm 50 \text{ cm}^{-1}$ for HC. For HC, the spectral shift seems larger for the FTIR measurements as the fabricated structures were not perfectly defined. Furthermore, using the FPA mode, the LSPR of BT is red-shifted by $\sim 10 \pm 5 \text{ cm}^{-1}$ while g is decreased by a step of 20 nm. Noteworthy, for a fixed selection of L and g , the advantage of the compact arrangement was expressed as an improvement of around 20% of the plasmonic resonance amplitude in comparison with the response of the BT arrays. Furthermore, the response of the HC has shown a slight red-shift ($\sim 20 \pm 4 \text{ cm}^{-1}$) compared to the BT resonance as the interaction between the

adjacent triangles is becoming more effective, and thus, arising at lower energy. These values are fairly matching the FDTD results.

Noteworthy, the imaging capability of the FTIR spectrometer mediated by the FPA detector was effectively used to evaluate a pixelated surface response and its homogeneity as well as to prove the molecule dispersion once the droplet covers the sample surface. FPA imaging is a challenging but compelling method to attempt for an immediate evaluation of surface sensing as it offers a unique advantage to assess qualitatively the SEIRA global zone activation.

SEIRA investigation was demonstrated for organic liquid solution (1 μl droplet of 2 mg/ml, 2 000 ppm of vanillin in IPA), and inorganic gas compound (a 400 ppm of ambient CO_2). Thanks to the flexible coverage of a wide IR spectral range, several absorption features of vanillin (ω_{vib}) were addressed and differently coupled to the intrinsic plasmonic resonance (ω_{res}) of the nanoantennas (L between 2.0 and 1.4 μm , with a step of 0.1 μm). In line with this, the well-known vibration frequency of CO_2 , ω_{vib} around 2 353 cm^{-1} , was interestingly enhanced as well via a set of nanoantennas with L ranging between 1.3 and 1.0 μm , with a step of 0.1 μm .

For all the SEIRA experiments, the coupling strength was interpreted through the amplitude and the shape of the resulting asymmetric profiles (vibrational signals) and is modulated by a tuning ratio $\omega_{vib}/\omega_{res}$. Indeed, when $\omega_{vib}/\omega_{res}$ is around 1, the amplitude vibrational signals achieves its maximum value for different L values, stating the best spectral overlap between ω_{vib} and ω_{res} . Moreover, the vibrational signal shapes were impacted by the tuning ratio: for $\omega_{vib}/\omega_{res}$ above 1, the signal shape keeps on the conformist asymmetric outline but with inverted minimum and maximum compared to tunings below 1. Noteworthy, SPR sensing is noticed using both NA in presence of vanillin/ethanol solution with a sensitivity $\sim 10^2$ nm/RIU, similar to the reported values for metallic nanoparticles by Mayer *et al.*³¹

The SEIRA enhancement factor (EF) has achieved a value of 10^7 for a tuning ratio $\omega_{vib}/\omega_{res} = 0.98$ under a co-polarized light, owing to the effective MIM configuration and the gap effects at the sharp apexes of both nanoantennas types. Approximately, 10^4 molecules were assumed per tip for both structures despite of the triangle arrangement, *i.e.* difference in A_0 definition and A_{SEIRA} quantification. Note that, given the symmetry invariance of the HC, an un-polarized light was used

for SEIRA demonstration. Under un-polarized light, the EF loses one order of magnitude (EF at 10^6) for the HC due to a reduction of the near E-field intensity under cross-polarized light based on FDTD simulations, as the un-polarized light embraces both polarization cases. Furthermore, the gap effect in the HC case was underlined using un-polarized light. The gap reduction of 20 nm showed a global red-shift of $\Delta\omega_{res} \sim 50 \text{ cm}^{-1} \pm 4 \text{ cm}^{-1}$ (simulated value of $\Delta\omega_{res} \sim 43 \pm 10 \text{ cm}^{-1}$), presenting a promising degree of freedom for an extended SEIRA study.

In sum, the main scientific barrier is lifted by enabling a multispectral optical measurement using the same transducer surface, as proposed by Altug's group using pixelated dielectric metasurfaces, but with Al structures. However, in our case, we took advantage of the broadening of LSPR (high FWHM) to enhance and spectrally evaluate the SEIRA features (Fano-like profiles). Each zone region with fixed geometric parameters will resonate in a small part of the electromagnetic spectrum. The collection of zones could cover the entire spectral range from the visible to the MIR. Then, the deposited molecules onto the plasmonic resonators will be identified through their enhanced absorption signature, similarly to the SEIRA proof-of-concept.

To implement such a promising barcode-like identification of different absorption features in a single test, the transducer surface should be CMOS-compatible. Herein, the second technical barrier is lifted by proposing an alternative material for noble metals, namely Al, that is abundant, affordable, and considered as "Drude metal". Furthermore, Al is wisely shaped to achieve important field enhancement in the different spectral regions by suggesting two arrangements of closely-placed sharp equilateral triangles arrays, *i.e.* as bowties or honeycombs. Both types are integrated into a MIM structure to further enhance the local EM-fields amplification at the gaps. Well-adapted technological processes were detailed for the fabrication of both nanoantennas with an achieved precision and repeatability at the nanoscale. Hence, a future transfer of the optical transducer to industrial mass-production is possible as it can rely on standard cleanroom technologies such as EBL, lift-off, argon etching, and plasmaO₂ for resist cleaning.

As for the perspectives, the near-field behavior at the tips was not evaluated by the lack of FTIR resolution and of other equipments. Here, scattering-type scanning near-field optical microscope (s-SNOM) imaging of the hotspot could be implemented in the IR. Photoemission electron

microscopy (PEEM) could be a promising method that allows high-resolution near-field mapping. In addition to PEEM imaging, in the low-energy electron microscopy (LEEM) mode. The backscattered electrons can be used to create an image that reflects the topography of the sample with a spatial resolution is close to 10 nm. Plus, a chemical evaluation can assist the near-field localization, using light-sensitive surface functionalization, *e.g.* diazonium salt. A possible collaboration could be established with the plasmonic team at the university of Paris Diderot for the diazonium salt experiments. Such a technique is still immature neither for Al nanostructures nor for addressing the IR. Nevertheless, it is an encouraging step for the BT which addresses the visible range (with $L \leq 0.2 \mu\text{m}$). Indeed, by preferentially grafting in the areas where the electric field enhancement is maximum, it will support the theoretical assumption of the activated tip of SEIRA (A_{SEIRA}). It could also be an attractive strategy for the spatially controlled surface functionalization of Al plasmonic nanoantennas, by using phosphoric acid for example, and to attach distinct molecules to hotspot regions on a single nanoparticle, opening promising prospects in sensing potential post-functionalization.

For more precision in SEIRA quantification, the upcoming work should focus on an extensive study of the smaller gap influence on the SEIRA readout. Special attention should be given to the surface functionalization and the precise area of the near-field taken into the EF calculations. Precise analysis should be investigated to evaluate the limit of detection for both liquid and gas sensing, by decreasing the analyte concentration and controlling the gas parameters as the flux and the pressure in a well-controlled environment. For fine control of the CO₂ concentration down to a few ppm, it is recommended to contact the IM2NP lab at Aix-Marseille University for possible setup assembly and/or measurements.

Regarding the optical characterization, the BT nanostructures could sustain an encouraging talent for second harmonic generation (SHG), the Nano-optics lab at Politecnico di Milano might be a potential destination for such nonlinear optical measurements.

The Al nanoantennas are also useful for performing spectroscopic measurements in the visible range where the electronic transitions of the molecules are situated. For other biomedical and environmental sensing applications, and to dive farther in the IR towards the THz range, on the

same platform, these metallic zones can be joined with a well-studied highly-doped semiconductors antennas, namely Ge, InAsSb, and GaSb, by controlling their geometry and doping levels. These materials offer the possibility of tuning an intrinsic parameter for traditional metals, namely their plasma frequency via the doping level. Interestingly, such an anticipated plasmonic platform, active from the visible to the THz, can be considered as a fascinating tool to decode the whole bio-information of any molecule in a single test.

In a long-term vision, the on-chip integration could combine a source and detector with some microfluidic circuits in a Si platform for a barcode-like sensing. This could be done at the Centrale Technologique en micro/nanoélectronique (CTM) of the University of Montpellier thanks to the know-how of the nanoMIR group in the field of the light source and the detectors fabrication on Si wafer. Further strategies can complete the sensing application in the IR and the THz ranges owing to the research methodology of the Plasmonics team that is focusing on implementing the intentionally-doped semiconductors which are epitaxially grown as either perfect absorbers or ENZ materials, to detect in the MIR and the THz. Potential detections of biomolecules in the MIR and the THz using III-V materials are parallel projects in which I was also engaged.

The actual work is the first Ph.D. project in the nanoMIR group dedicated to realize detection assays in a broad spectral range using metallic-based plasmonic nanoresonators with sophisticated geometries. The structures were fabricated thanks to an excellent knowledge exchange with the LAAS. It is hoped that this thesis brings a good understanding of the four settled axes, notably in simulation, fabrication, optical characterization, and detection evaluation using Al-based optical transducer. It is wished to be an encouraging conduction to achieve the foreseen steps for the amelioration of the actual transducer readout.

Bibliography

- (1) Maier, S. A. *Plasmonics: Fundamentals and Applications*; Springer, 2007.
- (2) Mihail Petrov, A. B. *Plasmonics: From Fundamentals to Modern Applications*. ITMO University and edx. <https://courses.edx.org/courses/course-v1:ITMOx+PLASMx+2T2020a/course/updates>.
- (3) BARBER, D. J.; FREESTONE, I. C. An Investigation of the Origin of the Colour of the Lycurgus Cup By Analytical Transmission Electron Microscopy. *Archaeometry* **1990**, *32* (1), 33–45. <https://doi.org/10.1111/j.1475-4754.1990.tb01079.x>.
- (4) Rodrigues, M. S.; Borges, J.; Lopes, C.; Pereira, R. M. S.; Vasilevskiy, M. I.; Vaz, F. Gas Sensors Based on Localized Surface Plasmon Resonances: Synthesis of Oxide Films with Embedded Metal Nanoparticles, Theory and Simulation, and Sensitivity Enhancement Strategies. *Appl. Sci.* **2021**, *11* (12). <https://doi.org/10.3390/app11125388>.
- (5) Stockman, M. I. Nanoplasmonics: The Physics behind the Applications. *Phys. Today* **2011**, *64* (2), 39–44. <https://doi.org/10.1063/1.3554315>.
- (6) Maier, S. A.; Atwater, H. A. Plasmonics : Localization and Guiding of Electromagnetic Energy in Metal / Dielectric Structures. *Appl. Phys. Rev. – Focus. Rev.* **2005**, *98* (011101), 1–10. <https://doi.org/10.1063/1.1951057>.
- (7) Ebbesen, T. W.; Lezec, H. J.; Ghaemi, H. F.; Thio, T.; Wolff, P. A. Extraordinary Optical Transmission through Sub-Wavelength Hole Arrays. *Nature* **1998**, *391* (6668), 667–669. <https://doi.org/10.1038/35570>.
- (8) Abasahl, B.; Santschi, C.; Raziman, T. V.; Martin, O. J. F. Fabrication of Plasmonic Structures with Well-Controlled Nanometric Features: A Comparison between Lift-off and Ion Beam Etching. *Nanotechnology* **2021**, *32* (47). <https://doi.org/10.1088/1361-6528/ac1a93>.
- (9) Aubry, A.; Lei, D. Y.; Ferna, A. I.; Sonnefraud, Y.; Maier, S. A.; Pendry, J. B. Plasmonic Light-Harvesting Devices over the Whole Visible Spectrum. *Nano Lett.* **2010**, *10* (7), 2574–2579. <https://doi.org/10.1021/nl101235d>.

- (10) Barbillon, G. Plasmonics and Its Applications. *Materials (Basel)*. **2019**, *12* (1502), 10–13. <https://doi.org/10.3390/ma12091502>.
- (11) Liu, J.; Jalali, M.; Mahshid, S.; Wachsmann-Hogiu, S. Are Plasmonic Optical Biosensors Ready for Use in Point-of-Need Applications? *Analyst* **2020**, *145* (2), 364–384. <https://doi.org/10.1039/c9an02149c>.
- (12) Chong, X.; Zhang, Y.; Li, E.; Kim, K. J.; Ohodnicki, P. R.; Chang, C. H.; Wang, A. X. Surface-Enhanced Infrared Absorption: Pushing the Frontier for On-Chip Gas Sensing. *ACS Sensors* **2018**, *3* (1), 230–238. <https://doi.org/10.1021/acssensors.7b00891>.
- (13) Davis, T. J.; Gómez, D. E.; Roberts, A. Review Article Plasmonic Circuits for Manipulating Optical Information. *Nanophotonics* **2017**, *6* (3), 543–559. <https://doi.org/10.1515/nanoph-2016-0131>. Le Plasmonic Circuits for Manipulating Optical Inf. *Nanophotonics* **2017**, *6* (3), 543–559. <https://doi.org/10.1515/nanoph-2016-0131>.
- (14) Ricciardi, A.; Crescitelli, A.; Vaiano, P.; Quero, G.; Consales, M.; Pisco, M.; Esposito, E.; Cusano, A. Lab-on-Fiber Technology: A New Vision for Chemical and Biological Sensing. *Analyst* **2015**, *140* (24), 8068–8079. <https://doi.org/10.1039/c5an01241d>.
- (15) Halas, N. J.; Lal, S.; Link, S.; Chang, W. S.; Natelson, D.; Hafner, J. H.; Nordlander, P. A Plethora of Plasmonics from the Laboratory for Nanophotonics at Rice University. *Adv. Mater.* **2012**, *24* (36), 4842–4877. <https://doi.org/10.1002/adma.201202331>.
- (16) Abdulhalim, I. A Comprehensive Review on Plasmonic-Based Biosensors Used in Viral Diagnostics. *Commun Biol* **2021**, *4* (70), 1–12. <https://doi.org/10.1038/s42003-020-01615-8>.
- (17) Drude, P. Zur Elektronentheorie Der Metalle. *Ann. Phys.* **1900**, *306* (3), 566–613.
- (18) Hoddeson, L.; Baym, G. The Development of the Quantum Mechanical Electron Theory of Metals: 1900–28. *Proc. R. Soc. A* **1980**, *371* (1744), 8–23. <https://doi.org/10.1098/rspa.1980.0051>.

- (19) Taliercio, T.; Biagioni, P. Semiconductor Infrared Plasmonics. *Nanophotonics* **2019**, *8* (6), 949–990. <https://doi.org/https://doi.org/10.1515/nanoph-2019-0077>.
- (20) BARHO, F. B. Ingénierie de Résonateurs Plasmoniques à Base de Semi - Conducteurs Fortement Dopés Pour l'exaltation de l'absorption de Molécules Dans Le Moyen Infrarouge, Université de Montpellier, 2017.
- (21) Kulkarni, M. B.; Ayachit, N. H.; Aminabhavi, T. M. Biosensors and Microfluidic Biosensors: From Fabrication to Application. *Biosensors* **2022**, *12* (543), 2–25. <https://doi.org/10.3390/bios12070543>.
- (22) Naresh, V.; Lee, N. A Review on Biosensors and Recent Development of Nanostructured Materials-Enabled Biosensors. *Sensors (Switzerland)* **2021**, *21* (4), 1–35. <https://doi.org/10.3390/s21041109>.
- (23) Minopoli, A.; Acunzo, A.; Della Ventura, B.; Velotta, R. Nanostructured Surfaces as Plasmonic Biosensors: A Review. *Adv. Mater. Interfaces* **2022**, *9* (2), 1–29. <https://doi.org/10.1002/admi.202101133>.
- (24) Liedberg, B.; Nylander, C.; Lundstrom, I. Surface Plasmon Resonance for Gas Detection and Biosensing. *Sensors and Actuators* **1983**, *4* (025–6874), 299–304. [https://doi.org/https://doi.org/10.1016/0250-6874\(83\)85036-7](https://doi.org/https://doi.org/10.1016/0250-6874(83)85036-7).
- (25) Chadha, U.; Bhardwaj, P.; Agarwal, R.; Rawat, P.; Agarwal, R.; Gupta, I.; Panjwani, M.; Singh, S.; Ahuja, C.; Selvaraj, S. K.; Banavoth, M.; Sonar, P.; Badoni, B.; Chakravorty, A. Recent Progress and Growth in Biosensors Technology: A Critical Review. *J. Ind. Eng. Chem.* **2022**, *109*, 21–51. <https://doi.org/https://doi.org/10.1016/j.jiec.2022.02.010>.
- (26) Chen, C.; Wang, J. Optical Biosensors: An Exhaustive and Comprehensive Review. *Analyst* **2020**, *145* (5), 1605–1628. <https://doi.org/10.1039/c9an01998g>.
- (27) Jongerius-Gortemaker, B. G. M.; Goverde, R. L. J.; van Knapen, F.; Bergwerff, A. A. Surface Plasmon Resonance (BIACORE) Detection of Serum Antibodies against Salmonella Enteritidis and Salmonella Typhimurium. *J. Immunol. Methods* **2002**, *266* (1), 33–44. [https://doi.org/https://doi.org/10.1016/S0022-1759\(02\)00102-3](https://doi.org/https://doi.org/10.1016/S0022-1759(02)00102-3).

- (28) Park, T. J.; Hyun, M. S.; Lee, H. J.; Lee, S. Y.; Ko, S. A Self-Assembled Fusion Protein-Based Surface Plasmon Resonance Biosensor for Rapid Diagnosis of Severe Acute Respiratory Syndrome. *Talanta* **2009**, *79* (2), 295–301. <https://doi.org/10.1016/j.talanta.2009.03.051>.
- (29) Calvo-Lozano, O.; Sierra, M.; Soler, M.; Estévez, M. C.; Chiscano-Camón, L.; Ruiz-Sanmartin, A.; Ruiz-Rodriguez, J. C.; Ferrer, R.; González-López, J. J.; Esperalba, J.; Fernández-Naval, C.; Bueno, L.; López-Aladid, R.; Torres, A.; Fernández-Barat, L.; Attoumani, S.; Charrel, R.; Coutard, B.; Lechuga, L. M. Label-Free Plasmonic Biosensor for Rapid, Quantitative, and Highly Sensitive COVID-19 Serology: Implementation and Clinical Validation. *Anal. Chem.* **2022**, *94* (2), 975–984. <https://doi.org/10.1021/acs.analchem.1c03850>.
- (30) Le, F.; Brandl, D. W.; Urzhumov, Y. A.; Wang, H.; Kundu, J.; Halas, N. J.; Aizpurua, J.; Nordlander, P. Metallic Nanoparticle Arrays : A Common. *ACS Nano* **2008**, *2* (4), 707–718. <https://doi.org/https://doi.org/10.1021/nn800047e>.
- (31) Mayer, K. M.; Hafner, J. H. Localized Surface Plasmon Resonance Sensors. *Chem. Rev.* **2011**, *111* (6), 3828–3857. <https://doi.org/10.1021/cr100313v>.
- (32) Li, W.; Ren, K.; Zhou, J. Aluminum-Based Localized Surface Plasmon Resonance for Biosensing. *TrAC - Trends Anal. Chem.* **2016**, *80*, 486–494. <https://doi.org/10.1016/j.trac.2015.08.013>.
- (33) Dos Santos, P. S. S.; de Almeida, J. M. M. M.; Pastoriza-santos, I.; Coelho, L. C. C. Advances in Plasmonic Sensing at the Nir—a Review. *Sensors* **2021**, *21* (6), 1–48. <https://doi.org/10.3390/s21062111>.
- (34) Forest, S.; Théorêt, T.; Coutu, J.; Masson, J. F. A High-Throughput Plasmonic Tongue Using an Aggregation Assay and Nonspecific Interactions: Classification of Taste Profiles in Maple Syrup. *Anal. Methods* **2020**, *12* (19), 2460–2468. <https://doi.org/10.1039/c9ay01942a>.
- (35) Etezadi, D.; Warner, J. B.; Lashuel, H. A.; Altug, H. Real-Time in Situ Secondary Structure Analysis of Protein Monolayer with Mid-Infrared Plasmonic Nanoantennas. *ACS Sensors* **2018**, *3* (6), 1109–1117. <https://doi.org/10.1021/acssensors.8b00115>.
- (36) Kalluri, R.; S.LeBleu, V. The Biology, Function, and Biomedical Applications of Exosomes.

- Science* (80-.). **2020**, *367* (6478), 1–40. <https://doi.org/10.1126/science.aau6977>.The.
- (37) Jahani, Y.; Arvelo, E. R.; Yesilkoy, F.; Koshelev, K.; Cianciaruso, C.; De Palma, M.; Kivshar, Y.; Altug, H. Imaging-Based Spectrometer-Less Optofluidic Biosensors Based on Dielectric Metasurfaces for Detecting Extracellular Vesicles. *Nat. Commun.* **2021**, *12* (1), 4–13. <https://doi.org/10.1038/s41467-021-23257-y>.
- (38) Beliaev, L. Y.; Stounbjerg, P. G.; Finco, G.; Bunea, A. I.; Malureanu, R.; Lindvold, L. R.; Takayama, O.; Andersen, P. E.; Lavrinenko, A. V. Pedestal High-Contrast Gratings for Biosensing. *Nanomaterials* **2022**, *12* (10), 1–10. <https://doi.org/10.3390/nano12101748>.
- (39) Wang, B.; Singh, S. C.; Lu, H.; Guo, C. Design of Aluminum Bowtie Nanoantenna Array with Geometrical Control to Tune LSPR from UV to Near-IR for Optical Sensing. *Plasmonics* **2020**, *15* (3), 609–621. <https://doi.org/10.1007/s11468-019-01071-z>.
- (40) Wang, H. L.; You, E. M.; Panneerselvam, R.; Ding, S. Y.; Tian, Z. Q. Advances of Surface-Enhanced Raman and IR Spectroscopies: From Nano/Microstructures to Macro-Optical Design. *Light Sci. Appl.* **2021**, *10* (1). <https://doi.org/10.1038/s41377-021-00599-2>.
- (41) Zheng, Y.; Rosa, L.; Thai, T.; Ng, S. H.; Juodkazis, S.; Bach, U. Phase Controlled SERS Enhancement. *Sci. Rep.* **2019**, *9* (1), 1–9. <https://doi.org/10.1038/s41598-018-36491-0>.
- (42) Ataka, K.; Heberle, J. Biochemical Applications of Surface-Enhanced Infrared Absorption Spectroscopy. *Anal. Bioanal. Chem.* **2007**, *388* (1), 47–54. <https://doi.org/10.1007/s00216-006-1071-4>.
- (43) Neubrech, F.; Huck, C.; Weber, K.; Pucci, A.; Giessen, H. Surface-Enhanced Infrared Spectroscopy Using Resonant Nanoantennas. *Chem. Rev.* **2017**, *117* (7), 5110–5145. <https://doi.org/10.1021/acs.chemrev.6b00743>.
- (44) Adato, R.; Artar, A.; Erramilli, S.; Altug, H. Engineered Absorption Enhancement and Induced Transparency in Coupled Molecular and Plasmonic Resonator Systems. *Nano Lett.* **2013**, *13* (6), 2584–2591. <https://doi.org/10.1021/nl400689q>.
- (45) John-Herpin, A.; Tittl, A.; Kühner, L.; Richter, F.; Huang, S. H.; Shvets, G.; Oh, S.; Altug, H.

- Metasurface-Enhanced Infrared Spectroscopy: An Abundance of Materials and Functionalities. *Adv. Mater.* **2022**, 2110163. <https://doi.org/10.1002/adma.202110163>.
- (46) Vogt, J.; Huck, C.; Neubrech, F.; Toma, A.; Gerbert, D.; Pucci, A. Impact of the Plasmonic Near- and Far-Field Resonance-Energy Shift on the Enhancement of Infrared Vibrational Signals. *Phys. Chem. Chem. Phys.* **2014**, *17* (33), 21169–21175. <https://doi.org/10.1039/c4cp04851b>.
- (47) Huck, C.; Neubrech, F.; Vogt, J.; Toma, A.; Gerbert, D.; Katzmann, J.; Härtling, T.; Pucci, A. Surface-Enhanced Infrared Spectroscopy Using Nanometer-Sized Gaps. *ACS Nano* **2014**, *8* (5), 4908–4914. <https://doi.org/10.1021/nn500903v>.
- (48) Zuloaga, J.; Nordlander, P. On the Energy Shift between Near-Field and Far-Field Peak Intensities in Localized Plasmon Systems. *Nano Lett.* **2011**, *11* (3), 1280–1283. <https://doi.org/10.1021/nl1043242>.
- (49) Alonso-González, P.; Albella, P.; Neubrech, F.; Huck, C.; Chen, J.; Golmar, F.; Casanova, F.; Hueso, L. E.; Pucci, A.; Aizpurua, J.; Hillenbrand, R. Experimental Verification of the Spectral Shift between Near- and Far-Field Peak Intensities of Plasmonic Infrared Nanoantennas. *Phys. Rev. Lett.* **2013**, *110* (20), 1–6. <https://doi.org/10.1103/PhysRevLett.110.203902>.
- (50) Kherbouche, I.; Macrae, D.; Geronimi Jourdain, T.; Lagugné-Labarthet, F.; Lamouri, A.; Chevillot Biraud, A.; Mangeney, C.; Félidj, N. Extending Nanoscale Patterning with Multipolar Surface Plasmon Resonances. *Nanoscale* **2021**, *13* (25), 11051–11057. <https://doi.org/10.1039/d1nr02181h>.
- (51) Zhou, J.; Wang, Y.; Zhang, L.; Li, X. Plasmonic Biosensing Based on Non-Noble-Metal Materials. *Chinese Chem. Lett.* **2018**, *29* (1), 54–60. <https://doi.org/10.1016/j.ccllet.2017.09.003>.
- (52) Chung, T.; Lee, S. Y.; Song, E. Y.; Chun, H.; Lee, B. Plasmonic Nanostructures for Nano-Scale Bio-Sensing. *Sensors* **2011**, *11* (11), 10907–10929. <https://doi.org/10.3390/s111110907>.
- (53) Barizuddin S, Bok S, G. S. Plasmonic Sensors for Disease Detection - A Review. *J. Nanomed. Nanotechnol.* **2016**, *7* (3). <https://doi.org/10.4172/2157-7439.1000373>.

- (54) Gonçalves, M. R. Plasmonic Nanoparticles: Fabrication, Simulation and Experiments. *J. Phys. D. Appl. Phys.* **2014**, *47* (21). <https://doi.org/10.1088/0022-3727/47/21/213001>.
- (55) Lin, L.; Zheng, Y. Optimizing Plasmonic Nanoantennas via Coordinated Multiple Coupling. *Sci. Rep.* **2015**, *5* (14788), 1–11. <https://doi.org/10.1038/srep14788>.
- (56) Olmon, R. L.; Krenz, P. M.; Jones, A. C.; Boreman, G. D.; Raschke, M. B. Near-Field Imaging of Optical Antenna Modes in the Mid-Infrared. *Opt. Express* **2008**, *16* (25), 20295. <https://doi.org/10.1364/oe.16.020295>.
- (57) Tramarin, L.; Barrios, C. A. Design of an Aluminum/Polymer Plasmonic 2d Crystal for Label-Free Optical Biosensing. *Sensors (Switzerland)* **2018**, *18* (10). <https://doi.org/10.3390/s18103335>.
- (58) Subbaiah, G. B.; Ratnam, K. V.; Janardhan, S.; Shiprath, K.; Manjunatha, H.; Ramesha, M.; Prasad, N. V. K.; Ramesh, S.; Babu, T. A. Metal and Metal Oxide Based Advanced Ceramics for Electrochemical Biosensors-A Short Review. *Front. Mater.* **2021**, *8* (June), 1–9. <https://doi.org/10.3389/fmats.2021.682025>.
- (59) Abb, M.; Wang, Y.; Papisimakis, N.; De Groot, C. H.; Muskens, O. L. Surface-Enhanced Infrared Spectroscopy Using Metal Oxide Plasmonic Antenna Arrays. *Nano Lett.* **2014**, *14* (1), 346–352. <https://doi.org/10.1021/nl404115g>.
- (60) Gerard, D.; Gray, S. K. Aluminium Plasmonics. *J. Phys. D. Appl. Phys.* **2015**, *48* (18), 184001. <https://doi.org/10.1088/0022-3727/48/18/184001>.
- (61) Knight, M. W.; King, N. S.; Liu, L.; Everitt, H. O.; Nordlander, P.; Halas, N. J. Aluminum for Plasmonics. *ACS Nano* **2014**, *8* (1), 834–840. <https://doi.org/10.1021/nn405495q>.
- (62) Shiles, E.; Sasaki, T.; Inokuti, M.; Smith, D. Y. Self-Consistency and Sum-Rule Tests in the Kramers-Kronig Analysis of Optical Data: Applications to Aluminum. *Phys. Rev. B* **1980**, *22* (4), 1612–1628. <https://doi.org/10.1103/PhysRevB.22.1612>.
- (63) Li, Z.; Wang, W.; Rosenmann, D.; Czaplewski, D. A.; Yang, X.; Gao, J. All-Metal Structural Color Printing Based on Aluminum Plasmonic Metasurfaces. *Opt. Express* **2016**, *24* (18),

20472. <https://doi.org/10.1364/oe.24.020472>.
- (64) Martin, J.; Plain, J. Fabrication of Aluminium Nanostructures for Plasmonics. *J. Phys. D. Appl. Phys.* **2015**, *48* (18), 184002. <https://doi.org/10.1088/0022-3727/48/18/184002>.
- (65) Cerjan, B.; Yang, X.; Nordlander, P.; Halas, N. J. Asymmetric Aluminum Antennas for Self-Calibrating Surface-Enhanced Infrared Absorption Spectroscopy. *ACS Photonics* **2016**, *3* (3), 354–360. <https://doi.org/10.1021/acsp Photonics.6b00024>.
- (66) Lecarme, O.; Sun, Q.; Ueno, K.; Misawa, H. Robust and Versatile Light Absorption at Near-Infrared Wavelengths by Plasmonic Aluminum Nanorods. *ACS Photonics* **2014**, *1* (6), 538–546. <https://doi.org/10.1021/ph500096q>.
- (67) Arora, P.; Awasthi, H. V. Aluminum-Based Engineered Plasmonic Nanostructures for the Enhanced Refractive Index and Thickness Sensing in Ultraviolet-Visible-near Infrared Spectral Range. *Prog. Electromagn. Res. M* **2019**, *79* (January), 167–174. <https://doi.org/10.2528/PIERM19012401>.
- (68) Dodson, S.; Haggui, M.; Bachelot, R.; Plain, J.; Li, S.; Xiong, Q. Optimizing Electromagnetic Hotspots in Plasmonic Bowtie Nanoantennae. *J. Phys. Chem. Lett.* **2013**, *4* (3), 496–501. <https://doi.org/10.1021/jz302018x>.
- (69) Li, L.; Fang Lim, S.; Puretzky, A. A.; Riehn, R.; Hallen, H. D. Near-Field Enhanced Ultraviolet Resonance Raman Spectroscopy Using Aluminum Bow-Tie Nano-Antenna. *Appl. Phys. Lett.* **2012**, *101* (11), 1–5. <https://doi.org/10.1063/1.4746747>.
- (70) Cerjan, B.; Halas, N. J. Toward a Nanophotonic Nose: A Compressive Sensing-Enhanced, Optoelectronic Mid-Infrared Spectrometer. *ACS Photonics* **2019**, *6* (1), 79–86. <https://doi.org/10.1021/acsp Photonics.8b01503>.
- (71) Wang, H.; Brandl, D. W.; Nordlander, P.; Halas, N. J. Plasmonic Nanostructures: Artificial Molecules. *Acc. Chem. Res.* **2007**, *40* (1), 53–62. <https://doi.org/10.1021/ar0401045>.
- (72) Chen, K.; Dao, T. D.; Ishii, S.; Aono, M.; Nagao, T. Infrared Aluminum Metamaterial Perfect Absorbers for Plasmon-Enhanced Infrared Spectroscopy. *Adv. Funct. Mater.* **2015**, *25* (42),

- 6637–6643. <https://doi.org/10.1002/adfm.201501151>.
- (73) Biagioni, P.; Huang, J. S.; Hecht, B. Nanoantennas for Visible and Infrared Radiation. *Reports Prog. Phys.* **2012**, *75* (2), 1–40. <https://doi.org/10.1088/0034-4885/75/2/024402>.
- (74) Kasani, S.; Curtin, K.; Wu, N. A Review of 2D and 3D Plasmonic Nanostructure Array Patterns: Fabrication, Light Management and Sensing Applications. *Nanophotonics* **2019**, *8* (12), 2065–2089. <https://doi.org/10.1515/nanoph-2019-0158>.
- (75) Simon, T.; Li, X.; Martin, J.; Khlopin, D.; Stéphan, O.; Kociak, M.; Gérard, D. Aluminum Cayley Trees as Scalable, Broadband, Multiresonant Optical Antennas. *Appl. Phys. Sci.* **2022**, *119* (4), 1–6. <https://doi.org/10.1073/pnas.2116833119/-/DCSupplemental>. Published.
- (76) Tan, S. J.; Zhang, L.; Zhu, D.; Goh, X. M.; Wang, Y. M.; Kumar, K.; Qiu, C. W.; Yang, J. K. W. Plasmonic Color Palettes for Photorealistic Printing with Aluminum Nanostructures. *Nano Lett.* **2014**, *14* (7), 4023–4029. <https://doi.org/10.1021/nl501460x>.
- (77) Korkmaz, S.; Turkmen, M.; Aksu, S. Mid-Infrared Narrow Band Plasmonic Perfect Absorber for Vibrational Spectroscopy. *Sensors Actuators A Phys.* **2020**, *301* (111757), 1–9. <https://doi.org/10.1016/j.sna.2019.111757>.
- (78) Barho, F. B.; Gonzalez-Posada, F.; Milla, M. J.; Bomers, M.; Cerutti, L.; Tournié, E.; Taliercio, T. Highly Doped Semiconductor Plasmonic Nanoantenna Arrays for Polarization Selective Broadband Surface-Enhanced Infrared Absorption Spectroscopy of Vanillin. *Nanophotonics* **2017**, *7* (2), 507–516. <https://doi.org/10.1515/nanoph-2017-0052>.
- (79) Neubrech, F.; Pucci, A.; Cornelius, T. W.; Karim, S.; García-Etxarri, A.; Aizpurua, J. Resonant Plasmonic and Vibrational Coupling in a Tailored Nanoantenna for Infrared Detection. *Phys. Rev. Lett.* **2008**, *101* (15), 2–5. <https://doi.org/10.1103/PhysRevLett.101.157403>.
- (80) Neubrech, F.; Beck, S.; Glaser, T.; Hentschel, M.; Giessen, H.; Pucci, A. Spatial Extent of Plasmonic Enhancement of Vibrational Signals in the Infrared. *ACS Nano* **2014**, *8* (6), 6250–6258. <https://doi.org/10.1021/nn5017204>.
- (81) Adato, R.; Yanik, A. A.; Amsden, J. J.; Kaplan, D. L.; Omenetto, F. G.; Hong, M. K.; Erramilli,

- S.; Altug, H. Ultra-Sensitive Vibrational Spectroscopy of Protein Monolayers with Plasmonic Nanoantenna Arrays. *Proc. Natl. Acad. Sci. U. S. A.* **2009**, *106* (46), 19227–19232. <https://doi.org/10.1073/pnas.0907459106>.
- (82) Brown, L. V.; Zhao, K.; King, N.; Sobhani, H.; Nordlander, P.; Halas, N. J. Surface-Enhanced Infrared Absorption Using Individual Cross Antennas Tailored to Chemical Moieties. *J. Am. Chem. Soc.* **2013**, *135* (9), 3688–3695. <https://doi.org/10.1021/ja312694g>.
- (83) Semenyshyn, R.; Mörz, F.; Steinle, T.; Ubl, M.; Hentschel, M.; Neubrech, F.; Giessen, H. Pushing down the Limit: In Vitro Detection of a Polypeptide Monolayer on a Single Infrared Resonant Nanoantenna. *ACS Photonics* **2019**, *6* (11), 2636–2642. <https://doi.org/10.1021/acsp Photonics.9b01125>.
- (84) Bagheri, S.; Weber, K.; Gissibl, T.; Weiss, T.; Neubrech, F.; Giessen, H. Fabrication of Square-Centimeter Plasmonic Nanoantenna Arrays by Femtosecond Direct Laser Writing Lithography: Effects of Collective Excitations on SEIRA Enhancement. *ACS Photonics* **2015**, *2* (6), 779–786. <https://doi.org/10.1021/acsp Photonics.5b00141>.
- (85) Brown, L. V.; Yang, X.; Zhao, K.; Zheng, B. Y.; Nordlander, P.; Halas, N. J. Fan-Shaped Gold Nanoantennas above Reflective Substrates for Surface-Enhanced Infrared Absorption (SEIRA). *Nano Lett.* **2015**, *15* (2), 1272–1280. <https://doi.org/10.1021/nl504455s>.
- (86) Urbietta, M.; Barbry, M.; Zhang, Y.; Koval, P.; Sánchez-Portal, D.; Zabala, N.; Aizpurua, J. Atomic-Scale Lightning Rod Effect in Plasmonic Picocavities: A Classical View to a Quantum Effect. *ACS Nano* **2018**, *12* (1), 585–595. <https://doi.org/10.1021/acsnano.7b07401>.
- (87) Dong, L.; Yang, X.; Zhang, C.; Cerjan, B.; Zhou, L.; Tseng, M. L.; Zhang, Y.; Alabastri, A.; Nordlander, P.; Halas, N. J. Nanogapped Au Antennas for Ultrasensitive Surface-Enhanced Infrared Absorption Spectroscopy. *Nano Lett.* **2017**, *17* (9), 5768–5774. <https://doi.org/10.1021/acsnanolett.7b02736>.
- (88) Liu, N.; Mesch, M.; Weiss, T.; Hentschel, M.; Giessen, H. Infrared Perfect Absorber and Its Application as Plasmonic Sensor. *Nano Lett.* **2010**, *10* (7), 2342–2348. <https://doi.org/10.1021/nl9041033>.

- (89) Barho, F. B.; Gonzalez-Posada, F.; Cerutti, L.; Taliercio, T. Heavily Doped Semiconductor Metamaterials for Mid-Infrared Multispectral Perfect Absorption and Thermal Emission. *Adv. Opt. Mater.* **2020**, *8* (6), 1–10. <https://doi.org/10.1002/adom.201901502>.
- (90) Wallace, G. Q.; Foy, H. C.; Rosendahl, S. M.; Lagugné-Labarthe, F. Dendritic Plasmonics for Mid-Infrared Spectroscopy. *J. Phys. Chem. C* **2017**, *121* (17), 9497–9507. <https://doi.org/10.1021/acs.jpcc.7b02039>.
- (91) Wallace, G. Q.; Read, S. T.; McRae, D. M.; Rosendahl, S. M.; Lagugné-Labarthe, F. Exploiting Anisotropy of Plasmonic Nanostructures with Polarization Modulation Infrared Linear Dichroism Microscopy (MPM-IRLD). *Adv. Opt. Mater.* **2018**, *6* (6), 1–10. <https://doi.org/10.1002/adom.201701336>.
- (92) Rodrigo, D.; Tittl, A.; John-Herpin, A.; Limaj, O.; Altug, H. Self-Similar Multiresonant Nanoantenna Arrays for Sensing from Near- to Mid-Infrared. *ACS Photonics* **2018**, *5* (12), 4903–4911. <https://doi.org/10.1021/acsp Photonics.8b01050>.
- (93) Kühner, L.; Hentschel, M.; Zschieschang, U.; Klauk, H.; Vogt, J.; Huck, C.; Giessen, H.; Neubrech, F. Nanoantenna-Enhanced Infrared Spectroscopic Chemical Imaging. *ACS Sensors* **2017**, *2* (5), 655–662. <https://doi.org/10.1021/acssensors.7b00063>.
- (94) Wallace, G. Q.; McRae, D. M.; Lagugné-Labarthe, F. Probing Mid-Infrared Plasmon Resonances in Extended Radial Fractal Structures. *Opt. Lett.* **2019**, *44* (15), 3865–3868. <https://doi.org/10.1364/OL.44.003865>.
- (95) Gottheim, S.; Zhang, H.; Govorov, A. O.; Halas, N. J. Fractal Nanoparticle Plasmonics: The Cayley Tree. *ACS Nano* **2015**, *9* (3), 3284–3292. <https://doi.org/10.1021/acsnano.5b00412>.
- (96) Simon, T.; Li, X.; Martin, J.; Khlopin, D.; Stéphan, O.; Kociak, M.; Gérard, D. Aluminum Cayley Trees as Scalable, Broadband, Multi-Resonant Optical Antennas. *Appl. Phys. Sci.* **2022**, *119* (4), 1–6. <https://doi.org/https://doi.org/10.1073/pnas.2116833119>.
- (97) Love, J. C.; Estroff, L. A.; Kriebel, J. K.; Nuzzo, R. G.; Whitesides, G. M. Self-Assembled Monolayers of Thiolates on Metals as a Form of Nanotechnology. *Chem. Rev.* **2005**, *105* (4), 1103–1169. <https://doi.org/10.1021/cr0300789>.

- (98) Leitis, A.; Tseng, M. L.; John-Herpin, A.; Kivshar, Y. S.; Altug, H. Wafer-Scale Functional Metasurfaces for Mid-Infrared Photonics and Biosensing. *Adv. Mater.* **2021**, *33* (43). <https://doi.org/10.1002/adma.202102232>.
- (99) Hsieh, W. T.; Wu, P. C.; Khurgin, J. B.; Tsai, D. P.; Liu, N.; Sun, G. Comparative Analysis of Metals and Alternative Infrared Plasmonic Materials. *ACS Photonics* **2018**, *5* (7), 2541–2548. <https://doi.org/10.1021/acsp Photonics.7b01166>.
- (100) Koshelev, K.; Kivshar, Y. Dielectric Resonant Metaphotonics. *ACS Photonics* **2021**, *8* (1), 102–112. <https://doi.org/10.1021/acsp Photonics.0c01315>.
- (101) Baranov, D. G.; Zuev, D. A.; Lepeshov, S. I.; Kotov, O. V.; Krasnok, A. E.; Evlyukhin, A. B.; Chichkov, B. N. All-Dielectric Nanophotonics: The Quest for Better Materials and Fabrication Techniques. *Optica* **2017**, *4* (7), 814–825. <https://doi.org/10.1364/OPTICA.4.000814>.
- (102) Tittl, A.; Leitis, A.; Liu, M.; Yesilkoy, F.; Choi, D. Y.; Neshev, D. N.; Kivshar, Y. S.; Altug, H. Imaging-Based Molecular Barcoding with Pixelated Dielectric Metasurfaces. *Science* (80-.). **2018**, *360* (6393), 1105–1109. <https://doi.org/10.1126/science.aas9768>.
- (103) Leitis, A.; Tittl, A.; Liu, M.; Lee, B. H.; Gu, M. B.; Kivshar, Y. S.; Altug, H. Angle-Multiplexed All-Dielectric Metasurfaces for Broadband Molecular Fingerprint Retrieval. *Sci. Adv.* **2019**, *5* (5), 1–9. <https://doi.org/10.1126/sciadv.aaw2871>.
- (104) Chang, Y.; Hasan, D.; Dong, B.; Wei, J.; Ma, Y.; Zhou, G.; Ang, K. W.; Lee, C. All-Dielectric Surface-Enhanced Infrared Absorption-Based Gas Sensor Using Guided Resonance. *ACS Appl. Mater. Interfaces* **2018**, *10* (44), 38272–38279. <https://doi.org/10.1021/acсами.8b16623>.
- (105) Tittl, A.; John-Herpin, A.; Leitis, A.; Arvelo, E. R.; Altug, H. Metasurface-Based Molecular Biosensing Aided by Artificial Intelligence. *Angew. Chemie Int. Ed.* **2019**, *58* (42), 14810–14822. <https://doi.org/10.1002/anie.201901443>.
- (106) Freddi, S.; Sangaletti, L. Trends in the Development of Electronic Noses Based on Carbon Nanotubes Chemiresistors for Breathomics. *Nanomaterials* **2022**, *12* (17), 2992.

<https://doi.org/10.3390/nano12172992>.

- (107) Freddi, S.; Gonzalez, M. C. R.; Carro, P.; Sangaletti, L.; De Feyter, S. Chemical Defect-Driven Response on Graphene-Based Chemiresistors for Sub-ppm Ammonia Detection. *Angew. Chemie* **2022**, *134* (16), 1–6. <https://doi.org/10.1002/ange.202200115>.
- (108) Palik, E. D. *Handbook of Optical Constants of Solids*, Vol.2.; Academic Press: San Diego, USA, 1991. <https://doi.org/https://doi.org/10.1016/C2009-0-20920-2>.
- (109) Novotny, L. Strong Coupling, Energy Splitting, and Level Crossings: A Classical Perspective. *Am. J. Phys.* **2010**, *78* (11), 1199–1202. <https://doi.org/10.1119/1.3471177>.
- (110) Milla, M. J.; Barho, F.; González-Posada, F.; Cerutti, L.; Bomers, M.; Rodriguez, J. B.; Tournié, E.; Taliercio, T. Localized Surface Plasmon Resonance Frequency Tuning in Highly Doped InAsSb/GaSb One-Dimensional Nanostructures. *Nanotechnology* **2016**, *27* (42), 1–8. <https://doi.org/10.1088/0957-4484/27/42/425201>.
- (111) Yang, J.; Sauvan, C.; Jouanin, A.; Collin, S.; Pelouard, J.-L.; Lalanne, P. Ultrasmall Metal-Insulator-Metal Nanoresonators: Impact of Slow-Wave Effects on the Quality Factor. *Opt. Express* **2012**, *20* (15), 16880. <https://doi.org/10.1364/oe.20.016880>.
- (112) Knight, M. W.; Liu, L.; Wang, Y.; Brown, L.; Mukherjee, S.; King, N. S.; Everitt, H. O.; Nordlander, P.; Halas, N. J. Aluminum Plasmonic Nanoantennas. *Nano Lett.* **2012**, *12* (11), 6000–6004. <https://doi.org/10.1021/nl303517v>.
- (113) Špačková, B.; Wrobel, P.; Bocková, M.; Homola, J. Optical Biosensors Based on Plasmonic Nanostructures: A Review. *Proc. IEEE* **2016**, *104* (12), 2380–2408. <https://doi.org/10.1109/JPROC.2016.2624340>.
- (114) Kravets, V. G.; Kabashin, A. V.; Barnes, W. L.; Grigorenko, A. N. Plasmonic Surface Lattice Resonances: A Review of Properties and Applications. *Chem. Rev.* **2018**, *118* (12), 5912–5951. <https://doi.org/10.1021/acs.chemrev.8b00243>.
- (115) Kittel, C. *Introduction to Solid State Physics*, 8th ed.; Wiley: New York, 2005.
- (116) Madiomanana, K. Intégration Des Matériaux III-V Antimoniures Sur Substrat de Silicium,

2015.

- (117) Chen, Y. Nanofabrication by Electron Beam Lithography and Its Applications: A Review. *Microelectron. Eng.* **2015**, *135* (5), 57–72. <https://doi.org/10.1016/j.mee.2015.02.042>.
- (118) Altissimo, M. E-Beam Lithography for Micro-/Nanofabrication. *Biomicrofluidics* **2010**, *4* (2), 1–6. <https://doi.org/10.1063/1.3437589>.
- (119) Gangnaik, A. S.; Georgiev, Y. M.; Holmes, J. D. New Generation Electron Beam Resists: A Review. *Chem. Mater.* **2017**, *29* (5), 1898–1917. <https://doi.org/10.1021/acs.chemmater.6b03483>.
- (120) Hatzakis, M. Electron Resists for Microcircuit and Mask Production. *J. Electrochem. Soc.* **1969**, *116* (7), 1033–1037. <https://doi.org/10.1149/1.2412145>.
- (121) ALLRESIST. *Ar-P6200 Csar-62*; 2020; Vol. 2.
- (122) Grigorescu, A. E.; Hagen, C. W. ZResists for Sub-20-Nm Electron Beam Lithography with a Focus on HSQ: State of the Art. *Nanotechnology* **2009**, *20* (29). <https://doi.org/10.1088/0957-4484/20/29/292001>.
- (123) Dorling, K. M.; Baker, M. J. Rapid FTIR Chemical Imaging: Highlighting FPA Detectors. *Trends Biotechnol.* **2013**, *31* (8), 437–438. <https://doi.org/10.1016/j.tibtech.2013.05.008>.
- (124) Hornemann, A.; Eichert, D.; Flemig, S.; Ulm, G.; Beckhoff, B. Qualifying Label Components for Effective Biosensing Using Advanced High-Throughput SEIRA Methodology. *Phys. Chem. Chem. Phys.* **2015**, *17* (14), 9471–9479. <https://doi.org/10.1039/c4cp05944a>.
- (125) Zucchiatti, P.; Birarda, G.; Cerea, A.; Semrau, M. S.; Hubarevich, A.; Storici, P.; De Angelis, F.; Toma, A.; Vaccari, L. Binding of Tyrosine Kinase Inhibitor to Epidermal Growth Factor Receptor: Surface-Enhanced Infrared Absorption Microscopy Reveals Subtle Protein Secondary Structure Variations. *Nanoscale* **2021**, *13* (16), 7667–7677. <https://doi.org/10.1039/d0nr09200b>.
- (126) Langhammer, C.; Schwind, M.; Kasemo, B.; Zorić, I. Localized Surface Plasmon Resonances in Aluminum Nanodisks. *Nano Lett.* **2008**, *8* (5), 1461–1471.

<https://doi.org/10.1021/nl080453i>.

- (127) Valdez-Flores, C.; Cañizares-Macias, M. P. On-Line Dilution and Detection of Vanillin in Vanilla Extracts Obtained by Ultrasound. *Food Chem.* **2007**, *105* (3), 1201–1208. <https://doi.org/10.1016/j.foodchem.2007.02.028>.
- (128) Liu, G.-A.; Zheng, R.-L. Protection against Damaged DNA in the Single Cell by Polyphenols. *Pharmazie* **2002**, *57* (12), 852–854.
- (129) Farthing, D.; Domenic, S.; Abernathy, C.; Fakhry, I.; Roberts, J. D.; Abraham, D. J.; Swerdlow, P. High-Performance Liquid Chromatographic Method for Determination of Vanillin and Vanillic Acid in Human Plasma, Red Blood Cells and Urine. *J. Chromatogr. B Biomed. Sci. Appl.* **1999**, *723* (1–2), 303–307. [https://doi.org/10.1016/S0378-4347\(98\)00514-3](https://doi.org/10.1016/S0378-4347(98)00514-3).
- (130) El-Etre, A. Y. Inhibition of Acid Corrosion of Aluminum Using Vanillin. *Corros. Sci.* **2001**, *43* (6), 1031–1039. [https://doi.org/10.1016/S0010-938X\(00\)00127-X](https://doi.org/10.1016/S0010-938X(00)00127-X).
- (131) Eilers, P. H. C. A Perfect Smoother. *Anal. Chem.* **2003**, *75* (14), 3631–3636. <https://doi.org/10.1021/ac034173t>.
- (132) Balachandran, V.; Parimala, K. Vanillin and Isovanillin: Comparative Vibrational Spectroscopic Studies, Conformational Stability and NLO Properties by Density Functional Theory Calculations. *Spectrochim. Acta - Part A Mol. Biomol. Spectrosc.* **2012**, *95* (1386–1425), 354–368. <https://doi.org/10.1016/j.saa.2012.03.087>.
- (133) GmbH, M. MicroChemicals Aluminium Etching. **2013**.

Annexes

1.1. Annexe.1.1. Wave vector matching mechanisms

1.1.1. Evanescent coupling

Prisms allow to increase the wave vector of the incident light by a factor of $\sqrt{\varepsilon_p}$ as the incident light passes through the prism, ε_p being the dielectric constant of the prism. By this, through an evanescent wave, by SPPs can be excited at an interface between a metal and a medium with a lower refractive index than the prism (e.g. often air). Typically, two configurations are employed, the Kretschmann-Raether configuration (**Figure A.1.1a**) and the Otto configuration (**Figure A.1.1b**).

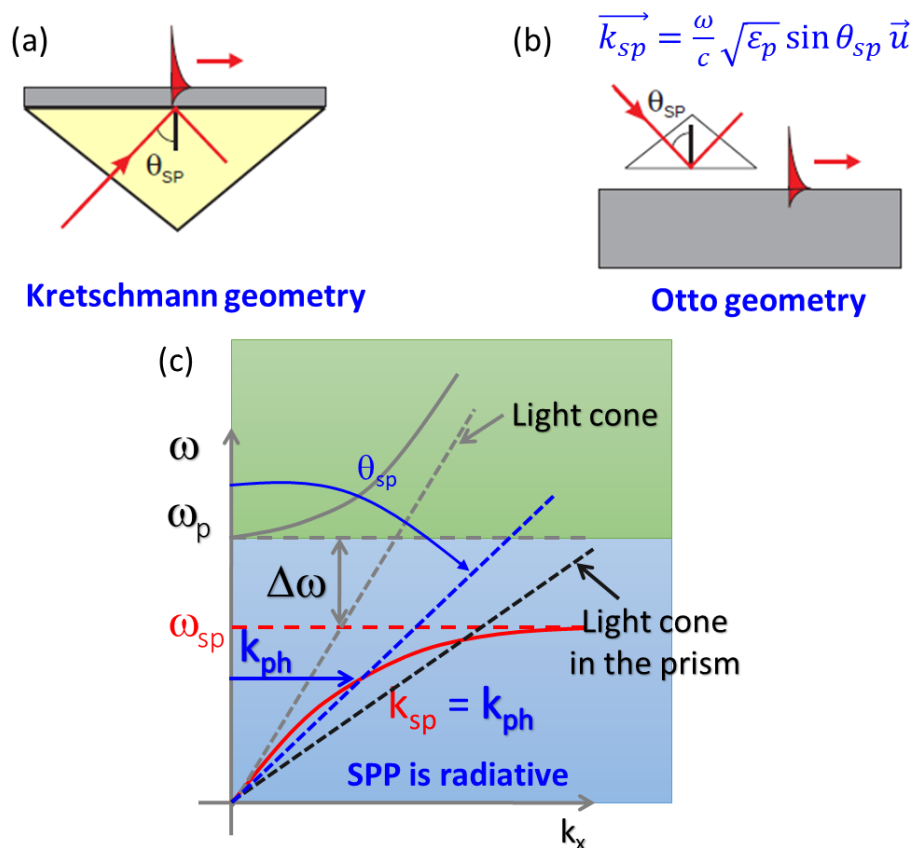


Figure A.1. 1. Evanescent coupling through (a) the Kretschmann-Raether configuration and (b) the Otto configuration. (c) Once the in-plane momentum of the photons matches the in-plane momentum of the SPP for an adapted incidence angle θ_{sp} , the SPP can be excited.

In the Kretschmann-Raether configuration, a metallic film is directly evaporated onto the prism. The metal serves as a spacer layer through which the evanescent wave passes. In the Otto configuration, light enters through the prism and impinges on an interface between the prism and the lower refractive index spacer (air). Only with small spacer thicknesses, an evanescent wave, due to the total reflection, can traverse the spacer and excite a propagating SPP. If the in-plane momentum of the photons matches the in-plane momentum of the SPP for an adapted incidence angle θ_{sp} , the SPP can be excited as described in **Figure A.1.1c**.

$$\vec{k}_{sp} = \frac{\omega}{c} \sqrt{\epsilon_p} \sin \theta_{sp} \vec{u}$$

1.1.2. Grating coupling

Due to the periodicity of the grating, the dispersion relation might be reduced to an equivalent of the first Brillouin zone. The initial SPP dispersion curves are translated by $m(2\pi/a)$ with various values of m . In the **Figure A.1.2a**, we see that many branches are folded into the radiative region (the shaded blue region representing the light cone). SPPs in the plasmonic crystal can be excited by the incident light with a wave vector into the light cone.

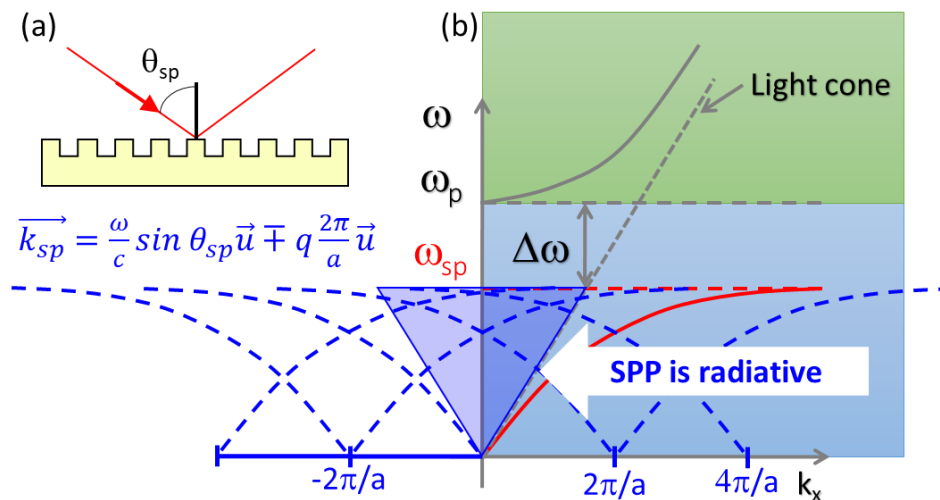


Figure A.1. 2. (a) Schematic of the grating. (b) Grating coupling as the initial SPP dispersion curve (red) are translated by $m(2\pi/a)$ in both positive and negative directions (blue curves) along the x-axis. The SPP can be excited if the wave vector of the incident light is into the light cone (shaded blue).

1.2. Annexe.3.1. Trial sample: BT and HC fabrication by metallization and lift-off

Firstly, BT and HC patterns are defined in the same spirit: the triangles placed in tip-to-tip facing configuration (BT) or packed in a HC arrangement were meant to be scanned by the electron beam and defined by metallization and lift-off. This technological process was done completely using the cleanroom facilities of the CTM-Montpellier. The next paragraphs sum up the most important technological details for each step of **Figure A.3.1**:

- (iii) **Resist Coating**: Dehydrate the sample surface on a 180°C hot plate for 5 min. a bilayer resist is employed, consisting of a spin-coated EI10 (MMA (8.5) MAA) layer (300 nm thick), on top of which, 200 nm thick PMMA 950K A4 layer is spin-coated with the same parameters: 5 000 rpm for 30 s, each coating is followed by a resist baking at 170°C for 5 min on a hotplate to expel the solvent. The bottom layer (EI10) has a copolymer that has minor molecular weight and higher sensibility than the upper PMMA layer. The EI10 layer serves as an undercut to ease the lift-off step and to avoid coating the sidewall of the resist when metal is evaporated. The lower layer of bilayer resist should be at least 2x the thickness of the metal to be deposited.¹¹⁷
- (iv) **EBL Exposure**: the exposure is done using an EBL-devoted SEM chamber pumped under 10^{-6} atm (LaB6 filament) and coupled to a RAITH program. To define the triangular holes that will be filled with Al atoms during metallization, the nominal area dose value is set to $300 \mu\text{C}/\text{cm}^2$ (based on previous tests) and the area step size to 2 nm. A beam current of 0.1 nA is measured at the Faraday cup, this value will be further useful to calculate the adequate dwell time before scanning (voltage of 30 keV, spot size equals 39 and LC equals 44 μA), and the working distance is 12 mm. On the same sample holder, a fine focus at 0.5 μm of scale was achieved on a reference sample with gold squares of a 1 μm minimum size. Once the sample origin is fixed and the angle correction is done, subsequent contamination dots of ~20 s exposure are used in high magnification to set the focus and correct the stigmatism. To limit stitching errors, a writing field alignment on the contamination dot adjusts the zoom, rotation, and

stigmatism. All these parameters are well-controlled during the exposure thanks to a built-in focus tracking system.

(v) Resist Development: The resist is developed in a Methyl Isobutyl Ketone (MIBK): 2-Propanol (IPA) solution (MIBK:IPA/1:3) for 30s. Then, the sample is immediately rinsed in IPA (stopper solution) for 30s ensuring the best profile for a metallization lift-off with an $\sim 80^\circ$ inclined side-walls.

(vi) Al deposition: A 50 nm thick layer is thermally evaporated from a 99.99% pure aluminum pellets source at 1 \AA/s at 10^{-6} mbar. The sample holder is continuously rotated to provide a homogenous deposition. P.S. the resist mask is reticulated compared to sputtering deposition.

(vii) Lift-off process: It is done in acetone solution at room temperature, followed by an ultra-sonication bath at 35 kHz for 60 s in ethanol to guarantee a clean lift-off of the unwanted Al film. The sample is thoroughly rinsed under deionized running water and blown with dry N_2 . Note this technique is benefiting from the bilayer construction and molecular weight dissimilarity that exists in dissolution rates of the layers at the developer step, leading to the anticipated resist sidewall silhouette (**Figure A.3.1** (iii)).

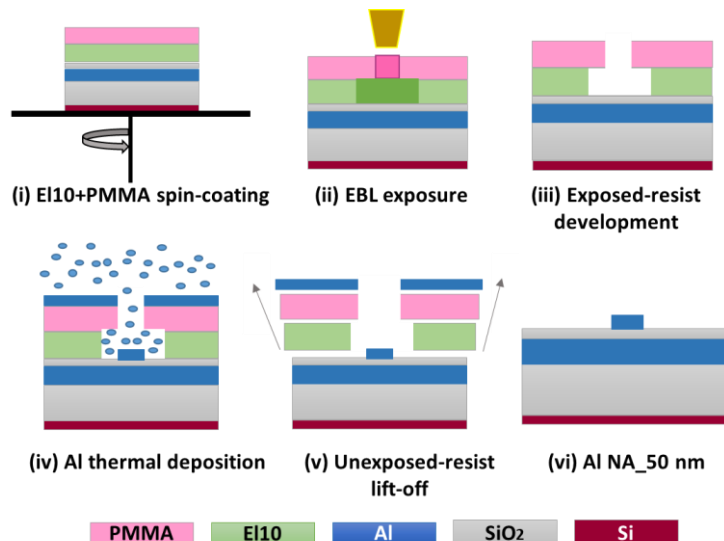


Figure.A.3. 1. Technological process flow starts with (i) bilayer resist spin-coating, followed by (ii) an EBL exposure and (iii) a standard development in acetone and ethanol solvents, then (iv) a metallization and ending with (v) a lift-off process, to retrieve (vi) the final Al-NA.

Morphology SEM and AFM images

Following this process, nanostructure arrays consisting of BT or a HC shape are created as displayed in the SEM image in **Figure A.3.2**. In addition, the lift-off of a thin metallic layer is evaluated: some bilayer residues are found similar to the zoomed-red zone of **Figure A.3.2**. Under a polarized optical microscope, the elements of the residual bilayer (with around 200 nm of thickness) are revealed with curved side walls, at the bottom of which the Al remains (yellow residues). The curved walls are due to the flaw of the resist remover solvents at the sample surface.

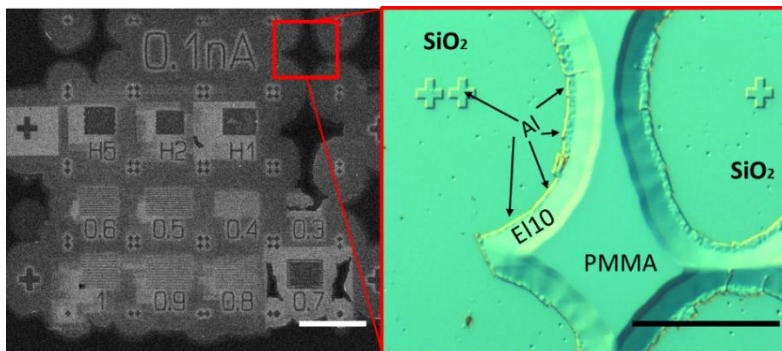


Figure.A.3. 2. SEM of the sample showing the final results of a bilayer sample. At the edges of the lithographed zone, *e.g* as delimited within the red square, the bilayer resists the lift-off. The shades of both layers are displayed under an optical microscope as well as the residual Al at the bilayer/ SiO₂ interface. All scales are 100 μm long.

HC trial zones:

Using a bilayer, the H2 and H1 zones are perfectly defined as illustrated in **Figure A.3.3**. It demonstrates a good definition of both structures having the desired height of around 50 nm in agreement with the thermally evaporated Al film. However, an inhomogeneous lift-off is marked on the right edge of the H1 zone. In summary, the lift-off is limited by the side walls of the bilayer resist, which confront the flow of the resist removal solvent, and consequently, Al film and resist are leftover in both cases in these regions for the HC.

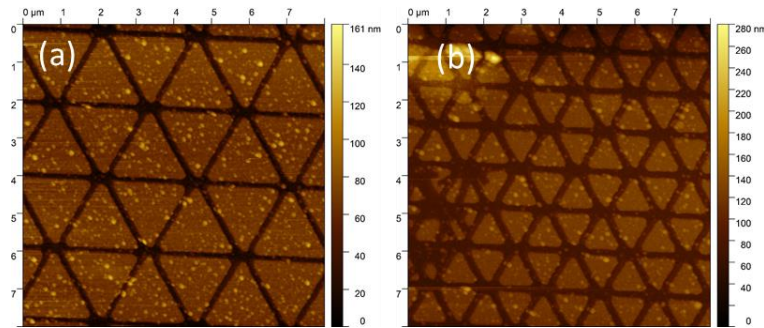


Figure.A.3. 3. AFM images of (a) H2 and (b) H1 patterned on the bilayer sample. The roughness on top of the triangles is respectively around 6 and 2.5 nm in (a) and (b). The height of the triangles is (a) 49.7 ± 5 nm and (b) 48.9 ± 2.9 nm.

BT trial zones:

The lift-off seems to work for some BT. For $L = 1.0$, the AFM image of the BT is displayed in **Figure°A.3.4.**

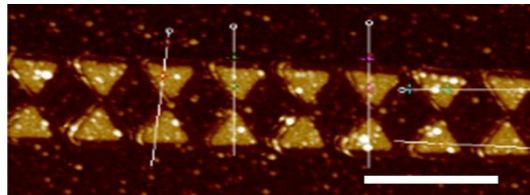


Figure.A.3. 4. AFM image of BT with $L = 1.0$ μm patterned on the bilayer sample. The triangle's thickness is measured through the gray cross-sections and found to be equal to 50 ± 4 nm. The scale is 2 μm long.

In conclusion, the BT and HC can be defined by a procedure that is combining EBL of the triangles, metallization, and lift-off. However, the sharpness of the triangle's tips and the control of the side lengths as well as the spacing between the triangles are not perfectly achieved, keeping in mind that the aim is to finally fabricate BT and HC with nanometric precision, so their experimental plasmonic resonance could match the theoretical ones detailed in **Chapter 2**. For that reason, we have chosen to collaborate with the LAAS thanks to their matured expertise in nanostructuration with an advanced and well-controlled EBL machine.

1.3. Annexe.3.2. Morphology analysis in relation to the dose factor

Exposure

The exposure dose factors affect the BT geometric parameters. The first step is to define the right dose factor for each combination, avoiding any touching between the triangle's inner tips or outer corners. Plus, a beam current choice is also to be done between 300 pA and 20 pA.

Several zones are elaborated for L ranging from 2.0 to 0.3 μm with a step of 0.1 μm and 5 spacing g ranging from 0.02 μm to 0.1 μm with a step of 0.01 μm . Dose factors ranging from x1 to x2.5 with a step of 0.1 are investigated. In each zone, each line is written with a dose factor. A dose color palette is introduced to illustrate the dose variation from one line to another, going from dark blue to red, representing the dose factor sweeping, as shown in **Figure A.3. 5**. The nominal dose is maintained constant at 240 $\mu\text{C}/\text{cm}^2$. This value is set according to previous deep optimizations of dose factors for this PMMA resist.

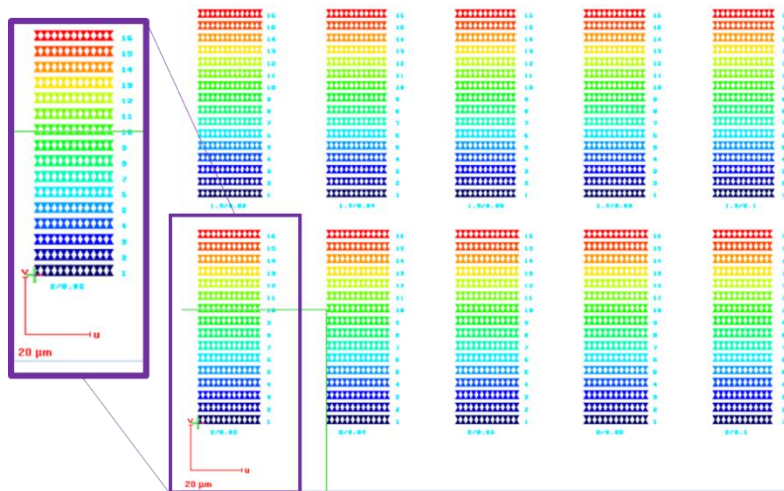


Figure.A.3. 5. Color-coded patterns with different dose factors for each line of each zone. In the first level L is fixed to 2.0 μm and g is varied from 0.02 to 0.1 μm (from the left to the right). A similar configuration is selected for each L value.

Morphology analysis with the beam current and the dose factor

To determine the adequate operating beam to define sharp corners with challenging nanoscale spacing and to choose the right dose factor for each (L/g) combination, the complete design of **Figure A.3.5** is written twice on the same sample with 2 different beam currents, namely 20 pA and 300 pA. In **Figure A.3.6**, the geometrical definition of triangles and superior tip-to-tip alignment are compared for a 20 and 300 pA e-beam current intensity. For the same dose factor, the respective distances between the tip-to-tip and corner-to-corner triangles are more accurate in **Figure A.3.6a** and **Figure A.3.6c** than in **Figure A.3.6b** and **Figure A.3.6d**. Indeed, g is equal to $0.042\mu\text{m} \pm 0.002\mu\text{m}$ in **Figure A.3.6b**, and equal to $0.024\mu\text{m} \pm 0.002\mu\text{m}$ in **Figure A.3.6d**, so the desired gap, *i.e.*, $0.02\mu\text{m}$ in our example is not even achieved, yet the outer corners for the adjacent triangles are largely touched.

Consequently, the beam current of 20 pA is selected as it provides a better definition of the triangle corners and better control of the g and L alternatively. However, the exposure time increases exponentially while choosing this current value, but such decision is fundamental for the geometrical precision of patterns that may affect their optical responses.

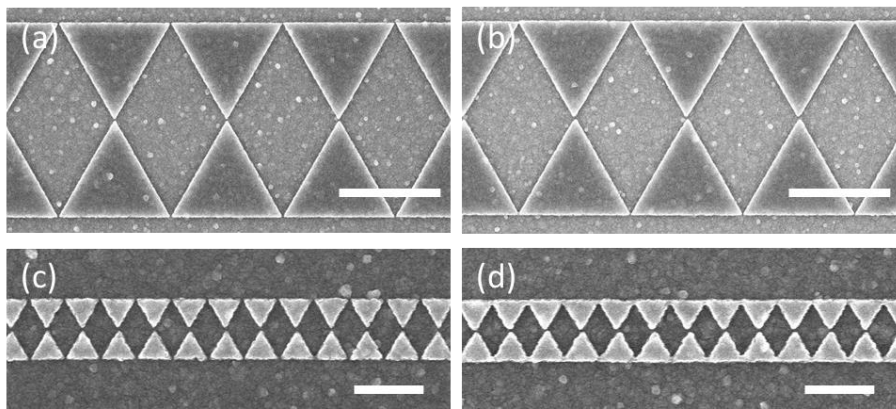


Figure.A.3. 6. SEM calibrated images of BT insolated with 20 pA (a) and (c) and 300 pA (b) and (d). The desired gap is $0.02\mu\text{m}$. (a) and (b) refer to $L = 2.0\mu\text{m}$ and a dose factor of $\times 1.8$, while (c) and (d) to $L = 0.3\mu\text{m}$ and a dose factor of $\times 2.5$.

Once 20 pA is chosen as beam current, all SEM images (1845 images) for each L and g combination are carefully analyzed using Image-J to extract their values as a function of dose factors. The study in **Figure A.3.7** presents the correlation between the dose factor and spacing for $L = 2.0$

and 1.7 μm . Generally, for the same BT size: the greater the spacing, the greater the dose; and for the same spacing: the larger the dimension, the lower the dose factor. To determine the dose that will give the intended BT parameters a linear fitting of the tendency is presented for each L and g combination, where the ideal dose factor is obtained at the intersection point that refers to the expected gap distance. As for $L= 2.0 \mu\text{m}$, to reach $g = 0.02 \mu\text{m}$ and $0.1 \mu\text{m}$, a dose factor of x1.8 and x2.1 should be applied respectively. For $L= 1.7 \mu\text{m}$, to reach $g = 0.02 \mu\text{m}$ and $0.1 \mu\text{m}$, a dose factor has to be x1.9 and x2.2 respectively.

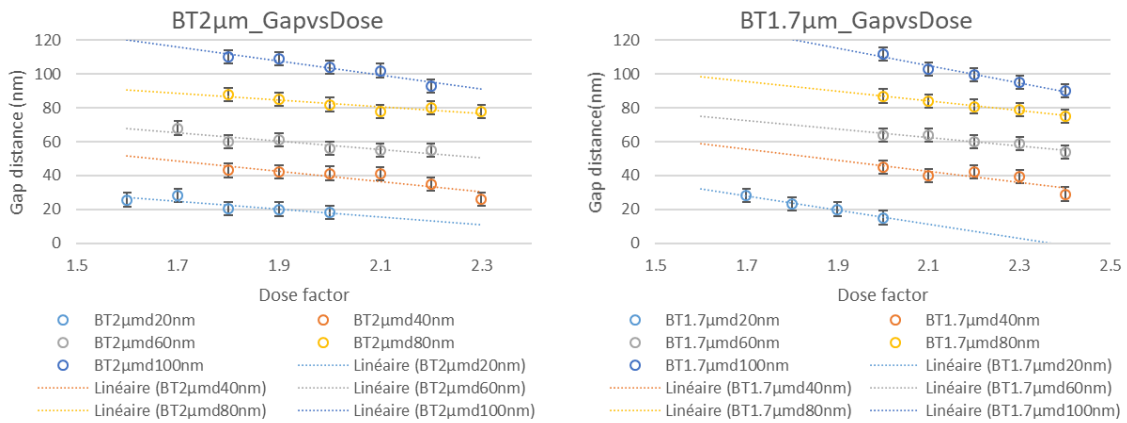


Figure.A.3. 7. The dose factor selection for each L/g combination. $L = 2.0$ and $1.0 \mu\text{m}$ are selected. A linear dependency of the g versus the dose factors for the picked L values is marked.

1.4. Annexe.3.3. Table 1 and 2 for the small BT, L, and g

SEM images are studied over 4 zones (No. 1, 3, 5, and 8) to provide a statistical study of L and g , in **Table A.3.1.** as well as their pitches along x and y, *i.e.*, Λ_x and Λ_y .

	$L = 0.3$	$L = 0.2$	$L = 0.15$	$L = 0.1$	$L = 0.08$	Mean g
$g = 0.1$	$L = 0.29 \pm 0.01$ $g = 0.108 \pm 0.005$	$L = 0.195 \pm 0.007$ $g = 0.11 \pm 0.003$	$L = 0.143 \pm 0.005$ $g = 0.110 \pm 0.005$	$L = 0.098 \pm 0.012$ $g = 0.100 \pm 0.003$	$d = 0.085 \pm 0.005$ $g = 0.099 \pm 0.006$	0.105 ± 0.005
$g = 0.06$	$L = 0.283 \pm 0.009$ $g = 0.07 \pm 0.002$	$L = 0.19 \pm 0.01$ $g = 0.07 \pm 0.04$	$L = 0.144 \pm 0.005$ $g = 0.066 \pm 0.009$	$L = 0.096 \pm 0.006$ $g = 0.062 \pm 0.008$	$d = 0.077 \pm 0.005$ $g = 0.063 \pm 0.005$	0.066 ± 0.008
$g = 0.02$	$L = 0.28 \pm 0.014$ $g = 0.025 \pm 0.04$	$L = 0.187 \pm 0.005$ $g = 0.03 \pm 0.01$	$L = 0.145 \pm 0.002$ $g = 0.029 \pm 0.006$	$L = 0.091 \pm 0.006$ $g = 0.026 \pm 0.004$	$d = 0.081 \pm 0.004$ $g = 0.026 \pm 0.005$	0.027 ± 0.005
$g = 0.1$	$L = 0.291 \pm 0.008$ $g = 0.10 \pm 0.01$	$L = 0.195 \pm 0.003$ $g = 0.100 \pm 0.004$	$L = 0.142 \pm 0.004$ $g = 0.11 \pm 0.01$	$L = 0.098 \pm 0.004$ $g = 0.106 \pm 0.006$	$d = 0.077 \pm 0.003$ $g = 0.112 \pm 0.004$	0.105 ± 0.004
$g = 0.06$	$L = 0.291 \pm 0.006$ $g = 0.061 \pm 0.005$	$L = 0.194 \pm 0.005$ $g = 0.064 \pm 0.003$	$L = 0.144 \pm 0.007$ $g = 0.064 \pm 0.004$	$L = 0.101 \pm 0.005$ $g = 0.063 \pm 0.003$	$d = 0.077 \pm 0.003$ $g = 0.068 \pm 0.002$	0.064 ± 0.003
$g = 0.02$	$L = 0.294 \pm 0.004$ $g = 0.021 \pm 0.004$	$L = 0.203 \pm 0.007$ $g = 0.023 \pm 0.008$	$L = 0.151 \pm 0.007$ $g = 0.03 \pm 0.004$	$L = 0.098 \pm 0.002$ $g = 0.022 \pm 0.005$	$d = 0.080 \pm 0.004$ $g = 0.028 \pm 0.004$	0.025 ± 0.004
$g = 0.1$	$L = 0.295 \pm 0.005$ $g = 0.102 \pm 0.001$	$L = 0.195 \pm 0.007$ $g = 0.101 \pm 0.006$	$L = 0.145 \pm 0.005$ $g = 0.099 \pm 0.005$	$L = 0.096 \pm 0.006$ $g = 0.102 \pm 0.007$	$d = 0.087 \pm 0.02$ $g = 0.098 \pm 0.008$	0.100 ± 0.008
$g = 0.06$	$L = 0.295 \pm 0.009$ $g = 0.056 \pm 0.009$	$L = 0.193 \pm 0.007$ $g = 0.063 \pm 0.006$	$L = 0.145 \pm 0.005$ $g = 0.056 \pm 0.005$	$L = 0.097 \pm 0.003$ $g = 0.059 \pm 0.003$	$d = 0.074 \pm 0.002$ $g = 0.056 \pm 0.008$	0.058 ± 0.008
$g = 0.02$	$L = 0.296 \pm 0.005$ $g = 0.019 \pm 0.003$	$L = 0.194 \pm 0.007$ $g = 0.024 \pm 0.008$	$L = 0.144 \pm 0.006$ $g = 0.025 \pm 0.006$	$L = 0.094 \pm 0.006$ $g = 0.023 \pm 0.004$	$d = 0.072 \pm 0.004$ $g = 0.019 \pm 0.002$	0.022 ± 0.004
$g = 0.1$	$L = 0.29 \pm 0.01$ $g = 0.106 \pm 0.003$	$L = 0.192 \pm 0.007$ $g = 0.106 \pm 0.004$	$L = 0.145 \pm 0.005$ $g = 0.11 \pm 0.01$	$L = 0.091 \pm 0.004$ $g = 0.102 \pm 0.006$	$d = 0.076 \pm 0.003$ $g = 0.11 \pm 0.01$	0.107 ± 0.010
$g = 0.06$	$L = 0.30 \pm 0.01$ $g = 0.06 \pm 0.01$	$L = 0.194 \pm 0.007$ $g = 0.068 \pm 0.004$	$L = 0.143 \pm 0.004$ $g = 0.07 \pm 0.01$	$L = 0.08 \pm 0.01$ $g = 0.072 \pm 0.006$	$d = 0.075 \pm 0.005$ $g = 0.071 \pm 0.006$	0.068 ± 0.006
$g = 0.02$	$L = 0.30 \pm 0.01$ $g = 0.022 \pm 0.005$	$L = 0.195 \pm 0.006$ $g = 0.03 \pm 0.01$	$L = 0.145 \pm 0.005$ $g = 0.027 \pm 0.004$	$L = 0.09 \pm 0.01$ $g = 0.023 \pm 0.002$	$d = 0.077 \pm 0.006$ $g = 0.025 \pm 0.005$	0.025 ± 0.006
Mean L	0.292 ± 0.01	0.194 ± 0.008	0.145 ± 0.004	0.095 ± 0.005	0.078 ± 0.005	

Table A.3. 1. Geometric parameter values were found based on Image-J treatment. Typical configuration L/g , all the values are in μm .

To fulfill the geometric parameters study of sample No. 5, it is important to calculate the periodicity in **Table A.3.2** through equations (1) and (2):

$$\Lambda_x = L + g \quad (1);$$

$$\Lambda_y = 2 \times L \times \sin 60^\circ + g + Y \quad (2); Y = 2\mu\text{m}$$

Geometry		$\Lambda_x(\mu\text{m})$		$\Lambda_y(\mu\text{m})$	
$L(\mu\text{m})$	$g(\mu\text{m})$	Calculated	SEM (± 0.002)	Calculated	SEM (± 0.002)
0.3	0.02	0.320	0.318	2.540	2.552
	0.06	0.360	0.360	2.580	2.584
	0.1	0.400	0.328	2.620	2.600
0.2	0.02	0.220	0.223	2.366	2.365
	0.06	0.260	0.261	2.406	2.398
	0.1	0.300	0.302	2.446	2.424
0.15	0.02	0.170	0.169	2.280	2.274
	0.06	0.210	0.210	2.320	2.316
	0.1	0.250	0.251	2.360	2.346
0.1	0.02	0.120	0.122	2.193	2.196
	0.06	0.160	0.161	2.233	2.226
	0.1	0.200	0.201	2.273	2.280
0.08	0.02	0.100	0.100	2.159	2.161
	0.06	0.140	0.139	2.199	2.196
	0.1	0.180	0.183	2.239	2.238

Table A.3. 2. BT pitches along the x- and y-axis are mathematically calculated and measured on SEM images of zone No. 5.

1.5. Annexe.3.4. Argon etching optimization

Sample V2481 (50 nm Al on doped-GaSb)

Firstly, the definition of the triangles within the HC configuration is conceived similarly to the primary trial sample: the triangles are exposed on a 50 nm thick Al layer covering a 100 nm thick layer of doped gallium antimonite (GaSb) layer (SC of the III-V family) epitaxially grown on thick and undoped GaSb substrate; yet, transferred to the Al layer by physical or chemical etching.

The complete technological process flow is:

- (vi) **Resist Coating**: The sample is cleaned in acetone and IPA for 2 min then dried with N₂ jet gun and dehydrated for 2 min on a 110°C hotplate. A negative tone resist, namely a diluted AZ2020 (AZ2020:AZ EBR/100:80), is spin-coated with 6 000 rpm for 30 s and baked for 1 min at 110°C, forming thus a 300 nm thick resist layer.
- (vii) **EBL Exposure**: The triangle side length L is set to 1, 2, 5, 10, and 20 μm and the in-between distance is varied from 0.25 to 1 μm with a step of 0.25 μm . EBL exposure is done with four different beam currents equal to 25 pA. The nominal dose is fixed at 14.67 $\mu\text{C}/\text{cm}^2$.
- (viii) **Resist Development**: After the exposure, the resist is directly baked for 1 min at 110°C (inversion bake) and then developed in an AZ726 solution for 10 s. The sample is finally rinsed under running water and dried under N₂ flow.
- (ix) **Argon etching**: the etching results of a critical thin metallic layer using both the chemical and the physical protocols will be detailed.
- (x) **Residual resist cleaning**: At the end, the sample is cleaned using acetone and ethanol, then plasma O₂ for 3 min to clean the residual resist.

Chemical etching:

As reported on the Micro Chemicals website¹³³, the chemical etching solution of Al is a mixture of 3.1 % HNO₃ (for Al oxidation), 73 % H₃PO₄ (to dissolve the Al₂O₃), 3.3 % CH₃COOH (for wetting and buffering) and 20.6 % H₂O dilution to define the etch rate at a given temperature. Indeed, this etchant solution is highly exothermic, thus for a certain etch rate, a certain temperature should

be achieved. For this reason, the solution beaker¹ is placed into a water bath in which the temperature will be measured, indicating the etch temperature. For an etching rate of 0.5×10^3 Å/min (50 nm/min), the etch temperature should be 24°C.

At the end of the process, the triangles are transferred to the Al layer, as shown in the SEM images of **Figure A.3.8** on which additional Energy-dispersive X-ray spectroscopy (EDX) analysis is performed. The data generated by EDX analysis consist of peaked spectra corresponding to the true elemental composition of the analyzed specimen. The selected area 1 is representing the zone outside the triangles and area 2 is the one onto the triangles. As detailed in the accompanying table, the masses percentages of area 1 confirm the formation of a mixture of aluminum and/or gallium oxide on the doped GaSb layer as well as the presence of phosphorous acid residues issued from the etchant solution. A spotless surface of the Al triangles is retrieved based on area 2 analysis, mentioning that both Ga and Sb components are inevitably perceived due to the volume of the beam interacting with the sample surface.

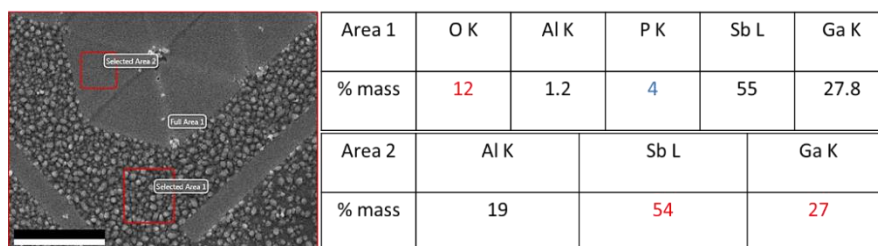


Figure.A.3. 8. EDX analysis of the SEM image of the chemically etched HC transferred to the Al layer (area 2) and surrounded by the doped GaSb layer (area 1) grown on an undoped GaSb substrate. The scale bar is 20 µm long. As detailed in the associated table, Area 1 is covered with Al and or GaSb beads, and P residues, while area 2 is designating a spotless surface of Al triangles.

AFM images stress the roughness of Al and GaSb areas as well as the etch depth. The in-between line shows a depth of around $110 \text{ nm} \pm 10 \text{ nm}$. The GaSb was also attacked during the etching. The RMS of the Al surface is equal to $3.9 \pm 0.6 \text{ nm}$ and $16.0 \pm 3.0 \text{ nm}$ for GaSb into the slit. It is important to note that the Al surface shows some oxide spots of 20 nm as diameter. Plus, the diameter of the oxide beads on the GaSb surface seen on the SEM image in **Figure A.3.8** is around 1.5 µm. Such huge oxide particles are bigger than the width of the open line in-between the Al

¹ To prepare 40 ml etchant solution, we added 29 ml of H₃PO₄, 1.24 ml of HNO₃, 1.32 ml of CH₃COOH and 8.24 ml of H₂O.

triangles (around 1 μm); thus, they can be strictly present on the free GaSb surface (giving there a roughness of 230 ± 90 nm) and not into the slit.

Based on the great damage to the surface following the wet chemical etching of Al, a physical etching process has to be considered.

Physical etching:

In this section, neither the etch rate nor the Al-to-AZ2020 selectivity will be studied, but only the surface state is highlighted following the physical etch. The etching is done in the ICP Corial machine, followed by an argon sputtering recipe (Rf 150 W, Lf 200 W) for 3 min. As illustrated in **Figure A.3.9**, the hexagonally placed triangles are properly defined and the surrounding surface of GaSb seems spotless in comparison to **Figure A.3.10**. Furthermore, the EDX analysis of the selected areas, namely area 1 on the triangles and area 2 on the substrate, proves that the substrate surface is still bearing a small percentage of Al compared to the one revealed at the triangles. Hence, the etching was insufficient to etch the ultimate 50 nm of Al and a considerable thickness of Al film is still covering the GaSb layer. To prove the previous hypothesis, AFM measurements are done to measure the surface roughness after the etching by Ar sputtering. The roughness on the Al is equal to 10 ± 2 nm and 16 ± 3 nm on the surrounding surface (GaSb). Please note that the thickness of the initial Al layer is 11 ± 2 nm. So the retrieved Al after Ar etching is considered proper and smooth. Although the etch rate is not perfectly controlled, Ar sputtering is adopted for etching thin Al layers as the subsequent sample surface will be spotless possible using a physical etching.



Figure.A.3. 9. EDX analysis of the SEM image of the physically etched HC transferred to the Al layer (area 1) and surrounded by the doped GaSb layer (area 2) grown on an undoped GaSb substrate. The scale bar is 10 μm long. As detailed in the associated table, Area 2 is revealing a considerable percentage of Al due to insufficient etching time.

1.6. Annexe.5.1. SEIRA vibrational signal calculation

Systematically, to demonstrate the refractive index variation upon the deposition of the molecules in the vicinity of the plasmonic antennas, the measurement curves with and without vanillin are presented respectively in black and blue curves. The shifting of ω_{res} towards a smaller energy level evidences the SPR effect.

To evaluate the efficiency of the coupling between ω_{res} and ω_{vib} of interest, it is crucial to create a baseline for each measured curve in presence of vanillin, *i.e.* the dashed curve (**Figure A.5.1**).

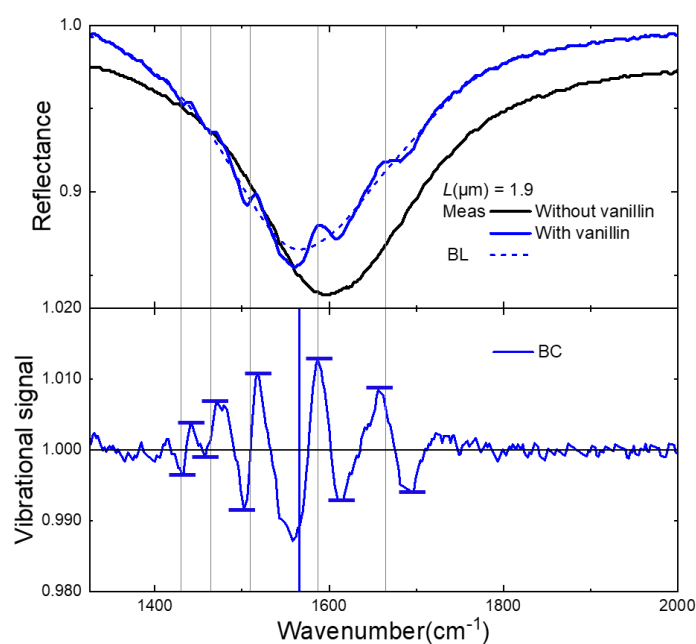


Figure.A.5.1. Evaluation of the SEIRA effect for BT with $L = 1.9 \mu\text{m}$ using Euler's smoothing algorithm. The reference spectrum (without vanillin) and the measured data (with vanillin) are plotted in black and blue curves respectively. The created baseline (BL), blue dashed curve, is flattening the measured data with vanillin by neglecting the asymmetric features. The baseline-line corrected signal (BC) is generated as the ratio between the measured data and its own BL. The former, denoting the vibration signal, is normalized apart from the Fano-like profiles showing the coupling between ω_{res} (blue vertical line) and the assigned ω_{vib} (gray vertical lines).

The flattening of the blue measured curve is done using Elier's smoothing algorithm provided by Dr. Frank Neubrech from University of Stuttgart/ Heidelberg, Germany. This Matlab script is created in a way to perform a baseline correction by introducing the reference spectrum, *i.e.*

measured spectrum without analyte, and the measured data in presence of the analyte. The baseline curve (BL) is produced by smoothing the measured data by neglecting all the asymmetric features using interpolation. Then, a baseline-corrected or background-corrected (BC) signal is generated by dividing the measured data by its BL. The BC will be defined as the vibrational signal, which is normally flat apart from the enhanced ω_{vib} . Note, the shape and size of the asymmetric lines are evaluated in function of their energetic position to the ω_{res} . The ω_{res} is corresponding to each antenna size after the deposition of vanillin and is marked by a colored vertical line. The asymmetric lines (Fano-like profiles) are defined by horizontal bars, and their amplitude is calculated as a peak-to-peak value. The following **Figure A.5.1** shows a sampling of the Fano-like profile analysis.

1.7. Annexe.5.2. EF error propagation formula

Following **Equation 5.2** and the definition of error calculation, a ΔEF is calculated for each L value as follows:

$$\Delta EF = \Delta S_{SEIRA} \times \left| \frac{\partial EF}{\partial S_{SEIRA}} \right| + \Delta S_0 \times \left| \frac{\partial EF}{\partial S_0} \right| + \Delta A_0 \times \left| \frac{\partial EF}{\partial A_0} \right| + \Delta A_{SEIRA} \times \left| \frac{\partial EF}{\partial A_{SEIRA}} \right|$$

Please note that $\Delta S_{SEIRA} = \Delta S_0 = \pm 10^{-4}$ and $\Delta A_0 = 0$ as it is defined based on the FDTD unit cell. A_{SEIRA} is defined around the triangle tip in a radius of 8 nm (based on a FDTD estimation) and excluding the internal part of the tip thanks to the occurring lightning-rod effect.

$$\Delta A_{SEIRA} = \Delta R \times \left| \frac{\partial A_{SEIRA}}{\partial R} \right| ; A_{SEIRA} = 2 \times \frac{5}{6} \pi R^2 ; R = 8 \times 10^{-3} ; \Delta R = \pm 10^{-3} \mu\text{m} ;$$

$$\Delta A_{SEIRA} = \frac{5}{3} \pi R \cdot \Delta R \approx 10^{-5} \mu\text{m}^2. \text{ Thus, } \Delta A_{SEIRA} \times \left| \frac{\partial EF}{\partial A_{SEIRA}} \right| = 10^{-5} \times \left| - \frac{A_0}{(A_{SEIRA})^2} \cdot \frac{S_{SEIRA}}{S_0} \right|.$$

$$\Delta EF = 10^{-4} \times \left| \frac{1}{S_0} \cdot \frac{A_0}{A_{SEIRA}} \right| + 10^{-4} \times \left| - \frac{S_{SEIRA}}{(S_0)^2} \cdot \frac{A_0}{A_{SEIRA}} \right| + 10^{-5} \times \left| - \frac{A_0}{(A_{SEIRA})^2} \cdot \frac{S_{SEIRA}}{S_0} \right|.$$

In detail, the calculation of ΔEF is meticulously presented for the BT ($L = 2 \mu\text{m}$) case in the following table, under co-polarized light and with a gap of 100 nm as plotted in **Chapter 5, Figure 5.6**. A_{SEIRA} (μm^2) = 0.00034 and A_0 (μm^2) = 11.68.

Note that $\Delta A_{SEIRA} \times \left| \frac{\partial EF}{\partial A_{SEIRA}} \right|$ term is considered as a systematic (geometric) error that is only provided for $L = 2.0 \mu\text{m}$ in **Figure 5.6** and is in the order of 10^5 .

L (μm) = 2	ω_{vib} (cm^{-1})	S_0	S_{SEIRA}	$\Delta S_{SEIRA} \times \left \frac{\partial EF}{\partial S_{SEIRA}} \right $	$\Delta S_0 \times \left \frac{\partial EF}{\partial S_0} \right $	ΔEF
ω_{res} (cm^{-1}) = 1523	1430	0.002	0.97	1.74E+03	8.46E+05	8.47E+05
	1464	0.002	1	1.74E+03	8.72E+05	8.73E+05
	1509	0.004	2.04	8.72E+02	4.45E+05	4.45E+05
	1587	0.005	2.13	6.97E+02	2.97E+05	2.98E+05
	1665	0.005	1.248	6.97E+02	1.74E+05	1.75E+05

Table A.5. Error propagation for BT, $L = 2 \mu\text{m}$, $g = 100 \text{ nm}$. In the same manner, the error propagations are calculated for all the L cases.

Communication

Publication:

Najem, M., Carcenac, F., Taliercio, T., Gonzalez-Posada, F., **Aluminum Bowties for Plasmonic-Enhanced Infrared Sensing.** *Adv. Optical Mater.* 2022, 2201025.
<https://doi.org/10.1002/adom.202201025>

International conferences:

- Oral at the 5th International Nanophotonics and Micro/Nano Optics (NANOP) Conference, (October 2022), Paris, France. (**Best oral presentation award winner**).
- Poster at the 48th international conference on Micro and Nano Engineering - Eurosensors (MNE-ES) (Septembre 2022), Leuven, Belgium.
- Oral at the 8th edition of the Workshop on Plasmonics and its Applications, "PLASMONICA 2022", (July 2022), Torino, Italy. (**Best oral presentation award winner**).
- Oral at the Metallic Nano Object (MNO) conference (Octobre 2021), Saint-Etienne, France.
- Oral at the 15th MIOMD virtual conference, (September 2021), University of Surrey, United Kingdom. (**Student oral presentation prize winner**).
- Poster at the 1st International Paris-Saclay/Munich Summer School on Surface Plasmons, (July 2021), Paris-Saclay University, France.

National conferences:

- Oral at the Groupement de recherche (GDR) Plasmonique Active (June 2021), University of Technology (UTT), Troyes, France.
- Oral at the Colloque annuel virtuel du GDR NanoTeraMIR (June 2021), Metz, France.

Ongoing publications:

- Extended SEIRA sensing using Honeycomb plasmonic resonators.
- Plasmonic-based SEIRA for enhancing the CO₂ feature.
- THz time-domain spectroscopy modulated with semiconductor plasmonic perfect absorbers.

Abstract

Plasmonic biosensors have received increasing appreciation owing to their ability to monitor and detect a variety of analytes down to some low concentrations. They are targeting a wide scope of applications mainly in cancer treatment, environmental monitoring, and COVID-19 testing. In the last decade, plasmonic biosensors are flourishing thanks to the fast development in nanofabrication techniques. Indeed, the implemented plasmonic nanoantennas are wisely tailored to combine three key elements: (1) their tunable plasmonic resonances based on their size, composition and arrangement, (2) their aptitude to generate hotspots at their sharp apexes by the lightning-rod effect, and (3) the possibility to improve the intensity of the accompanying near EM-field by involving the activated hotspots into the created gaps. In line with this, we conceive triangular plasmonic resonators, assimilated in a MIM configuration that is integrated on a Si wafer. The triangles are assembled in tip-to-tip faced triangles, so-called Bowties (BT), and in a compact arrangement mimicking the natural Honeycomb (HC) aspect. The scientific breakthrough of this thesis is to develop a barcode-like plasmonic transducer compatible with Si-technology. It will open the route toward the detection of several molecular features in a single test. Actually, it is tailored to cover a wide IR spectrum ranging from 1 000 to 10 000 cm^{-1} by simply modulating the side length of the triangles and their in-between gap size. Alternative to noble metals, Al is selected for being a good plasmonic material, affordable, abundant, and compatible with MOS knowledge. To investigate the spectral response of these periodic Al nanoantennas arrays, FDTD solver (Lumerical) is employed. The excitation source is polarized along or across the tip-to-tip main axis to enhance the near E-field into the corresponding gap where it will be strongly localized. It reaches $\sim 10^3$ for a BT with a gap of 20 nm. Special attention is paid to the insensitivity of the HC resonance thanks to their symmetry invariance regardless of the light polarization direction. For each L value, one main plasmonic resonance peak is detected. Al nanoantennas are mainly characterized using Fourier Transform IR (FTIR) spectrometer. A good agreement is achieved between simulation (FDTD) and experiment (FTIR) results. 50 nm-thick Al nanoantennas are fabricated by combining electron-beam lithography with either metallization and lift-off processes or argon etching and resist cleaning technology. The Al nanoantennas are built on a 20 nm-thick SiO_2 layer, sputtered on top of a 100 nm thick Al layer as a mirror. The

metallic sharp-ended nanostructures are appealing to highly localize and enhance the near-field that is engaged in boosting the sensing applications, especially the surface-enhanced IR absorption (SEIRA) spectroscopy. Indeed, SEIRA is arising from the coupling between the plasmonic resonance and the triggered molecular vibration frequency owing to the increased interaction cross-section which is a limiting factor for traditional Raman and IR spectroscopies. Our multiresonant surface is combining two complementary methods, namely the refractive index or surface plasmon resonance (SPR) sensing and the SEIRA spectroscopy. Both are relying on surface plasmon-based effects to probe the molecule presence in the vicinity of the plasmonic nanoantennas. Furthermore, the coupling strength between both the broad plasmonic and the discrete vibrational frequencies is modulated and expressed by different asymmetric features. The shape and amplitude of these features will be modulated by a frequency tuning ratio. A maximum value of the SEIRA spectral features and enhancement factors (EF) is spectrally found for a tuning ratio below 1. The SEIRA demonstration is proved for an aromatic component in solution as well as for ambient carbon dioxide. The SEIRA results were matching the state-of-art, *e.g.* EF up to 10^7 could be achieved while sensing around 10^4 molecules in solution per hotspot, and EF around 10^5 for a few hundreds of gaseous molecules into the gap. Ultimately, this research paves the way toward extended and cost-effective SEIRA transducers. We foresee an integral combination with microfluidic channels, source, and detector suitable for a selected application for liquid and/or gas sensing.

Résumé

Les biocapteurs plasmoniques ont reçu une appréciation croissante en raison de leur capacité à surveiller et à détecter une variété d'analytes jusqu'à de faibles concentrations. Ils ciblent un large éventail d'applications, principalement dans le traitement du cancer, la surveillance environnementale et les tests du COVID-19. Au cours de la dernière décennie, les biocapteurs plasmoniques ont prospéré grâce au développement rapide des techniques de nanofabrication. En effet, les nanoantennes plasmoniques mises en œuvre sont judicieusement adaptées pour combiner trois éléments clés : (1) une résonance plasmonique accordable en fonction de leurs tailles, de leurs compositions et de leurs arrangements, (2) leur capacité à générer des points chauds à leurs sommets pointus par l'effet de pointe, et (3) la possibilité d'améliorer l'intensité du champ proche électromagnétique qui l'accompagne en impliquant les points chauds activés dans les gaps créés. En vue de cela, nous concevons des résonateurs plasmoniques triangulaires, intégrés dans une configuration MIM reposant sur un substrat de Si. Les triangles sont arrangés face à face, appelés nœuds de papillon (Bowties, BT), et dans un arrangement compact imitant la forme naturelle du nid d'abeille (Honeycombs, HC). La découverte scientifique capitale de cette thèse est de développer un transducteur plasmonique de type barre-code compatible avec la technologie MOS. Il ouvrira la voie à la détection de plusieurs caractéristiques moléculaires en un seul test. En fait, il est conçu pour couvrir un large spectre de l'IR allant de 1 000 à 10 000 cm^{-1} , simplement en modulant la longueur des côtés des triangles et la taille de leur espacement. Alternative aux métaux nobles, l'Al est sélectionné étant un bon matériau plasmonique, abordable, abondant et compatible avec les connaissances MOS. Pour étudier la réponse spectrale de ces réseaux périodiques de nanoantennes d'Al, le calcul FDTD est mis en place en utilisant le programme Lumerical. La source incidente est polarisée le long ou à travers l'axe principal de l'antenne (pointe-à-pointe) pour exalter le champ électrique proche dans les gaps correspondant, où il sera fortement localisé. L'intensité du champ électrique atteint $\sim 10^3$ pour les BT d'un gap de 20 nm. Une attention particulière est portée à l'invariance de la réponse des HC grâce à leur symétrie quelle que soit la direction de polarisation de la lumière. Pour chaque valeur L , un pic principal de résonance plasmonique est détecté. Les nanoantennes d'Al sont principalement caractérisées à l'aide d'un spectromètre infrarouge à transformée de Fourier

(FTIR). Un bon accord se manifeste entre la simulation (FDTD) et l'expérience (FTIR). Les nanoantennes d'Al de 50 nm d'épaisseur sont fabriquées en combinant la lithographie électronique avec des processus de métallisation et de décollage (lift-off) ou une gravure à l'argon et une technologie de nettoyage de résine. Les nanoantennes d'Al sont construites sur une couche de SiO₂ de 20 nm d'épaisseur, pulvérisée sur une couche d'Al de 100 nm d'épaisseur qui sert de miroir. Les nanostructures métalliques à extrémités pointues sont séduisantes pour localiser et améliorer le champ proche qui est exploité dans la stimulation des applications de détection, en particulier la spectroscopie vibrationnelle exaltée dans l'infrarouge par des effets plasmonique de surface, nommée SEIRA. En effet, la SEIRA est issue du couplage entre la résonance plasmonique et la fréquence de vibration moléculaire provoquée en raison de l'augmentation de la section efficace d'interaction qui est un facteur limitant pour les spectroscopies Raman et IR traditionnelles. Notre surface multirésonante combine deux méthodes complémentaires : la détection de l'indice de réfraction ou de la résonance plasmonique de surface (SPR) et la spectroscopie SEIRA. Toutes les deux reposent sur des effets basés sur les plasmons de surface pour sonder la présence de molécules au voisinage des nanoantennes plasmoniques. De plus, la prononciation du couplage entre les larges fréquences plasmoniques et les fréquences vibratoires discrètes sera modulée. La forme et l'amplitude de ces modulations asymétriques seront analysées par un rapport d'accord de fréquence (tuning ratio). Une valeur maximale des modulations asymétriques de la SEIRA et de ses facteurs d'exaltation (EF) est trouvée spectralement pour un rapport d'accord légèrement inférieur à 1. La démonstration SEIRA est prouvée pour un composant aromatique en solution ainsi que pour le dioxyde de carbone ambiant. Les résultats de la SEIRA correspondaient à l'état de l'art, par exemple un EF de l'ordre de 10^7 pourrait être atteint tout en détectant environ 10^4 molécules en solution par pointe, et un EF est de l'ordre d'environ 10^5 pour quelques centaines de molécules gazeuses. En fin de compte, ces recherches ouvrent la voie à des transducteurs SEIRA étendus sur une large bande spectrale et rentables. Nous prévoyons une combinaison intégrale avec des canaux microfluidiques, une source et un détecteur adaptés à une application sélectionnée pour la détection de liquide et/ou de gaz.

